



HAL
open science

Determination of fatigue properties of Multidirectional composite laminates (MD) based on thermography measurements

Zijiao Jia

► **To cite this version:**

Zijiao Jia. Determination of fatigue properties of Multidirectional composite laminates (MD) based on thermography measurements. Mechanical engineering [physics.class-ph]. Université Paul Sabatier - Toulouse III, 2022. English. NNT : 2022TOU30323 . tel-04213713

HAL Id: tel-04213713

<https://theses.hal.science/tel-04213713>

Submitted on 21 Sep 2023

HAL is a multi-disciplinary open access archive for the deposit and dissemination of scientific research documents, whether they are published or not. The documents may come from teaching and research institutions in France or abroad, or from public or private research centers.

L'archive ouverte pluridisciplinaire **HAL**, est destinée au dépôt et à la diffusion de documents scientifiques de niveau recherche, publiés ou non, émanant des établissements d'enseignement et de recherche français ou étrangers, des laboratoires publics ou privés.



THÈSE

En vue de l'obtention du

DOCTORAT DE L'UNIVERSITÉ DE TOULOUSE

Délivré par :

Université Toulouse 3 Paul Sabatier (UT3 Paul Sabatier)

Présentée et soutenue par :

Zijiao JIA

le jeudi 15 décembre 2022

Titre :

Determination of fatigue properties of MultiDirectional composite laminates (MD) based on thermography measurements

École doctorale et discipline ou spécialité :

ED MEGEP : Génie mécanique, mécanique des matériaux

Unité de recherche :

Institut Clément Ader, site de Tarbes; Laboratoire Génie de Production (LGP) de l'ENIT

Directeur/trice(s) de Thèse :

XiaoJing GONG

Jury :

Zoheir ABOURA	Professeur, l'université de Technologie de Compiègne	Examineur
Pascal CASARI	Professeur, Nantes l'université	Rapporteur
Alexis BEAKOU	Professeur, Sigma Clermont	Rapporteur
Xiaojing GONG	Professeur, IUT Tarbes	Directrice du thèse
Marie-Laetitia PASTOR	MCF, IUT-Tarbes	Co-encadrant
Christian GARNIER	MCF, l'ENIT Tarbes	Co-encadrant

Acknowledgements

Firstly, I would like to express my special thanks of gratitude to my research supervisors Prof. Xiaojing Gong as well as Dr. Marie-Laetitia Pastor and Dr. Christian Garnier for providing invaluable guidance and compelling support throughout the study. I am grateful for their patience, enthusiasm and immense knowledge. Their rigorous and serious attitude towards scientific research has deeply inspired me.

My special thanks also go to Mr. Guillaume Morel, Mr. Frederic Leroy, Mrs. Virginie Lagarde, Mr. Jérôme Rousseau, Mr. Marc Chartrou, Mrs. Louison Bernardi, Mr. Jean-Noël Périé, Mr. Olivier Sicot for their kind help.

I thank my fellow labmates for their help in the life and work, and for all the fun we have had in the last three years.

I am extremely grateful to China Scholarship Council (CSC) for the three years financial support to cover all my living costs in France. I would like to thank Education Section of the Embassy of the People's Republic of China in the French Republic, “Union des Chercheurs et des Etudiants Chinois en France”, Tarbes local government, local friendly citizens and all the Chinese people and students in Tarbes for all their support and assistance.

Last but not the least, I would like to thank my parents for their love, caring and supports. They are always the source of power in my life.

Contents

Abstract	1
Résumé	3
General Introduction	5
Chapter 1 Literature review	9
1.1 Introduction and background	9
1.1.1 Definition of composite materials	9
1.1.2 Properties and preparation of CFRP	10
1.1.3 Applications of CFRP	14
1.2 Determination of fatigue property	16
1.2.1 Traditional fatigue testing	16
1.2.2 Fatigue damages in CFRP	17
1.3 Rapid determination of fatigue property based on IRT	21
1.3.1 Theoretical framework	21
1.3.2 Infrared thermography	24
1.3.3 Review of fatigue property determination method based on IRT	27
1.4 Determination of post-impact fatigue properties	38
1.4.1 Characterization of impact damage	38
1.4.2 Post-impact residual properties	40
1.4.3 Post-impact-fatigue life prediction of composite materials	41
1.4.4 Rapid determination of post-impact fatigue properties with IRT	45
1.5 Summary	47
Chapter 2 Determination of fatigue limit of MultiDirectional (MD) composite materials under tensile loading	49
2.1 Materials and specimens	49
2.1.1 Materials	49

2.1.2	Preparation of CFRP laminates	50
2.2	Quasi-static tensile tests	52
2.2.1	Experiments.....	52
2.2.2	Results and discussion.....	53
2.3	Fatigue tensile tests	55
2.3.1	Experiments.....	55
2.3.2	Traditional fatigue test results	58
2.4	Rapid determination methodology for fatigue limit.....	59
2.4.1	Introduction	59
2.4.2	A review of fatigue limit determination methods.....	61
2.4.3	Thermographic data treatment method proposed by Huang et al. [17].....	63
2.4.4	Proposed method	65
2.4.5	Influence of loading step length on measured fatigue limit by the proposed method.....	66
2.4.6	Application of proposed method to the experimental data of present work	69
2.4.7	Application of proposed method to the data published in the literature	72
2.5	Summery	75
Chapter 3	Determination of S-N curve of MultiDirectional (MD) composite materials.....	76
3.1.1	Introduction	76
3.1.2	Huang' model [18].....	77
3.1.3	Application of the model proposed by Huang et al. [18] to QI laminates ...	79
3.1.4	Proposition of the modification of Huang's model for characterization of S-N curve	82
3.2	Validation of the proposed model.....	85
3.2.1	QI laminates	85
3.2.2	Cross-ply laminates	87
3.3	Determination of an average S-N curve considering the variability of thermographic data	89

3.3.1	Cross-ply laminates	89
3.3.2	QI laminates	95
3.4	Summary	97
Chapter 4	Compression-compression fatigue behavior of CFRP	99
4.1	QIQH laminates.....	99
4.1.1	Classical Laminated Plate Theory (CLPT)	100
4.1.2	Polar description of plane anisotropy [236]	101
4.1.3	Application of polar method to the laminates	104
4.1.4	Design of QIQH laminates	105
4.2	Materials and specimens	105
4.2.1	Materials.....	105
4.2.2	Preparation of specimens	108
4.3	Static compression tests	110
4.3.1	Experiments.....	110
4.3.2	Results and discussion.....	111
4.4	Compression-compression fatigue test.....	117
4.4.1	Experiments.....	117
4.4.2	Determination of the fatigue limit.....	119
4.4.3	S-N curves	120
4.4.4	Determination of a more overall average reliable S-N curve.....	123
4.4.5	Damage morphology	124
4.5	Chapter summary	127
Chapter 5	Post-impact compression fatigue behavior	129
5.1	Impact tests.....	129
5.1.1	Materials and specimens	129
5.1.2	Preliminary impact tests	130
5.1.3	Experiments.....	134
5.1.4	Results and discussion.....	136

5.2	Compression After Impact (CAI) tests	146
5.2.1	Experiments.....	146
5.2.2	Static CAI test results	146
5.2.3	Fracture surfaces observations	148
5.3	Post-impact compression-compression fatigue test	154
5.3.1	Experiments.....	154
5.3.2	Temperature distribution	155
5.3.3	Rapid determination of the fatigue limit	155
5.3.4	Determination of S-N curves for each configuration	157
5.3.5	Determination of overall “average” S-N curves based on the data of all specimens	159
5.3.6	Fracture surfaces observations	161
5.4	Comparison of non-impacted and impacted specimens	163
5.4.1	Static compression properties.....	163
5.4.2	Fatigue limit	164
5.4.3	S-N curves	165
5.4.4	Fracture surface observations.....	166
5.5	Chapter summary	166
	Conclusions and perspectives.....	170
	References	176
	Relevant publications	192

List of figures

Figure 1-1. Formation of a composite material using reinforcement (fiber) and matrix (resin) [21]	10
Figure 1-2. Schematic figure of directions in CFRP [25].....	11
Figure 1-3. Schematic presentation of manufacturing methods of CFRP [39][40].....	13
Figure 1-4. Airframe material distributions and percentages for the Boeing 787 [43]	14
Figure 1-5. Principle of staircase approach [56]	16
Figure 1-6. S-N curves of carbon/PEEK and carbon/epoxy laminates loaded in tension-tension fatigue [56].....	17
Figure 1-7. Mid-ply matrix cracking observed during fatigue test of different layups [62] ...	18
Figure 1-8. Edge view of a CFRP laminate showing delamination between plies:(a) overall view;	18
Figure 1-9. Coalescence of fiber-matrix debonding into a crack [70].....	19
Figure 1-10. SEM micrograph of fiber pull-out [71]	20
Figure 1-11. The fracture morphologies of fiber broken in fatigue [72]	20
Figure 1-12. Typical time dependent temperature evolution during fatigue tests [84]	24
Figure 1-13. Evolution of surface temperature profile [102]	28
Figure 1-14. Temperature and normalized axial stiffness profile [103]	28
Figure 1-15. Thermographs showing the crack growth during composite fracture and contour plots of maximum damage zones at crack tip [110].....	29
Figure 1-16. The difficulty of determining unique fitting cut-off point	31
Figure 1-17. 316L stainless steel sample submitted to a fatigue test at frequency $f=2Hz$ ($R=-1$). Lock-in thermography provides an image of ΔT , $T1$ and $T2$: (a) $\Delta T(\sigma)$; (b) $T1(\sigma)$; (c) the difference between and the linear fit of its initial part; (d) $T2(\sigma)$. Each point is the result of 10 cycles. Failures occurs during the test at 270MPa [140].....	33
Figure 1-18. Fatigue limit determination by D-mode method [144].....	34

Figure 1-19. Qualitative increase in temperature ΔT and energetic parameter ϕ for	35
Figure 1-20. Rate of temperature in stage I and stabilized temperature rise in stage II increase with the increase of stress level [147]	36
Figure 1-21. Universal curve of $Nf/c1$ versus $R\theta$ [148]	36
Figure 1-22. Schematic presentation of temperature variation with time used for fatigue life prediction [14]	37
Figure 1-23. Schematic definition of ΔT_{ind} [150]	37
Figure 1-24. Individual delamination caused by impact: (a) distribution of delamination [157][158];	39
Figure 1-25. Fiber fractures in the laminates: (a) 16 plies; (b) 48 plies [161]	40
Figure 1-26. Failure mechanisms for compression after impact	41
Figure 1-27. Strength reduction behavior due to impact and fatigue loading [170]	43
Figure 2-1. Autoclave process schematic [139]	51
Figure 2-2. Recommended curing cycle.....	51
Figure 2-3. Dimensions of specimens (in accordance with ISO 527-4: 2021 [184]).....	52
Figure 2-4. Experimental set-up of quasi-static tensile test with DIC	52
Figure 2-5. Principle of DIC.....	53
Figure 2-6. Load-displacement curve of tensile tests	54
Figure 2-7. Stress-strain curve of tensile tests.....	54
Figure 2-8. Fatigue tests with IR camera: (a) staircase loading procedure; (b) experimental set-up	57
Figure 2-9. IR temperature distribution at center portion of specimen	57
Figure 2-10. Hysteresis loops during fatigue tests	58
Figure 2-11. S-N curve determined by traditional fatigue tests for the QI CFRP laminates... ..	59
Figure 2-12. S-N curve determined by traditional fatigue tests for the cross-ply CFRP laminates.....	59
Figure 2-13. Variation of temperature over time during constant amplitude fatigue loading [17]	62

Figure 2-14. Step-loading procedure for R=0.1	62
Figure 2-15. Fatigue limit determination by TCM and OCM	63
Figure 2-16 Definition of angle θ_i [17].....	64
Figure 2-17 Loci of normalized angle change versus sequence number of point [17]	65
Figure 2-18. Schematic explanation of the special case: (a) stabilized temperature rise remains constant; (b) stabilized temperature rise decreases with the increase of stress level..	66
Figure 2-19. Loci of normalized angle change vs. sequence number of the point based on data	66
Figure 2-20. The influence of loading step length on the determined fatigue limit.....	67
Figure 2-21. Relative error between determined results and the results obtained by the smallest loading step length in Ref. [199] and [203]	68
Figure 2-22. Influence of loading step length on the fatigue limit for CFRP of different stacking sequences	69
Figure 2-23 Surface temperature rise versus number of loading cycles of specimen 1 of QI laminates.....	69
Figure 2-24 Surface temperature rise versus number of loading cycles of specimen 1 of cross-ply laminates	70
Figure 2-25. Stabilized temperature rise vs maximum stress of QI specimen 1	70
Figure 2-26. Stabilized temperature rise vs maximum stress of cross-ply specimen 1.....	71
Figure 2-27. Loci of θ_{ic} versus number of points in the sequence of specimens 1 of QI and	72
Figure 2-28. Experimental data of stabilized temperature rise vs maximum stress in [211] ..	73
Figure 3-1 A typical trend for stiffness degradation and damage accumulation during fatigue loading [139]	77
Figure 3-2. Variation of temperature rise with the number of loading cycles of QI specimen 2	80
Figure 3-3. Fatigue limit determination of QI laminate (specimen 2): (a) stabilized temperature rise vs maximum stress; (b) loci of normalized angle change vs sequence number	

of the point	80
Figure 3-4. Surface fitting of Eq. (3-3) by MATLAB [®]	81
Figure 3-5. Comparison of S-N curves determined by Huang's model with traditional experimental results.....	82
Figure 3-6. Normalized stiffness degradation vs stabilized temperature rise for UD and $\pm 45^\circ$ laminates (data from [18] and [19]).....	84
Figure 3-7. Normalized stiffness degradation vs stabilized temperature rise for QI laminates	84
Figure 3-8 Comparison of S-N curve determined by proposed model with traditional fatigue test results	86
Figure 3-9 Evolution of temperature rise vs number of cycles of cross-ply specimen 2	87
Figure 3-10 Fatigue limit determination of cross-ply specimen 2: (a) stabilized temperature rise vs.....	87
Figure 3-11 Surface fitting of Eq. (3-11) by MATLAB [®]	88
Figure 3-12 Comparison of S-N curve obtained by proposed model with traditional fatigue test results	89
Figure 3-13. Comparison of S-N curves based on thermographic data of three specimens with	90
Figure 3-14. Fatigue limit determination based on data of three specimens: (a) normalized stabilized temperature rise vs maximum stress; (b) loci of normalized angle change vs sequence number of the point.....	91
Figure 3-15. Surface fitting using Eq. (3-11) in MATLAB [®]	92
Figure 3-16. Determined S-N curve calculated based on the average data of three cross-ply specimens and traditional fatigue test results	92
Figure 3-17. Fatigue limit determination based on data of specimens 1 and 2: (a) normalized stabilized temperature rise vs maximum stress; (b) loci of normalized angle change vs sequence number of the point.....	93
Figure 3-18. Surface fitting using Eq. (3-11) in MATLAB [®]	94

Figure 3-19. Determined S-N curve calculated based on the average data of specimens 1 and 2.....	95
Figure 3-20. Determined S-N curve calculated based on the average data of two QI specimens	96
Figure 4-1. Sketch for the numbering of layers and interfaces [235].....	101
Figure 4-2. Schematic illustration of the rotation of frames	102
Figure 4-3. Polar description of quasi-isotropy in stiffnesses for the three stacking sequences:	108
Figure 4-4. Schematic illustration of pre-cure compaction process	109
Figure 4-5. Preparation of specimens: (a) recommended curing cycle; (b) specimens.....	109
Figure 4-6. Dimensions of specimens: (a) compression and CAI test specimens; (b) fatigue and post-impact fatigue test specimens	110
Figure 4-7. Experimental set-up of static compression tests	111
Figure 4-8. Force-displacement curves of static compression tests	112
Figure 4-9. Typical load-displacement curve of compression tests.....	112
Figure 4-10. Details of fracture surfaces	117
Figure 4-11. Experimental set-up of fatigue and post-impact fatigue tests.....	118
Figure 4-12. Modification of CAI fixture.....	118
Figure 4-13. Variation of temperature rise vs number of loading cycles	119
Figure 4-14. Fatigue limit determination of QIQH-1-1: (a) stabilized temperature rise vs maximum stress; (b) loci of normalized angle change vs. sequence number of point.....	120
Figure 4-15. Determined fatigue lives for three QIQH stacking sequences:	122
Figure 4-16. S-N curves of specimens with identical fatigue limits but different stacking sequences.....	123
Figure 4-17. Individual predicted S-N curves and more reliable S-N curves for QIQH laminates.....	124
Figure 4-18. Fracture surfaces having first ply fibers at 0° of compression fatigue specimens:	127

Figure 5-1. Theoretical dimensions of post-impact fatigue test specimens [241].....	130
Figure 5-2. Schematic illustration of adaptation of specimens to fixture of impact tower: (a) specimens with dimensions of L150×W100 mm; (b) L250×W90 mm.....	130
Figure 5-3. C-scan images of preliminary impact test specimens: (a) specimen 1; (b) specimen 2.....	131
Figure 5-4. Observation of cut-sections of laminates defined as Side 1 and Side 2	132
Figure 5-5. Cut-sectional photographs of preliminary impact test specimens:	133
Figure 5-6. Schematic diagram of indentator at the front surface of specimen (front view)	134
Figure 5-7. Impact testing instrument	135
Figure 5-8 C-scan inspection: (a) experimental set-up; (b) scanning directions.....	136
Figure 5-9. Raw and filtered force-time curve of QIQH-1-3 with dimensions of 150*100mm	136
Figure 5-10. Load-time curves for QIQH-1: (a) 150×100mm; (b) 250×90mm.....	138
Figure 5-11. Load-time curves for QIQH-2: (a) 150×100mm; (b) 250×90mm.....	138
Figure 5-12. Load-time curves for QIQH-3: (a) 150×100mm; (b) 250×90mm.....	138
Figure 5-13. Load-displacement curve for QIQH-1: (a) 150×100mm; (b) 250×90mm.....	139
Figure 5-14. Load-displacement curve for QIQH-2: (a) 150×100mm; (b) 250×90mm.....	139
Figure 5-15. Load-displacement curve for QIQH-3: (a) 150×100mm; (b) 250×90mm.....	139
Figure 5-16. Energy-time curve for QIQH-1: (a) 150×100mm; (b) 250×90mm	141
Figure 5-17. Energy-time curve for QIQH-2: (a) 150×100mm; (b) 250×90mm	141
Figure 5-18. Energy-time curve for QIQH-3: (a) 150×100mm; (b) 250×90mm	141
Figure 5-19. Load vs. displacement curves of CAI tests.....	147
Figure 5-20. Commonly observed acceptable CAI failure modes [240].....	152
Figure 5-21. Details of fracture surfaces:	153
Figure 5-22. Temperature distribution on the specimen surface during post-impact fatigue tests.....	154
Figure 5-23. Thermographic images and damage characteristics: (a) - (c): thermographic images in different stages; (d) specimen profile after failure (front impacted surface);.....	155

Figure 5-24. Variation of temperature rise of impact damage zone as a function of.....	156
Figure 5-25. Fatigue limit determination of impacted QIQH-1 specimen.	156
Figure 5-26. Determined post-impact fatigue lives for three QIQH stacking sequences: (a) QIQH-1; (b) QIQH-2; (c) QIQH-3.....	159
Figure 5-27. S-N curves of all post-impact fatigue specimens having identical fatigue limits	159
Figure 5-28. Individual predicted S-N curves and more reliable S-N curves for post-impact compression fatigue QIQH laminates	161
Figure 5-29. Details of fracture surfaces: (a) QIQH-1 (left: 45°; right:0°); (b) QIQH-2 (left: 0°; right: 45°); (c) QIQH-3 (left: 0°; right: 90°).....	163
Figure 5-30. Comparison of fatigue limits between non-impacted and impacted specimens	165
Figure 5-31. Comparison of predicted S-N curves ($N_{fl} = 106$ cycles) between non-impacted and	165

List of tables

Table 1-1. Summary of the last 5 years (2018-2022) work of fatigue limit prediction based on Risitano and Luong's method (sorted according to year).....	31
Table 2-1 Basic physical properties of HexPly®M79	49
Table 2-2 Basic mechanical property of the cured epoxy carbon fiber prepreg	50
Table 2-3. Average experimental results of tensile tests	55
Table 2-4. Summarized results of fatigue limit determined by manual graphic method, conventional experimental method and proposed method	74
Table 3-1. Fatigue limit and calibration parameters of specimen 1, 2 and 3	90
Table 3-2. Fatigue limit and calibration parameters	96
Table 4-1 Basic mechanical properties of SE84LV/HEC/150/400/37+/-3%.....	106
Table 4-2. Laminate configurations: stacking sequences	107
Table 4-3. Laminate configurations: number of interfaces.....	107
Table 4-4. In-plane and bending elastic properties (GPa)	107
Table 4-5. UCS of compression test specimens.....	113
Table 4-6. Fracture surfaces of specimens under compression loading	114
Table 4-7. Fatigue limit of each specimen using proposed method	120
Table 4-8. Determined parameters for different stacking sequences.....	121
Table 4-9. Fatigue limit and calibration parameters	124
Table 5-1. Impact testing conditions.....	135
Table 5-2. Impact testing results	142
Table 5-3. Visual inspections of BVID impact damage (dimensions of each image: 76×76mm)	143
Table 5-4. Matrix cracks observed by optical microscope at back surface of the specimens	143
Table 5-5. C-scan results of impacted specimens with dimensions of 150×100mm.....	145
Table 5-6. C-scan results of impacted specimens with dimensions of 250×90mm.....	145

Table 5-7. Projected delamination area A_{proj} and diameter d_{proj}	146
Table 5-8. Compression test results of non-impacted and impacted specimens.....	148
Table 5-9. Fracture surfaces of impacted specimens under CAI loading	149
Table 5-10. Three-place failure mode codes [240]	152
Table 5-11. Determined fatigue limit and corresponding stabilized temperature rise of each QIQH specimen.....	157
Table 5-12. Determined parameters for different stacking sequences.....	158
Table 5-13. Fatigue limit and calibration parameters	160
Table 5-14. Fracture surfaces of post-impact compression fatigue specimens.....	161
Table 5-15. Comparison of relative difference between the forces at point B and at the point C for the non-impacted and impacted specimens	164

Nomenclature

σ_{am}	stress amplitude of cyclic loading	$T_{exp}(t_i)$	experimental temperature value at time t_i
σ	maximum stress	$T_{mod}(t_i)$	model temperature at time t_i
N_f	number of cycles at failure	$P_i (i = n)$	the points
ρ	mass density	T_1	amplitude of the first Fourier component of temperature T_{mod}
C	specific heat density	φ_1	phase of the first Fourier component of temperature T_{mod}
k	thermal conductivity	T_2	amplitude of the second Fourier component of temperature T_{mod}
ε	strain tensor	φ_2	phase of the second Fourier component of temperature T_{mod}
α	internal variable	ΔT	mean rise of temperature per cycle
φ	Helmholtz free energy	p'	constants of Huang's model [18]
d_1	intrinsic dissipation	q	constants of Huang's model [18]
S_{the}	thermoelastic source	r	Constants of our proposed normalized stiffness degradation model
S_{int}	thermo-mechanical couplings	σ	Stefan-Boltzmann constant
q_e	external heat supply	ε	emissivity of the surface
T	absolute temperature	N_{env}	radiance emitted by the surrounding environment
T_0	ambient temperature	E_c	amount of energy to failure per unit volume (limiting energy)
θ	temperature rise	Φ	energetic parameter: cumulative amount of the thermal increments per volume unit in the fracture zone
ΔT_{stab}	stabilized temperature rise	N_{fi}	fatigue life under different stress levels σ_i
θ_{the}	temperature rise induced by thermoelastic source	R_θ	rate of temperature rise in stage I
θ_{int}	temperature rise induced by intrinsic dissipation	ΔT_{ind}	temperature variation index
λ	linear thermal expansion coefficient	σ_0	tensile strength
f	loading frequency	n_i	number of cycles at σ_i
τ_{eq}	time constant en 2D	N_i	fatigue life when σ_i is applied
Q_{diss}	generated dissipated energy	D	diameter of impactor
N_{imp}	fatigue life of impacted composite materials	E_a	absorbed impact energy
σ_{HR}	tensile strength of notched specimen	D_0	initial impact damage
D_i	diameter of permanent impression	R^2	coefficient of determination
$K(N)$	experimental stiffness	ΔT_{stab}^*	normalized stabilized temperature rise

θ_i	angle between the line determined by the point set $\{P_{i-1}, P_i\}$	$(\Delta T_{stab})_{max}$	maximum value of stabilized temperature rise
θ_i^c	Normalized angle change	p	constant, $p = p' \times (\Delta T_{stab})_{max}^r$
K_f^*	residual stiffness corresponding to final cycle prior to failure N_f^*	ΔT_{stab_fl}	stabilized temperature rise at fatigue limit
$k(N)$	normalized residual stiffness at N^{th} cycle	$\overline{\Delta T_{stab}^*}$	average normalized stabilized temperature rise
k_f^*	normalized residual stiffness at final cycle N_f^*	$Q(\delta_k)$	intrinsic stiffness of the ply
N	in-plane forces	δ_k	global coordinate axes
M	bending moments	z_k	distances between the top surfaces and the middle plane
ε^0	middles-plane strains	R	modulus of polar decomposition of a vector F
κ	curvatures	b, b_0, b_1	polar angles
A	in-plane or membrane stiffness	A_1, A_2	Cartesian components of vector F
D	out-of-plane or bending stiffness	B_0, B_1	scalars of polar decomposition of a plane tensor of 4 th order
B	membrane-bending coupling stiffness	R_0, R_1	modulus of polar decomposition of a plane tensor of 4 th order
F	contact force	k	rigidity associated with deformation
α	indentation depth	A_{proj}	projected delamination area
d_{proj}	diameter of projected delamination area		

Abstract

Fatigue of Carbon Fiber Reinforced Polymer (CFRP) composites is one of the topics that receive more and more attention since these materials are increasingly used for the manufacturing of loading-bearing components in the aeronautical, automotive and marine industries. The objective of this thesis is to develop methodologies that allow to evaluate the fatigue and post-impact fatigue properties of MultiDirectional (MD) CFRP in a short time based on the analysis of thermographic data measured by the infrared camera.

A new fatigue limit determination method is first proposed to overcome the limitations of traditional graphic methods (Luong and Risitano's methods). The stress amplitude corresponding to the peak value of angle change normalized by their amplitude, is defined as the fatigue limit. The proposed method was evaluated by the experimental data of cross-ply and Quasi-Isotropic (QI) CFRP laminates obtained in this study, as well as the data of various materials in the literature. Then, in view of more complex damage mechanisms in MD laminates, a previously proposed fatigue life prediction model, which combines the stiffness degradation with thermographic data and which has been successfully applied to Unidirectional (UD) and $\pm 45^\circ$ CFRP laminates, is modified. A new parameter r is introduced into the expression of residual stiffness to overcome the conservative predictions resulted from the original model. In addition, the stabilized temperature rise is normalized by the maximum value reached for the ease of comparison between different specimens. A protocol to determine a more reliable S-N curve from individual predicted S-N curves of several specimens is also proposed. To further demonstrate the generality of proposed methodologies, the above-mentioned fatigue limit determination method and fatigue life prediction model were also applied to the compression-compression fatigue and post-impact compression fatigue Quasi-Isotropic Quasi-Homogeneous (QIQH) CFRP laminates with three different stacking sequences. The results imply that the fatigue limit determination method and fatigue

life prediction model proposed in this study can be used to rapidly determine the fatigue limit and predict the S-N curves of MD CFRP composite materials with more than 87% of precision. The results of this work are interesting for industrial application because with the use of proposed methodologies, the duration of fatigue test is considerably reduced (saving at least 50 times of time) and it makes possible to know the fatigue properties of composites irrespective of stacking sequence and mode of loading (tension or compression).

Key words: Infrared Thermography, Fatigue Limit, Fatigue Life Prediction, Multidirectional CFRP, Post-impact Fatigue

Résumé

La fatigue des composites polymères renforcés par des fibres de carbone (CFRP) est un sujet important puisque ces matériaux sont de plus en plus utilisés pour la fabrication des éléments porteurs dans les industries aéronautique, automobile et maritime. L'objectif de cette thèse est de développer des méthodologies permettant d'évaluer les propriétés de fatigue et de fatigue post-impact de MultiDirectionnel (MD) CFRP en un temps court sur la base de l'analyse des données thermographiques mesurées par la caméra infrarouge.

Une nouvelle méthode de détermination de la limite de fatigue a d'abord été proposée pour surmonter les limites des méthodes graphiques traditionnelles (méthodes de Luong et de Risitano). L'amplitude de contrainte correspondant à la valeur maximale du changement d'angle normalisé par leur amplitude, est définie comme la limite de fatigue. La méthode proposée a été évaluée à partir des données expérimentales obtenues dans cette étude sur les stratifiés CFRP à plis croisés et Quasi-Isotropes (QI), ainsi que sur des données de divers matériaux de la littérature. Ensuite, compte tenu des mécanismes d'endommagement plus complexes dans les stratifiés MD, un modèle de prédiction de durée de vie en fatigue précédemment proposé, qui combine la dégradation de la rigidité avec des données thermographiques et qui a été appliqué avec succès aux stratifiés Unidirectionnels (UD) et $\pm 45^\circ$ CFRP, est modifié. Un nouveau paramètre r est introduit dans l'expression de la rigidité résiduelle pour surmonter les prédictions conservatrices résultant du modèle original. De plus, l'élévation de température stabilisée est normalisée à sa valeur maximale à des fins de comparaison entre différents spécimens. Un protocole pour déterminer une courbe S-N plus fiable à partir des courbes S-N prédites individuelles de plusieurs spécimens a été proposé. Pour démontrer davantage la généralité des méthodologies proposées, la méthode de détermination de la limite de fatigue et le modèle de prédiction de la durée de vie mentionnés ci-dessus ont également été appliqués aux résultats obtenus lors d'essais en fatigue en compression-compression et en fatigue en compression après impact sur des stratifiés CFRP

Quasi-Isotropes Quasi Homogènes (QIQH) avec trois séquences d'empilement différentes. Les résultats obtenus ont montré que la méthode de détermination de la limite de fatigue et le modèle de prédiction de la durée de vie proposés dans cette étude peuvent être utilisés pour déterminer rapidement la limite de fatigue et prédire les courbes S-N des matériaux composites MD CFRP avec plus de 87% de précision. Les résultats de ce travail sont intéressants d'un point de vue industriel car avec l'utilisation des méthodologies proposées, la durée des essais de fatigue est considérablement réduite (gain de temps d'au moins 50 fois) et les propriétés de fatigue des composites peuvent être obtenues quels que soient la séquence d'empilement et le mode de chargement (tension ou compression).

Mots-clés : Thermographie Infrarouge, Limite de Fatigue, Prédiction de la Durée de Vie, Multi-Directionnel CFRP, Fatigue Post-impact.

General Introduction

In 1829, the history of fatigue begins. Wilhlem Albert, a German mining engineer, was the first to carry out the fatigue tests on the metallic conveyor chains and published his observations. Afterwards, between 1852 and 1870, a German engineer, August Wöhler, constructed the first experimental program to formulate the stress-fatigue life (S-N) curve. Since then, fatigue is well recognized as a critical loading pattern that could be the reason for a significant percentage of engineering failure and the fatigue properties of materials are therefore considered as an important parameter of structural design.

Owing to their high strength and high stiffness to weight ratios, composite materials have replaced part of traditional metallic materials, being extensively used as structural materials in the aerospace, automotive and marine industries since 1950s. Components manufactured from composite materials are inevitably used in the situations where fatigue loads are present. Therefore, it is of great importance to understand thoroughly the fatigue behavior of these composite structures.

The fatigue properties of metallic materials are conventionally determined by Wöhler curve or S-N curve [1]. However, to plot a S-N curve, a number of long-lasting tests under different stress levels must be carried out [2], which is a rather costly and time-consuming process [3]. Besides, for a given material, its fatigue properties depend on different parameters, such as loading frequencies, stress ratios, geometrical shapes and dimensions, manufacturing processes and surface roughnesses, etc...[4]-[7]. Moreover, in comparison with metals, the fatigue behavior of composite materials is considerably more complicated due to their inherent anisotropy and heterogeneity. Fiber orientation and content [8][9], stacking sequence [10][11], fiber/matrix interface quality [12][13], etc... can all have an influence on their fatigue properties. As a consequence, new methods that allow for accelerating the

determination of fatigue properties are highly desired.

From the view of thermodynamics, fatigue of materials is an irreversible energy dissipation process accompanied by temperature variation. InfraRed Thermography (IRT), as a full-field, non-contact and non-destructive method, enables the visible identification of the surface temperature field of a material when it is subjected to mechanical loading. It can be applied not only to access the damage initiation and propagation in real time, but also, based on the infrared thermographic analysis, to predict fatigue properties in a short time [14]-[16]. The fatigue properties mentioned here mainly refer to the fatigue limit and fatigue life.

In the previous work, new data treatment methods of thermographic data that allows to rapidly determine the fatigue limit with uniqueness by using graphic methods (Luong and Risitano's methods) were developed by Huang et al [17]. The methods have been successfully applied to the metals, UD and $\pm 45^\circ$ laminates in the literature. Besides, a fatigue life model based on stiffness degradation was also proposed by combining the IRT data with damage accumulation process. The proposed model allows to determine S-N curve just in about ten hours of machine time, and has been applied to predict the tension-tension fatigue S-N curves of triaxially braided, UD [18] and $\pm 45^\circ$ [19] CFRP laminates. Nevertheless, the case of a more complex composite material such as MD laminates, other modes of loading such as compression-compression and the situation that the laminates may suffer from an impact, all of these have not been considered in this model. Therefore, in this paper, all the above mentioned more complex cases or situations will be investigated.

In the present PhD thesis, the author aims to work on the following aspects:

1. Carry out the static tension, conventional tension-tension fatigue tests, tension-tension fatigue tests monitored by IRT on cross-ply and Quasi-Isotropic (QI) CFRP laminates; static compression and Compression After Impact (CAI) tests, compression-compression and post-impact compression fatigue tests with the use of IRT on the QIQH CFRP

laminates

2. Propose a new fatigue limit determination method for the composite materials to overcome the shortages of the existing graphic methods (Luong's and Risitano's methods). Verify the proposed methods by experimental data of MD CFRP in two different stacking sequences and data found in the literature of different materials.
3. Modify the rapid fatigue life prediction model proposed by Huang et al. [18], which combines the stiffness degradation with thermographic data, to take into account of the more complex damage mechanisms in the MD CFRP laminates.
4. Propose a protocol to determine a more reliable S-N curve from a set of individual S-N curves of several specimens.
5. Verify the proposed fatigue limit method and modified fatigue life prediction model by the compression fatigue and post-impact fatigue experimental data of QIQH laminates.

So, the entire thesis can be divided into 5 chapters, and the overview is given below:

In chapter 1, the definition, properties, preparation process and application of CFRP are first presented, followed by the introduction of conventional fatigue property determination methods and fatigue damage mechanisms in CFRP. The theoretical framework of IRT together with the fatigue property determination methods based on IRT are reviewed. Finally, impact damage mechanisms, post-impact residual properties and post-impact fatigue properties prediction based on IRT are given.

Chapter 2 starts with the introduction of basic material properties of CFRP prepreg and the detailed manufacturing process of CFRP specimens used for the static and tension-tension fatigue tests. The experimental procedure of static tensile tests and the test results are given first, followed by the experimental procedure of conventional tension-tension fatigue tests and tension fatigue tests with use of infrared camera. A new fatigue limit determination method is developed to overcome the shortage of the existing fatigue limit determination methods. Then the experimental data of QI and cross-ply CFRP laminates and those from numerous

publications are used to verify the proposed model. Besides, numerical analysis is carried out to investigate the influence of loading step length on the determined fatigue limit values.

In the chapter 3, taking into account of the influence of more complex damage mechanisms in the MD laminates throughout the fatigue loading, a modified fatigue life prediction model is proposed. The modified model has been applied to the experimental data of QI and cross-ply laminates and compared with the S-N curves determined by traditional fatigue tests. A protocol was developed to determine a more reliable S-N curve from individual S-N curves of several specimens. The protocol is evaluated by the experimental data of QI and cross-ply laminates.

The objective of chapter 4 is to investigate whether the fatigue limit determination method and the modified fatigue life prediction model proposed in chapter 2 and 3 can be applied to compression-compression fatigue QIQH CFRP laminates. A different CFRP prepreg was used for the preparation of QIQH specimens with three different stacking sequences. Static compression tests were conducted first to determine the Ultimate Compressive Strength (UCS), then followed by the compression-compression fatigue tests with the use of IRT. The determined fatigue limits and predicted S-N curves of three different stacking sequences are compared with each other.

In chapter 5, the focus is to study the CAI and post-impact fatigue behavior of QIQH CFRP laminates, because CFRP laminates is very sensitive to the impact loading. The same material as that in chapter 4 was used. The CAI strength and damage modes of specimens with three different stacking sequences are compared with each other, also with those without impact. Again, the fatigue limit determination method and the modified fatigue life prediction model proposed in chapter 2 and 3 are applied to the experimental data of post-impact compression fatigue QIQH laminates. Finally, the fatigue limits and fatigue life obtained by the proposed methodologies are compared with those without impact.

Chapter 1 Literature review

1.1 Introduction and background

1.1.1 Definition of composite materials

As the term indicates, a composite material refers to a material made from two or more constituents or phases that have different properties that, when combined, produce a material/structure with properties superior to the properties of its individual components [20].

Composites are made up of individual basic materials, which are named as so-called constituent materials (**Figure 1-1**). There are two main categories of constituent materials: the reinforcement and the matrix. At least one representative from each category is required to create a composite. The role of matrix phase is to surround and bind the reinforcement, giving the composite material its net shape. Also, the matrix acts as the load-transferring media. While the reinforcement is added to the matrix material to enhance the mechanical properties such as stiffness or strength of composites [21]. There is a wide variety of materials that can be used as matrix and reinforcement materials. The classification of composite materials is usually just based on these two constituent materials.

The first classification criterion refers to the matrix constituents. Here, Ceramic Matrix Composites (CMCs), Metal Matrix Composites (MMCs) and Polymer Matrix Composites (PMCs) are distinguished. The most commonly used CMCs include C/C, C/SiC, SiC/SiC and Al₂O₃/ Al₂O₃. For MMCs, numerous metallic materials and metal alloys have been explored as matrix materials, including Al, Mg, Ti and its alloys [22]. Boron, carbon (C), alumina and silicon carbide (SiC) are popular continuous fiber reinforcement, while silicon carbide (SiC), alumina (Al₂O₃) and boron carbide (B₄C) are often used as particle reinforcement. As for PMCs, the commonly used matrix include polyesters, epoxies, vinyl esters, polyamide imide [23], while carbon, glass, graphite and aramid are the most important fibers in current use.

The second classification criterion refers to the reinforcement constituents. Three broad classes of composite materials are fiber reinforced composites (FRCs), laminar composites and particulate composites. For the FRCs, the principle fibers in use are various types of glass and carbon fibers. Other fibers, such as boron, aramid, silicon carbide, etc..., are used in limited quantities. A typical example of laminar composites is plywood, in which the layers are made of the same wood, but the grains are oriented differently. As for particulate composites, the well-known examples are concrete and particle board.

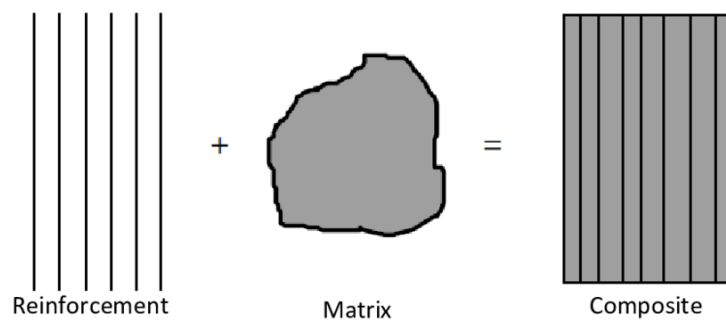


Figure 1-1. Formation of a composite material using reinforcement (fiber) and matrix (resin) [21]

Among the various composite materials, one of the most commonly used composite materials is CFRP, the short for Carbon Fiber Reinforced Polymer, which is composed of carbon fibers and polymer matrix. This is also the material that will be investigated in this study.

1.1.2 Properties and preparation of CFRP

For CFRP, the incorporation of long carbon fiber into the polymer matrix results in the anisotropic mechanical and thermal behavior of material system. The mechanical and thermal properties parallel to the reinforcement fibers are dominated by the fiber properties. While transverse to the fibers and in the laminate-through-the-thickness direction, the properties are dominated by the polymer matrix (see **Figure 1-2**). In terms of mechanical properties, the fact that carbon fiber is five times stronger than steel results in the tensile strength of CFRP in the fiber direction falling between 1500 and 3500 MPa, whereas its metallic counterparts such as steel and aluminum only possess tensile strength of 750-1500 MPa and 450-600 MPa, respectively [24][26]. The stiffness of CFRP is around 200 GPa, which is similar to steel but

two times as much as aluminum [27]. However, since the density of CFRP is approximately 20% of that of steel and 57% of aluminum [28], the strength-to-weight and stiffness-to-weight ratio of CFRP is remarkably higher than the metallic materials. In the direction transverse to the fibers and through-the-thickness, the strength and stiffness of CFRP are only in the order of 15-100 MPa and 10-100 GPa [29].

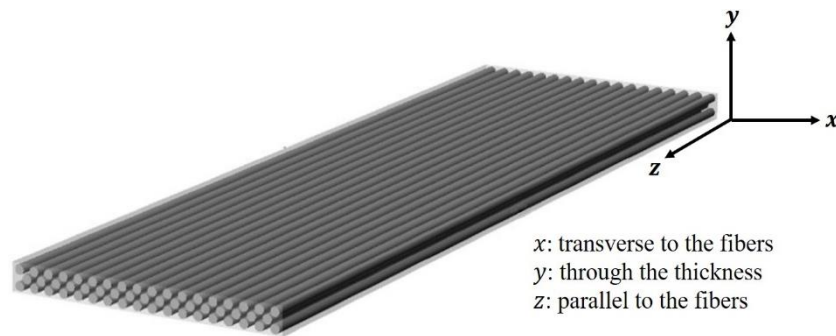


Figure 1-2. Schematic figure of directions in CFRP [25]

As for the thermal properties, Thermal Conductivity (TC) is taken as an example here. Generally speaking, the TC of carbon fiber ranges from 21 to 180 W/(m·K), with exceptions that some graphite and diamond could be even more conductive than copper and silver which have the highest conductivity of metallic materials [30]. On the contrast, the TC of polymers is usually very low, being in the order of 0.1–0.5 W/(m·K), due to the complex morphology of polymer chains [31]. Since the thermal conductivity of carbon fibers is significantly higher than the polymeric resins, the TC transverse to the fibers and in the laminate-through-the-thickness direction is much lower than that parallel to the fiber direction [32].

After the introduction of the mechanical and thermal properties of CFRP, the manufacturing methods of CFRP will then be described in detail.

There are various ways of producing CFRP, which offer different advantages in terms of production costs and range of properties. The common manufacturing methods include the following: open molding, vacuum bag molding/autoclave molding, compression molding and filament winding.

As the name implies, the open molding process is achieved by utilizing a single open mold that is in the shape of the final product. Carbon fiber together with the polymer matrix or the mixture of the carbon fiber and polymer compounds are placed into the mold and are then cured or hardened (see **Figure 1-3(a)**). Open molding is a rather reliable and simple method to manufacture CFRP. The process is inexpensive, however, since the whole process has been exposed to the air, the produced part quality in terms of void content and fiber volume fraction will be largely reliant on the skill of the operators (the best achievable void content is between 5-6%) [33].

In the vacuum bagging process, the prepreg material is first laid up on the mold, thereafter, the mold together with the material are inserted into a vacuum bag and then they are evacuated (**Figure 1-3 (b)**). The homogeneous consolidation pressure on the laminate entrapped air, volatiles and excess resin, which in turn results in few voids and stronger adhesion between the fiber and matrix. Hence the quality of the fabricated part is more consistent and can be guaranteed [34]. If the laid-up mold inserted in the vacuum bag is placed in an autoclave for cure and consolidation under controlled temperature and pressure, it is called autoclave molding. Similar to vacuum bagging, the combination of vacuum and pressure during the autoclave molding process results in high fiber reinforcement fraction, high quality composite part with low void content. However, since the method requires substantial investment in the autoclave itself, making this process prohibitively expensive. Besides, the size of the fabricated components is limited by the dimensions of the autoclave.

Compression molding is a manufacturing process by which materials ready to be processed are cured between two matching molds under intensive pressure and heat [36] (**Figure 1-3(c)**). The most common intermediate or raw materials used for this process are Sheet Molding Compound (SMC) and Bulk Molding Compound (BMC) [37]. Due to the ease of manufacturing, there is a high success rate of producing CFRP parts free of inclusions and air bubbles. Besides, compression molding is also recognized as one of the least expensive

manufacturing methods for mass-produce products. However, a major drawback of the method is the initial cost. A compression molding machine is rather expensive. The matching molds alone can cost even 50 times as much as an open mold.

Filament winding is an automated process that applies resin-impregnated, continuous strands of carbon fiber reinforcements over a rotating mandrel which served as the mold (**Figure 1-3** (d)). The method is typically used for manufacturing open (tubes, cylinders, pipes, etc.) or closed end structures (pressure vessels or tanks) [38]. Filament winding is fast and economic, and may be achieved by automation and robotic procedures. However, the process is limited to convex-shaped components.

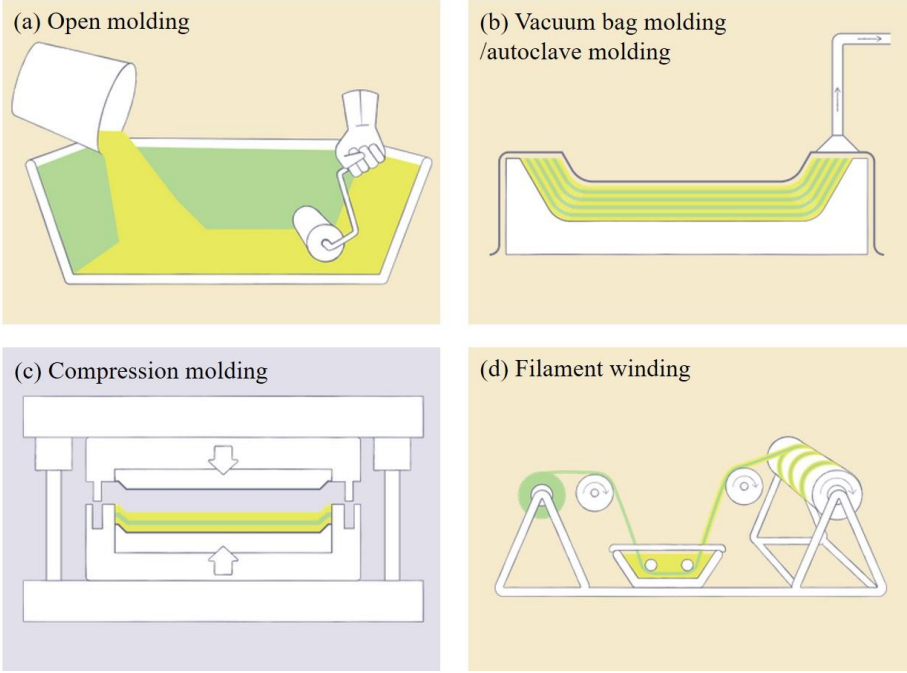


Figure 1-3. Schematic presentation of manufacturing methods of CFRP [39][40]

Since in the laboratory, there already exists an autoclave. Based on the consideration of cost and the geometry of fabricated plates, the autoclave molding process is chosen for the manufacturing of CFRP laminates in this study.

As previously mentioned, since the stiffness and strength properties with respect to weight of CFRP are superior to a range of conventional materials, the CFRP components have been

adopted in a variety of applications.

1.1.3 Applications of CFRP

CFRP are finding increased applications in many areas, ranging from the aeronautical, marine industry to automotive industry, as well as in the advancing sporting goods, civil engineering structures, etc...

The major structural material application of CFRP is in the aeronautical field, for which weight reduction is critical. Compared with making the same aircraft component with conventional metallic materials, the use of composites allows one to obtain a weight reduction varying from 10% to 50% with equal performance, while at the same time, reducing the cost from 10% to 20% [41]. In addition, composite materials also provide greater flexibility since the material can be tailored to the user's requirements by selecting the constituent material, stacking sequence, geometrical arrangement and so on.

In recent years, the usage of CFRP has continued to deepen in the commercial aircraft. In the 1970s, CFRP were marginally used in tertiary and secondary bearing components of aircraft structures [42]. Now, they are the most preferred materials for large primary structures, such as central wing box, beams, vertical and horizontal stabilizers and numerous parts of fuselage [43] (Figure 1-4).

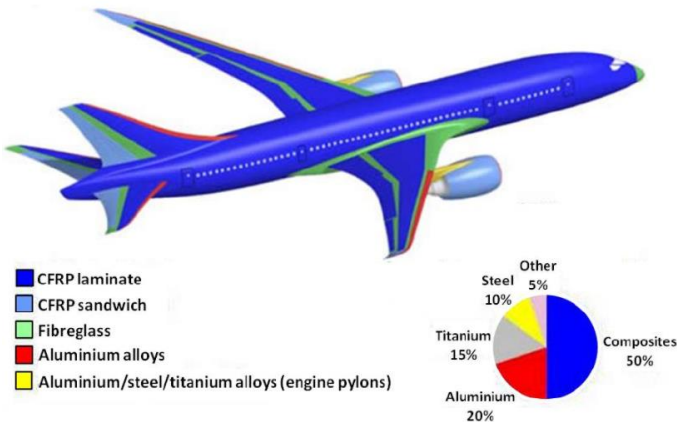


Figure 1-4. Airframe material distributions and percentages for the Boeing 787 [43]

In the marine industry, CFRP are perfect choice for the challenging marine environment for

being light in weight, which offers potential savings in the structural weight, and having strong environmental resistance properties, including freedom from rotting, corrosion, marine organisms, etc... [44]. CFRP are common in various structures and components of vessels, including hulls, floors, wall panels, decks as well as piping systems, fuel tanks, sonar hoods, pipes, pumps and valves [45].

In the automotive industry, the outstanding specific strength, specific stiffness and fatigue properties of CFRP compared to the commonly used metallic materials have drawn increasing attention. Nowadays, the CFRP components are included in virtually all facets of a vehicle's design: chassis members, body panel, brake rotor and driveshaft components, etc... [46].

Besides, CFRP are also extensively used in sporting goods ranging from tennis rackets to bicycles and are displacing traditional materials like wood, metals, and leather in many of these applications [47]. The key advantages of using this material are reduction of weight, vibration damping and design flexibility.

CFRP also have a great potential for replacing wood, steel and reinforced concrete in bridges, buildings and other civil infrastructures [48]. The principal reason for choosing this material is their corrosion resistance, which leads to longer life, lower maintenance costs and possible reduction in seismic problems.

During service, the CFRP components, such as the fuselage, wings and vertical tail of an aircraft, frame stiffener of an automobile, are often employed in the situation where fatigue loads are present. The fatigue durability properties of these components are critical for the long-life safety of the whole structure. As a consequence, there have been extensive studies investigating the fatigue properties of CFRP materials [49]-[52].

1.2 Determination of fatigue property

1.2.1 Traditional fatigue testing

Fatigue properties are commonly described by fatigue limit or the Stress-Life (S-N) curve. Fatigue limit is defined as the threshold value of stress level below which fatigue failure occurs when the fatigue life N_f is sufficiently high (e.g., 10^6 or 10^7 cycles) [53][54]. It can be conventionally determined by the staircase approach or the S-N curve.

The staircase approach, is also named as the up and down method. When performing a staircase test, the expected range of stress level for fatigue limit is first selected. A constant factor d (staircase factor) is chosen to separate the region into several neighboring stress levels which equally spaced in a logarithmic scale. The first specimen is tested at an arbitrary stress level. If the test is completed without failure, then the subsequent specimen is tested at the next higher stress level. In contrast, if the test failed prior to a predetermined number of cycles (usually 10^6 cycles), the consecutive test is conducted at next lower stress level, as shown in **Figure 1-5**. Therefore, each test depends on the previous test results. In practice, it is recommended to run the test with at least 15 specimens [55]. The duration of fatigue limit determination by this approach is at least 20 days.

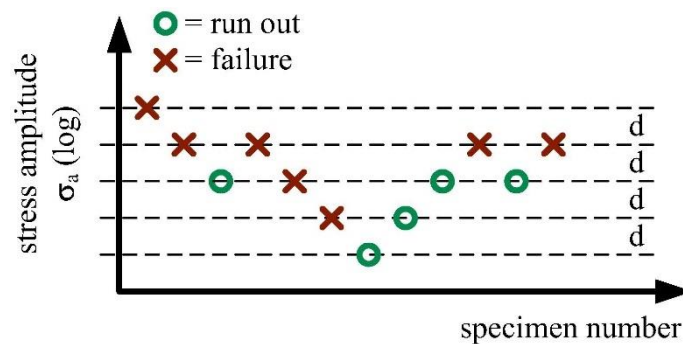


Figure 1-5. Principle of staircase approach [56]

S-N curve is a plot of the relation between magnitude of cyclic stress (S) and the number of cycles to failure (N), preferably on a log-log or linear-log scale, as presented in **Figure 1-6**. The fatigue life for any loading level could be directly read from the curve. In general, the S-

N curves are plotted for a constant value of stress ratio R. Due to the large scatter of experimental fatigue life, to plot a S-N curve, a number of long-lasting tests (at least 15 specimens) on similar specimens under different stress levels must be carried out.

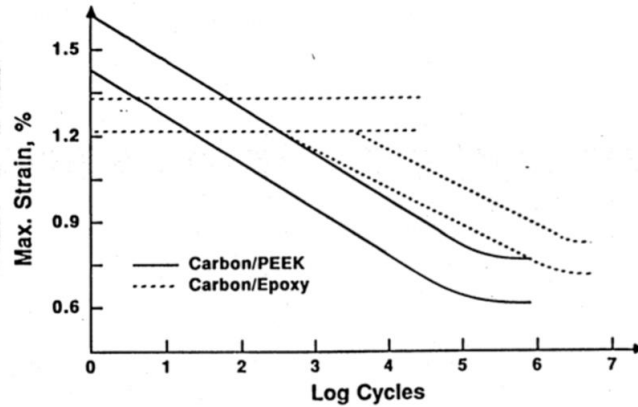


Figure 1-6. S-N curves of carbon/PEEK and carbon/epoxy laminates loaded in tension-tension fatigue [56]

1.2.2 Fatigue damages in CFRP

The fatigue damage in the CFRP depends on the loading mode, for example tensile or compressive, the stress ratio R, the frequency of test, and various material factors including constituent materials: fiber and matrix, architecture of reinforcement, stacking sequence, etc.... Previous studies [57]-[60] have identified a number of damage mechanisms involved, which are: matrix cracking, delamination, fiber-matrix debonding, fiber pull-out and fiber fracture.

1.2.2.1 Matrix cracking

Due to the large difference in stiffness between matrix and reinforcement, matrix cracking becomes a very common mode of fatigue damage in CFRP. Matrix cracking often initiates at the free edges of a specimen where the stress state is different from that away from the edge, then extending across the thickness of the ply but not necessarily across the width of specimen [61]. An example of matrix cracking observed during fatigue test of different layups is shown in **Figure 1-7**. In addition to reducing the mechanical properties (stiffness [63], Poisson's ratio [64], etc...) of composite materials, the development of matrix cracking can further lead to other types of damage such as delamination and/or fiber fracture.

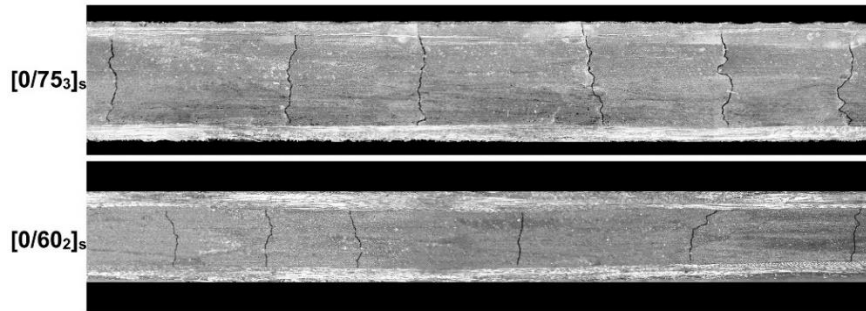


Figure 1-7. Mid-ply matrix cracking observed during fatigue test of different layups [62]

1.2.2.2 Delamination

Delamination is an inter-ply damage form induced by the mismatch of elastic properties between adjacent layers. A typical figure of delamination fracture is shown in **Figure 1-8**. As can be seen from the figure, delamination is associated with matrix crack damage because matrix cracking is almost always a necessary precursor for delamination to occur.

Delamination is a crucial damage for CFRP. In the short term, it can lead to a lack of support of load-bearing layers in the material, promoting damage growth and premature failure [66][67]. In the longer term, it provides opportunities for the moisture and contaminant to invade into the interior of material [68].

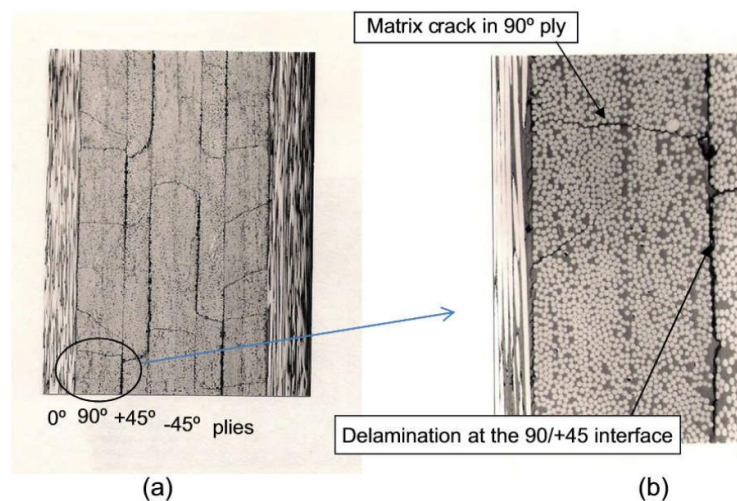


Figure 1-8. Edge view of a CFRP laminate showing delamination between plies:(a) overall view;
(b) The circular region of (a) at higher magnification [65]

1.2.2.3 Fiber-matrix debonding

When the stress at fiber-matrix interface exceeds the local strength, debonding occurs and cracks form [69]. Fiber-matrix debonding, therefore, is a localized mode of damage that is rather difficult to detect using conventional technique. **Figure 1-9** illustrates when a load is applied perpendicular to the fiber direction, the raise of average strain magnification in the matrix between two fibers giving rise to fiber-matrix debonding.

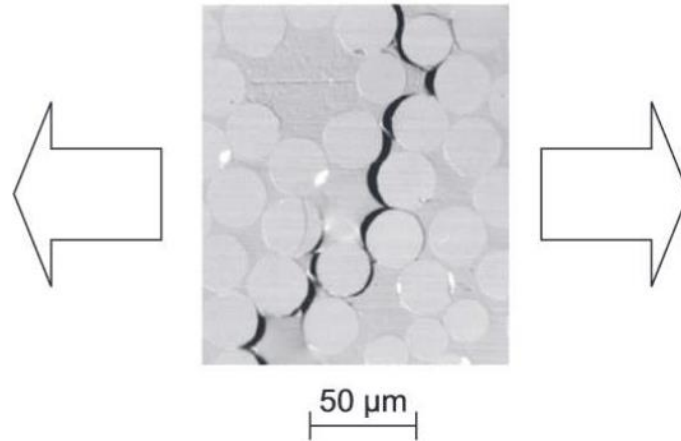


Figure 1-9. Coalescence of fiber-matrix debonding into a crack [70]

Fiber-matrix debonding does not appear to have a significant influence on the load-carrying capabilities of composite materials. However, it acts as a precursor to matrix cracking - a more detrimental form of damage.

1.2.2.4 Fiber pull-out

Fiber pull-out is a typical tensile fiber failure mode, especially when both fiber and matrix are brittle. In the region of high stress concentration, such as the tip of an advancing crack, fibers often fail and fracture [69]. As the crack front continues to propagate, these fibers are pulled out of the surrounding matrix and fiber pull-out occurs (**Figure 1-10**).

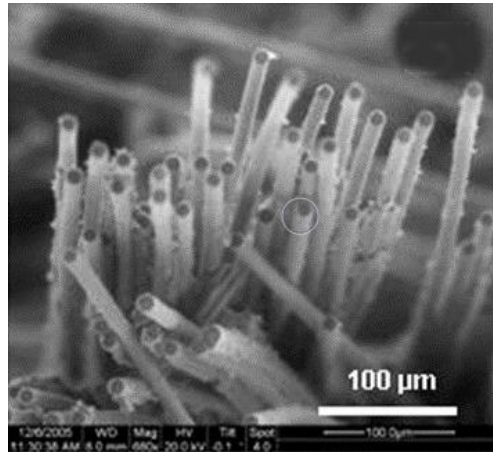


Figure 1-10. SEM micrograph of fiber pull-out [71]

1.2.2.5 Fiber fracture

As a type of fiber-reinforced composite materials, CFRP is manufactured from bundles of carbon fibers, with the strength and failure strain of each fiber within the bundle being different from each other. With the initiation of fatigue loading, the fibers fail under different values of applied strain, generating isolated fiber fractures. Then at higher strains, localized stress concentration resulted from isolated fiber fractures can induce failure in adjacent fibers, leading to an accumulation of fiber fractures [61].

Fiber fracture is often seen as the final step towards failure for CFRP, since fibers represent the principal load-bearing constituent of a fiber-reinforced composite, the fracture of fibers can have a severe effect on the stiffness and strength of composite materials [69]. **Figure 1-11** gives the fracture morphologies of fiber fractured in fatigue.

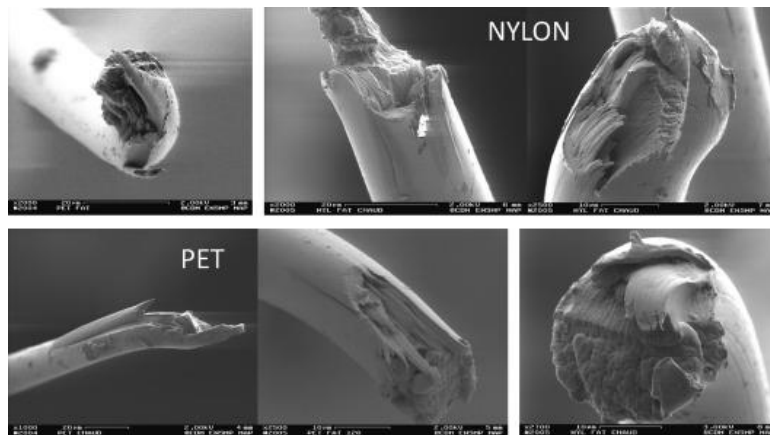


Figure 1-11. The fracture morphologies of fiber broken in fatigue [72]

As previously mentioned, investigating the fatigue properties of CFRP by traditional fatigue tests is costly and time consuming. Besides, for a given material, its fatigue properties can be dependent on different parameters, such as loading frequencies [4], stress ratios [5], geometrical shapes and dimensions [73], manufacturing processes [74] and surface roughnesses [6], etc.... Moreover, in comparison with metals, the fatigue behavior of CFRP is considerably more complicated due to their inherent anisotropy and heterogeneity. Therefore, there is a strong need for new approaches to rapidly evaluate the fatigue behavior of CFRP.

With the development of high resolution infrared camera and the improvement in relevant theories, InfraRed Thermography (IRT), as a non-contact, real-time, full-field technology, has been extensively used for the rapid prediction of fatigue properties.

1.3 Rapid determination of fatigue property based on IRT

1.3.1 Theoretical framework

Fatigue can be specified as a cyclic damage evolution process, accompanied by thermal energy dissipation which macroscopically leads to temperature changes on the material's surface. The framework used to interpret the fatigue behavior is the Thermodynamics of Irreversible Processes (TIP) [77][78]. Combining the first and second thermographic principle, the local heat equation can be expressed as follows [79]-[81]:

$$\rho C \dot{T} - \text{div}(k: \overrightarrow{\text{grad}T}) = d_1 + s_{the} + s_{inT} + q_e \quad (1-1)$$

With

$$d_1 = \sigma: D - \rho \frac{\partial \varphi}{\partial \varepsilon} : \dot{\varepsilon} - \rho \frac{\partial \varphi}{\partial \alpha} : \dot{\alpha} \quad (1-2)$$

$$s_{the} = \rho T \frac{\partial^2 \varphi}{\partial T \partial \varepsilon} : \dot{\varepsilon} \quad (1-3)$$

$$s_{inT} = \rho T \frac{\partial^2 \varphi}{\partial t \partial \alpha} \cdot \dot{\alpha} \quad (1-4)$$

Here, ρ denotes the mass density, C is the specific heat capacity, k is the thermal conductivity, T is the absolute temperature, σ is Cauchy stress tensor, D is the strain rate tensor, ε is the

strain tensor, α is the internal variable describing the change of microstructure within the material, φ is the Helmholtz free energy and q_e stands for the external heat supply.

The first term $\rho C \dot{T}$ on the left-hand side of the Eq. (1-1) denotes the heat storage rate due to increase in the thermal inertia of specimen, the second term $-\text{div}(k: \overline{\text{grad}T})$ characterizes the rate of heat conduction through the specimen. In Eq. (1-2) to (1-4), d_1 is the intrinsic dissipation caused by irreversible deformation, s_{the} represents the thermoelastic coupling effect between the temperature and strain and s_{int} stands for the thermo-mechanical couplings between temperature and internal variables.

In order to simplify Eq. (1-1), the following hypothesis are put forward [79]:

- (1) The parameters mass density ρ , specific heat capacity C and thermal conductivity k are material constants, independent of the thermodynamic state.
- (2) At a mesoscopic scale, thermoelastic coupling s_{the} and intrinsic dissipation d_1 are uniform throughout the gauge volume.
- (3) The coupling effect between temperature and internal variables, s_{int} , is neglected.
- (4) The external heat supply q_e due to heat exchange is supposed to be independent of time, therefore, the equilibrium temperature field T_0 verifies:

$$-\bar{k}: \Delta T_0 = q_e \quad (1-5)$$

Under the above hypothesis, the local heat equation can be simplified into the following form:

$$\rho C \left(\frac{\partial \theta}{\partial t} + \frac{\theta}{\tau_{eq}} \right) - k \left(\frac{\partial^2 \theta}{\partial^2 x} + \frac{\partial^2 \theta}{\partial^2 y} \right) = d_1 + s_{the} \quad (1-6)$$

Where $\theta = T - T_0$ denotes the temperature variation at the center gauge part of specimen. The time constant τ_{eq} characterizes the heat losses through the specimen surfaces $z = \pm e/2$ (e denotes the thickness of specimen).

The linearity of Eq. (1-6) allows us to study separately the respective influence of source d_1 and s_{the} on the temperature. The temperature variation induced by thermoelastic coupling

s_{the} and intrinsic dissipation d_1 is denoted as θ_{the} and θ_d , respectively. Assuming that the thermoelastic behavior is linear and isotropic, under cyclic loading, the expression for θ_{the} can be deduced by solving Eq. (1-6):

$$\theta_{the}(t) = -\frac{T_0\lambda\sigma_a}{\rho C} \frac{\pi f}{\sqrt{\tau_{eq}^{-2} + 4\pi^2 f^2}} \sin(2\pi f t + \varphi) \quad (1-7)$$

Where λ denotes the linear thermal expansion coefficient, σ_a represents the stress amplitude of cyclic loading, f stands for loading frequency, and $\tan\varphi = 2\pi f\tau_{eq}$. From Eq. (1-7), it is observed that the temperature θ_{the} is directly related to the applied stress: it has the same frequency f as the applied stress signal and is proportional to the amplitude of applied stress σ_a [83].

As for θ_d , since the intrinsic dissipation is always positive, the temperature variation θ_d induced by d_1 is also positive according to Eq. (1-6). This temperature rise is caused by the dissipated energy due to mechanical damping, which corresponds to the encircled area by the hysteresis loop [84]:

$$\theta_d = \frac{Q_{diss}}{\rho \cdot C} \quad (1-8)$$

Where Q_{diss} is the generated dissipated energy.

A typical average temperature evolution in the gauge section of a specimen with the increase of number of cycles is illustrated in **Figure 1-12**. As can be seen from the figure, the temperature fluctuation θ_{the} caused by reversible thermoelastic heating and cooling during each cycle is significantly smaller when compared with the temperature rise θ_d . Besides, it is demonstrated that this thermoelastic effect can be eliminated by a time dependent averaging of ΔT [84]. Therefore, the thermoelastic term s_{the} can be neglected [82][85]. Eq. (1-6) can be rewritten as:

$$\rho C \left(\frac{\partial \theta}{\partial t} + \frac{\theta}{\tau_{eq}} \right) - k \left(\frac{\partial^2 \theta}{\partial^2 x} + \frac{\partial^2 \theta}{\partial^2 y} \right) = d_1 \quad (1-9)$$

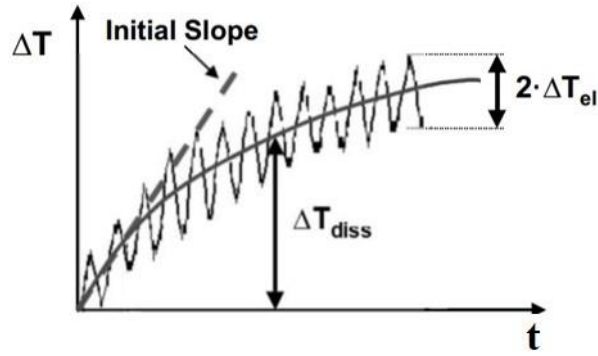


Figure 1-12. Typical time dependent temperature evolution during fatigue tests [84]

According to Eq. (1-9), the total heat generation under cyclic fatigue loading is mainly influenced by intrinsic dissipation, which paves the way for the analysis of fatigue behavior based on temperature data measured by IRT.

1.3.2 Infrared thermography

InfraRed Thermography (IRT) is a non-destructive technique concerned with the detection, registration, processing and visualization of thermal information. Laying on the principle that anybody at a temperature above absolute zero (i.e., $T > 0K$) emits electromagnetic radiation due to its thermal conditions, IRT allows performing the non-contact measurements of the surface temperature variation of emitting object [86]-[88]. Practically, it includes an infrared detecting device (infrared camera in **Figure 2-8**) to sense the emission of thermal energy from the objects; such energy, with the aid of specific software, is convert into an electrical signal and then processed to produce the surface temperature profile of the viewed object in the form of gray scale or colored infrared images [89][90].

The measurement of emitted radiation in the IR range of the electromagnetic spectrum is the basis for IRT, which corresponds to wavelengths longer than the visible light portion of the spectrum. Every physical body spontaneously and continuously emits electromagnetic radiation. The bodies in real life show very diverse radiation properties. Therefore, it is worthwhile to initially consider the simplified laws of a model body of ideal radiation properties, and then applied the laws to actually occurring objects. This model body is known

as the “black body”, The spectral radiance, defined as the spectral emissive power per unit area of a surface for a particular frequency, emitted by a black body is described by Planck’s law [91]:

$$N_{\lambda,b} = \frac{2hc^2}{\lambda^5} \frac{1}{\exp\left(\frac{hc}{\lambda KT} - 1\right)} \quad (1-10)$$

Where h is the Planck’s constant, c is the speed of light, K is the Boltzmann’s constant [92] ($K=1.381 \times 10^{-23} JK^{-1}$), λ is the wavelength of emitted radiation (μm), T is the absolute temperature of the surface and subscript b denotes black body.

By integrating the above equation across all wavelengths, the total emitted energy across the entire spectrum of wavelengths at a given temperature could be obtained. This correlation is called Stefan-Boltzmann’s law [93]:

$$P(T) = \sigma T^4 \quad (1-11)$$

Where σ is the Stefan-Boltzmann constant ($\sigma = 5.670 \times 10^{-8} W/(m^2 \cdot K^4)$).

A black body is a perfect absorber and emitter of electromagnetic radiation, regardless of wavelength or angle of incidence. In the case of a real object, only part of the energy will be radiated out from the surface, for which the Stefan-Boltzmann’s law is modified as:

$$P(T) = \varepsilon \sigma T^4 \quad (1-12)$$

Where ε is the emissivity of the surface. Emissivity is a measure of the ability of a surface to radiate energy in comparison to a black body. The value of emissivity ranges from 0 (perfect mirror reflector) to 1 (perfect black body). It depends on temperature, wavelength and nature of the surface.

The fundamental equation of IRT relates the radiance received by an infrared camera to the radiance emitted from the surface of object and environment at a given temperature T , neglecting the atmosphere contribution [94]:

$$N_{cam} \approx \varepsilon N_{obj} + (1 - \varepsilon) N_{env} \quad (1-13)$$

Where N_{env} is the radiance emitted by the surrounding environment considered as a black body. Since an IR camera is not a thermometer but a radiometer. To allow for a successful measurement, the value of emissivity of the object should be close to 1. If the emissivity ε of surface is high, Eq. (1-13) reduces to $N_{cam} \sim N_{obj}$ and knowledge of the calibration curve of camera linking N_{obj} to T allows the retrieval of the surface temperature. There are plenty of methods to solve the low or uneven emissivity problems. Among them, covering the viewed surface with a high emissivity flat paint or grease is the most common one for imaging applications [95]. In practice, black coating is often used.

A typical thermography testing experimental set-up is presented in **Figure 2-8**. An IR camera is placed in front of the testing machine and specimen. The camera is connected to a laptop computer to process the acquired data. The orientation and position of camera, the distance between camera and specimen should be justified before the tests to obtain the desired field of view (FOV). Also, the thermal scene must be isolated to avoid external disturbance that can alter the measurements. This could be achieved by using an obscuring insulator curtain or keeping the surrounding in dark. Before the testing begins, the camera needs to be calibrated with a reference blackbody simulator. After calibration and setting the parameters, the mechanical tests start and the observation shall begin. The detected IR energy is displayed as a digital temperature-profile map. This image is presented on the screen of a color monitor, with the various colors (up to 256) indicating temperature differences of 0.1°C . The temperature indicated has taken into account of the emissivity of the object. The IR images was recorded over a period of time, which can be represented by a 3-D matrix.

IRT can be applied in a passive or active configuration [96]: the former is often applied on materials which experience a different temperature from the surroundings, the latter, instead needs an external thermal stimulation to induce the surface temperature variation. The external stimulations can be a mechanical or heat source.

1.3.3 Review of fatigue property determination method based on IRT

Initially, IRT was widely used for the metallic materials in terms of fatigue property determination, a number of methods and theories were created based on the observations on these materials. Later on, these methods have been applied to the composite materials. In general, the studies that utilize IRT to study the fatigue behavior of materials mainly contains the following three aspects: damage evolution during fatigue process, determination of fatigue limit and evaluation of fatigue life [97].

Damage evolution

When the material is deformed or damaged, part of the energy necessary to initiate and propagate the damage will transform into heat, which can be captured by IR camera. The study of Liaw et al. [98], Yang [99] and Yang et al. [100] suggests that the temperature profile obtained by IRT could be used to reveal the damage in the metallic materials. In the work of Naderi et al. [101], entropy production evaluated by the surface temperature of specimen is utilized as an effective tool to access the damage variation under both constant and variable amplitude fatigue loading. A strong correlation between accumulated damage and entropy production is observed, independent of load, frequency, load history and geometry for the two materials tested: Al 6066-T6 and SS304.

As for the composite materials, Naderi et al. [102] utilized IRT combined with acoustic emission to explore the temperature evolution and various damage state of woven glass/epoxy composites during fully reversed bending fatigue tests. The obtained results of both methods revealed the existence of three separated stages during the whole lifespan, which accounts for 10-20%, 70-75% and 10-20% of total fatigue life, respectively (**Figure 1-13**). The three stages are characterized by matrix cracking, delamination and fiber/matrix debonding and fiber fracture, respectively.

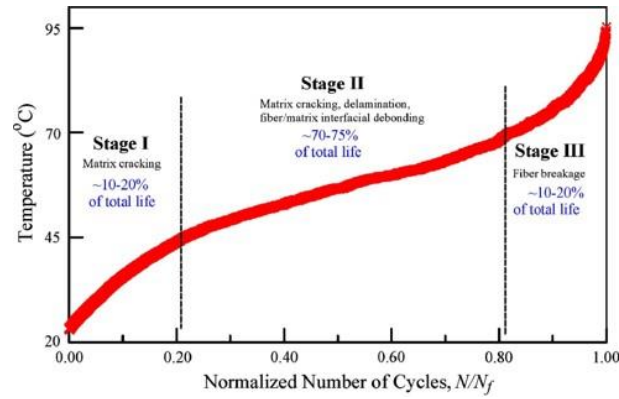


Figure 1-13. Evolution of surface temperature profile [102]

Montesano et al. [103] pointed out that the temperature evolution profile detected by IRT is directly correlated with stiffness degradation (**Figure 1-14**). The critical damage states at cyclic transition regions together with the evolving damage mechanisms can also be clearly identified via temperature data.

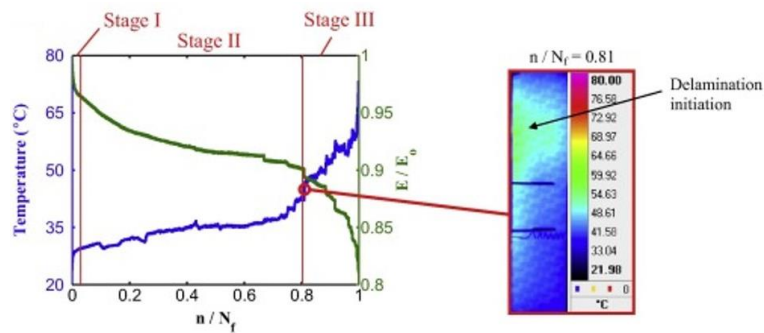


Figure 1-14. Temperature and normalized axial stiffness profile [103]

An in-situ damage characterization of CFRP was achieved by Steinberger et al. [104] via two thermographic testing approaches: passive and active. It was shown that the thermal images of passive thermography allow the identification of starting point of damage growth via localized heat source. The results of active thermography suggests that it was possible to characterize fatigue damage via heat conductivity.

Two different full-field techniques, Digital Image Correlation (DIC) and IRT, are employed in the study of Dattoma et al. [105] to evaluate the energy of fatigue damage in notched GFRP during the fatigue tests. The strain field images together with thermal images were elaborated to relate the hysteresis area with heat sources. The thermographic data shows a clear intensification of dissipative phenomena in the region where final failure is about to occur.

In most cases, fatigue cracks act as a precursor of the final failure of the structure, which makes the detection of fatigue cracks during damage evolution process become rather important. Direct observation of fatigue crack initiation and propagation is generally not possible by the naked eyes. During fatigue testing, since fatigue cracks tend to initiate in the plastic deformation localization area and lead to an extensive heat dissipation, it makes possible the detection of initiation of fatigue cracks by IRT. The observation of Charles et al. [106] suggests that IRT was not only able to visualize the surface temperature of steel during fatigue tests, but also allows the prediction of location of fatigue crack origins. Barile et al. [107] reported that the crack position and propagation path could be precisely evaluated by the temperature rise around the crack tip. In the work of Plekhov et al. [108], the temporal evolution of spatial Standard Deviation of the Temperature (SDT) field is proposed as an indicator to monitor the crack initiation in 35CrMo4 steel. Wagner et al. [109] evidenced that the sudden increase in temperature at the end of the tests corresponds to the initiation of crack. In the study Dassios et al. [110], crack growth in SiC fiber/ ceramic matrix composites is measured using combined IRT and Acoustic Emission (AE). By identifying the time instances where the maximum temperature occurred and quantifying the damage span within the thermographic image at specific instance, the crack growth can be established (**Figure 1-15**).

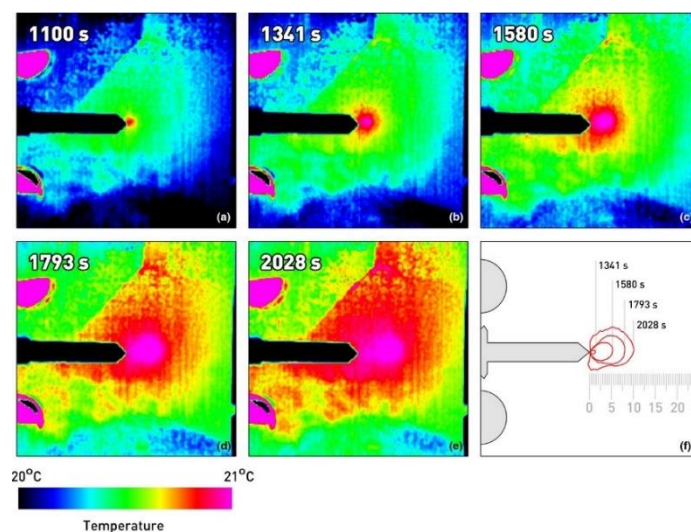


Figure 1-15. Thermographs showing the crack growth during composite fracture and contour plots of maximum damage zones at crack tip [110]

Fatigue limit

In terms of fatigue limit, Risitano et al. [111]-[115] firstly developed an empirical method, i.e. One-Curve Method (OCM), to rapidly access the fatigue limit of metallic materials by monitoring the temperature increase data ΔT corresponding to different stress levels σ through the step-loading procedure performed on only one specimen (**Figure 2-14**). After that, Luong et al. [116]-[119] put forward a Two-Curve Methodology (TCM), which is similar to OCM. Fatigue limit is interpreted as the stress level where an abrupt change in intrinsic dissipation heat occurs. The details of these two methods will be described in section 2.4.2. The aforementioned methods have been widely explored in literature for a vast range of materials, from steel, aluminum, alloy, cast iron to polymers, CFRP and GFRP, hybrid composites. The geometry of specimen varies from plat, dog-bone, hourglass to welded joints, notched and pipe specimens. The range of stress ratio R ($R = R_{min}/R_{max}$), ranges from -1 to 0.2, being suitable for almost any value of R . A summary of part of last 5 years work (2018-2022) that utilizes Risitano and Luong's method for fatigue limit determination is listed in **Table 1-1**.

However, it should be noted that in both methods, since they purely rely on graphical presentations and are sensitive to the choice of data points used for interpolation below and above the fatigue limit, the value of determined fatigue limit may not be unique, as illustrated in **Figure 1-16**. To solve this problem, Cura et al. [138] developed an iteration approach. The method starts by choosing a first trial stress σ_i , which is used to split the data pairs $(\Delta T, \sigma)$ into two temporary groups, below and above σ_i . Two different curves are then utilized to interpolate the data pairs below and above σ_i and stress level corresponding to the intersection of the two lines is determined as the first trial fatigue limit σ_{Ai} . The difference between first trial stress σ_i and first trial fatigue limit σ_{Ai} , also named as first trial error, can then be calculated. If the so obtained error is positive (negative), the second trial stress σ_{i+1} will be chosen lower (greater) than the first one. This iteration process stopped when the error is less than a prefixed value. In this approach, the author did not point out how to choose the step length $\sigma_{i+1} - \sigma_i$ between σ_{i+1} and σ_i and the prefixed value in the final step. Besides, study

of Huang [139] demonstrated that the value of determined fatigue limit depends on the choice of first trial stress.

Table 1-1. Summary of the last 5 years (2018-2022) work of fatigue limit prediction based on Risitano and

Luong's method (sorted according to year)					
Method	Year	Reference	Geometry of specimen	Materials	R
Risitano	2019	[120]	Dog-bone	AISI 304L steel	Not mentioned
	2020	[121]	V-notched	AISI 1035 steel	-1
	2020	[122]	Dog-bone	PE 100 polyethylene	0.1
	2021	[123]	Dog-bone	C45 steel	-1
	2021	[124]	Welded joint	TI6AL4V/INCONEL 625 alloy	0.1
	2021	[125]	Dog-bone	AZ31B Magnesium alloy	0.1
	2021	[126]	Plat	Modified GFRP	-1
	2022	[127]	Plat	S275JR steel	-1
Luong	2018	[128]	Pipe	Steel	0.1
	2018	[129]	Hourglass	Cast iron	Not mentioned
	2019	[120]	Dog-bone	AISI 304L steel	Not mentioned
	2019	[130]	Dog-bone	S355 steel	-1
	2019	[131]	Plat	Jute/glass woven reinforced polyester hybrid composites	0.1
	2021	[132]	Hourglass	Al 6351-T6 alloy	-1
	2021	[133]	Notched dog-bone	LCS 1018 carbon steel	-1
	2021	[134]	Dog-bone	High density polyethylene	0.2
	2021	[135]	Dog-bone	Polyamide	0.1
	2021	[136]	Dog-bone	Short CFRP	0.1
2022	[137]	Dog-bone	GFRP	-0.1	

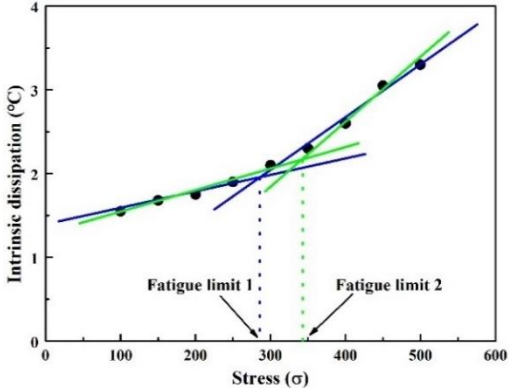


Figure 1-16. The difficulty of determining unique fitting cut-off point

Under such circumstance, Huang et al. [17] proposed three data treatment methods. The first method utilizes the angle change to separate the data points below and above the fatigue limit, followed by the application of Luong's method. The detail of this method is presented in section 2.4.3. The second method consists in fitting the data points with a consistent exponential curve. The radius of curvature is calculated for each stress level and the point with minimum radius of curvature is estimated as fatigue limit. The third method is inspired by the previously mentioned idea of Cura et al. [138]. For a total of n data points, all the possible combinations of two data points groups $\{P_1, P_2, P_3, \dots, P_k\}$ and $\{P_{k+1}, P_{k+2}, \dots, P_n\}$ are first listed. The data points in the two groups are interpolated by two different linear lines to obtain the intersection point P_i . If the stress amplitude of P_i lays between that of P_k and P_{k+1} ($\sigma_{P_k} \leq \sigma_{P_i} \leq \sigma_{P_{k+1}}$), the average of fitting goodness of two lines will be calculated to determine the combination of data points that achieves the best fitting results. The maximum stress of intersection point obtained by this combination is fatigue limit.

In the work of Krapez et al. [140]-[142], the lock-in thermography (LT) is adopted to evaluate the fatigue limit of metallic materials. LT, also known as modulated thermography, is one of the active thermography which consists in applying a periodic (sinusoidal) heat wave to the surface of tested object. The thermal waves get reflected when it reaches the region where the heat propagation parameters change. The internal defects of the tested object can then be derived by evaluating the phase shift of the reflected waves in relation to the input thermal waves.

In this study, the specimen is subjected to a series of stress levels with increasing loads. At each stress level, the specimen is only tested for a few tens of cycles. A specific demodulation procedure is performed for each pixel in the thermographic image recorded during the test:

$$J = \sum_{i=1}^n (T_{exp}(t_i) - T_{mod}(t_i))^2 \quad (1-14)$$

Where $T_{exp}(t_i)$ is the experimental temperature value at time t_i and $T_{mod}(t_i)$ is the model temperature defined by:

$$T_{mod} = T_0 + \Delta T f t + T_1 \sin(\omega t + \varphi_1) + T_2 \sin(2\omega t + \varphi_2) \quad (1-15)$$

$f = \omega/2\pi$ is the stress frequency, T_0 is the temperature level at which the temperature recording starts, ΔT is the mean rise of temperature per cycle, T_1 and φ_1 are the amplitude and phase of the first Fourier component, T_2 and φ_2 are the same for the second component.

The author pointed out that most previous works that utilized IRT for the determination of fatigue limit focused on the temperature increment that is equivalent to ΔT [143][144], but in fact, all three measured parameters ΔT , T_1 and T_2 may give valuable insight on the fatigue limit. As shown in **Figure 1-17** (a), (c) and (d), the characteristic value corresponding to the stress amplitude above which a significant heat dissipation is revealed could be derived for each figure. These three values are similar to each other and are close to the fatigue limit determined by traditional experiments.

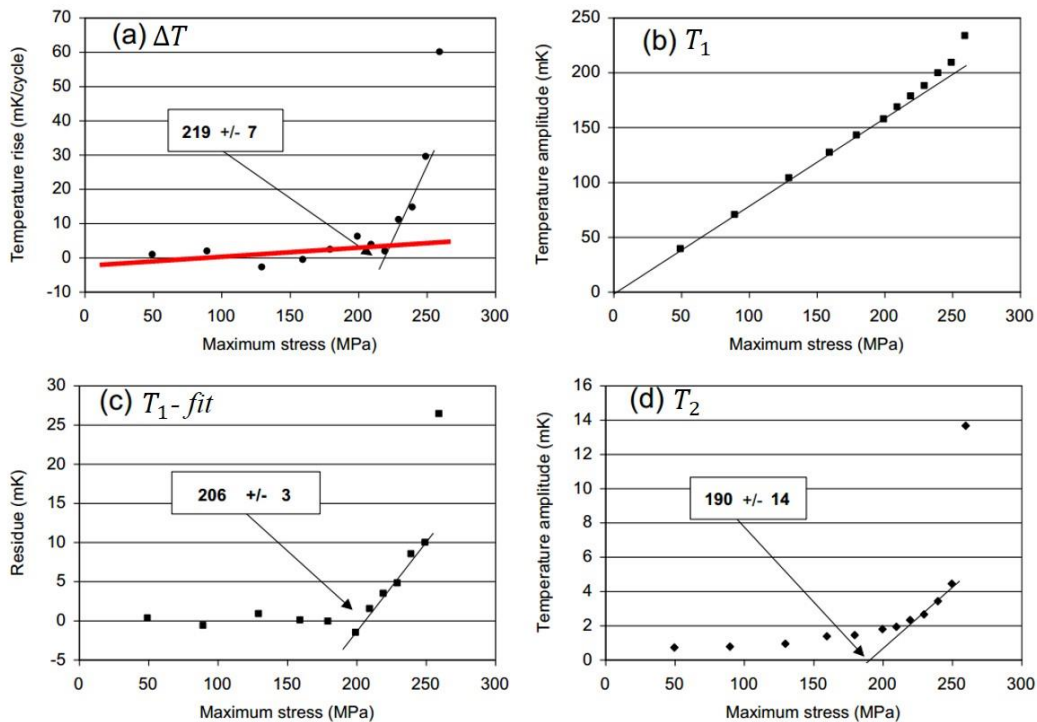


Figure 1-17. 316L stainless steel sample submitted to a fatigue test at frequency $f=2\text{Hz}$ ($R=-1$). Lock-in thermography provides an image of ΔT , T_1 and T_2 : (a) $\Delta T(\sigma)$; (b) $T_1(\sigma)$; (c) the difference between and the linear fit of its initial part; (d) $T_2(\sigma)$. Each point is the result of 10 cycles. Failures occurs during the

test at 270MPa [140].

Besides, there is also other fatigue limit prediction method based on lock-in thermography. For example, based on Luong's method, Bremond et al [145] developed a digital processing 'D-mode' method to evaluate the fatigue limit of a gravity die-cast Aluminium alloy. This digital processing algorithm D-mode allows to separate the non-linear coupled thermomechanical effects (dissipated energy) from thermoelastic source. With the application of Luong's method to the data of dissipated energy against the stress level, the fatigue limit could be determined (**Figure 1-18**).

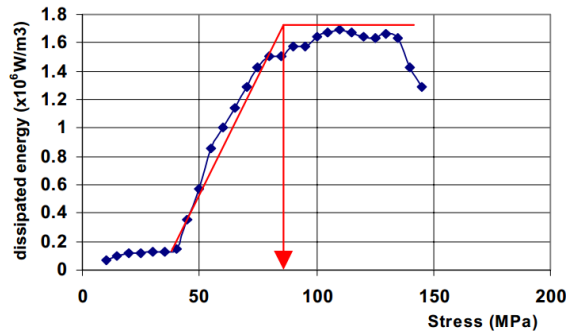


Figure 1-18. Fatigue limit determination by D-mode method [144]

Fatigue life

According to Risitano et al [146], from the energy standpoint, the failure of materials through fatigue occurs when the energy of plastic deformation reaches the limiting energy E_c , a constant that is independent of the loading level and loading history. By neglecting the variation of stored energy within the material, then the limiting energy E_c will be equal to the energy dissipated as heat Q . Since the heat energy $Q \propto \Phi$ (Φ : the integral of $\Delta T-N$ curve which is an energetic constant), accordingly $E_c \propto \Phi$. During fatigue tests, the stabilized temperature stage is reached in a short time and occupies almost the whole fatigue life (70-80%) for the cyclic loads higher than the fatigue limit but lower than the yield limit. Hence, the energetic parameter Φ , defined as $\Phi = \int_0^{N_f} \Delta T dN$, can be simplified as the product of stabilized temperature ΔT_s and the fatigue life N_f :

$$\Phi \approx \Delta T_s \cdot N_f \quad (1-16)$$

If a succession of increasing loads is stepwise applied to the same specimen for a certain number of loading cycles with the unchanged loading frequency. The stabilized temperature rise ΔT_{si} under different stress levels σ_i could be recorded by the infrared camera. Consequently, the fatigue life N_{fi} under different stress levels could be conveniently determined:

$$N_{fi} = \Phi / \Delta T_{si} \quad (1-17)$$

The whole S-N curve can then be plotted by a set of data pairs (N_{fi}, σ_i) (**Figure 1-19**).

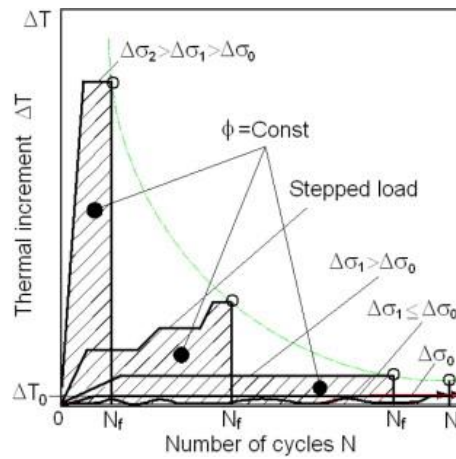


Figure 1-19. Qualitative increase in temperature ΔT and energetic parameter ϕ for different histories of stress over the fatigue limit $\Delta\sigma_0$ [115]

Figure 1-20 plots an idealization of the temperature evolution under cyclic loads. It is observed that for loads greater than fatigue limit, the stabilized temperature rise of stage II and temperature gradient in stage I, are higher the greater the stress level with respect to fatigue limit. Amiri et al. [147] [148] pointed out that the initial slope of temperature rise plotted as a function of fatigue cycles could be used as an index for fatigue life prediction. More specifically, the relationship between the rate of temperature rise in stage I R_θ and the number of cycles to failure $2N_f$ could be described by:

$$2N_f = c_1 R_\theta^{c_2} \quad (1-18)$$

Where c_1 and c_2 are two constants. The value of c_2 is found to be independent of tested materials, and holds for different types of experiments, including torsion, bending, as well as

rotating-bending fatigue tests. As for c_1 , even though its value strongly depends on the material but the experimental data of a series of tests shows that the plot of N_f/c_1 against R_θ can be consolidated into a universal curve, as presented in **Figure 1-21** [148].

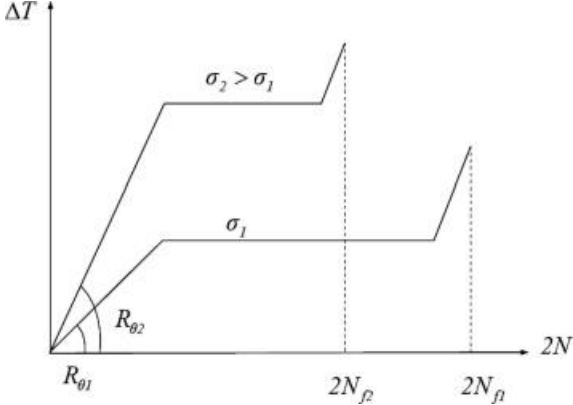


Figure 1-20. Rate of temperature in stage I and stabilized temperature rise in stage II increase with the increase of stress level [147]

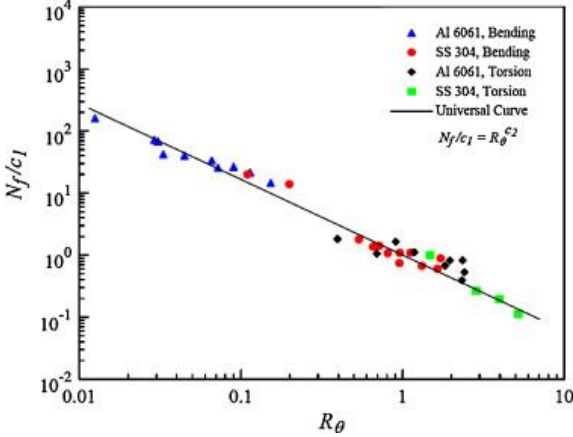


Figure 1-21. Universal curve of N_f/c_1 versus R_θ [148]

Huang et al. [14] showed that the rate of temperature rise of high ductility material near the end of the fatigue testing is related to the fatigue life. Their experimental results revealed that very close to the final failure, there is a sharp increase of temperature rise (see **Figure 1-22**) just after the steady-state stage II. This temperature rise is associated with initiation and propagation of macrocracks [149] and imminent fracture. The relation between the rate of temperature rise ΔT and fatigue life was given as:

$$\frac{\Delta T}{\Delta t} = C' \cdot \exp\left(\frac{G}{N_f^{1/b}}\right) \tag{1-19}$$

where t is time. C' , G and b are constants which depend on the properties of the material and

the test conditions.

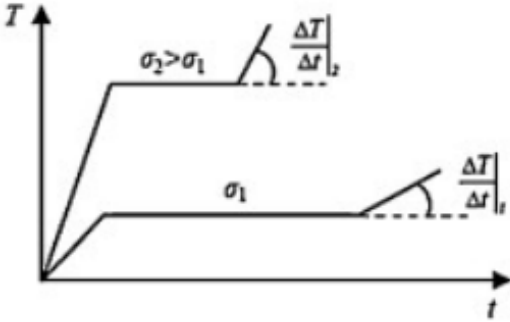


Figure 1-22. Schematic presentation of temperature variation with time used for fatigue life prediction [14]

Jiang et al. [150] showed that the stabilized temperature rise could be used as an index and is correlated with the fatigue life (**Figure 1-23**). They reported the following relationship between the fatigue life N_f and the temperature index ΔT_{ind} , defined as the temperature difference between steady-state temperature and the temperature of the initial stress-free stage:

$$(N_f)^m = C \Delta T_{ind} \tag{1-20}$$

where m and C are material constants. The temperature index exhibits a linear relationship with the fatigue life on a logarithmic scale.

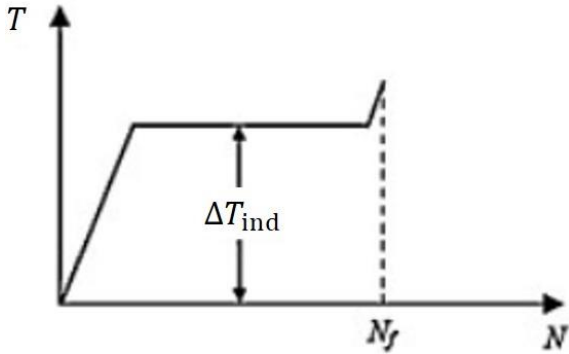


Figure 1-23. Schematic definition of ΔT_{ind} [150]

Based on the damage accumulation mechanism, Huang et al. [18] developed a two-parameter fatigue life model for CFRP by combining the stiffness degradation with the temperature variation measured by IRT. The details of this method will be presented in section 3.1.2.

During the service life, it is highly likely that CFRP structures can be exposed to unexpected impact damage from foreign objects. Very often, damage introduced in this way is not visible by the naked eyes and difficult to detect. However, various damage mechanisms including

matrix cracking, delamination and fiber fracture may be induced inside the material. Under fatigue loading, the initial impact damage behaves as a discontinuity and tends to propagate and leads to premature failure of the structure. Therefore, apart from the study on the fatigue behavior of CFRP, it is also important to investigate the post-impact fatigue behavior of CFRP for safety and reliability considerations.

1.4 Determination of post-impact fatigue properties

1.4.1 Characterization of impact damage

Impact is defined as the collision between two or more objects, where the interaction between the objects can be elastic, plastic, fluid or any combination of these. The impact velocity is one of the fundamental quantities in impact dynamics. The nature of all forms of impact damage is best classified with respect to the impact velocity, which may span several orders of magnitude. Generally, there are four types of velocity: low, intermediate, high and hypervelocity. In particular, low velocity impact usually implies the impact with velocity of projectile in the range of 4-10 m/s and energies no more than 50 J. Dropped hand tools during maintenance or service, hail hit endured by the aircraft during flight operations all fall into this category. In the intermediate velocity impact range, bird strikes and impacts due to runway debris are typical examples. The velocity of impact varies from 10 m/s to 300 m/s and the energy could reach up to 10 kJ. When the impact velocity increases further, there is high velocity impact. High velocity impact is understood to be in the range of 300-2000 m/s with impact energy varies between 10-20 kJ. Ballistic impact caused by the missile fragments can be classified into this category. Finally, there is hypervelocity impact, which has been applied to characterize spacecraft or satellite that may be struck by the space debris at velocities of order of 30-70 km/s.

When subjected to impact loading, composite materials are capable of absorbing and dissipating the impact energy in the following elastic and fracture processes [151][152]. As a consequence, when a projectile hits the composite materials with low velocity, the incident

energy of projectile is basically absorbed by the whole structure. Damage usually occurred inside the material without any significant evidence on the surface, which is also known as Barely Visible Impact Damage (BVID). Whereas in a high velocity impact, most of the impact energy is dissipated over a small zone immediate to the point of contact. Hence, the impact will leave an obvious local indentation on the impacted surface.

All forms of composite damages can take place in the laminate after impact. However, the most common damage characteristics are matrix cracks, delamination and fiber fracture. Matrix cracking caused by high transverse stresses is normally dispersed within the entire damage zone with a concentration under the impactor.

Delamination is primarily driven by the interlaminar shear stress. It normally appears between the composite plies of different orientations and are found to be manifested in a spiral-stair manner in the through the thickness direction [153][154]. A typical distribution of delamination in composite laminates is shown in **Figure 1-24** (a). As can be seen from the figure, the delamination is lemniscate or ‘peanut’ shaped with major axes oriented along the fibers of the lower layer [155]. The envelope of region affected by delamination is usually in a conical shape with the largest damage extent nearest to the rear face (**Figure 1-24** (b)) [156].

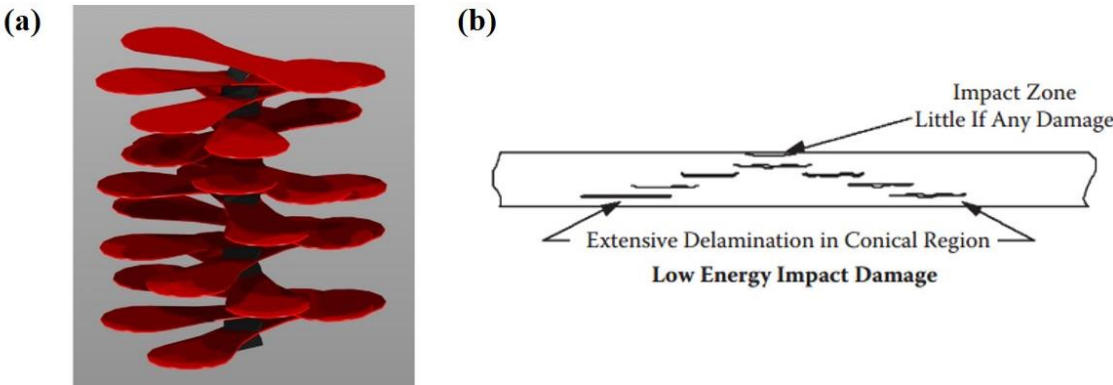


Figure 1-24. Individual delamination caused by impact: (a) distribution of delamination [157][158];
 (b) envelope of delamination [159]

Fiber fracture generally occurs much later than matrix cracking and delamination in the

damage process. Under the contact area, fibers failed due to locally high stresses and indentation effects of shear stresses, while local tensile failure of fibers has been observed on the back face. More extensive fiber fracture normally occurs in the central part of the impact zones, extending to approximately half the delamination width with direction perpendicular to fibers in each ply [160] and appears to be fairly uniformly distributed through the thickness [161]. A projected view of delamination and fiber fracture is presented in Figure 1-25.

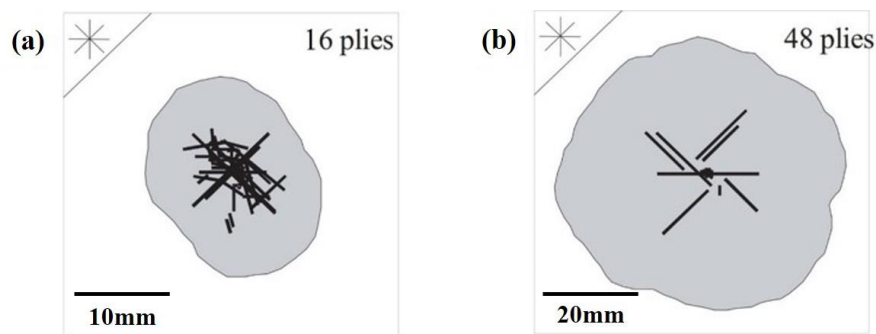


Figure 1-25. Fiber fractures in the laminates: (a) 16 plies; (b) 48 plies [161]

1.4.2 Post-impact residual properties

After the impact loading, impact damage formed inside the structure can not only degrade the material properties, but also impair its structural integrity and static load-bearing capacity, or namely, the residual strength and stiffness [162][163]. The degradation of strength and stiffness is affected by a wide variety of factors, including the impact energy, size and geometry of impactor as well as material property, geometry, stacking sequence of the structure, etc.

The influence of impact events on the tensile and compression strength is quite different, mainly due to the differences in tensile and compressive failure mechanisms. Tensile failure of impacted composite materials is basically governed by fiber fracture, although it may be preceded by matrix cracking and subsequent delamination growth. Fiber damage can cause a degradation of local tensile stiffness by more than 80% [164][165], but the reduction in global strength is smaller owing to the inherent toughness of composite material.

The compressive strength, by contrast, is strongly affected by impact events, even of very low energy. Compressive failure of impacted composite laminates includes several types of competing and interacting damage mechanisms, i.e., notch effect, global buckling, local buckling and a combination of the local and global buckling (**Figure 1-26**). These failure mechanisms lead to a more significant reduction in the residual properties. In the study of Mitrovic et al [166], the reduction in the compressive strength of AS4/3501-6 QI composites was amounted to 25%, once the impact energy slightly exceeds the impact threshold level (2.1 J). Stellbrink et al [167] observed a reduction of 50% in residual compressive strength for T300/69 and T300/914 when the ratio of delamination diameter to specimen width varied from 0.32 to 0.44, while Uda et al [168] reported a 60% and 45% reduction for UT500/epoxy and AS4/PEEK laminates.

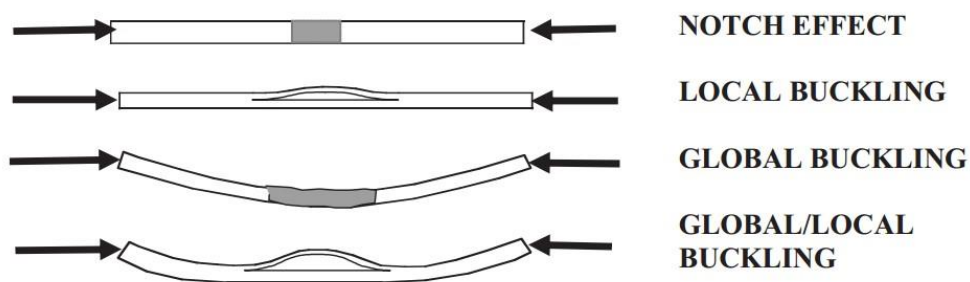


Figure 1-26. Failure mechanisms for compression after impact

1.4.3 Post-impact-fatigue life prediction of composite materials

Very often, impact damaged components, particularly when damage can barely be detected by visible inspection, will continue to fulfill their function unless the damages visibly affect the safety of structure. If the cyclic fatigue loading is applied to the impacted composite structure, since the properties of impacted structure are already degraded, it will fail prematurely compared to the unimpacted ones. Therefore, in order to evaluate the fatigue life of impacted composite structures, it is needed to consider the behaviors under both impact and fatigue loading simultaneously. In this regard, a strength reduction concept based on the Broutman's model is introduced here.

Broutman et al [169] reported that the residual strength of composite structure decreases linearly in accordance with the cycle number of fatigue loading and based on the experimental observations, developed a fatigue life prediction model under block loading. When a series of m fatigue blocks with cycle number n_i at stress level σ_i is applied, the residual strength σ_m is given by:

$$\sum_{i=1}^m \left(\frac{\sigma_0 - \sigma_i}{\sigma_0 - \sigma_m} \right) \frac{n_i}{N_i} = 1 \quad (1-21)$$

Where σ_0 is the tensile strength and n_i denotes the number of cycles at σ_i under constant amplitude loading. N_i is the fatigue life when σ_i is applied.

For the case of a 2-stage block loading, Eq. (1-21) becomes:

$$\left(\frac{\sigma_0 - \sigma_1}{\sigma_0 - \sigma_2} \right) \frac{n_1}{N_1} + \frac{n_2}{N_2} = 1 \quad (1-22)$$

From Eq. (1-22), it is obvious that the strength reduction by the first loading block can be expressed as $(\sigma_0 - \sigma_1)n_1/N_1$. As stated above, all of the impact and fatigue loading contribute to the residual strength degradation of structure. It can be, therefore, occurred that the strength reduction due to impact damage, $\sigma_0 - \sigma_R$, is equivalent to that due to the first loading block, as shown in **Figure 1-27**. Then the following relationship can be obtained:

$$\sigma_0 - \sigma_R = (\sigma_0 - \sigma_1) \frac{n_1}{N_1} \quad (1-23)$$

Substituting Eq. (1-23) into Eq. (1-22) leads to

$$\left(\frac{\sigma_0 - \sigma_R}{\sigma_0 - \sigma_2} \right) + \frac{n_2}{N_2} = 1 \quad (1-24)$$

In order to avoid a confusion of symbols, the constant amplitude fatigue maximum stress σ_{max} is substituted for σ_2 , the fatigue life of impacted composite materials N_{imp} is substituted for n_2 and the fatigue life of non-impacted composite materials N_f is substituted for N_2 , thus Eq. (1-24) can be rewritten as follows:

$$N_{imp} = N_f \left(1 - \frac{\sigma_0 - \sigma_R}{\sigma_0 - \sigma_{max}} \right) \quad (1-25)$$

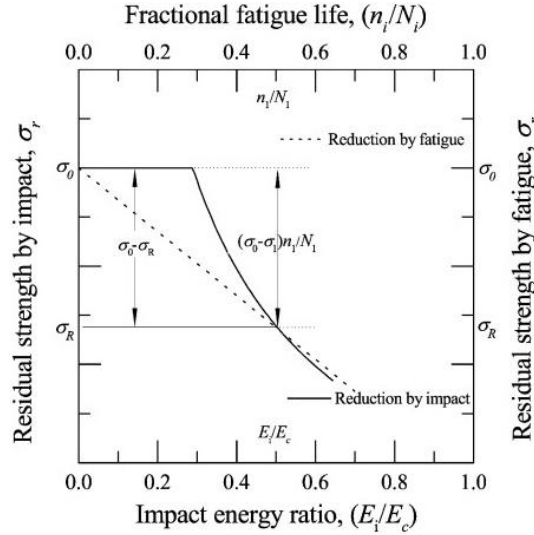


Figure 1-27. Strength reduction behavior due to impact and fatigue loading [170]

From Eq. (1-25), the residual fatigue life of impacted composite materials is formulated as a function of the residual strength σ_R and fatigue life N_f of non-impacted composite materials. Therefore, if N_f and σ_R are available, then N_{imp} can be obtained. This leads us to identify the fatigue life of non-impacted composite materials N_f and residual strength of impacted composite materials σ_R .

Huang et al [171] suggested that the fatigue life of composite materials without impact N_f can be predicted by the expression:

$$N_f = A \left(1 - \frac{\sigma_{max}}{\sigma_0} \right)^B \quad (1-26)$$

Where A and B are the parameters that can be obtained from the fatigue tests of unimpacted composite materials.

Substituting Eq. (1-26) into Eq. (1-25), one obtains:

$$N_{imp} = \left(1 - \frac{\sigma_0 - \sigma_R}{\sigma_0 - \sigma_{max}} \right) A \left(1 - \frac{\sigma_{max}}{\sigma_0} \right)^B \quad (1-27)$$

As N_f is already evaluated, the only thing left is to identify the residual strength σ_R .

As stated in the work of Kang et al [170], the residual tensile strength σ_R of impacted

CU125NS carbon/epoxy composite material can be obtained by Caprino's model [172]:

$$\frac{\sigma_R}{\sigma_0} = \left(\frac{E_{th}}{E_i} \right)^\beta \quad (1-28)$$

Where σ_R is the residual strength, σ_0 is the tensile strength of undamaged structure, E_i and E_{th} are the incident impact energy and threshold impact energy, respectively and the exponent α is a constant which depends on the geometry and material.

Hence, the fatigue life prediction model for the impacted CU125NS composites can be expressed as follows:

$$N_{imp} = \frac{\sigma_0 (E_{th}/E_i)^\beta - \sigma_a}{\sigma_0 - \sigma_a} A \left(1 - \frac{\sigma_{max}}{\sigma_0} \right)^B \quad (1-29)$$

While Koo and co-workers [173] developed another strength reduction model for the woven CFRP composites assuming the permanent impression left on the surface as a hole notch. The model was able to account for the convergence of residual strength with the increase of impact energy:

$$\frac{\sigma_R - \sigma_{HR}}{\sigma_0} = \left[1 + 0.67 \left(\frac{D_i}{D} \right) \cdot \left(\frac{E_a}{E_{th}} \right) \right]^{-2} - 0.01 \quad (1-30)$$

Where σ_{HR} is the tensile strength of notched specimen with hole notch diameter equivalent to that of permanent impression. D_i and D is the diameter of permanent impression and impactor, respectively. E_a is the absorbed impact energy.

Substituting Eq. (1-30) into Eq. (1-27), the residual fatigue life becomes:

$$N_{imp} = \left[\left(1 + 0.67 \left(\frac{D_i}{D} \right) \cdot \left(\frac{E_a}{E_{th}} \right) \right)^{-2} + \frac{\sigma_{HR} - \sigma_a}{\sigma_0} - 0.01 \right] \left(\frac{\sigma_0}{\sigma_0 - \sigma_a} \right) A \left(1 - \frac{\sigma_a}{\sigma_0} \right)^B \quad (1-31)$$

The model was further shown to be also valid for the damaged C-shaped CFRP structure in a later study.

Vasconcellos et al [174] extended the empirical fatigue life model developed by Epaarachchi

et al [175] for composites without impact to predict the fatigue life of impact-damaged woven hemp composites in tension-tension mode. To adapt the model to impacted specimens, the static tensile strength of the non-impacted specimens σ_0 is replaced by the residual static strength of impacted specimens σ_R . The number of cycles to failure N_{imp} has the following form:

$$N_{imp} = \left[1 + \left(\frac{\sigma_R}{\sigma_{max}} - 1 \right) \frac{f^\beta}{\alpha(1-R)^{1.6-R}} \left(\frac{\sigma_R}{\sigma_{max}} \right)^{0.6-R} \right]^{\frac{1}{\beta}} \quad (1-32)$$

Where σ_{max} is the maximum stress during fatigue cycling, R is the stress ratio, f is the frequency, α and β are the two material parameters experimentally evaluated on non-impacted specimens.

Even though the exact expression of three above mentioned models are different from each other, the basic idea of these models are similar: it is to predict the fatigue life of impacted composites based on the fatigue life of composites without impact and the residual strength for a given impact energy.

As previously mentioned, IRT can be applied to determine the fatigue properties of non-impacted materials in a short time. Similarly, it can be also used for the rapid prediction of the post-impact fatigue properties .

1.4.4 Rapid determination of post-impact fatigue properties with IRT

Compared to the studies that utilize IRT for the rapid prediction of fatigue properties, the number of studies that evaluating the post-impact fatigue properties with the use of IRT is rather limited.

Kosmann et al. [176] studied the temperature evolution of impacted GFRP during fatigue through the use of IRT. The results show that the temperature curves is well correlated with

the stiffness degradation curve, as expected. In addition, the temperature curves have a higher sensitivity in displaying damage in the material. Locally increased damage could be well shown by the hotspot in the IR images, which occurred in the area of impact damage during tests. In the study of Christian et al [177], the evolution and propagation of impact damage in CFRP during fatigue testing is evaluated by IRT. The temperature of impact damage is superior to its surrounding area and could be clearly identified by the hotspot in the IR photographs. Similar observations were also made by the authors of Ref. [178] for impacted CFRP, but with the use of Pulse Phase Thermography (PPT). PPT is one type of active thermography which preserved the advantages of LT but with reduced measurement time. It is because the external excitation of PPT is a rectangular pulse which is decomposed of a multitude of sinusoidal components with different frequencies. This way, magnitude and phase images for various excitation frequencies and accordingly depths can be obtained with one measurement.

In the work of Li et al. [180], the maximum surface temperature difference, ΔT_{max} , is defined to investigate the temperature variation of impacted CFRP during fatigue. The evolution of ΔT_{max} increase by three stages in a ‘rapidly-slowly-rapidly’ manner, with each stage occupies less than 5%, more than 85% and less than 10% of fatigue life, respectively. The corresponding damage mechanisms for each stage is similar to those of unimpacted specimens. But the duration of first stage is shorter for impacted specimens. This is because the friction between the cracked matrix that caused by impact test, promotes a quicker temperature increase. Tuo et al. [179] studied the damage evolution and failure mechanisms of impacted CFRP under fatigue loading using both IRT and ultrasonic C-scan approach. Similar results in maximum temperature increase have been observed by the authors. Besides, a method to distinguish the fiber, matrix and delamination damage based on the temperature and C-scan data has been proposed. It is observed that the evolution of different types of damage with loading cycles can all be divided into two stages. In the other two studies of Li et al. [180][181], the damage evolution was quantitatively investigated via damage area using

passive and active IRT, respectively. The damage area of impacted CFRP being inspected under different fatigue cycles was acquired through post-processed IR images. It is revealed that even though due to the difference in stacking sequence and impact energy, the evolution of damage area with respect to the number of loading cycles may be composed of two stages or three stages. Quantitatively, the relationship between these two terms could be well described by the following expression regardless of the configuration of IRT:

$$D_{damage} = D_0 + \alpha \left(\frac{\beta}{\beta - N} - 1 \right)^p \quad (1-33)$$

Where D_{damage} is the damage area of the specimen, D_0 is the initial impact damage, α , β and p are parameters which depend on material, loading, structure, etc. in a complex manner.

In the study of Katunin et al. [182], the influence of Low-Velocity Impact Damage (LVID) on the fatigue limits of both CFRP and GFRP was investigated by IRT. The tests have been performed on CFRP and GFRP that have been subjected to different impact energies. The maximal self-heating temperature rise of each image obtained from IR camera is plotted against the applied stress levels to determine the fatigue limit following Luong's method. The results suggest a clear decreasing tendency of fatigue limit with the increase of impact energy for both materials.

1.5 Summary

In this chapter, the general definition, constitution and classification of composite materials are first given. CFRP, as one of the composite materials that have been extensively used as structural materials in the aerospace, automotive and marine industries, is the focus of this study. Components manufactured from CFRP are inevitably used in the situations where fatigue loads are present. Therefore, it is of great importance to understand thoroughly the fatigue behavior of this material. However, the traditional fatigue tests are rather expensive and time consuming. To overcome these shortcomings, new methods that allows for the accelerated determination of fatigue properties of materials are highly desired. Among the various methods, the thermographic approach, which is based on the self-heating phenomenon

in a material under loading, allows to determine fatigue properties of the material in a short time. This method was originally designated for metallic materials, but later successfully applied to a variety of composite materials. Nevertheless, the fiber orientation of these composite materials was basically unidirectional [18], $\pm 45^\circ$ [19] or woven [18], but rarely in MD. Whether these methods can be applied to all kinds of composite materials, especially the MD composite materials or not? Do these methods have clear physical mechanisms, or they are just empirical?

These questions are needed to be answer in this thesis.

Furthermore, it should be noted that even though the stiffness and strength to weight properties of CFRP are superior to a range of conventional materials, due to the lack of through-the-thickness reinforcement, CFRP are extremely susceptible to impact loading, even the imperceptible impact can cause such internal barely visible impact damages as matrix cracking, delamination and fiber fracture. The employment of impacted composites under cyclic loads seriously causes a significant drop in the material property, raising concerns for the safety of composite structures. Therefore, it is also important to understand the post-impact fatigue behavior of CFRP. Considering the shortage of traditional fatigue testing, the previously mentioned thermographic approach, is still the first choice for this case. However, in the literature, the number of studies that utilize IRT to investigate the post-impact-fatigue behavior of composite materials is rather limited. Besides, in these studies, IRT is mainly used as an NDE method to characterize the fatigue damage evolution, but not for fatigue life prediction. As a consequence, in this thesis, the possibility to extend the thermographic approach of unimpacted composite materials to impacted ones for fatigue life prediction will be discussed.

Chapter 2 Determination of fatigue limit of MultiDirectional (MD) composite materials under tensile loading

Compared to the UD and angle-ply laminates, the fatigue damage mechanisms in the MD laminates are more complex, leading to different thermographic behaviour. Taking into account of this, a new fatigue limit determination method based on thermographic data is proposed in this chapter.

2.1 Materials and specimens

2.1.1 Materials

Composite laminates used for the fatigue tests were manufactured from unidirectional carbon fiber epoxy prepreg (Hexcel). The carbon fiber is UD150/CHS/12K high resistant with area weight 150 g/m². The resin is a formulated epoxy HexPly®M79 with a resin volume fraction V_f of 38%, well adapted for low temperature curing process (below 100 °C). The basic physical properties of matrix and the mechanical properties of carbon fiber epoxy prepreg used in this work are listed in **Table 2-1** and **Table 2-2**, respectively, which are both provided by the manufacturer.

Table 2-1 Basic physical properties of HexPly®M79

Parameters	Values
Density	1.15 g/cm ³
Color	Translucent
T _{onset}	120 °C [± 5°C]
T _{peak}	145 °C [± 5°C]
Enthalpy	100 J/g [± 20%]
Cure cycle	70°C*480 min/80°C*360 min/90°C*240 min
Recommended heat rate	0.5-5 °C/min
Pressure gauge	0.5-5 bar

Table 2-2. Basic mechanical property of the cured epoxy carbon fiber prepreg

Properties	Values
0° tensile strength	2280 MPa
0° tensile modulus	117 GPa
0° compression strength	1270 MPa
0° compression modulus	128 GPa
0° flexural strength	1810 MPa
0° flexural modulus	120 GPa
0° interlaminar strength	68 MPa
Nominal mass	455 g/m ²

2.1.2 Preparation of CFRP laminates

The composite layers were first cut from the prepreg row with a size of L500×W300 mm and then hand laid into two MD stacking sequences: cross-ply-[(0/90)₂/0/(90/0)₂] and QI - [0/45/90/−45]₅. The cross-ply stacking sequence is chosen to complete the unfinished work of Huang et al [139]. While the reasons for the choice of QI stacking sequence are: i) this laminate is usually used in composite structures, having the same in-plane stiffness regardless of the loading direction; ii) in the literature, the thermographic approaches were barely applied to QI laminates. The stacked plies, which are covered on both sides by a fine polyester cloth peel-ply (for enhancing surface effect) are laid onto the mold surface, on top of which a porous release film, bleeder ply and vacuum bag are placed (**Figure 2-1**). Two valves with gasket and tightening wheel are also embedded in the bag. One is used for exhausting air from the inside of the bag by a vacuum pump and the other one is used to measure the actual pressure. A minimum pressure value of -0.85 bar should be applied to meet the requirement of airtightness. Thereafter, the entire assembly is placed inside an autoclave for cure. During the cure cycle, the pressure in the autoclave is set as 2.0 bar. The temperature is raised at a 1 °C/min rate up to 80 °C and held for 4 hours, as depicted in **Figure 2-2**. Subsequently, the layup is cooled down naturally to the room temperature under the same pressure, which results in a laminate of nominal thickness 1.204 (± 0.018)/1.012 (± 0.025) mm, respectively.

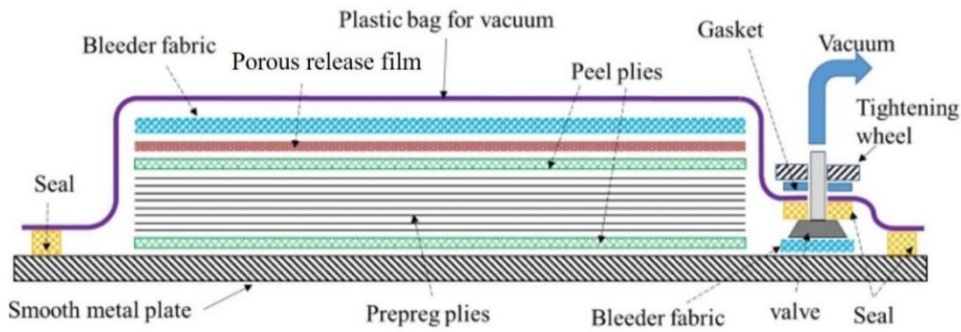


Figure 2-1. Autoclave process schematic [139]

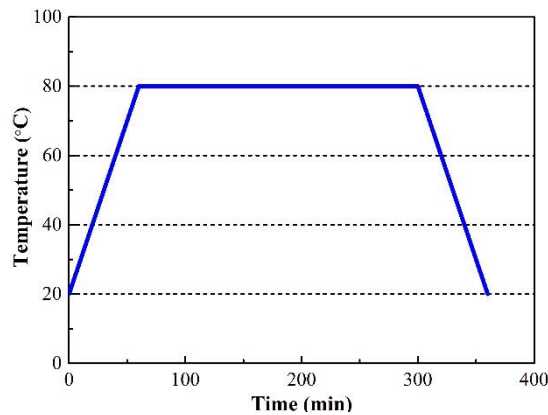


Figure 2-2. Recommended curing cycle

The specimens were water-jet cut from the fabricated composite laminates to the dimensions given in **Figure 2-3**. The main advantage of using water-jet cutting is that the cuts made by waterjets are significantly more accurate and precise than those made by other tool (the accuracy is close as 0.001" (0.025 mm). Besides, since flow waterjets cut the specimens by erosive action rather than friction and shearing, they produce a uniform smooth edge free of frayed or delaminated areas. This point is rather important because as is well known, the fatigue property of composite material is significantly affected by the edge quality [183].

To prevent rupture and slippage in the grip region of the test device, Glass Fiber Reinforced Plastic (GFRP) glued end-tabs were used at either end of the specimens. Tabs of dimensions L50 mm × W25 mm were adhered to the specimens' surface using Hysol EA 9394 Part A + B epoxy after curing at 66 °C for more than 24 h in an oven. The fibers in the tabs were oriented in the $\pm 45^\circ$ direction.

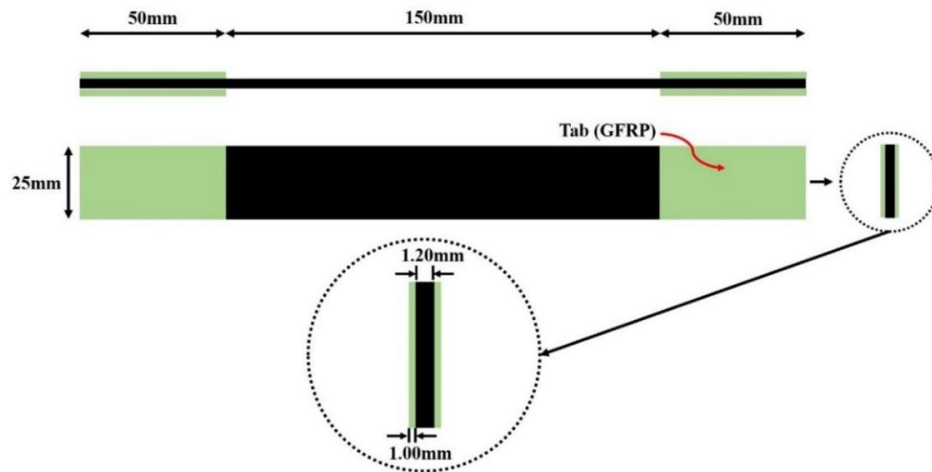


Figure 2-3. Dimensions of specimens (in accordance with ISO 527-4: 2021 [184])

2.2 Quasi-static tensile tests

2.2.1 Experiments

In order to determine the Ultimate Tensile Strength (UTS) for the fatigue tests, quasi-static tensile tests were conducted at room temperature using INSTRON universal testing machine (INSTRON 5500R), equipped with a 100 KN load cell (see **Figure 2-4**). The tensile tests were performed according to standard ISO 527-4: 2021 [184], in displacement control with a 2.0 mm/min cross-head speed. 3 specimens were tested for each stacking sequence. During the tests, the tensile force was recorded by the sensor of Instron 5500R testing machine and the tensile strain was measured with a Digital Image Correlation (DIC) system Aramis 2M (GOM, Braunschweig, Germany).

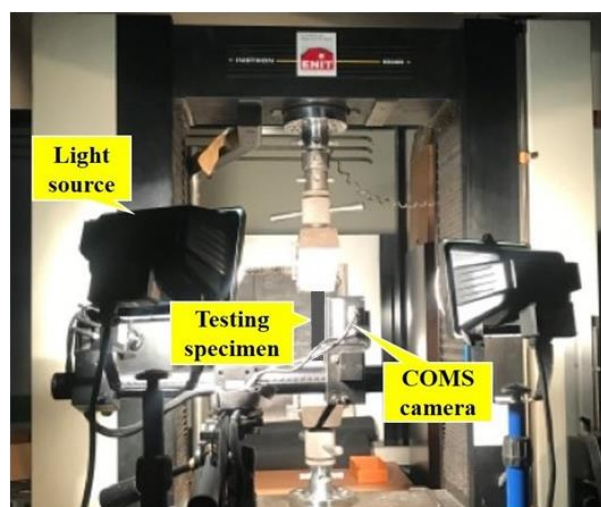


Figure 2-4. Experimental set-up of quasi-static tensile test with DIC

DIC is a non-contact, optical full-field deformation measurement technique which combines modern optoelectronic technology, digital image processing technology with computer technology. The basic concept of DIC is based on the comparison of images before and after deformation. By correlating the location of pixel subsets or facets in the original and deformed image (see **Figure 2-5**), normally based upon light intensity (i.e., grey level), the full field displacements and strain field can be accurately determined, which facilitates the accurate and efficient measurement of elastic modulus.

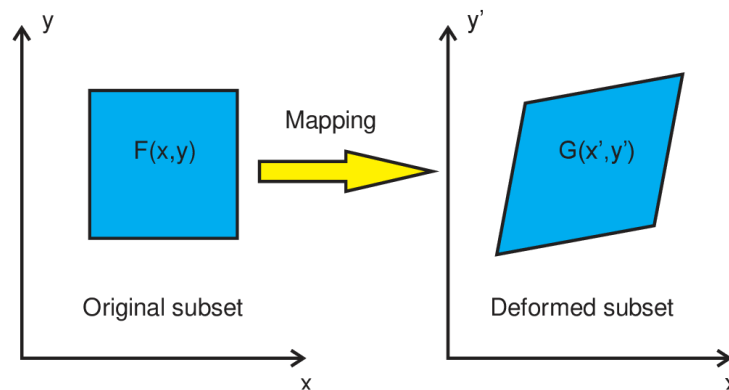


Figure 2-5. Principle of DIC

A DIC system consists mainly of light sources, digital cameras and correlation analysis software. In this study, two 8-bits Complementary Metal Oxide Semiconductor (CMOS) cameras with a resolution of 1624×1236 pixels were positioned on the same side of the specimen to capture the images of the specimen surface, as shown in **Figure 2-4**. Before testing, a random speckle pattern which was created by the black and white spray paints is applied on the surface of the specimen. The data recording rate is one frame per second and the post-processing of the obtained results was performed by the Aramis software. The calculation of the strain field is carried out after the measurement of the displacement field.

2.2.2 Results and discussion

The experimental results of quasi-static tensile tests are reported in **Figure 2-6** and **Figure 2-7**. **Figure 2-6** gives the evolution of load versus displacement for the specimens of each stacking sequence. For the cross-ply laminates, the initiation of matrix cracking and rapid growth of cracks in 90° layers occurred at the beginning of the test [185]. But the global stiffness is not

really influenced by this damage. The curves show an almost linear elastic behavior, then followed by a quasi-brittle failure. The final failure of the laminate occurred at the failure stress of 0° plies. For the QI laminates, transverse cracking in the 90° occurs at the beginning of tests [186], which causes delamination at 90/45 and 90/-45 interfaces at the same time. These damage lead to the change of slope (stiffness reduction), as shown in **Figure 2-6**. With the increase in load, off-axis cracks in the 45 and -45 plies initiate [186]. Before arriving at the failure load, fluctuations are observed in the loading curves accompanied by a continuous crackling sound, which is mainly caused by the fiber fracture in the ± 45° plies [186]. The final failure of the specimen is caused by the failure of 0° plies.

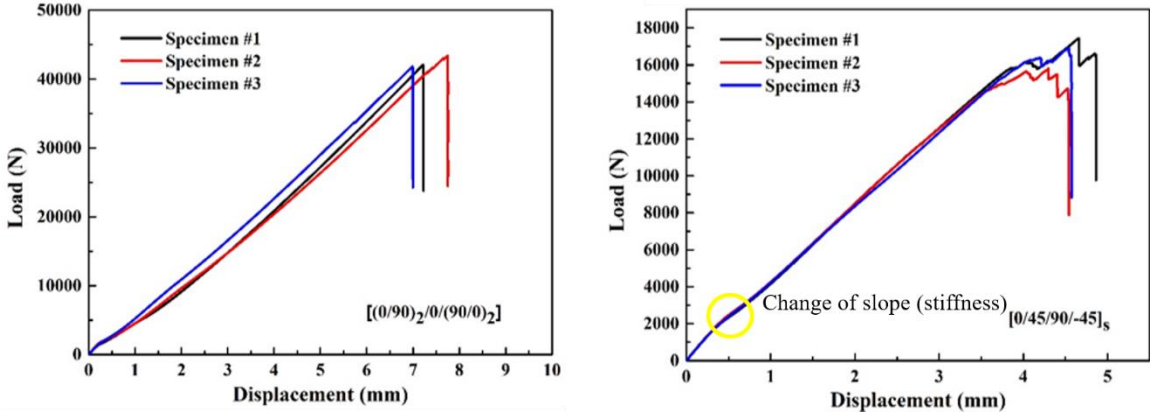


Figure 2-6. Load-displacement curve of tensile tests

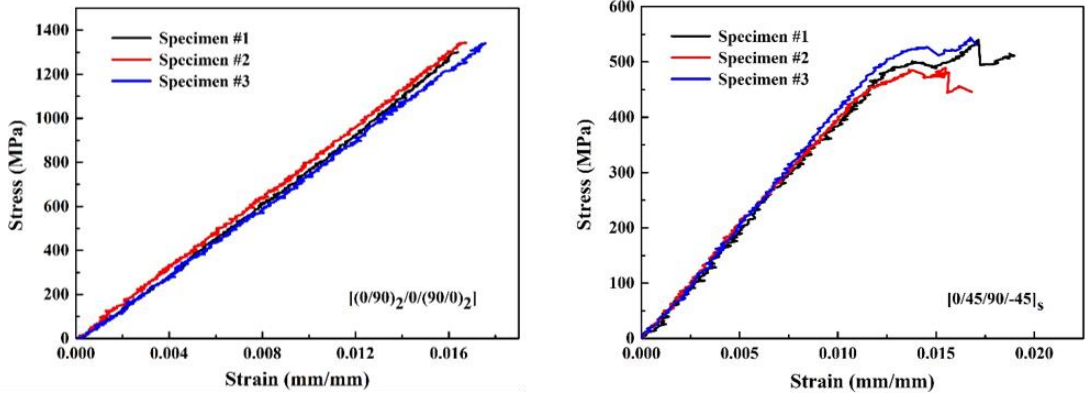


Figure 2-7. Stress-strain curve of tensile tests

The stress-strain response is presented in **Figure 2-7**. The tensile stress is computed by dividing the applied load by the initial cross-section of the specimen, while the tensile strain is evaluated based on the DIC results. All the cross-ply laminates clearly exhibit an elastic

behavior until failure. For the QI laminates, similar to the load-displacement curve, the stress-strain curves first showed an elastic behavior, and then followed by some fluctuations in the curves.

The average tensile properties of cross-ply and QI laminates are summarized in **Table 2-3**. Young's modulus of the laminates was determined using linear regression between strain of 0.05% and 0.25%. The tensile strength for each laminate obtained here, named as UTS will be referenced in fatigue tests.

Table 2-3. Average experimental results of tensile tests

Stacking sequence	UTS/MPa	Young's modulus/GPa
$[(0/90)_2/0/(90/0)_2]$	1329.4 ± 24.7	79.53 ± 1.96
$[0/45/90/-45]_5$	607.45 ± 22.14	42.04 ± 0.14

2.3 Fatigue tensile tests

2.3.1 Experiments

All the uniaxial fatigue tensile tests were carried out at room temperature by using the Instron servo-hydraulic fatigue testing system (cross-ply laminates using INSTRON model 8800, 250 kN capacity of load; QI laminates using INSTRON model 1342, 100 kN capacity of load). The fatigue tests were performed in a load amplitude control mode at a frequency of 5 Hz and with a stress ratio of $R=0.1$. This frequency allowed obtaining reasonable test duration without excessive temperature increase of specimen due to the self-heating effect, which may in turn have an influence on the mechanical, especially fatigue properties.

A FLIR X6800sc Series IR camera was utilized to measure the changeable surface temperature of the specimen in-situ and in real time. The device used in this work was a mid-wavelength InfraRed camera, with a spectrum response covering the range from 3 to 5 μm . The detector spatial resolution was 640×512 pixels and the thermal sensitivity was 18 mK at 30°C. The data recording rate of IR camera was set as 520 Hz. Optimal Field-Of-View (FOV)

conditions were achieved by placing the IR camera at a distance of approximately 68 cm in front of the specimen. To increase the thermal emissivity of the specimen surface, before fatigue tests, the surface of the specimen was coated with a thin and mat layer of black paint. A rectangular region of interest (ROI) of pixels was defined on each image to measure the mean temperature of the specimen. The detailed experimental set-up is depicted in **Figure 2-8** (a). A reference specimen is placed nearby the testing specimen to monitor the temperature change of ambient.

There are two type of fatigues tests conducted in this study to obtain the fatigue properties of material, both in accordance with the test standard ASTM D3479 [187]. The first set of tests is the traditional fatigue tests, various stress levels were chosen for different tests, where each test was stopped at specimen's failure or until a run-out of 10^6 cycles was reached. At least three tests were conducted at each stress level in order to produce a reliable S-N curve. The second set of tests is the step-loading fatigue tests monitored by IR camera. Herein, loading level applied on one specimen increases a step after certain cycles. In each loading step, the specimen was tested for a duration of 6000 cycles, which was sufficient to achieve temperature stabilization. The stabilized temperature rise is subsequently used for the fatigue limit determination. The first loading maximum stress starts with 30% UTS because the temperature rise is practical nil for the maximum stresses below. Up to 50% UTS, the maximum stress was increased by 5% UTS for each step. Beyond 50% UTS, the loading step decreased to 2.5% UTS and remained the same until failure, as shown in **Figure 2-8** (b). This variation in loading step size is aimed to provide higher resolution in the stress region closer to the expected fatigue limit. The duration of unloading between two loading steps was set as 10 min, which was necessary for stabilizing the temperature of a tested specimen to the ambient temperature. In total, three specimens were tested in this approach.

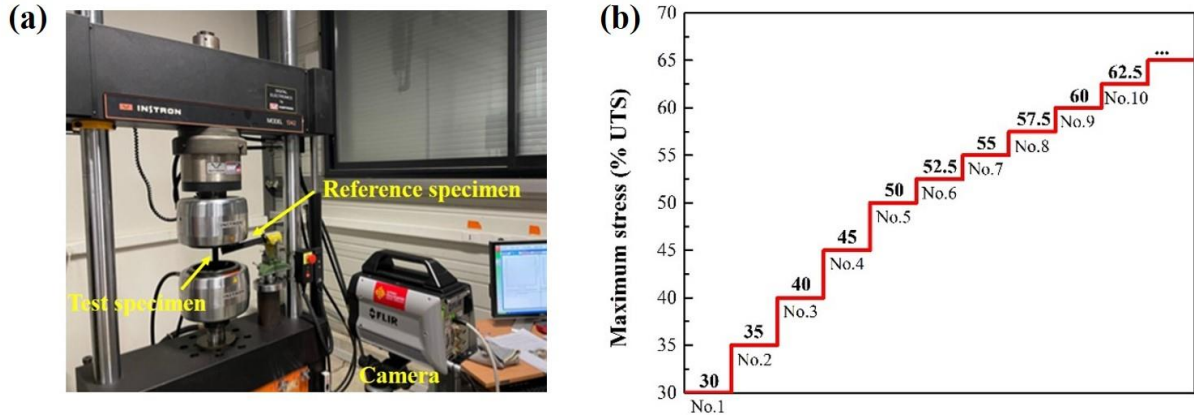


Figure 2-8. Fatigue tests with IR camera: (a) experimental set-up; (b) staircase loading procedure

A typical thermographic image of a specimen during the test is shown in **Figure 2-9**. The hot zone on the specimen surface is visibly identified through the thermographic images recorded by IR camera. The average temperature T of ROI could be obtained from the temperature distribution in the gauge length of the specimen (Box 1). The Box 2 records the temperature T_0 of the reference specimen. For the sake of characterizing the temperature variation caused by intrinsic dissipation and thermoelastic effect and eliminating the influence caused by ambient environment, the real-time average temperature rise, defined as $\Delta T = T - T_0$, is introduced to analyze the temperature variation.

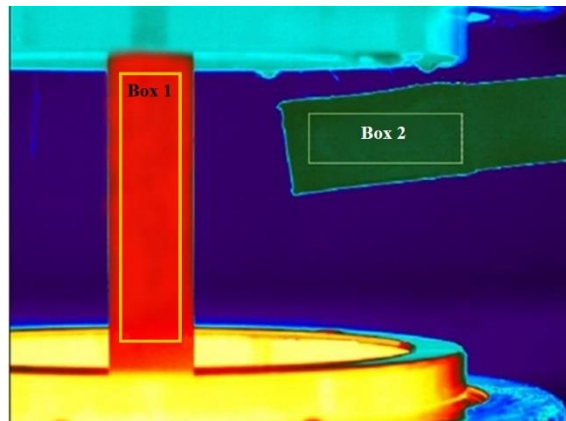


Figure 2-9. IR temperature distribution at center portion of specimen

Figure 2-10 plotted the hysteretic load-displacement curves at initial and subsequent number of loading cycles. From these curves, the experimental stiffness $K(N)$, which is defined as the slope of line joining the peak and valley of the hysteresis curve, can be identified as well as its evolution with respect to the cycle number. As can be seen from the figure, as the fatigue

cycle increases, the slope of the load-displacement curve, i.e., the stiffness constantly decreases. This is due to the softening of matrix and the weakening of bond between fiber and resin [188].

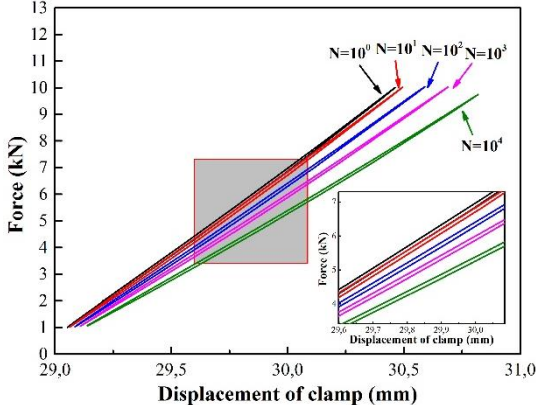


Figure 2-10. Hysteresis loops during fatigue tests

2.3.2 Traditional fatigue test results

For the QI laminates, five different stress levels were examined in the traditional fatigue tests, which ranging from 70% to 90% UTS with steps of 5% UTS. The fatigue tests were performed on at least 3 specimens for each loading level. The number of cycles to failure corresponding to each loading level was recorded to establish the S-N curve illustrated in **Figure 2-11**. As can be seen from the figure, the curve is linear in a semi-log scale over fatigue life from 10^3 to 10^7 cycles. In the literature, the number of cycles corresponding to the fatigue limit is often taken between 10^6 and 10^7 cycles [189][190]. Therefore, both values are considered here. The fatigue limit corresponding to a fatigue life of 10^6 cycles is 74.76 % UTS and that corresponding to 10^7 cycles is estimated to be 65.62 % UTS, by extrapolating the S-N curve.

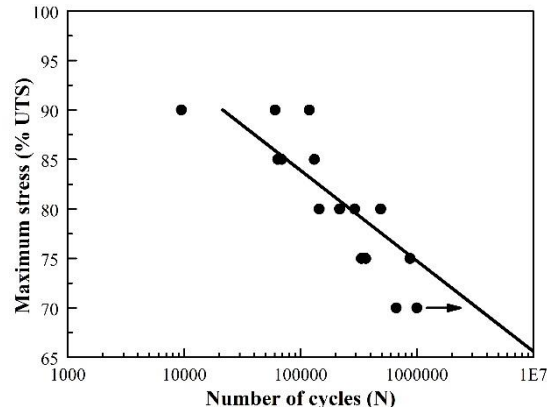


Figure 2-11. S-N curve determined by traditional fatigue tests for the QI CFRP laminates

For the cross-ply CFRP laminates, the traditional fatigue tests were performed on the loading level ranging from 65% UTS to 85% UTS. At least 3 specimens for each loading level were tested and the fatigue life values corresponding to each level were used so as to create the S-N curve presented in **Figure 2-12**. The curve is linear in semi-logarithm scale over four decades of life from 10^2 to 10^7 cycles. The fatigue limit corresponding to a fatigue life of 10^6 cycles is 68.94% UTS and that corresponding to 10^7 cycles is estimated to be 64.94 % UTS, by the extrapolation of the best-fit line.

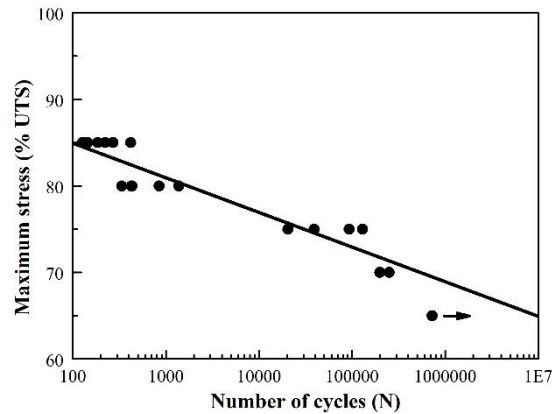


Figure 2-12. S-N curve determined by traditional fatigue tests for the cross-ply CFRP laminates

2.4 Rapid determination methodology for fatigue limit

2.4.1 Introduction

Compared to the conventional fatigue tests, the thermographic approach, which is based on the self-heating phenomenon in a material under loading, allows to determine fatigue limit of the material in a short time. As previously mentioned, the two graphic methods proposed by

Risitano et al. [111]-[115] and Luong et al. [116]-[119] allow to access the fatigue limit of metallic materials by monitoring the stabilized temperature rise ΔT_{stab} corresponding to different increasing loading levels σ through the stepwise loading procedure (**Figure 2-14**). Both authors assume that the increasing rate of stabilized temperature rise above the fatigue limit is greater than that below the fatigue limit and consists in performing the linear regression to fit the data pairs $(\sigma, \Delta T_{stab})$. Later on, in a number of studies, both graphic approaches have also been employed to determine the fatigue limit of various composite materials. It is worth noting that in the study of Gornet et al. [195][196], the author intended to use Risitano's method to access the fatigue limit of CFRP with three different stacking sequences ($\pm 45^\circ$, cross-ply and QI). However, the stabilized temperature rise does not show a linear increase with the applied loading level. Even though the authors interpolated the last few data points with a linear line, a relative important error of 20.12% was observed for $\pm 45^\circ$ compared to the traditional fatigue test results. From this, it can be concluded that both graphic methods were efficient for the fatigue limit determination, but showed some limitations.

First, although these graphic approaches which were originally designed for the metallic materials [197]-[202], have been successfully applied to some composite materials [191]-[196], most of them are unidirectional, $0^\circ/90^\circ$ cross-ply or $\pm 45^\circ$. They are barely applied to QI laminates usually used in composite structures. Second, these graphic methods are disputed: why should we use straight line instead of other kinds of lines to fit the experimental data [139]? Third, the application of these graphic methods is based on the assumption that the temperature increasing rate above the fatigue limit is greater than that below. But in the cases where the thermographic data does not satisfy this assumption or involves fluctuation, the usage of the methods will be restricted or cannot ensure the accuracy.

In this context, a new method for fatigue limit determination based on the thermographic data is proposed in this section. In order to make the reader clearer of the difference between

different fatigue limit determination methods, the two graphic methods and the thermographic data treatment method proposed by Huang et al [17] are firstly reviewed, followed by a detailed description of proposed method, where the fatigue limit is defined as the maximum stress corresponding to the peak value of the angle change normalized by their amplitude. Thirdly, the feasibility of the new method to determine the fatigue limit is verified by the fatigue experimental data of cross-ply and QI CFRP laminates and also by the data found in the literature. Finally, the predicted fatigue limit values are compared with the ones determined based on traditional experiments, graphic methods and Huang's method. Besides, a study has been realized to understand the influence of loading step length imposed during the test on the accuracy of the fatigue limit determined by the proposed method.

2.4.2 A review of fatigue limit determination methods

2.1.2.1 Luong's method (Two-curve method) [116]-[119]

Luong et al. [116]-[119] proposed an experimental approach to rapidly evaluate the fatigue limit based on the experimental measurement of a metallic material undergoing a fatigue test. This last is subjected to an increase of surface temperature, such that the higher the stress amplitude, the higher the temperature increase. More precisely, the temperature evolution during the fatigue test can be divided into three distinctive stages: at the beginning of the test, microcracks initiate in multiple locations in the matrix, the temperature increases quickly owing to the friction between cracked matrix. After a relatively small number of cycles, the growth of matrix cracking and delamination propagation tend to stabilize, the friction induced heat decreases and the temperature rise increases slowly, covering almost the whole life-span until an abrupt increase prior to failure (**Figure 2-13**). From this, it can be seen that it is not necessary to run the fatigue test until the failure of specimen to obtain the value of stabilized temperature rise. Therefore, the step-loading procedure presented in **Figure 2-14** is adopted. A succession of increasing cyclic loads at a given stress ratio is applied stepwise to the same specimen. For each loading level, the corresponding stabilized temperature rise ΔT_{stab} is recorded by the infrared camera and then plotted as a function of the applied stress amplitude

σ as presented schematically in **Figure 2-15**.

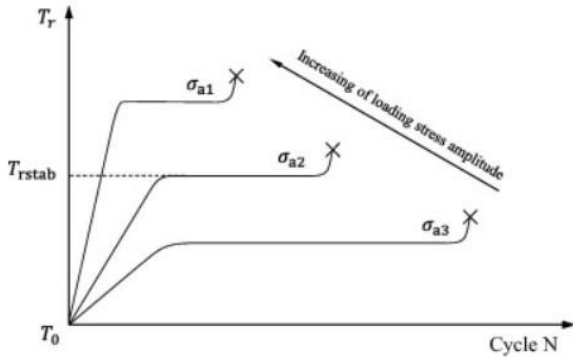


Figure 2-13. Variation of temperature over time during constant amplitude fatigue loading [17]

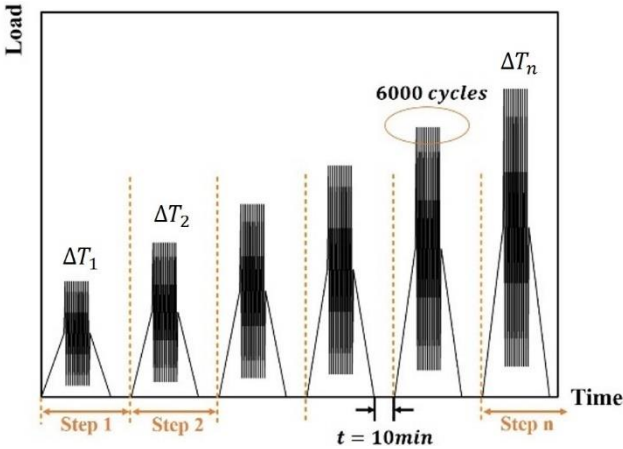


Figure 2-14. Step-loading procedure for R=0.1

According to Luong’s method, when the stress amplitude (or maximum stress) does not surpass the fatigue limit, it is expected that the plot of stabilized temperature rise vs stress amplitude (or maximum stress) shows a straight-line trend with flat slope. As soon as the stress amplitude (or maximum stress) exceeds the fatigue limit, the irreversible phenomenon becomes dominant. The stabilized temperature rise starts to increase significantly and can be described by another straight line with a steeper slope. Therefore, the method is also named as Two-Curve Method (TCM). **Figure 2-15** illustrates the determination process of Luong’s method. The abscissa of the intersection point of the two lines is considered as the fatigue limit.

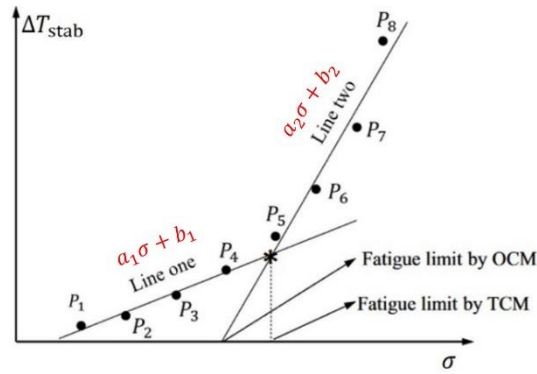


Figure 2-15. Fatigue limit determination by TCM and OCM

2.1.2.2 Risitano's method (One-curve method) [111]-[115]

Similar to Luong's method, Risitano's method also comprises of applying successive blocks of cyclic loading with increasing amplitude. However, the stress amplitudes below the fatigue limit are not taken into account since the temperature rises under these loading levels are extremely limited (practically nil). By plotting the stabilized temperature rise ΔT_{stab} or the initial thermal gradient $\Delta T/\Delta N$ against the applied stress, the fatigue limit is determined by the intersection between the regression line of ΔT_{stab} (second line in Luong's method) or $\Delta T/\Delta N$ and the x -axis ($\Delta T_{stab} = 0$), as shown in **Figure 2-15**. In other words, fatigue limit is the maximum stress level at which that there is no significant increase in temperature rise.

2.4.3 Thermographic data treatment method proposed by Huang et al. [17]

As has already been explained in the section 1.3.3, in the study of Huang et al. [17], three new data treatment methods have been proposed to overcome the difficulty of determining unique cut-off point that encountered with Luong's method. Among these three methods, the basic idea of first method is to use angle (θ_i) change instead of slope change to determine the point of drastic change in the stabilized temperature rise ΔT_{stab} .

Herein, angle θ_i is defined by one pair of points P_i and P_{i-1} as illustrated in **Figure 2-16**. The measured points are numbered as $P_1, P_2, P_3, \dots, P_n$, where n is the total number of points.

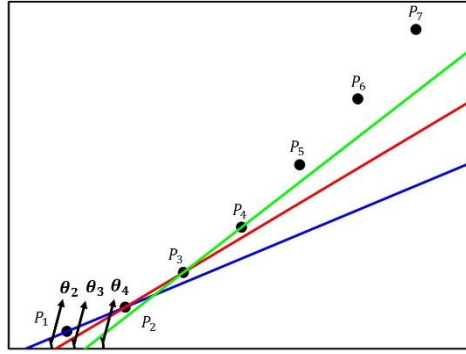


Figure 2-16 Definition of angle θ_i [17]

In this study, the normalized angle change is employed instead of angle change:

$$\theta_i^c = \left| \frac{\theta_{i+1} - \theta_i}{\max(\theta_{2,3,4..}) - \min(\theta_{2,3,4..})} \right| \quad (i = 2, 3, \dots, n - 1) \quad (2-1)$$

Where the subscript $i (i \geq 2)$ denotes the number of point in the sequence. θ_i and θ_{i+1} are the angle between the line determined by the point set $\{P_{i-1}, P_i\}$, $\{P_i, P_{i+1}\}$ and x-axis, respectively. The amplitude of angle change defined as: $\max(\theta_{2,3,4..}) - \min(\theta_{2,3,4..})$, is used for the normalization of angle change.

Figure 2-17 presents the normalized angle change θ_i^c versus sequence number of the point computed based on the data in **Figure 2-16**. If the thermographic data exhibit a good bilinear behavior, the peak value of normalized angle change could be easily found, as depicted in **Figure 2-17**. Huang et al. [17] proposed that the point corresponding to the peak value of normalized angle change could be first used to separate the data into two groups, and then Luong's method can be applied to determine the fatigue limit. This method works well for the cases where the temperature rise is a monotone function of maximum stress. However, if the function contains some fluctuations, the precision of the method can be significantly perturbed or the method may be failed to be applied.

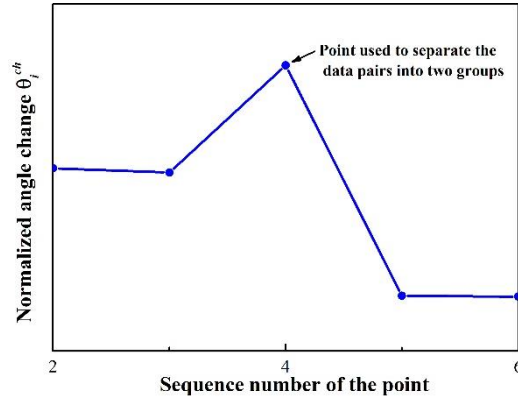


Figure 2-17 Loci of normalized angle change versus sequence number of point [17]

2.4.4 Proposed method

Compared to the isotropic metallic materials, the damage mechanisms in the composite materials are more complex due to their inherent heterogeneity and anisotropy, especially in the MD composite laminates. As what has already been stated in Ref. [195][196], the stabilized temperature rise does not increase monotonically with the increase of maximum stress, as shown in **Figure 2-18**. In fact, in the MD composite laminates, delamination between plies with different fiber orientations occurs early in fatigue testing from specimen edges where interlaminar stresses exist. As the stress level increases, the growth of the delamination could destroy the symmetry of the initial laminate and split it into different non-symmetrical sub-laminates. Under tensile fatigue loading, the coupling effects of these sub-laminates, such as tensile-bending and tensile-torsion, should increase the contact surface of the specimen with the ambient air so as to promote the release of heat to the environment. Therefore, it is possible that the stabilized temperature rise could be constant, or even decrease with the increase of the stress level as shown in **Figure 2-18**. Under this circumstance, even though the thermographic data could be interpolated by two straight lines, the slope of the second line will be flatter than the first line, which is contradictory with the assumption of Luong and Risitano's methods: the increasing rate of stabilized temperature rise above the fatigue limit should be superior than that below the fatigue limit. Consequently, both graphic methods could no more be used for the fatigue limit determination for the case shown in the figure.

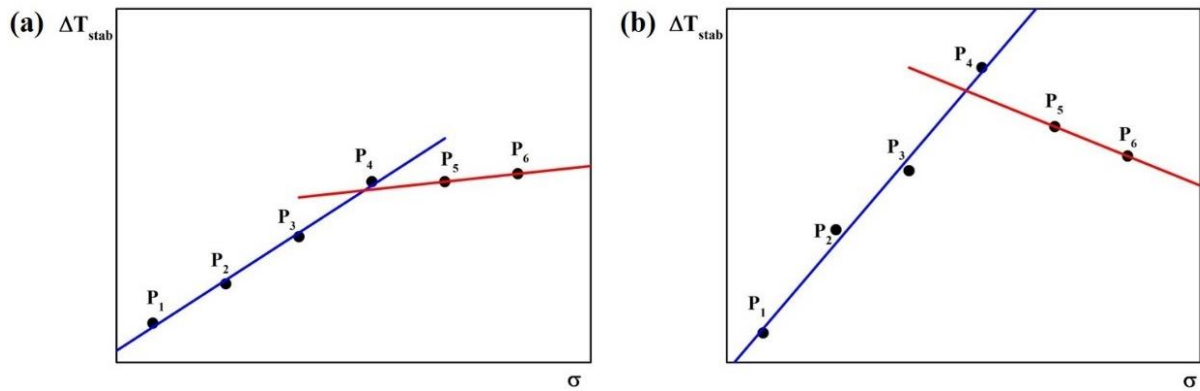


Figure 2-18. Schematic explanation of the special case: (a) stabilized temperature rise remains constant; (b) stabilized temperature rise decreases with the increase of stress level

Facing with this problem, a new fatigue limit determination was proposed here. The normalized angle change corresponding to each point ($i \geq 2$) is first calculated with Eq. (2-1) based on the data pairs $(\sigma, \Delta T_{stab})$. Thereafter, the point corresponding to the peak value of normalized angle change can be determined, which signifies a dramatic change in the intrinsic dissipation mechanisms [118]. The maximum stress corresponding to this point is identified as the fatigue limit. For the data shown in **Figure 2-18**, the loci of normalized angle change versus the sequence number of the point are illustrated in **Figure 2-19**. For both cases, the peak value of normalized angle change occurs at point P_4 . Hence, the maximum stress of point P_4 is determined as the fatigue limit.

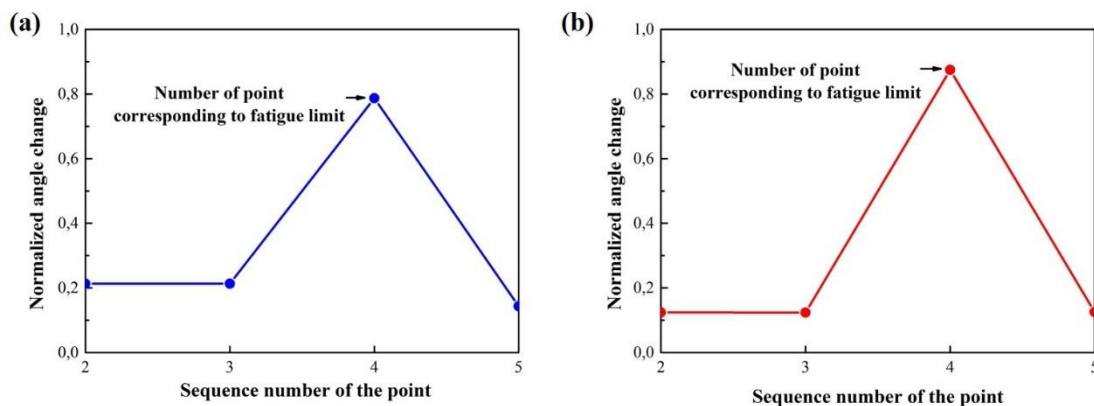


Figure 2-19. Loci of normalized angle change vs. sequence number of the point based on data in **Figure 2-18**

2.4.5 Influence of loading step length on measured fatigue limit by the proposed method

It should be noted that the fatigue limit determined by the proposed method is influenced by

the length of loading step. The smaller length of loading step, the more precise the fatigue limit determined. So, the length of loading step should be enough small so as to have enough points for the reliable determination of fatigue limit. In order to evaluate this influence, the thermographic data in Ref. [199] for a stainless steel and [203] for woven carbon fiber reinforced thermoplastic are analyzed here since the quantity of original data points is up to 23 and 41 points, respectively. To facilitate comparison, the loading step length is normalized with their UTS in both reference papers. The loading step length used is 10 MPa, equalizes to 0.74% and 2.21% UTS in Ref. [199] and [203], respectively. By the proposed method, the fatigue limit determined based on all points is 350 MPa and 274 MPa, respectively. **Figure 2-20** shows the fatigue limit values obtained by the proposed method as a function of loading step length. It can be seen that with the increase of loading step length, the fatigue limit values can be away from the values obtained at the smallest loading step length. The error relative to these last values is plotted as a function of the loading step length in **Figure 2-21**. It is observed that with the decrease of loading step length, the relative error gradually decreases. In order to limit relative error less than 5%, loading step length less than about 3% UTS should be needed for the stainless steel according to Ref. [199], whereas for woven carbon fiber reinforced thermoplastic (Ref. [203]), it is better to use the loading step length no more than 10% UTS.

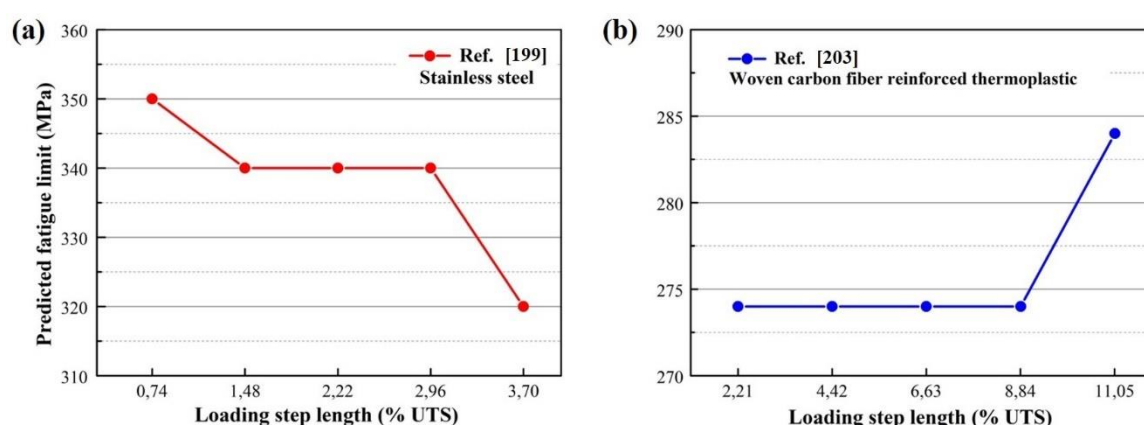


Figure 2-20. The influence of loading step length on the determined fatigue limit

(a) Results from Ref. [199]; (b) Results from Ref. [203]

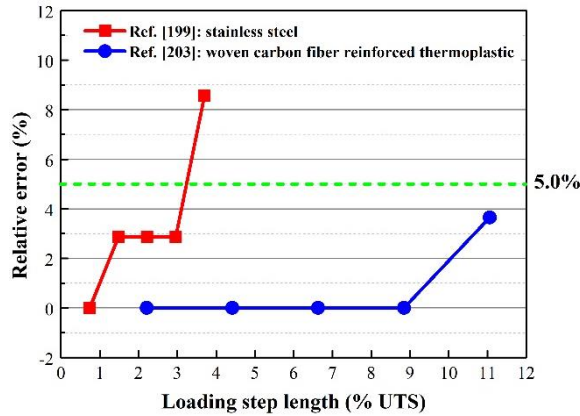


Figure 2-21. Relative error between determined results and the results obtained by the smallest loading step length in Ref. [199] and [203]

However, if this last criterion (loading step length=10% UTS) is applied to our experimental data of QI and cross-ply laminates and the data in Ref. [139] of UD and $\pm 45^\circ$ laminates, as shown in **Figure 2-22**, the fatigue limit is determined as 70% UTS for UD laminate, 70% UTS for $\pm 45^\circ$ laminate, 70% UTS for QI and 50% UTS for cross-ply laminates, respectively. If 5% UTS is chosen as the loading step length, the fatigue limit determined for three premier laminates is unchanged, but 55% UTS for cross-ply laminate is obtained. Recall that the fatigue limit determined by traditional fatigue tests is about 75.8% UTS for UD laminates, 65.6% UTS for $\pm 45^\circ$ laminates, 75% UTS (10^6 cycles) or 66% UTS (extrapolation to 10^7 cycles) for the QI laminates and 69% UTS (10^6 cycles) or 65% UTS (extrapolation to 10^7 cycles) for the cross-ply laminates, and that the total testing duration for one specimen when the loading step length is 5% UTS is only 4-5 hours longer than that when the loading step length is 10% UTS. Therefore, the measurement using loading step length of 5% UTS is more acceptable. Consequently, to ensure the accuracy of the results, the loading step length no more than 5% UTS is recommended for composite materials when using the proposed method.

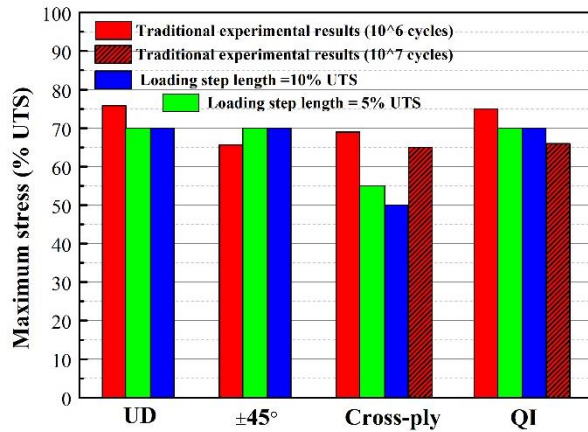


Figure 2-22. Influence of loading step length on the fatigue limit for CFRP of different stacking sequences

2.4.6 Application of proposed method to the experimental data of present work

The variation of average surface temperature rise as a function of loading cycles is shown in **Figure 2-23** and **Figure 2-24** for QI and cross-ply laminates, respectively. The maximum stress is indicated at the end of each profile. As can be seen from both figures, the temperature profiles reached a steady-state plateau after a certain number of loading cycles for the maximum stress from 30% to 87.5% and 30% to 67.5% UTS for QI and cross-ply laminates, respectively. The stabilized temperature rise plotted against the corresponding maximum stress is depicted in **Figure 2-25** and **Figure 2-26**.

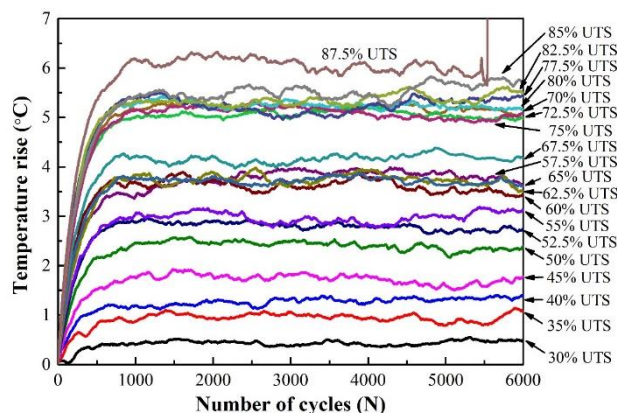


Figure 2-23 Surface temperature rise versus number of loading cycles of specimen 1 of QI laminates

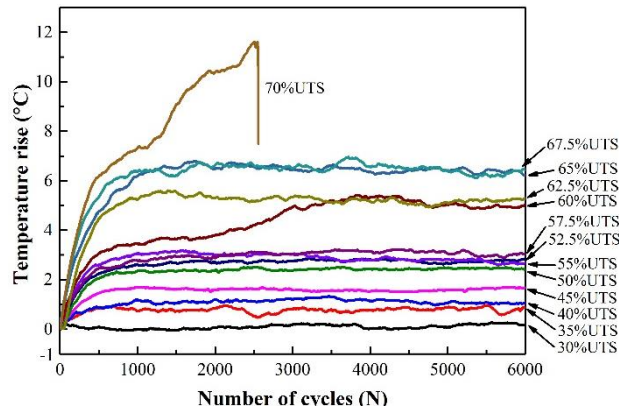


Figure 2-24 Surface temperature rise versus number of loading cycles of specimen 1 of cross-ply laminates. The two graphic methods (TCM and OCM) were first applied to determine the fatigue limit. For the QI laminates, even though the data pairs ($\Delta T_{stab}, \sigma$) could be interpolated by two straight lines, as shown in **Figure 2-25**, both methods fail to access the fatigue limit as the slope of the straight line above the fatigue limit is flatter than that below the fatigue limit. This is contradictory with the hypothesis of the methods: the difference in stabilized temperature rise between two consecutive loading steps above the fatigue limit is expected to be greater than that below the fatigue limit. Whereas for the cross-ply laminates, both TCM and OCM have been successfully applied to determine the fatigue limit as 44.55% and 36.33% UTS, respectively. However, these two values are both far from that evaluated by the traditional fatigue tests (68.94% UTS at 10^6 cycles).

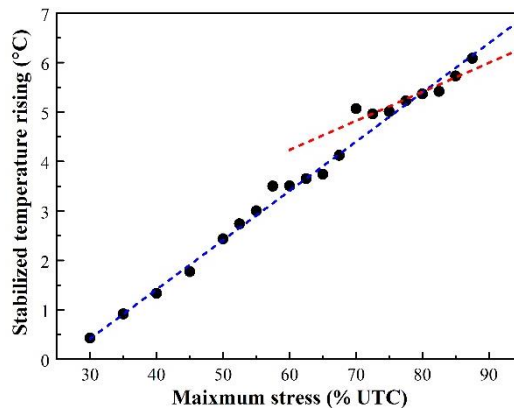


Figure 2-25. Stabilized temperature rise vs maximum stress of QI specimen 1

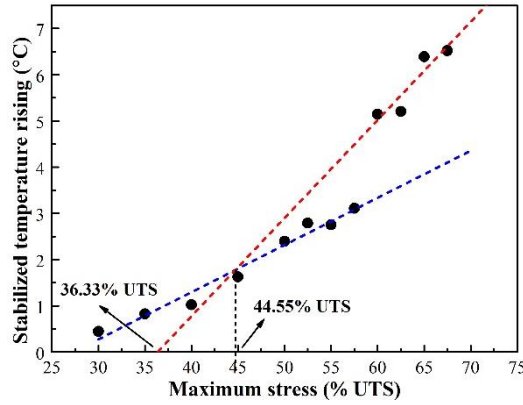


Figure 2-26. Stabilized temperature rise vs maximum stress of cross-ply specimen 1

Since both graphic methods fail to evaluate the fatigue limit accurately, the proposed method is employed. **Figure 2-27** plots the loci of θ_i^c versus the number of points computed based on the data in **Figure 2-25** and **Figure 2-26**. The number of the point corresponding to the peak value of θ_i^c is 13 and 9 for the QI and cross-ply laminates, which corresponds to maximum stress of 70% and 60% UTS in **Figure 2-25** and **Figure 2-26**, respectively. Therefore, fatigue limit is determined as 70% and 60% UTS for the QI and cross-ply laminates, respectively.

In fact, the fatigue life (number of cycles) corresponding to the fatigue limit determined by the graphic methods based on thermographic data is not defined in the Luong [118] and Risitano's [112] methods. In the engineering design processes, 10^6 to 10^7 cycles are usually considered as conventional fatigue lives for most materials. Therefore, as can be seen in the studies of **Table 2-4**, the fatigue limit determined by the graphic methods is always compared with that determined by conventional fatigue tests in which the fatigue life was set between 10^6 and 10^7 cycles. Similarly, in our work, the fatigue limit, no matter it is determined by the graphic methods or by the proposed method, is compared with that determined by traditional fatigue tests in which the fatigue life is between 10^6 and 10^7 cycles. The comparison between the values determined by traditional experiments and those by the proposed method is listed in the last two rows of **Table 2-4**. A good agreement is found between the predicted values and experimental results for both laminates configurations. The relative error between the fatigue limit corresponding to a fatigue life of 10^6 cycles determined by the traditional

experiments and that by the proposed model is -6.37% and -12.97% for the QI and cross-ply laminates, respectively. For the fatigue limit corresponding to a fatigue life of 10^7 cycles, these two values turn out to be 6.67% and -7.61% for the QI and cross-ply laminates, respectively.

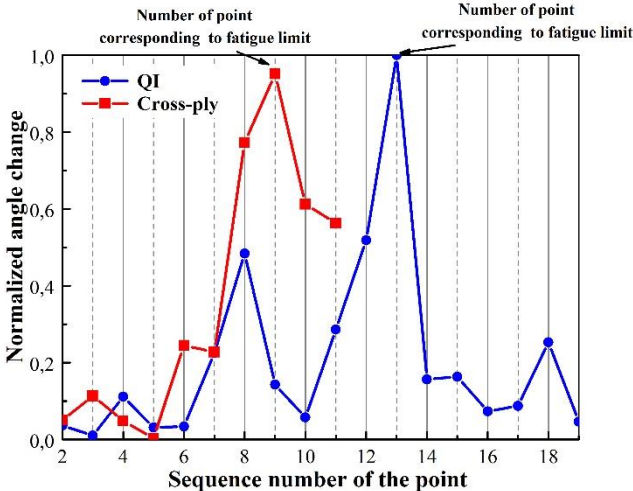


Figure 2-27. Loci of θ_i^c versus number of points in the sequence of specimens 1 of QI and cross-ply laminates

2.4.7 Application of proposed method to the data published in the literature

After the validation of proposed method by the experimental data of QI and cross-ply laminates, it has been further applied to the data published in the literature. Table 2-4 gives the fatigue limits determined by Huang’s method and proposed method for various composite and metallic materials reported in the articles. The results evaluated by the traditional fatigue experiments (staircase method or S-N curve) in which the fatigue life is between 10^6 and 10^7 cycles and graphic methods are also listed in the same table for comparison. It is noted that the results obtained by the proposed model agree well with those from the literature by traditional experimental measurement. The relative error ranges from 0.13% to 13.04%. While the relative error of Huang’s method and graphic methods are in the range of 0-65.69% and 0-35.38%, respectively.

Comparing with the graphic methods and Huang’s method, it is obvious that the scope of

application of the proposed method is the widest. The proposed method can be applied to all the experimental data in **Table 2-4**, whereas Huang’s method fails to be applied to the thermographic data in [206][207]. In the case where the plot of temperature rise as a function of stress amplitude (or maximum stress) contains some fluctuations, as in [204][205][211], or even shows a typical trilinear behavior, as shown in **Figure 2-28** of [211], although both Huang’s method and graphic methods can generate the fatigue limit value, the precision is significantly perturbed. Maximum relative errors of 35.28% and 65.39% between the fatigue limits evaluated by traditional experiments and those determined by Huang’s method and graphic methods can even be reached. From these, it can be concluded that the proposed model can not only be applied to more cases, but also give more reliable predicted results. The accuracy of predicted fatigue limit is reassured even without conducting the costly and time-consuming traditional fatigue test.

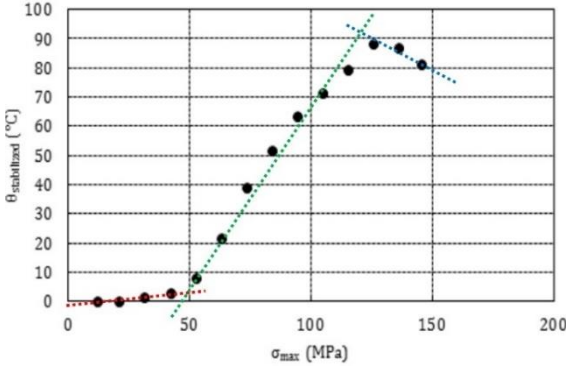


Figure 2-28. Experimental data of stabilized temperature rise vs maximum stress in [211]

Table 2-4. Summarized results of fatigue limit determined by manual graphic method, conventional experimental method and proposed method

No	Geometry	Material	Unit	TE	GM	Huang	P	$\frac{GM - TE}{TE}$	$\frac{Huang - TE}{TE}$	$\frac{Huang - GM}{GM}$	$\frac{P - TE}{TE}$	$\frac{P - GM}{GM}$
[197]	Dog-bone	C55E steel (5Hz)	MPa	Null	420	368.38	420	Null	Null	-12.05%	Null	0
[197]	Dog-bone	C55E steel (10Hz)	MPa	Null	400	394.27	410	Null	Null	-1.43%	Null	2.5%
[198]	Flat	Steel M800	MPa	333(2e6 cycles)	330	359.82	360	-0.90%	8.06%	9.04%	8.11%	9.09%
[199]	Flat	FV520B stainless steel	MPa	Null	357.48	357.39	350	Null	Null	-0.02%	Null	-2.09%
[206]	Flat	X5CrNi18-10 steel	MPa	278.2(e ⁷ cycles)	292.4	Failed	276.7	5.1%	Null	Null	-0.54%	-5.37%
[207]	Dog-bone	316L stainless steel	MPa	222	219	Failed	220	-1.35%	Null	Null	-0.90%	0.46%
[208]	Dog-bone	Spheroidal cast iron	MPa	265(e6 cycles)	285	285	275	7.55%	7.55%	0	3.77%	-3.51%
[209]	Dog-bone	JIS G3141 SPCC steel	MPa	130(e7 cycles)	155	155	140	19.23%	19.23%	0	7.69%	-9.68%
[210]	Dog-bone	Aluminum	UTS%	75.1(e6 cycles)	74.8	74.8	75	-0.40%	-0.40%	0	-0.13%	0.27%
[210]	Cross-ply dog-bone	Glass fiber ceramic matrix composite	UTS%	Null	70	70	70	Null	Null	0	Null	0
[196]	[+45/-45/+45/-45] ₅	CFRP	MPa	69(3e6 cycles)	82.9	80.14	78	20.15%	16.14%	-3.30%	13.04%	-5.91%
[212]	Flat	CFRP woven	UTS%	63(e7 cycles)	64	67	55	1.59%	7.69%	5.17%	-12.7%	14.06%
[194]	0° Flat	CFRP	UTS%	53(6e6 cycles)	51	51	50	-3.77%	-3.77%	0	-5.66%	-1.96%
[211]	0° Flat	CFRP (test 1)	MPa	400(2e6 cycles)	390	346.75	360	-2.50%	-13.31%	-11.09%	-10%	-7.69%
[211]	0° Flat	CFRP (test 2)	MPa	400(2e6 cycles)	390	311.57	360	-2.50%	-22.11%	-20.11%	-10%	-7.69%
[211]	[45] ₈	CFRP	MPa	130(2e6 cycles)	44.6	44.6	125	-3.85%	-65.69%	0	-3.85%	0
[192]	±45° Flat	GFRP	MPa	Null	36	37.57	36	Null	Null	4.36%	Null	0
[18]	0°	CFRP	UTS%	75.8(e6 cycles)	73.8	73.8	70	-2.64%	-2.64%	0	-7.65%	-5.15%
[19]	±45°	CFRP	UTS%	65.6(e6 cycles)	63.7	69.31	70	-2.90%	5.66%	8.81%	6.71%	9.89%
[203]	(0/90) ₄₅ flat	CFRP	MPa	273(2e6 cycles)	273	273	274	0	0	0	0.37%	0.37%
[191]	[0/90/45/-45] _{2s}	Basalt reinforced fibre Epoxy	MPa	65.9(5e6 cycles)	68.5	69	70	3.95%	4.70%	0.73%	6.22%	2.19%
[195]	[45/-45/90/0] ₅	CFRP	MPa	354(3e6 cycles)	352.1	351.4	338	-0.54%	-0.73%	-0.20%	-4.52%	-4.00%
	[(0/90) ₅ /0/(90/0) ₅]	CFRP	UTS%	69-65(e6-e7 cycles)	44.55	44.55	60	-35.38%	-35.38%	0	12.97%	34.68%
	[0/45/90/-45] ₅	CFRP	UTS%	75-66(e6-e7 cycles)	Failed	Failed	70	Null	Null	Null	-6.37%	Null

UTS: Ultimate Tensile Strength. Null: Non available value. Failed: the method failed to generate an acceptable value. TE: Traditional experiments. GM: Graphic Method (Luong or Risitano' method). Huang: angle change method proposed by Huang et al. P: Proposed method.

2.5 Summary

In this chapter, a new method has been developed for the rapid determination of fatigue limit based on thermographic data obtained by means of an infrared camera. The angle change normalized by their amplitude is adopted to describe the temperature increasing rate as a function of the applied maximum stress. The fatigue limit is defined as the maximum stress which corresponds to the peak value of normalized angle change. A comparison with the results from traditional fatigue tests on cross-ply and QI CFRP laminates and from those reported in the literature shows that the proposed method can rapidly determine the fatigue limit corresponding to a fatigue life between 10^6 and 10^7 cycles for both metallic and composite laminates, even in the case where the Risitano and Luong's graphic methods fail to be applied. The relative difference between the fatigue limit determined by the proposed method and that determined by traditional fatigue tests for different materials studied is less than 13.04%. However, it is revealed that to ensure the accuracy of the result obtained by the proposed method, loading step length no more than 5% UTS is recommended for composite materials.

Chapter 3 Determination of S-N curve of MultiDirectional (MD) composite materials

In this chapter, a modified fatigue life prediction model in term of S-N curve is proposed to take into account of the more complex damage mechanisms in the MD CFRP laminates. Besides, a protocol to determine a more reliable S-N curve by taking into account of the scatter of several obtained S-N curves is also discussed.

3.1.1 Introduction

In the section 2.2, a new method has been proposed for the rapid determination of fatigue limit. But besides fatigue limit, stress-life (S-N) curve is also an important fatigue property for engineering applications. As mentioned in Chapter 1, a number of methods which are based on thermographic data analysis have been developed to determine the S-N curve rapidly [146]-[148][150]. Notable is that these methods were mainly applied to unidirectional [18], $\pm 45^\circ$ [19] and braided composite materials [18] in the literature. However, to the author's knowledge, there are few studies which utilize IRT to determine the fatigue properties of MD composite laminates, probably due to the notably more complicated damage mechanisms in these materials. Apart from that, because of the same reason, these thermographic methods, which has been originally designed for metallic materials may not be applicable anymore for the MD composite laminates without modification or adaptation.

The damage mechanisms of composite materials under fatigue loading are very complex. However, three distinctive stages of damage evolution can be generally distinguished: interlaminar matrix cracking and fiber-matrix debonding at the beginning of fatigue life, followed by growth and coalescence of matrix cracks leading to delamination, and fiber fractures in the final stage [214][215]. The accumulation of damage is accompanied with the degradation of stiffness [216][217]. Therefore, measurement of residual stiffness could be

used as an indication of the extent of accumulated damage during fatigue loading and further will give predictions of fatigue life [213]-[221].

In a previous work, a fatigue life model based on stiffness degradation was proposed by Huang et al. by combining the IRT data with damage accumulation process [18]. The proposed method allows to determine S-N curve just in about ten hours of machine time. The model has been successfully applied to predict the fatigue S-N curves of triaxially braided, UD [18] and $\pm 45^\circ$ [19] CFRP laminates.

In this work, firstly Huang’s model has been applied to QI CFRP laminates. Nevertheless, it produces rather conservative fatigue life predictions because in a MD laminate, damage initiation and accumulation processes are more complex. Hence, the prediction model is modified in the present study. Herein, a new parameter r is introduced into the original Huang’s model to consider the influence of more complex damage mechanisms in MD CFRP laminates. The determination of the parameters of new model has been discussed. Lastly, the experimental data of QI CFRP laminates, as well as cross-ply CFRP laminates, are used to validate the proposed model.

3.1.2 Huang’ model [18]

The evolution of accumulative damage as a function of the number of loading cycles may be generally described by the curve in **Figure 3-1**. The accumulation of damage results in the degradation of stiffness, which can both be divided into three typical stages.

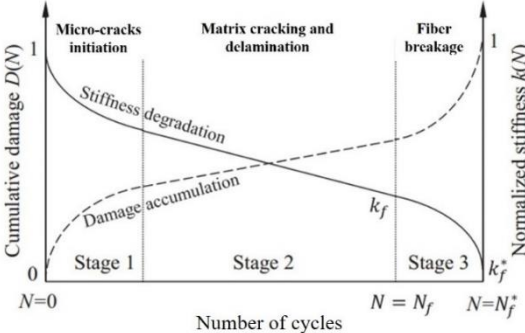


Figure 3-1 A typical trend for stiffness degradation and damage accumulation during fatigue loading [139]

In the work of Huang et al [18], the change in residual stiffness has been used to express the extent of accumulated damages in the material. The damage index D is defined as [222]:

$$D^*(N) = \frac{K_0 - K(N)}{K_0 - K_f^*} = \frac{1 - k(N)}{1 - k_f^*} \quad (3-1)$$

Where N is the number of loading cycles, K_0 , $K(N)$ and K_f^* are residual stiffness corresponding to the initial cycle, the N^{th} cycle and final cycle prior to failure N_f^* , respectively. $k(N)$ and k_f^* , defined as $K(N)/K_0$ and K_f^*/K_0 , are normalized residual stiffness at N^{th} and final cycle N_f^* , respectively.

In Eq. (3-1), the failure stiffness K_f^* (k_f^*), can not be determined until specimen failure occurs. Since the third stage only takes a rather small portion of fatigue life, during which damage propagation is relatively unstable and difficult to capture [223][224], only the first two stages will be taken into consideration. On account of this, N_f^* and k_f^* may be replaced by the number of cycles N_f and the normalized residual stiffness at the end of second stage k_f , respectively. Moreover, based on the fact that the critical value of normalized failure stiffness k_f^* is independent of maximum applied stress [225], thus k_f is also considered to be independent of the maximum applied stress. After simplification, we have:

$$D(N) = \frac{1 - k(N)}{1 - k_f} \quad (3-2)$$

Huang et al. [18] proposed that the normalized stiffness $k(N)$ is associated with the stabilized temperature rise ΔT_{stab} by the following relationship:

$$k(N) = 1 - p' \Delta T_{stab} N^{1/q} \text{ with } (q \geq 1) \quad (3-3)$$

Where p' and q are two constants, independent of temperature and loading cycles. ΔT_{stab} is the stabilized temperature rise.

Substituting Eq. (3-3) into Eq. (3-2) and then simplifying, Eq. (3-2) becomes:

$$D(N) = \frac{p' \Delta T_{stab} N^{1/q}}{1 - k_f} \text{ with } (q \geq 1) \quad (3-4)$$

The values of parameter p' , q and k_f can be determined empirically from the measurement

during the fatigue tests. Besides, the stabilized temperature rise ΔT_{stab} is related to maximum applied stress σ by:

$$\Delta T_{stab}(\sigma) = \begin{cases} a_1\sigma + b_1(0 < \sigma \leq \sigma_{fl}) \\ a_2\sigma + b_2(\sigma \geq \sigma_{fl}) \end{cases} \quad (3-5)$$

Where a_1 , a_2 , b_1 and b_2 are four constants determined by TCM shown in **Figure 2-15**. σ_{fl} denotes the maximum applied stress which corresponds to fatigue limit.

Considering the boundary condition that as the number of cycles approaches the fatigue life N_f , D approaches 1. Under this condition, Eq. (3-4) becomes:

$$1 = \frac{p' \Delta T_{stab} N_f^{1/q}}{1 - k_f} \quad (q \geq 1) \quad (3-6)$$

This formula can be expressed in another form and then the following fatigue life prediction model can be found:

$$N_f = \left(\frac{1 - k_f}{p' \Delta T_{stab}(\sigma)} \right)^q \quad (3-7)$$

3.1.3 Application of the model proposed by Huang et al. [18] to QI laminates

In this section, Huang's model is applied to the experimental data of QI CFRP laminates to validate model's generalization. The procedure and calibration details for fatigue limit determination and fatigue life prediction are listed below:

Step 1: determine fatigue limit and corresponding stabilized temperature rise based on thermographic data

Figure 3-2 is a plot of average surface temperature rising, collected by IRT, as a function of the number of cycles of specimen 2. The maximum applied stress is indicated at the end of each profile. It is observed that for all the stress levels indicated in the plot, the temperature profile reached a stabilized plateau after a certain loading cycles. The stabilized temperature rise for each profile was then plotted as a function of the maximum applied stress, as shown in **Figure 3-3** (a). The method proposed in section 2.2 was adopted here to determine the fatigue limit. The number of points corresponding to the peak value of normalized angle change θ_i^c is

8 (see **Figure 3-3** (b)), which corresponds to a maximum stress of 65% UTS (see **Figure 3-3** (a)). Hence, the fatigue limit is determined as 65% UTS. The stabilized temperature rise corresponding to the fatigue limit (ΔT_{stab_fl}) is 4.21°C.

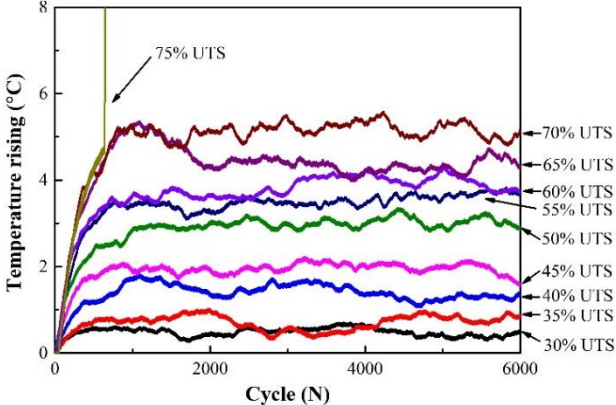


Figure 3-2. Variation of temperature rise with the number of loading cycles of QI specimen 2

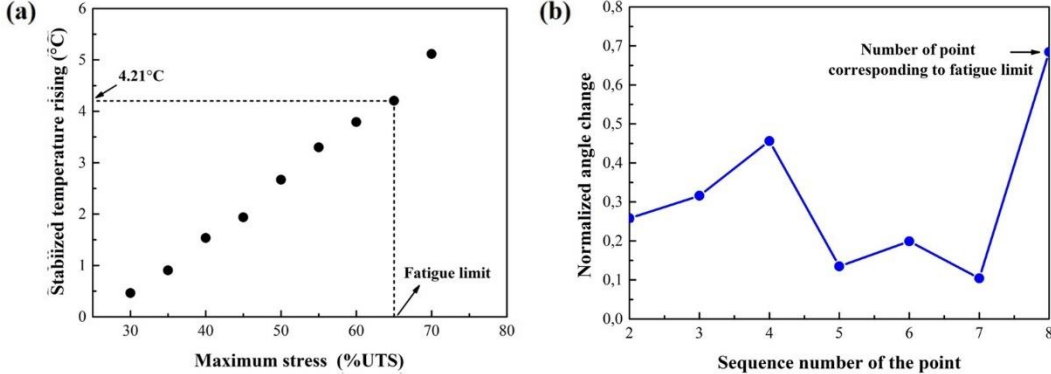


Figure 3-3. Fatigue limit determination of QI laminate (specimen 2): (a) stabilized temperature rise vs maximum stress; (b) loci of normalized angle change vs sequence number of the point

Step 2: calibrate the value of p' and q

Figure 3-4 is a plot of the normalized stiffness degradation as a function of the number of loading cycles and stabilized temperature rise for the specimens cycled at 50%, 55%, 60%, 65% and 70% of UTS. For each profile, 20 points were sampled, therefore, a total of 100 points were available for fitting. Herein, Eq. (3-3) is employed to fit the experimental data using 3D surface fitting in MATLAB[®]. The best fit value of p' and q are determined as $2.344e-2$ ($^{\circ}C \times Cycle^{1/q}$)⁻¹ and 11.80, respectively. The coefficient of determination R^2 , defined by Eq. (3-8) [180], is introduced to evaluate the accuracy of fitting. It can be seen from the

equation, the value of R^2 varies between 0 and 1. If the value of R^2 is close to 1, the result of fitting is great. Otherwise the result is not appropriate.

$$R^2 = 1 - \frac{\sum(y - D)^2}{\sum y^2} \quad (3-8)$$

Where y is the experimental data and D is the fitting data. The coefficient of determination R^2 using Eq. (3-3) is 0.884 for the data shown in **Figure 3-4**.

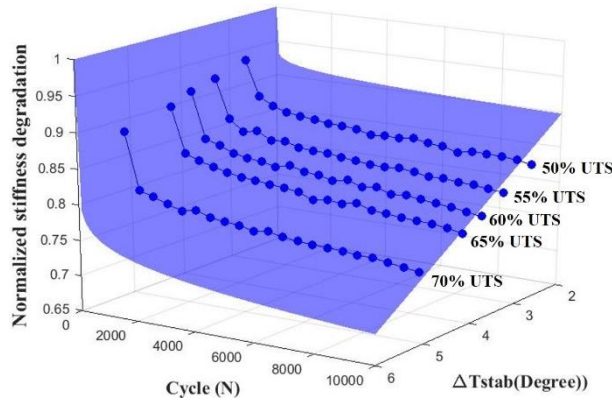


Figure 3-4. Surface fitting of Eq. (3-3) by MATLAB[®]

Step 3: calculate the failure threshold stiffness k_f

The number of cycles corresponding to the fatigue limit is often taken between 10^6 cycles and 10^7 cycles. Hereby, both $k(N_{fl} = 10^6 \text{ cycles})$ and $k(N_{fl} = 10^7 \text{ cycles})$ are considered for the calculation of failure threshold stiffness. According to Eq. (3-3), $k_f = 0.682$ when the fatigue life $N_{fl} = 10^6 \text{ cycles}$ while this value is 0.614 when $N_{fl} = 10^7 \text{ cycles}$.

Step 4: prediction of S-N curve

Having the values of p' , q and k_f , the whole S-N curve can be determined and a plot of the determined curve is shown in **Figure 3-5**. Traditional fatigue test results with 95% confidence interval are also included in the plot for comparison. As can be seen from the figure, the S-N curves corresponding to $N_{fl} = 10^6 \text{ cycles}$ and $N_{fl} = 10^7 \text{ cycles}$ are both below the 95% confidence interval. The determined fatigue life is much lower than the traditional fatigue test results overall. When the loading amplitude is 75% UTS, the fatigue life corresponding to $N_{fl} = 10^6 \text{ cycles}$ and $N_{fl} = 10^7 \text{ cycles}$ using Huang's model are 14421

and 144211 cycles, which is around 30.7 times and 2.2 times less than the values determined by the lower boundary line of 95% confidence interval. In conclusion, the fatigue life of the tested QI CFRP laminates determined by Huang’s model is too conservative to be accepted.

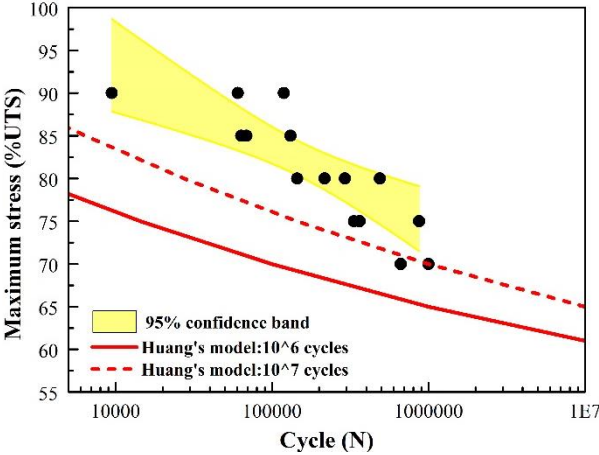


Figure 3-5. Comparison of S-N curves determined by Huang's model with traditional experimental results

3.1.4 Proposition of the modification of Huang’s model for characterization of S-N curve

Recall that Huang’s model has been applied successfully to UD [18] and $\pm 45^\circ$ [19] laminates made from the same prepreg as that used in this study, but it underestimates the fatigue life of a QI laminate. In fact, according to the study of Huang et al. [18], in Eq. (3-3), the parameter p' allows to regulate the scale of temperature rise, while the role of q is to control the shape of the function.

According to the work of Gamstedt et al [226] and Razvan et al [227], the main damage mechanisms in UD laminates under tensile fatigue loading are basically matrix cracking, fiber/matrix debonding and fiber breakage/splitting, while for the angle-ply laminates ($\pm 45^\circ$), the predominant damage mechanisms are matrix cracking, fiber/matrix debonding and delamination [52]. However, for a MD laminate under tensile loading, each ply with different fiber orientation can be subjected to different stresses, leading to more complex damage modes compared to that of UD and $\pm 45^\circ$ laminates. Investigations of fatigue damage mechanisms in cross-ply laminates by Broutman et al [228] have shown that the first event of failure is the debonding of transverse fibers. The debonding crack grows towards the ply

interfaces caused stress concentrations at the interfacial layers. Delamination then follows, reducing the laminate to a UD lamina. For the QI laminates, the sequence of damage mechanisms is found to be the failure of 90° plies, followed by delamination of 45° plies, leading to overstressing of the 0° plies and consequent failure. For both stacking sequences, the fatigue damage mechanisms including transverse cracking or splitting, delamination, fiber peeling (only for cross-ply laminates) and those of UD laminates [229][230].

The differences in damage mechanisms are reflected in the relationship between the normalized stiffness and the stabilized temperature rise. In Huang's model, when the values of p' , q and N are determined, the Eq. (2-4) becomes $k(N) = 1 - p' \Delta T_{stab}(\sigma) N^{1/q} = s \times \Delta T_{stab}(\sigma)$ with ($q \geq 1$) (s is a constant). As can be seen from the equation, there is a quasi-linear decrease of stiffness with the increase of stabilized temperature rise, which is well fitted for UD and $\pm 45^\circ$ laminates, while for the MD laminates, it is no more suitable. The experimental stiffness degradation data plotted as a function of stabilized temperature rise of specimens with different stacking sequence when the number of loading cycles equals to 4000 and 8000 cycles are illustrated in **Figure 3-6** and **Figure 3-7**. The values of these two numbers of loading cycles are chosen arbitrarily. For the UD (or for $\pm 45^\circ$) laminates, according to the study of Huang et al [18][19], the best-fit values of p' and q are $10.87 \times 10^{-2} (^\circ C \times cycle^{1/q})^{-1}$ ($1.68 \times 10^{-3} (^\circ C \times cycle^{1/q})^{-1}$) and 4.75 (5.56), respectively. When the values of N are taken as 4000 and 8000, the corresponding values of s become 0.623 (7.47×10^{-3}) $^\circ C^{-1}$ and 0.721 (8.46×10^{-3}) $^\circ C^{-1}$ and the exact expression for $k(N)$ will change to $k(4000) = 1 - 0.623 \times \Delta T_{stab}(\sigma)$ and $k(8000) = 1 - 0.721 \times \Delta T_{stab}(\sigma)$, respectively. Subsequently, these two linear equations are adopted to fit the experimental data, as shown in **Figure 3-6**. The coefficients of determination R^2 are determined as 0.922 (0.950) and 0.965 (0.9745) when $N=4000$ cycles and 8000 cycles, respectively, which indicates that the fitting curve agrees well with the experimental data. While for the QI laminates, the values of p' and q determined by Huang's model are $2.344e-2 (^\circ C \times Cycle^{1/q})^{-1}$ and 11.80, respectively. When the number of cycles is equal to 4000 and 8000 cycles, the corresponding

values of s turn out to be $4.73 \times 10^{-2} \text{ }^\circ\text{C}^{-1}$ and $5.02 \times 10^{-2} \text{ }^\circ\text{C}^{-1}$, respectively. The fitting results using these two linear equations for the experimental data are depicted in **Figure 3-7**. The corresponding R^2 are 0.806 and 0.827, respectively. Based on these R^2 values, it is clear that linear fitting is less accurate for QI laminates.

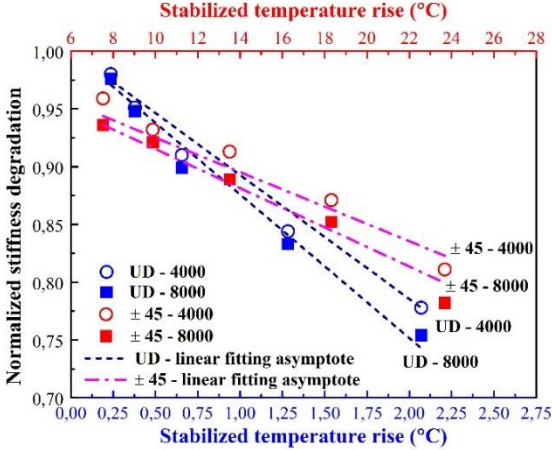


Figure 3-6. Normalized stiffness degradation vs stabilized temperature rise for UD and $\pm 45^\circ$ laminates (data from [18] and [19])

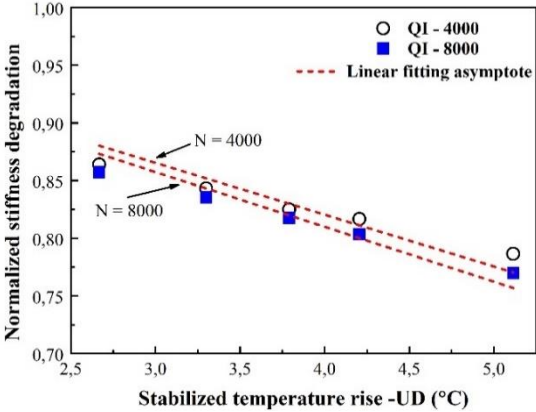


Figure 3-7. Normalized stiffness degradation vs stabilized temperature rise for QI laminates

In order to take the complex damage mechanisms in MD laminates into account, the expression of normalized stiffness $k(N)$ in Eq. (3-3) is modified by introducing another parameter r as follow:

$$k(N) = 1 - p' \Delta T_{stab}^r N^{1/q} \tag{3-9}$$

In addition, as can be seen from **Figure 3-6** and **Figure 3-7**, the scale of stabilized temperature rise of different stacking sequences varies deeply from each other. For example,

the stabilized temperature rise of UD laminates varies between 0.25 and 2.1°C, while that of $\pm 45^\circ$ laminates ranges from 7 to 24°C. For the ease of comparison between different specimens, a normalization process is proposed for the ΔT_{stab} :

$$\Delta T_{stab}^* = \Delta T_{stab} / (\Delta T_{stab})_{max} \quad (3-10)$$

Where ΔT_{stab}^* is the normalized stabilized temperature rise, $(\Delta T_{stab})_{max}$ is the maximum value of stabilized temperature rise of each specimen.

Substituting Eq. (3-10) into Eq. (3-9):

$$k(N) = 1 - p(\Delta T_{stab}^*)^r N^{1/q} \quad (3-11)$$

Where $p = p' \times (\Delta T_{stab})_{max}^r$.

The expression for the fatigue life model is then modified accordingly:

$$N_f = \left(\frac{1 - k_f}{p(\Delta T_{stab}^*(\sigma))^r} \right)^q \quad (3-12)$$

Now, there are three parameters p , q and r to determine empirically. The value of these three parameters can be calibrated by fitting experimental data with the help of MATLAB[®]. However, it should be noted that if the parameter r is close to 1, this model returns to Huang's model (Eq. (3-3)). Therefore, the modified model in Eq. (3-11) is more general, it includes the model in Eq. (3-3).

3.2 Validation of the proposed model

In this section, the experimental data of QI CFRP laminates is first employed to validate the proposed model. Thereafter, the proposed model is applied to the cross-ply laminates to further demonstrate the universality of model in the fatigue life determination of MD laminates.

3.2.1 QI laminates

In the first step, as previously mentioned, the fatigue limit and corresponding stabilized temperature rise are determined as 65% UTS and 4.21°C, respectively. In the second step, Eq. (3-11) is employed to fit the experimental data using MATLAB[®] software. The values of p , q

and r were determined as $3.736e-2$, 11.776 and 0.660 , respectively. The corresponding coefficient of determination R^2 is 0.980 . In the third step, according to Eq. (3-11), the failure threshold stiffness k_f was computed as 0.689 and 0.621 when $N_{fl} = 10^6$ cycles and 10^7 cycles, respectively. Finally, fatigue life calculated using proposed model is illustrated in **Figure 3-8**. In the meantime, traditional test results with 95% confidence interval and that determined by Huang’s model are also plotted in the same figure for comparison.

From **Figure 3-8**, it is found that, compared to the S-N curves determined by Huang’s model, those determined by the modified model are obviously closer to the 95% confidence interval. The S-N curve corresponding to fatigue life of $N_{fl} = 10^6$ cycles based on proposed model is still lower than the traditional fatigue test results overall. The error, defined as (Huang’s model-lower boundary of 95% confidence interval)/Huang’s model, between the S-N curve that corresponds to a fatigue life of $N_{fl} = 10^6$ cycles and the lower boundary of 95% confidence interval for a determinate maximum stress varies between 49.28% and 87.51%. This error is much less than that determined by Huang’s model, especially for higher loading maximum stresses. On the contrary, the determined S-N curve corresponding to $N_{fl} = 10^7$ cycles matches well with the traditional fatigue test results. The determined fatigue lives fall totally within the confidence interval. This suggests that in comparison to Huang’s model, the modified model is more accurate and reliable in predicting the fatigue life of QI CFRP laminates.

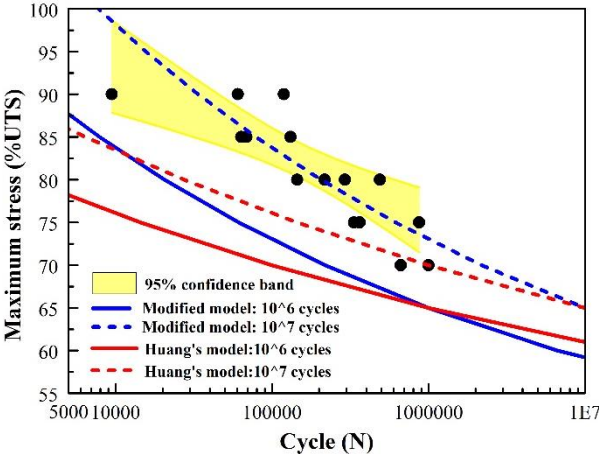


Figure 3-8 Comparison of S-N curve determined by proposed model with traditional fatigue test results

3.2.2 Cross-ply laminates

Step 1: determine fatigue limit and corresponding stabilized temperature rise based on thermographic data

Figure 3-9 illustrates the average surface temperature rise versus the number of loading cycles under 9 successive stress levels. As can be seen from the figure, for the stress levels from 30% UTS to 65% UTS, the profile reached temperature stabilizing after certain loading cycles. **Figure 3-10** (a) depicts the stabilized temperature rise plotted as a function of the maximum applied stress. Similar to the previous case, the new fatigue limit determination approach (**Figure 3-10** (b)) was employed here and the fatigue limit was determined as 65% UTS, which is near the results obtained by the traditional fatigue tests (68.94% UTS). The corresponding stabilized temperature rise (ΔT_{stab_fl}) is 2.73 °C.

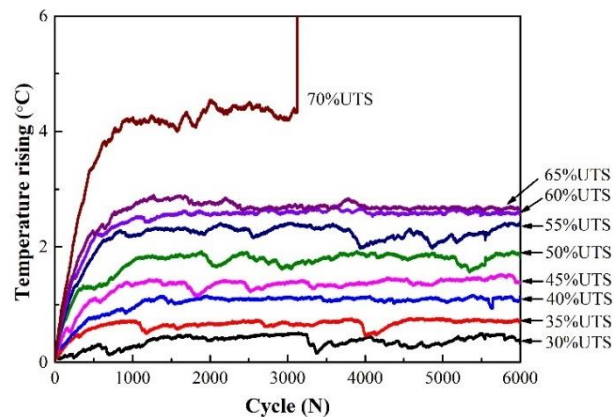


Figure 3-9 Evolution of temperature rise vs number of cycles of cross-ply specimen 2

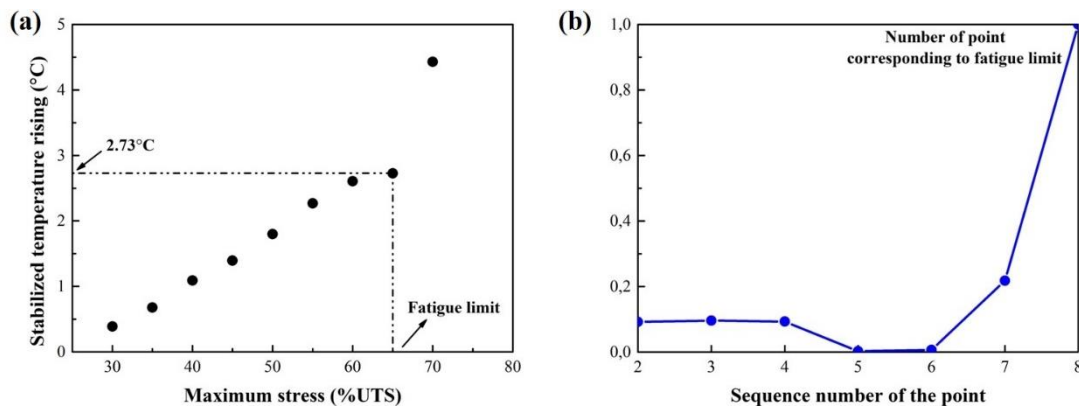


Figure 3-10 Fatigue limit determination of cross-ply specimen 2: (a) stabilized temperature rise vs maximum stress; (b) loci of normalized angle change vs sequence number of the point

Step 2: calibrate the values of p , q and r

A plot of normalized stiffness degradation against the number of loading cycles and stabilized temperature rise under stress level of 45%, 50%, 55%, 60% and 65% UTS is shown in **Figure 3-11**. Eq. (3-11) is adopted to fit the experimental data using MATLAB© 3D surface fitting Toolbox. The best-fit values of p , q and r are $8.301e-3$, 7.023 and 1.26, respectively.

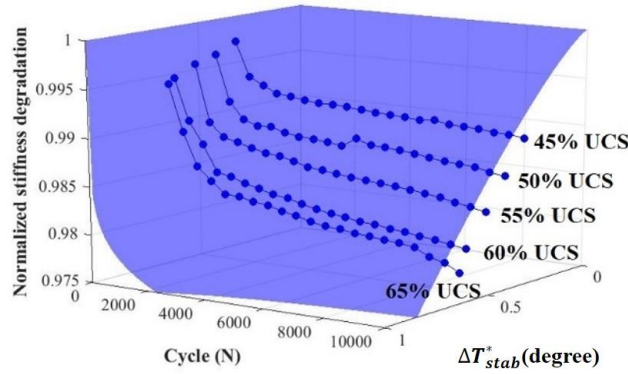


Figure 3-11 Surface fitting of Eq. (3-11) by MATLAB©

Step 3: calculate the failure threshold stiffness

Similar to the case of QI laminates, both $k(N_{fl} = 10^6 \text{ cycles})$ and $k(N_{fl} = 10^7 \text{ cycles})$ were chosen for the calculation of failure threshold stiffness. According to Eq. (2-9), $k_f = 0.952$ when $N_{fl} = 10^6$ cycles while this value is 0.938 when $N_{fl} = 10^7$ cycles.

Step 4: determination of S-N curve

The fatigue life calculated using proposed model and traditional fatigue test results with 95% confidence interval are plotted in **Figure 3-12**. It can be clearly seen that the determined S-N curve corresponding to $N_{fl} = 10^6$ cycles is relatively conservative. The determined fatigue life is lower than the traditional fatigue test results. The security factor, defined as the ratio between maximum stress of traditional fatigue tests and that determined by proposed model for a given number of fatigue cycle, lies between 1.04 and 1.08. Both values are very close to 1. In consideration of the variability of the fatigue test results, this is acceptable. Whereas the S-N curve corresponding to $N_{fl} = 10^7$ cycles lies totally within the 95% confidence interval.

The error induced by the determined S-N curve ($N_{fl} = 10^7$ cycles) is well within the measurement uncertainty. This approves that the proposed model can be used to predict the fatigue life of MD CFRP laminates.

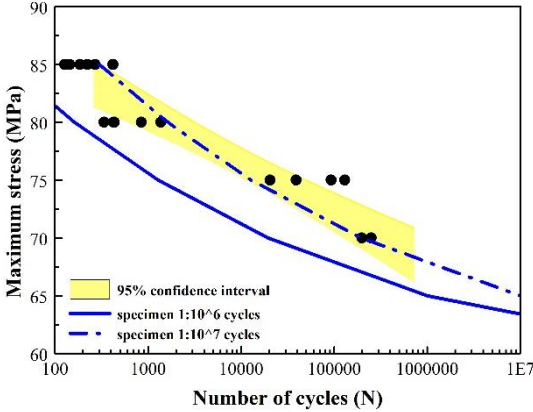


Figure 3-12 Comparison of S-N curve obtained by proposed model with traditional fatigue test results

3.3 Determination of an average S-N curve considering the variability of thermographic data

It is well known that the measurement of fatigue life on composite laminates under the same test condition presents a large scatter. Considering this variability of fatigue data, in the traditional fatigue tests, it is recommended to run the tests with at least three specimens for each stress levels in order to produce a reliable S-N curve. Similarly, in the fatigue tests accompanied with the use of IRT, each test should be run for at least two-three specimens. Without doubt, the S-N curve from thermographic data measured on different specimen could be quite different. Therefore, how to process the thermographic data from several specimens becomes a critical question in order to determine an “average” single S-N curve more reliable for engineering design. The possible solution to this question will be discussed in this section by using the data obtained on our laminates tested under tensile fatigue loading.

3.3.1 Cross-ply laminates

As already been stated before, in our previous tests, three specimens were tested for each stacking sequence. Since the data of three specimens are all available for cross-ply laminates, therefore, the discussion starts with this stacking sequence. Following the same fatigue limit

determination and fatigue life determination procedure in chapter 2 and section 3.2, the calibration results and obtained S-N curves of all three specimens (specimen 1, 2 and 3) using proposed model are directly given in **Table 3-1** and **Figure 3-13**.

Table 3-1. Fatigue limit and calibration parameters of specimen 1, 2 and 3

Parameters	Specimen 1	Specimen 2	Specimen 3
Fatigue limit	65	65	60
ΔT_{stab_fl}	3.96 °C	2.73 °C	5.15 °C
p	3.342×10^{-2}	8.301×10^{-3}	3.412×10^{-2}
q	25.79	7.023	19.56
r	0.40	1.26	0.77
$k_f(N_{fl} = 10^6 \text{ cycles})$	0.950	0.952	0.942
$k_f(N_{fl} = 10^7 \text{ cycles})$	0.945	0.938	0.935
R^2	0.95	0.98	0.97

As can be seen in **Figure 3-13**, for all the three specimens, the determined S-N curves corresponding to $N_{fl} = 10^6$ cycles are relatively conservative. The determined fatigue life is lower than the traditional fatigue test results. The S-N curve corresponding to $N_{fl} = 10^7$ cycles of specimen 1 lies totally within the 95% confidence interval. For the maximum stress between 65% and 80% UTS, the S-N curve corresponding to $N_{fl} = 10^7$ cycles of specimen 2 lies within the 95% confidence interval. Above 80% UTS, the determined curve is a little higher than the traditional test results. For specimen 3, the S-N curve corresponding to $N_{fl} = 10^7$ cycles is relatively lower than the 95% confidence interval for the maximum stress below 75% UTS.

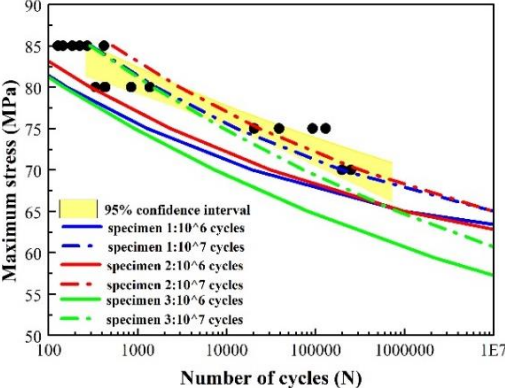


Figure 3-13. Comparison of S-N curves based on thermographic data of three specimens with traditional fatigue test results

To determine a more reliable S-N curve from the three different S-N curves, the initial thought is to ‘average’ the data of three S-N curves. Similar to the fatigue life determination procedure already stated before, the details of this ‘average’ process are described below:

‘Average’ process on all the specimens

Step 1: Determine the fatigue limit and corresponding stabilized temperature rise

The stabilized temperature rise of each laminate is first normalized with its own maximum value to obtain ΔT_{stab}^* corresponding to each stress level. Then, the average value of ΔT_{stab}^* of three specimens is calculated to obtain $\overline{\Delta T_{stab}^*}$ corresponding to each stress level. **Figure 3-14** (a) is a plot of average normalized stabilized temperature rise $\overline{\Delta T_{stab}^*}$ of three specimens as a function of maximum stress. The new fatigue limit determination approach (**Figure 3-14** (b)) was employed here and the fatigue limit was determined as 65% UTS, which is close to the results obtained by the traditional fatigue tests (68.94% UTS at 10^6 cycles). The corresponding normalized stabilized temperature rise ($\overline{\Delta T_{stab}^*}$) is 0.78.

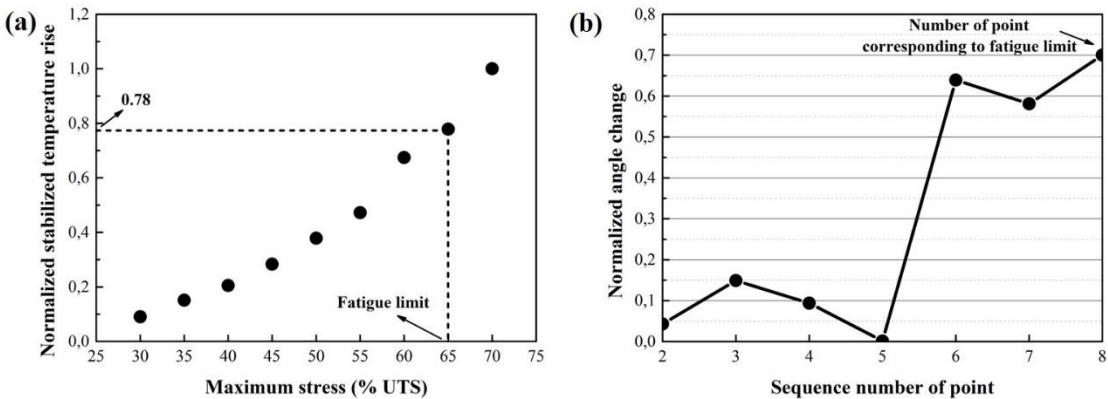


Figure 3-14. Fatigue limit determination based on data of three specimens: (a) normalized stabilized temperature rise vs maximum stress; (b) loci of normalized angle change vs sequence number of the point

Step 2: calibrate the values of p , q and r

The average normalized stiffness degradation of three specimens corresponding to stress level of 50%, 55%, 60%, 65% and 70% UTS is employed to plot against the number of loading cycles and average normalized stabilized temperature rise $\overline{\Delta T_{stab}^*}$, as shown in **Figure 3-15**. Eq. (3-11) is adopted to fit the experimental data using MATLAB[®] 3D surface fitting Toolbox. The best-fit values of p , q and r are 2.189e-2, 16.818 and 0.483, respectively. The coefficient

of determination R^2 is 0.73, which implies that the fitting results are not good.

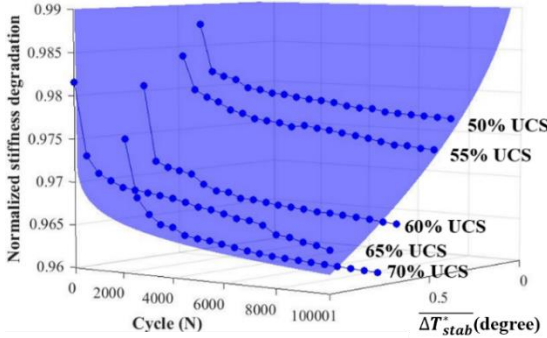


Figure 3-15. Surface fitting using Eq. (3-11) in MATLAB®

Step 3: calculate the failure threshold stiffness

Still, both $k(N_{fl} = 10^6 \text{ cycles})$ and $k(N_{fl} = 10^7 \text{ cycles})$ are chosen for the calculation of failure threshold stiffness. According to Eq. (3-11), $k_f = 0.956$ when $N_{fl} = 10^6$ cycles while this value is 0.950 when $N_{fl} = 10^7$ cycles.

Step 4: determination of S-N curve

The determined S-N curves calculated based on the average data of three specimens and traditional fatigue test results with 95% confidence interval are plotted in **Figure 3-16**. It can be clearly seen that starting from around 70%-75% UTS, with the increase of maximum stress, both the determined S-N curves corresponding to 10^6 cycles and 10^7 cycles tend to deviate largely from the 95% confidence interval. For a given maximum stress, the fatigue life is overestimated, especially for the S-N curves corresponding to 10^7 cycles. Less than half of the traditional fatigue test results lies between the two determined curves.

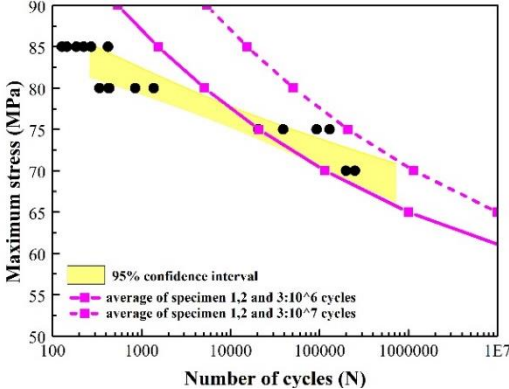


Figure 3-16. Determined S-N curve calculated based on the average data of three cross-ply specimens and traditional fatigue test results

Based on the above protocol, it can be concluded that the idea of calculating the S-N curve based on the average data of three specimens does not seem to work well.

In fact, it can be noted that the fatigue limit of specimen 1 and 2 are identical, and their S-N curves are closer to each other. However, the fatigue limit of specimen 3 is different from the others leading to a quite different S-N curve. A new idea comes up: only the data of specimens having the same fatigue limit will be used for the ‘average’ process. In this case, only the data from specimen 1 and 2 are treated.

‘Average’ process on the specimens having the same fatigue limit

Using the above stated the procedure, in the step 1, the average ΔT_{stab}^* value of specimens 1 and 2 is calculated to obtain $\overline{\Delta T_{stab}^*}$ corresponding to each stress level. The proposed method in Chapter 2 is employed to determine the fatigue limit using the data sets $(\sigma, \overline{\Delta T_{stab}^*})$. **Figure 3-17 (a)** is a plot of average normalized stabilized temperature rise $\overline{\Delta T_{stab}^*}$ of specimen 1 and 2 as a function of maximum stress. The normalized angle change calculated based on the data as a function of sequence of number of points is shown in **Figure 3-17 (b)**. The sequence number of point corresponding to fatigue limit is 8, which corresponds to 65% UTS in **Figure 3-17 (a)**. The corresponding normalized stabilized temperature rise is 0.68.

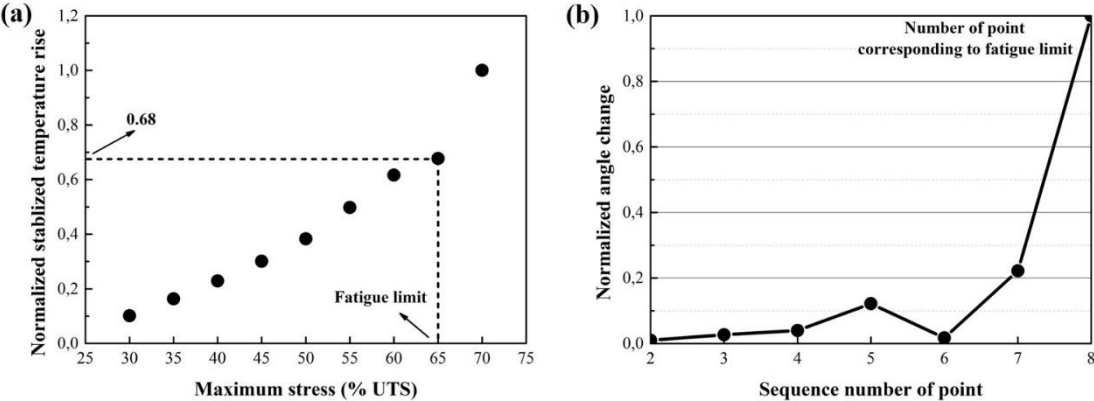


Figure 3-17. Fatigue limit determination based on data of specimens 1 and 2: (a) normalized stabilized temperature rise vs maximum stress; (b) loci of normalized angle change vs sequence number of the point

In the step 2, the average normalized stiffness degradation of specimens 1 and 2 corresponding to stress level of 50%, 55%, 60%, 65% and 70% UTS is employed to plot the number of loading cycles against normalized stabilized temperature rise, as shown in **Figure 3-18**. The best-fit values of p , q and r using MATLAB[®] 3D surface fitting are $2.026e-2$, 15.64 and 0.546, respectively. The coefficient of determination R^2 is 0.93, which is much closer to 1, indicating a better fitting result.

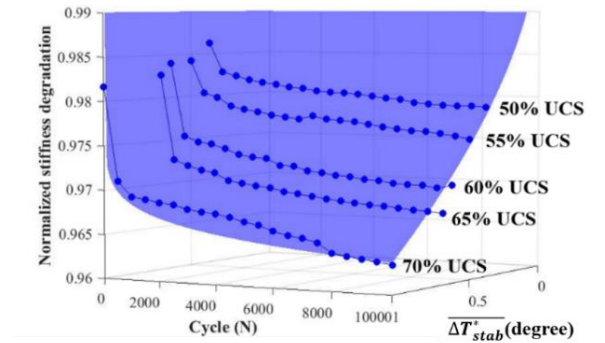


Figure 3-18. Surface fitting using Eq. (3-11) in MATLAB[®]

As for step 3, the failure threshold stiffnesses corresponding to fatigue life of 10^6 cycles and 10^7 cycles are 0.960 and 0.954, respectively. And finally, the determined S-N curves calculated based on the average data of specimens 1 and 2 and traditional fatigue test results with 95% confidence interval are illustrated in **Figure 3-19**. As can be seen from the figure, the obtained S-N curve corresponding to $N_{fl} = 10^6$ cycles is relatively lower than the experimental results, while that corresponding to fatigue life of $N_{fl} = 10^7$ cycles is little higher than the upper 95% confidence interval for the maximum stress above 75% UTS. Most of the experimental test results (11/16 specimens) are between the two determined S-N curves. Compared to S-N curves calculated based on the average of all specimens, better results are obtained based on the average of specimens 1 and 2.

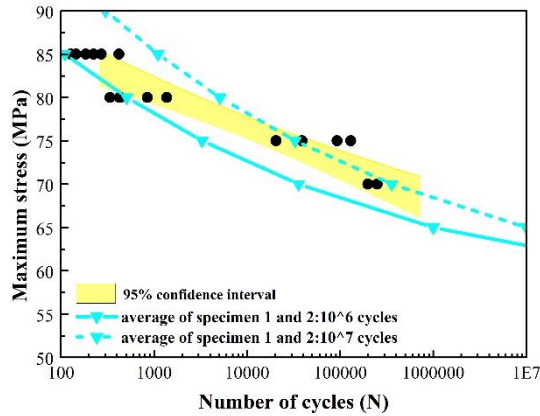


Figure 3-19. Determined S-N curve calculated based on the average data of specimens 1 and 2 and traditional fatigue test results

3.3.2 QI laminates

Herein the experimental data of QI laminates are adopted. Since one specimen failed at 45% UTS, only the data of two specimens are available. Using fatigue limit determination method proposed in chapter 2, the fatigue limit is 65% UTS and 70% UTS for specimens 1 and 2, respectively. The parameters of fatigue life for each specimen determined by the proposed model are listed in **Table 3-2**. If ‘Average’ process on all the specimens is applied following the steps of protocol cited above, the plot of average normalized stabilized temperature rise $\overline{\Delta T_{stab}^*}$ of two specimens as a function of maximum stress can be obtained.

In the step 3, 3D surface fitting in MATLAB[®] is employed to fit the average normalized stiffness degradation as a function of average stabilized temperature rise $\overline{\Delta T_{stab}^*}$ and number of cycles. The obtained values of p , q and r and coefficients of determination R^2 are listed in **Table 3-2**.

In step 4, the computed failure threshold stiffness corresponding to $N_{fl} = 10^6$ cycles and 10^7 cycles are also listed in **Table 3-2**.

Ultimately, the obtained S-N curves based on the ‘average’ of two specimens, the individual S-N curves of each specimen and traditional experimental results are compared in **Figure**

3-20.

Table 3-2. Fatigue limit and calibration parameters

Parameters	Specimen 1	Specimen 2	“Average”
Fatigue limit	70	65 % UTS	65% UTS
$\Delta T_{stab_fl} / \Delta T_{stab_fl}^*$	5.068	4.205	0.72
p	0.189	3.736e-2	0.148
q	61.01	11.78	20.63
r	0.42	0.66	0.518
$k_f(N_{fl} = 10^6 \text{ cycles})$	0.782	0.689	0.756
$k_f(N_{fl} = 10^7 \text{ cycles})$	0.773	0.621	0.728
R^2	0.98	0.98	0.99

As can be seen from the figure, even though the determined S-N curves corresponding to $N_{fl} = 10^6$ cycles of specimen 1 and that corresponding to $N_{fl} = 10^7$ cycles of specimen 2 are both within the 95% confidence interval of traditional experimental results, the curves corresponding to two fatigue lives calculated based on the average of two specimens are both below the 95% confidence interval. The determined fatigue life is significantly lower than the traditional fatigue test results overall. This proves that if the determined fatigue limits of two specimens are different from each other, the S-N curves obtained by the average data of these two specimens is not credible. In this situation, only a set of individual S-N curves of each specimen can be obtained to predict the fatigue life. It is absolutely necessary to redo a test to have another specimen whose fatigue limit is close to one of the 2 cases.

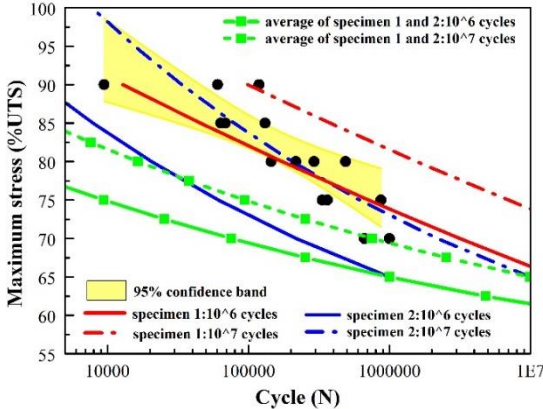


Figure 3-20. Determined S-N curve calculated based on the average data of two QI specimens and traditional fatigue test results

3.3.3 Proposition of a protocol to obtain a more reliable S-N curve

On the basis of above results, a protocol to obtain a more reliable S-N curve based on the data of several individual S-N curves is proposed here:

Step 1: Each test should be run for at least three specimens until the determined fatigue limits of two specimens are identical.

Step 2: the average ΔT_{stab}^* value of these two specimens is calculated to obtain $\overline{\Delta T_{stab}^*}$ corresponding to each stress level. The proposed method in Chapter 2 is employed to determine the new fatigue limit and corresponding normalized stabilized temperature rise using the data sets $(\sigma, \overline{\Delta T_{stab}^*})$.

Step 3: the average normalized stiffness degradation of these two specimens corresponding to a series of stress level is employed to plot the number of loading cycles against normalized stabilized temperature rise. Eq. (3-11) is adopted to fit the experimental data using 3D surface fitting Toolbox in MATLAB[®].

Step 4: the failure threshold stiffness corresponding to $N_{fl} = 10^6$ cycles and 10^7 cycles are calculated by Eq. (3-11).

Step 5: the more reliable determined S-N curves corresponding to fatigue life of 10^6 cycles and 10^7 cycles can be obtained by Eq. (3-12).

3.4 Summary

In this section, the fatigue life model in term of S-N curve proposed by Huang et al. [18] has been modified. Firstly, a new parameter r is introduced into original expression of normalized stiffness to take the more complex damage mechanisms in the MD CFRP laminates into account. Secondly, the variable “stabilized temperature rise” is replaced by its normalized value defined as $\Delta T_{stab}^* = (\Delta T_{stab})/(\Delta T_{stab})_{max}$. This modified model is an extension of Huang’s model. The results have shown that the modified model allows to determine the S-N curves of QI and cross-ply CFRP laminates much more closed to traditional test results. In particular, the S-N curves corresponding to $N_{fl} = 10^7$ cycles lie totally within the 95%

confidence intervals of traditional fatigue test results. To sum up, the modified model is more general, it can be applied to predict the fatigue life of CFRP with arbitrary stacking sequence. Moreover, a protocol of the treatment of thermographic data has been proposed by taking in account of the variability of experimental results in order to obtain a S-N curve more reliable for engineering design.

Chapter 4 Compression-compression fatigue behavior of CFRP

The focus of this chapter is to study the compression and compression-compression fatigue behavior of Quasi-Isotropic Quasi-Homogeneous (QIQH) CFRP laminates. The method proposed in chapter 2 for fatigue limit determination and the modified fatigue life model, described in chapter 3, will be applied to compression-compression fatigue experimental data of QIQH laminates to demonstrate the universality of both methods.

4.1 QIQH laminates

In the chapters 4 and 5, QIQH laminates were chosen for the compression (compressive fatigue) and CAI (Compression After Impact) tests. There are mainly three reasons for this choice: i) according to the standard ASTM D7136/D7136M [231], QI stacking sequence is recommended for the impact tests; 2) Most of the previous work focus on the study of compression and CAI behavior of QI laminates, the number of studies on the QIQH laminates is limited. 3) In most of the researches that aim to investigate the influence of stacking sequence on the behavior of CFRP, the global effects (membrane and bending stiffnesses modification) are not separated from the local effects (ply orientation). In order to isolate the local effects, QIQH stacking sequences are needed.

In order to explain what a QIQH laminate is, two main theoretical tools are used: the Classical Laminated Plate Theory (CLPT) and the polar description of plane anisotropy. In the composite materials, the presence of a reinforcement in an isotropic matrix results in a general anisotropy for laminas; laminates obtained by superposing laminas with different orientations of fibers are anisotropic, in general. The analysis of composite laminates by the classical CLPT needs the transformation of elastic properties of laminas by rotation. This transformation is rather cumbersome. However, with the use of polar description, material and frame rotations can be easily expressed, giving much simpler equations than those obtained by Cartesian transformation.

Another important advantage of polar description is the physical meaning of tensor polar components: taking the elastic tensor as an example, these are invariant parameters directly representing the symmetries of a given material. By polar components, it is possible to distinguish the kind of anisotropy of a lamina at a glance, independently of the reference frame.

4.1.1 Classical Laminated Plate Theory (CLPT)

Let us consider a laminate which is composed of a given number, n , of anisotropic laminas. Each ply is characterized by its basic elastic properties, its fiber orientation, its position and thickness. Assuming the ply with index k is oriented in the direction whose difference with the global coordinate axes is δ_k , extending from z_{k-1} to z_k (**Figure 4-1**), the intrinsic stiffness of the ply is $\mathbf{Q}(\delta_k)$.

In the frame work of CLPT [232]-[234], the mechanical behavior of laminates is described by the generalized Hooke's law, which linearly relates the generalized forces (in-plane forces N and bending moments M) to the generalized strains (middles-plane strains $\boldsymbol{\varepsilon}^0$ and curvatures $\boldsymbol{\kappa}$), which, in a compact form is written as :

$$\begin{aligned} N &= \mathbf{A}\boldsymbol{\varepsilon}^0 + \mathbf{B}\boldsymbol{\kappa} \\ M &= \mathbf{B}\boldsymbol{\varepsilon}^0 + \mathbf{D}\boldsymbol{\kappa} \end{aligned} \quad (4-1)$$

Where \mathbf{A} is the in-plane or membrane stiffness matrix, \mathbf{D} is the out-of-plane or bending stiffness matrix and \mathbf{B} is the membrane-bending coupling stiffness matrix. All these stiffnesses are fourth order tensors and can be expressed by the properties and stacking of plies:

$$\mathbf{A} = \sum_{k=-p}^p \mathbf{Q}(\delta_k)(z_k - z_{k-1}) \quad (4-2)$$

$$\mathbf{B} = \frac{1}{2} \sum_{k=-p}^p \mathbf{Q}(\delta_k)(z_k^2 - z_{k-1}^2) \quad (4-3)$$

$$\mathbf{D} = \frac{1}{3} \sum_{k=-p}^p \mathbf{Q}(\delta_k)(z_k^3 - z_{k-1}^3) \quad (4-4)$$

In the above formulas, $n = 2p$ if n is an even number ; $n = 2p + 1$ if n is an odd number; z_k are the distances between the top surfaces and the middle plane, as shown in **Figure 4-1**. In this way, if the thickness of each layer of the laminate is identical ($h_{one\ layer} = h/n$), we have:

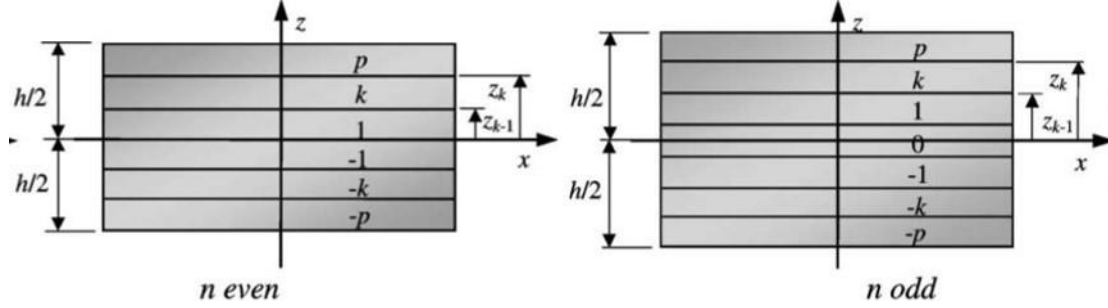


Figure 4-1. Sketch for the numbering of layers and interfaces [235]

$$z_k = \frac{2k + 1}{2} \frac{h}{n}, z_{k-1} = \frac{2k - 1}{2} \frac{h}{n} \text{ for } n = 2p + 1$$

$$z_k = k \frac{h}{n}, z_{k-1} = (k - 1) \frac{h}{n} \text{ if } k > 0 \text{ and } n = 2p \quad (4-5)$$

$$z_k = (k + 1) \frac{h}{n}, z_{k-1} = k \frac{h}{n} \text{ if } k < 0 \text{ and } n = 2p$$

4.1.2 Polar description of plane anisotropy [236]

Let us first consider simultaneously two Cartesian frames of reference, an old one, with coordinates x_1 and y_1 , and a new one, rotated by an angle θ , with coordinates x and y (**Figure 4-2**). The transformation formulas for these four coordinates can be written as:

$$\begin{aligned} x &= x_1 \cos\theta + y_1 \sin\theta \\ y &= -x_1 \sin\theta + y_1 \cos\theta \end{aligned} \quad (4-6)$$

To make easier the understanding of polar description, the vectors are first taken as an example. For a vector F , with Cartesian components A_1 and A_2 in the old frame, its polar decomposition with modulus R and polar angle b is given as:

$$\begin{aligned} A_1 &= R \cos b \\ A_2 &= R \sin b \end{aligned} \quad (4-7)$$

The reverse equations of Eq. (4-7) can be expressed in the complex form:

$$R e^{ib} = A_1 + iA_2 \quad (4-8)$$

If the old frame is rotated by an angle θ with respect to the other, the Cartesian components change according to the transformation of Eq. (4-6):

$$\begin{aligned} A_x &= A_1 \cos\theta + A_2 \sin\theta \\ A_y &= -A_1 \sin\theta + A_2 \cos\theta \end{aligned} \quad (4-9)$$

Where A_x and A_y are the Cartesian coordinates in the new frame.

While the polar form for the new components is:

$$\begin{aligned} A_x &= R \cos(b - \theta) \\ A_y &= R \sin(b - \theta) \end{aligned} \quad (4-10)$$

And the reverse equation in the complex formula is:

$$R e^{i(b-\theta)} = A_x + iA_y \quad (4-11)$$

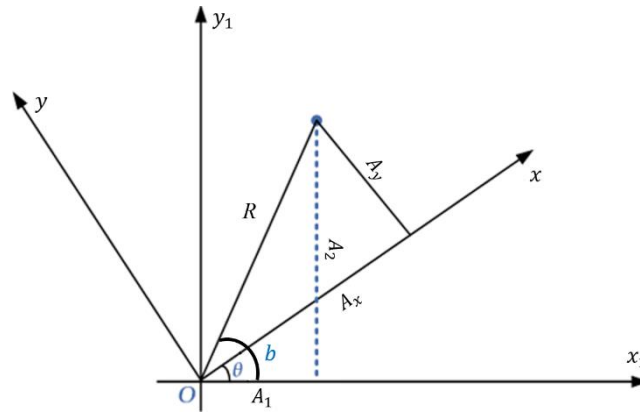


Figure 4-2. Schematic illustration of the rotation of frames

Comparing Eq. (4-11) with Eq. (4-8), the basic rule for transformation in polar form could be revealed: the modulus R is invariant during rotation and the polar angle b is decreased by the angle of rotation from the original to the new frame.

This polar decomposition can be extended to plane tensors of any order. For the case of a fourth order tensor with typical symmetry of elasticity, i.e.:

$$L_{ijkl} = L_{ijlk} = L_{jikl} = L_{klji} \quad (4-12)$$

Its six Cartesian components in the old frame can be expressed as:

$$\begin{aligned} L_{1111} &= B_0 + 2B_1 + R \cos 4b_0 + 4R_1 \cos 2b_1 \\ L_{1112} &= R_0 \sin 4b_0 + 2R_1 \sin 2b_1 \\ L_{1122} &= -B_0 + 2B_1 - R_0 \cos 4b_0 \\ L_{1212} &= B_0 - R_0 \cos 4b_0 \\ L_{1222} &= -R_0 \sin 4b_0 + 2R_1 \sin 2b_1 \\ L_{2222} &= B_0 + 2B_1 + R_0 \cos 4b_0 - 4R_1 \cos 2b_1 \end{aligned} \quad (4-13)$$

Where B_0 and B_1 are scalars, R_0 and R_1 are modulus, b_0 and b_1 are polar angles. Conversely,

these six polar components can also be expressed by the six Cartesian components following the complex equations:

$$\begin{aligned}
8B_0 &= L_{1111} - 2L_{1122} + 4L_{1212} + L_{2222} \\
8B_1 &= L_{1111} + 2L_{1122} + L_{2222} \\
8R_0 e^{4ib_0} &= L_{1111} - 2L_{1122} - 4L_{1212} + L_{2222} + 4i(L_{1112} - L_{1222}) \\
8R_1 e^{2ib_1} &= L_{1111} - L_{2222} + 2i(L_{1112} + L_{1222})
\end{aligned} \tag{4-14}$$

A rotation of coordinate axes results in the following expression for the Cartesian component:

$$\begin{aligned}
L_{xxxx} &= L_{1111} \cos^4 \theta + 4L_{1112} \cos^3 \theta \sin \theta + 2L_{1122} \cos^2 \theta \sin^2 \theta \\
&\quad + 4L_{1212} \cos^2 \theta \sin^2 \theta + 4L_{1222} \cos \theta \sin^3 \theta + L_{2222} \sin^4 \theta
\end{aligned} \tag{4-15}$$

And so forth for the other components.

From Eq. (4-15), it is obvious that the formula is rather complex and do not allow a clear insight into the occurring process. However, the use of polar composition may greatly simplify the transformation:

$$\begin{aligned}
L_{xxxx} &= B_0 + 2B_1 + R_0 \cos 4(b_0 - \theta) + 4R_1 \cos 2(b_1 - \theta) \\
L_{xxxy} &= R_0 \sin 4(b_0 - \theta) + 2R_1 \sin 2(b_1 - \theta) \\
L_{xxyy} &= -B_0 + 2B_1 - R_0 \cos 4(b_0 - \theta) \\
L_{xyxy} &= B_0 - R_0 \cos 4(b_0 - \theta) \\
L_{xyyy} &= -R_0 \sin 4(b_0 - \theta) + 2R_1 \sin 2(b_1 - \theta) \\
L_{yyyy} &= B_0 + 2B_1 + R_0 \cos 4(b_0 - \theta) - 4R_1 \cos 2(b_1 - \theta)
\end{aligned} \tag{4-16}$$

The comparison of Eq. (4-16) with Eq. (4-13) shows that, for a rotation θ of the reference frame, B_0 , B_1 , R_0 and R_1 are invariant, as well as the difference between the polar angles $b_0 - b_1$. This suggests that once one of the polar angle is determined, the other polar angle is found thanks to the invariance of difference $b_0 - b_1$.

And the reverse equations of Eq. (4-16) are:

$$\begin{aligned}
8B_0 &= L_{xxxx} - 2L_{xxyy} + 4L_{xyxy} + L_{yyyy} \\
8B_1 &= L_{xxxx} + 2L_{xxyy} + L_{yyyy} \\
8R_0 e^{4i(b_0 - \theta)} &= L_{xxxx} - 2L_{xxyy} - 4L_{xyxy} + L_{yyyy} + 4i(L_{xxxy} - L_{xyyy}) \\
8R_1 e^{2i(b_1 - \theta)} &= L_{xxxx} - L_{yyyy} + 2i(L_{xxxy} + L_{xyyy})
\end{aligned} \tag{4-17}$$

4.1.3 Application of polar method to the laminates

For each of the laminate stiffnesses \mathbf{A} , \mathbf{B} and \mathbf{D} , polar method can be introduced as they are linear combinations of Cartesian components. Eq. (4-2) to (4-4) can all be easily transcribed in polar form, with the polar components of tensor $Q(\delta_k)$ represented by T_{0k} , T_{1k} , R_{0k} , R_{1k} , Φ_{0k} and Φ_{1k} . Furthermore, in the case where all the plies of laminate are made of the same material, then T_{0k} , T_{1k} , R_{0k} , R_{1k} , Φ_{0k} and Φ_{1k} are the same. The terms $\sum_{k=-p}^p (z_k - z_{k-1})$, $\sum_{k=-p}^p (z_k^2 - z_{k-1}^2)$ and $\sum_{k=-p}^p (z_k^3 - z_{k-1}^3)$ can be simplified into [237]:

$$\begin{aligned} \sum_{k=-p}^p (z_k - z_{k-1}) &= h \\ \sum_{k=-p}^p (z_k^2 - z_{k-1}^2) &= 0 \\ \sum_{k=-p}^p (z_k^3 - z_{k-1}^3) &= \frac{h^3}{12} \end{aligned} \quad (4-18)$$

Then the polar components of \mathbf{A} , \mathbf{B} and \mathbf{D} can be simplified into the following forms [235]:

Tensor \mathbf{A} :

$$\begin{aligned} T_0^A &= T_0 h \\ T_1^A &= T_1 h \\ R_0^A e^{4i\Phi_0^A} &= \frac{h}{n} R_0 e^{4i\Phi_0} \sum_{k=-p}^p e^{4i\delta_k} \\ R_1^A e^{2i\Phi_1^A} &= \frac{h}{n} R_1 e^{2i\Phi_1} \sum_{k=-p}^p e^{2i\delta_k} \end{aligned} \quad (4-19)$$

Tensor \mathbf{B} :

$$\begin{aligned} T_0^B &= 0 \\ T_1^B &= 0 \\ R_0^B e^{4i\Phi_0^B} &= \frac{1}{2} R_0 e^{4i\Phi_0} \sum_{k=-p}^p e^{4i\delta_k} (z_k^2 - z_{k-1}^2) \end{aligned} \quad (4-20)$$

$$R_1^B e^{2i\Phi_1^B} = \frac{1}{2} R_1 e^{2i\Phi_1} \sum_{k=-p}^p e^{2i\delta_k} (z_k^2 - z_{k-1}^2)$$

Tensor \mathbf{D} :

$$T_0^D = T_0 \frac{h^3}{12}$$

$$T_1^D = T_1 \frac{h^3}{12}$$

$$R_0^D e^{4i\Phi_0^D} = \frac{1}{3} R_0 e^{4i\Phi_0} \sum_{k=-p}^p e^{4i\delta_k} (z_k^3 - z_{k-1}^3) \quad (4-21)$$

$$R_1^D e^{2i\Phi_1^D} = \frac{1}{2} R_1 e^{2i\Phi_1} \sum_{k=-p}^p e^{2i\delta_k} (z_k^3 - z_{k-1}^3)$$

4.1.4 Design of QIQH laminates

According to Ref. [238], a QIQH laminate is defined as a laminate with no membrane-bending coupling and equal normalized stiffnesses for bending and membrane:

$$\begin{aligned} \frac{1}{h} \mathbf{A} - \frac{12}{h^3} \mathbf{D} &= 0 \\ \mathbf{B} &= 0 \end{aligned} \quad (4-22)$$

Where $1/h$ and $12/h^3$ are the CLPT homogenizing coefficients for membrane \mathbf{A} and bending \mathbf{D} stiffness tensor.

This kind of laminates do exist. One trivial case is a laminate in which all the plies have the same material properties and direction. The detailed procedure for solving Eq. (4-22) will not be presented here (see [235]), since it is rather long and not the emphasis of the thesis.

4.2 Materials and specimens

4.2.1 Materials

The raw material used to fabricate the composite laminates for static and compression-compression fatigue tests is a unidirectional pre-impregnated (prepreg) carbon fiber epoxy

material from Gurit. The prepreg is made of High Elongation Carbon (HEC) fiber and SE84LV resin, with fiber weight of 150 g/m² and resin content between 34-40 %. The basic mechanical properties of the prepreg provided by the material manufacturer are summarized in **Table 4-1**.

Table 4-1 Basic mechanical properties of SE84LV/HEC/150/400/37+/-3%

Properties	Values
0° tensile strength	2458 MPa
0° tensile modulus	134 GPa
0° compression strength	1354 MPa
0° compression modulus	121 GPa
0° flexural strength	1448 MPa
0° flexural modulus	106 GPa
0° interlaminar strength	86.6 MPa
90° tensile strength	39.2 MPa
90° tensile modulus	8.3 GPa
in plane shear modulus	4.0 GPa
In plane Poisson's coefficient	0.3

In order to investigate the influence of ply orientation on the compression-compression fatigue properties of composite materials, QIQH laminates were used. Among all the potential sequences, three 24-ply QIQH laminate configurations were chosen for the study, as given in **Table 4-2** under the names QIQH-1, QIQH-2 and QIQH-3. Note that

1. These laminates are not symmetrical
2. The fibers at adjacent plies have always different orientation;
3. The fiber orientation at the surfaces of each configuration is different: one surface has fiber 0°, another one has fiber in $\pm 45^\circ$ or 90° ;
4. From the surface with fiber 0°, the fiber orientation at the adjacent ply (45° for QIQH-1 and QIQH-2; 90° for QIQH-3) or at sub-adjacent ply (90° , -45° and 45° for QIQH-1, 2 and 3, respectively) can be different; while from another surface, the fiber orientation at

the adjacent ply is always 0° , but different fiber orientation at sub-adjacent ply (-45° for QIQH-1 and 3, 90° for QIQH-2);

5. Number of each interface (see **Table 4-3**) is different one laminate to another one; the distribution of the interfaces is more homogeneous in laminate QIQH-3;
6. all of three laminates is composed by 6 plies of fibers at 0° , 6 plies at 90° , 6 plies at 45° and 6 plies at -45°
7. These laminates have the same stiffness matrix **A**, **B** and **D**, all anisotropic coupling terms are zero;
8. These laminates are QIQH: Their apparent elastic constants in-plane and out-of-plane, calculated using material properties in **Table 4-1** based on CLPT [232]-[234], are presented in **Table 4-4**, showing quasi-homogeneous. The graphics in **Figure 4-3**, shows that their stiffnesses are also quasi-isotropic.

Table 4-2. Laminate configurations: stacking sequences

Specimens	stacking sequences
QIQH-1	[-45/0/45/90/45/90/0/90/-45/45/-45/0/-45/0/90/0/45/-45/45/90/45/90/-45/0]
QIQH-2	[0/45/-45/90/-45/90/45/90/0/-45/0/45/0/45/90/45/-45/0/-45/90/-45/90/0/45]
QIQH-3	[0/90/45/-45/45/-45/90/-45/0/45/0/90/0/90/-45/90/45/0/45/-45/45/-45/0/90]

Table 4-3. Laminate configurations: number of interfaces

Specimens	Interfaces			
	0/45 or -45	90/45 or -45	0/90	45/-45
QIQH-1	7	8	4	4
QIQH-2	9	2	10	2
QIQH-3	6	6	5	6

Table 4-4. In-plane and bending elastic properties (GPa)

Properties	In-plane				Bending			
	E_x	E_y	G_{xy}	ν_{xy}	E_x	E_y	G_{xy}	ν_{xy}
Values	50.68	50.68	19.26	0.32	50.68	50.68	19.26	0.32

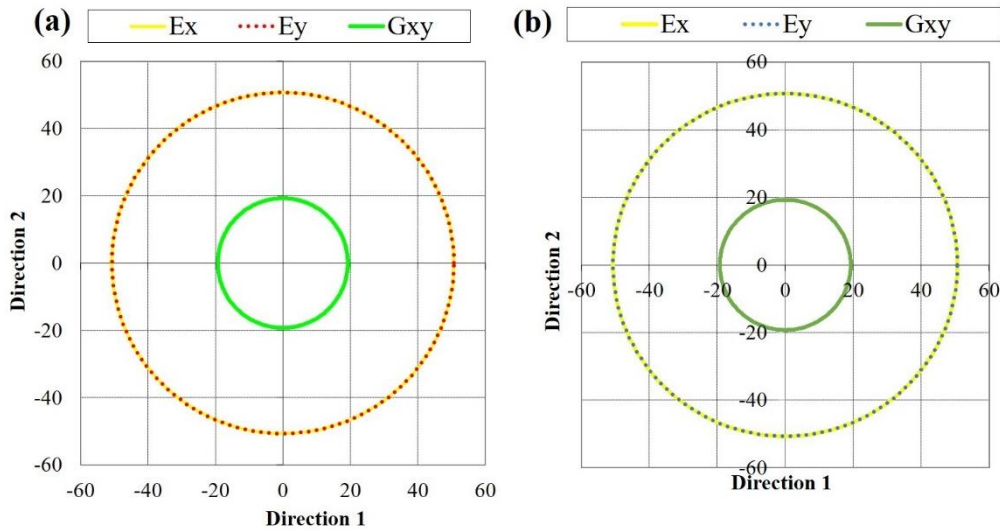


Figure 4-3. Polar description of quasi-isotropy in stiffnesses for the three stacking sequences:

(a) in-plane properties; (b) bending properties

4.2.2 Preparation of specimens

To consolidate cohesion between the plies and to reduce the potential defects (voids, bad compaction, entrapped air, humidity) before the final curing cycles, it is required to perform a pre-cure compaction process according to the Airbus technical Manual [239]. As presented in **Figure 4-4**, the individual plies of prepreg with dimensions of 360*200 mm/300*250 mm (for the impact /post-impact fatigue tests) were cut from the prepreg roll and then divided into two groups. Every group of twelve layers was laid-up with prescribed stacking sequence. The prepreg stacks, which are covered on both sides by a fine polyester cloth peel-ply are laid onto the metal plate, on top of which is placed with a bleeder ply and plastic vacuum bag. Two vacuum valves were also contained in the bag to allow the extraction of air from the interior of the plastic bag. A first compaction is then carried out at ambient temperature with 0.5 MPa of pressure for a duration of 30 min. Later on, the two 12-layer plates were stacked together to perform the correct stacking. Similar to the first compaction, the entire plates were sealed with a vacuum bag again and then further compacted at ambient temperature, at a constant compacting pressure of 0.8 MPa for another 30 min.

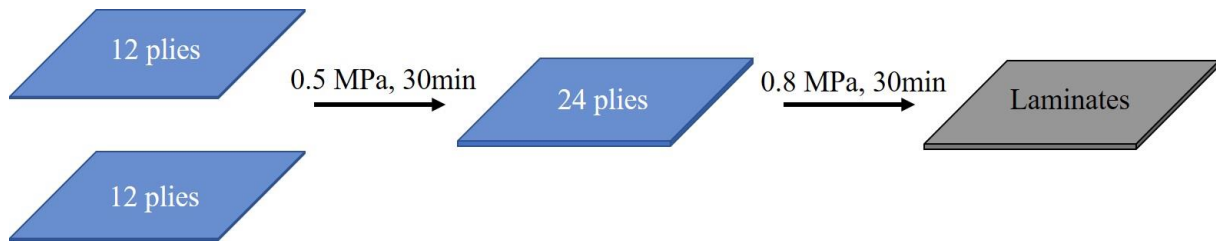


Figure 4-4. Schematic illustration of pre-cure compaction process

Once the described compaction process has been finished, the compacted plates were assembled in a standard vacuum bagging schedule and then cured in an autoclave. The curing of the laminates was carried out according to the process suggested by Gurit, Ltd. The temperature of the layup was raised at a $1^{\circ}\text{C}/\text{min}$ rate up to the maximum temperature 80°C and then held for 6 hours, as depicted in **Figure 4-5**. The differential pressure was set as 1.0 bar. Thereafter, specimens with two different dimensions (for static tests and for compression-compression fatigue tests) were cut from the cured laminates using water jet cutting machine.

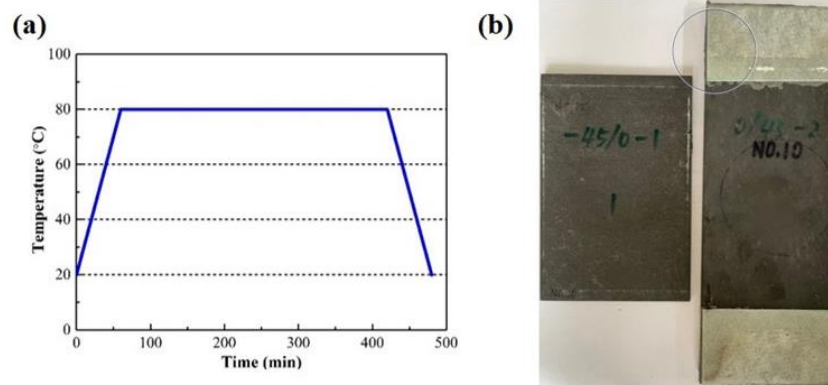


Figure 4-5. Preparation of specimens: (a) recommended curing cycle; (b) specimens

The dimensions of specimens used for the compression tests and compression fatigue tests were $L150 \times W100 \times \text{Thickness}3.65 \text{ mm}$ and $L250 \times W90 \times \text{Thickness}3.85 \text{ mm}$, respectively, as illustrated in **Figure 4-6**. The choice for dimensions of compression fatigue test specimen will be presented in section 4.1.2 in detail.

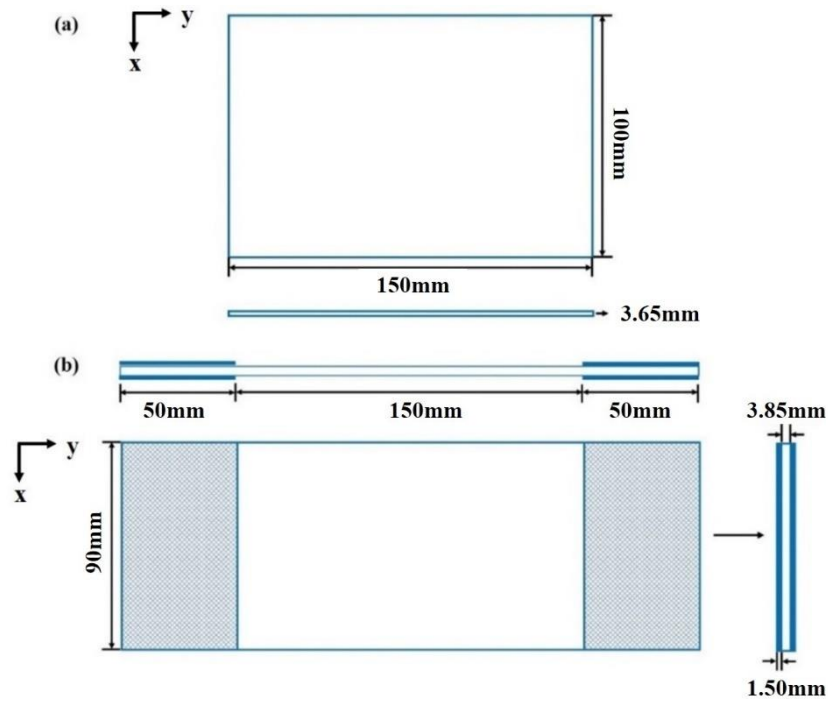


Figure 4-6. Dimensions of specimens: (a) compression and CAI test specimens; (b) fatigue and post-impact fatigue test specimens

To prevent premature failure in the grip region, glass fiber reinforced epoxy tabs oriented in $\pm 45^\circ$ of 1.5 mm thick were glued to each end of the compression fatigue test specimens using Hysol EA 9394 Part A + B epoxy adhesive following the same curing process as indicated in the previous chapter. The central gauge length of specimens is 150 mm (**Figure 4-6 (b)**).

4.3 Static compression tests

4.3.1 Experiments

The static compression tests were conducted at room temperature using a 100 KN Instron universal testing machine, according to the standard ASTM D7137 [240]. Three specimens were tested for each stacking sequence. All specimens were loaded in a displacement-controlled mode, with a crosshead displacement rate of 1.25 mm/min. This speed of the test was set such that the failure is produced within 1-10 min. The experimental set-up is shown in **Figure 4-7**. During the tests, the specimens were secured with the CAI fixture to prevent global buckling. The CAI fixture is made up of flat edges on the upper and lower ends in contact with the specimen surfaces and two pairs of plates with knife edges on the left and

right sides, leaving a central rectangular of 125×75 mm unsupported zone. Thus, constraints were provided such that the rotation and lateral movement of the upper and lower specimen edges were arrested and simply supporting conditions at the two vertical sides were achieved. Preloading was applied to the fixture/specimen assembly prior to the test in order to ensure that all loading surfaces are in contact and to align the specimens. Then the compressive force was reduced and made to zero to balance all the instrumentation. The crosshead displacement and applied force were recorded by the sensor of the testing machine.

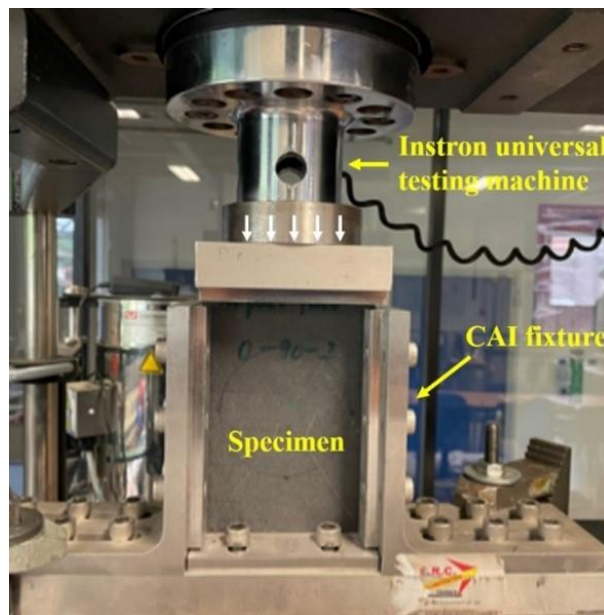


Figure 4-7. Experimental set-up of static compression tests

4.3.2 Results and discussion

Mechanical test results

The load versus displacement curves of static compression tests are depicted in **Figure 4-8** for three stacking sequences. It can be seen that the trends of load-displacement curves of different stacking sequences are quite similar to each other. Even though the curves from the specimens of the same stacking sequence show good repeatability, the stiffness and the strength of those QIQH-3 are lower than others.

One load-displacement curve is here taken as an example, as illustrated in **Figure 4-9**. The

global compressive load-displacement curve can be divided into three stages. At the beginning of the test, which includes the segment between origin O and the point A, since the specimen is not in perfect contact with the upper ends, the load showed an accelerated increase with the increasing of displacement. In the first stage (stage I), which includes the segment between the origin A and point B, the load showed a purely linear elastic relationship with the displacement. The stiffness in this stage is considered as the initial stiffness. When the compressive load further increased and reached point B, the initial stiffness begins to decrease, indicating the damage initiation and cumulation of matrix cracking, delamination and local buckling. Afterwards, delamination and matrix damage would be further induced and would eventually lead to fiber breaking. This stage II is shown relatively short for the specimens tested whatever the stacking sequence. Finally, the specimen failed completely with a sudden drop in load (Stage III).

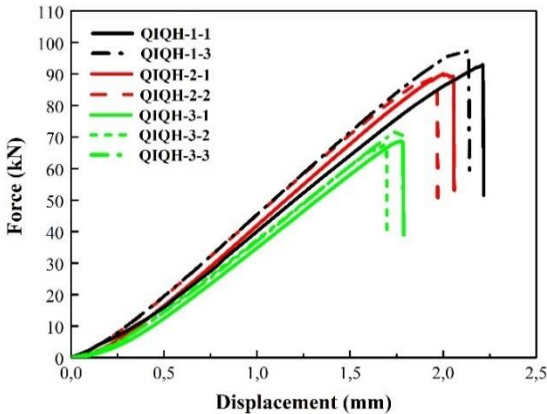


Figure 4-8. Force-displacement curves of static compression tests

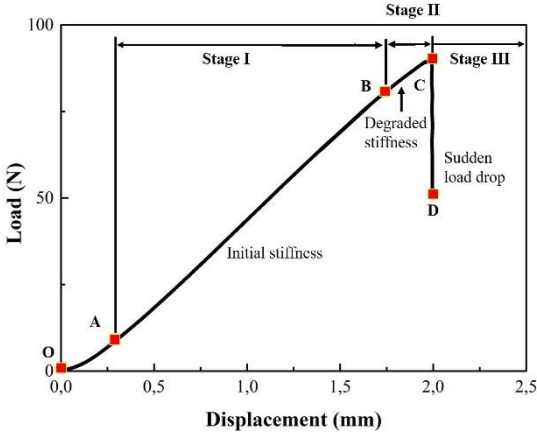


Figure 4-9. Typical load-displacement curve of compression tests

To accurately quantify the compressive performance of different stacking sequences, the average Ultimate Compressive Strength (UCS) is calculated based on the load-displacement curves in **Figure 4-8** for each stacking sequence according to:

$$UCS = P_{max}/A \quad (4-23)$$

Where UCS is the ultimate compressive strength, P_{max} is the maximum force prior to failure and A denotes the initial cross-sectional area.

Table 4-5 shows the average UCS of three QIQH CFRP laminates. The standard deviations are also listed in the table. It is observed that the UCS of QIQH-1 and QIQH-2 are nearly identical, the influence of stacking sequence on their static compressive strength does not seem to be significant. For QIQH-3, since on one surface, the specimens have fibers at 90° , during the tests, the damage introduced by stress concentration at the upper end of the specimens occurred early at this ply, accompanied by the edge-restrained delamination growth. This leads to the final premature fracture of the specimens closer to the upper ends which is not acceptable according to the ASTM D7137/D7137M [231]. As a result, its UCS is much smaller than QIQH-1 and QIQH-2. So, the average UCS of QIQH-1 and QIQH-2 is used to replace the measured value (i.e. 192.66 MPa) for QIQH-3 in following study.

Table 4-5. UCS of compression test specimens

	QIQH-1	QIQH-2	QIQH-3
UCS (average)/MPa	258.88	243.61	192.66*→251.25
Standard deviation/MPa	8.4	5.83	8.61*

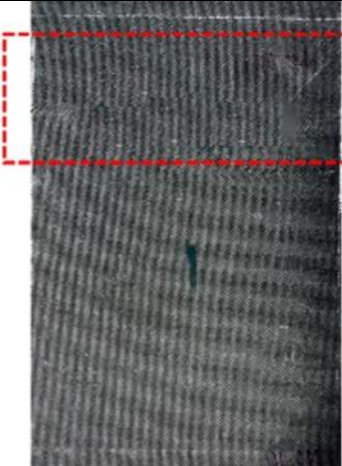
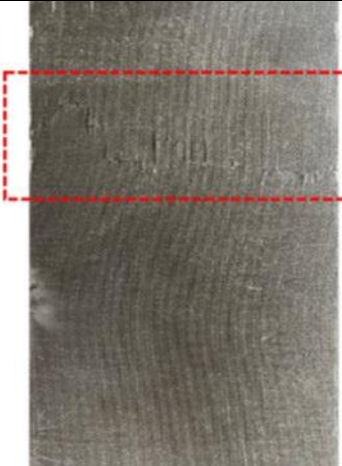
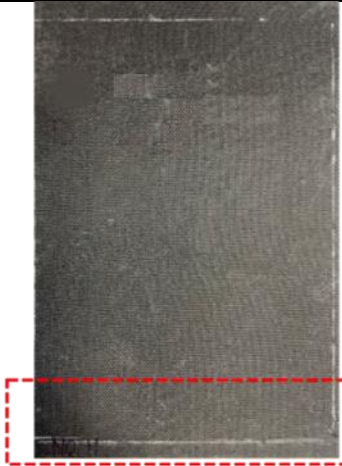

*: the measure value is not used in following studies.

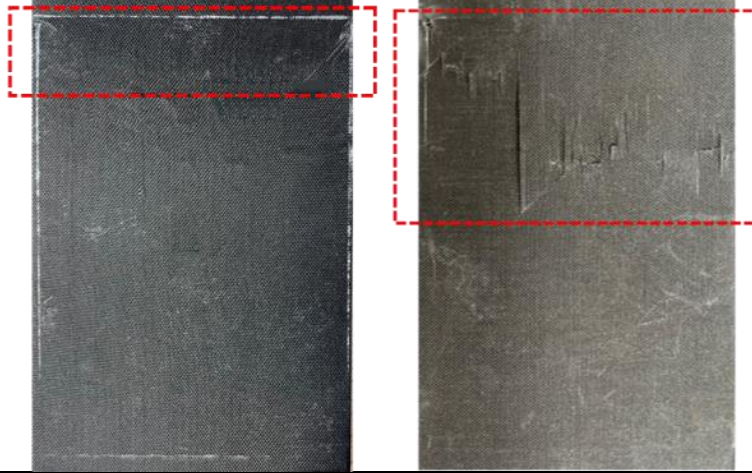
Fracture surfaces

The fracture surfaces of different stacking sequences under compressive loading are shown in **Table 4-6** by visual inspection. The region at which final failure occurred was highlighted by the red rectangle. Here, when the surface having the first ply fiber oriented at 45° or 90° is observed, the sign of 45° is inverted. Among the 8 specimens, it was evident that in specimen QIQH-1-2, damage is initiated only from the top side of the specimen, so that in practice the

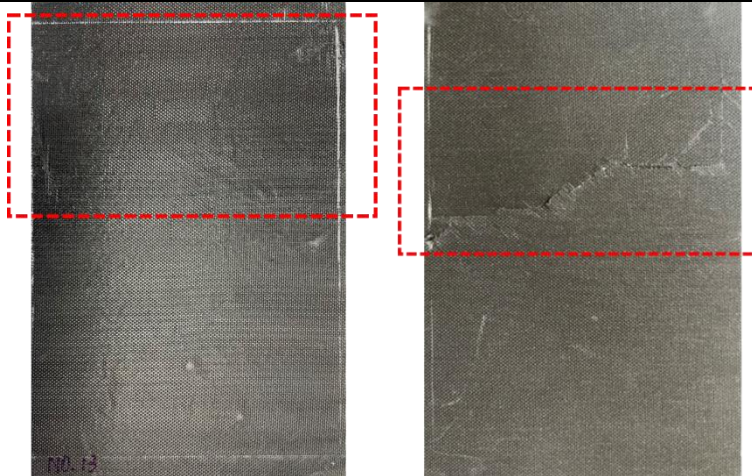
specimen failed by end crushing, which is not acceptable according to the ASTM D7137 standard. The three QIQH-3 specimens failed by edge-restrained delamination growth, which is also not acceptable according to the standard. Apart from these specimens, a good repeatability is observed for each stacking sequence. In general, the cracks on one surface are more visible than another one for each specimen, that could be explained by flexion-buckling direction at the final fracture. At the compression side, the crack propagation should be more developed than that at the tension side. Moreover, the cracking observed on the tensile side is essentially following the fiber orientation of the first ply, while on the compressive side, the cracking observed is not only influenced by the fiber orientation of the first ply on the surface, but also by the fibers on adjacent ply, even by those on sub-adjacent plies.

Table 4-6. Fracture surfaces of specimens under compression loading

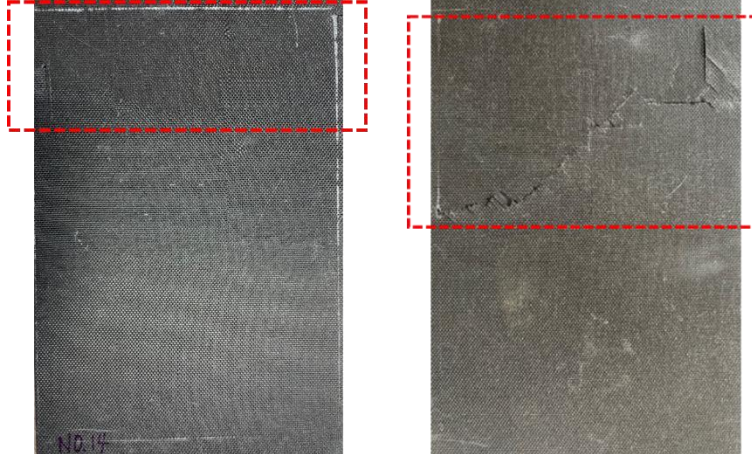
QIQH-1-1 (left: side with first ply fiber oriented in -45° ; right: side with first ply fiber oriented in 0°)	
	
QIQH-1-2 (left: side with first ply fiber oriented in -45° ; right: side with first ply fiber oriented in 0°)	
	
QIQH-1-3 (left: side with first ply fiber oriented in -45° ; right: side with first ply fiber oriented in 0°)	



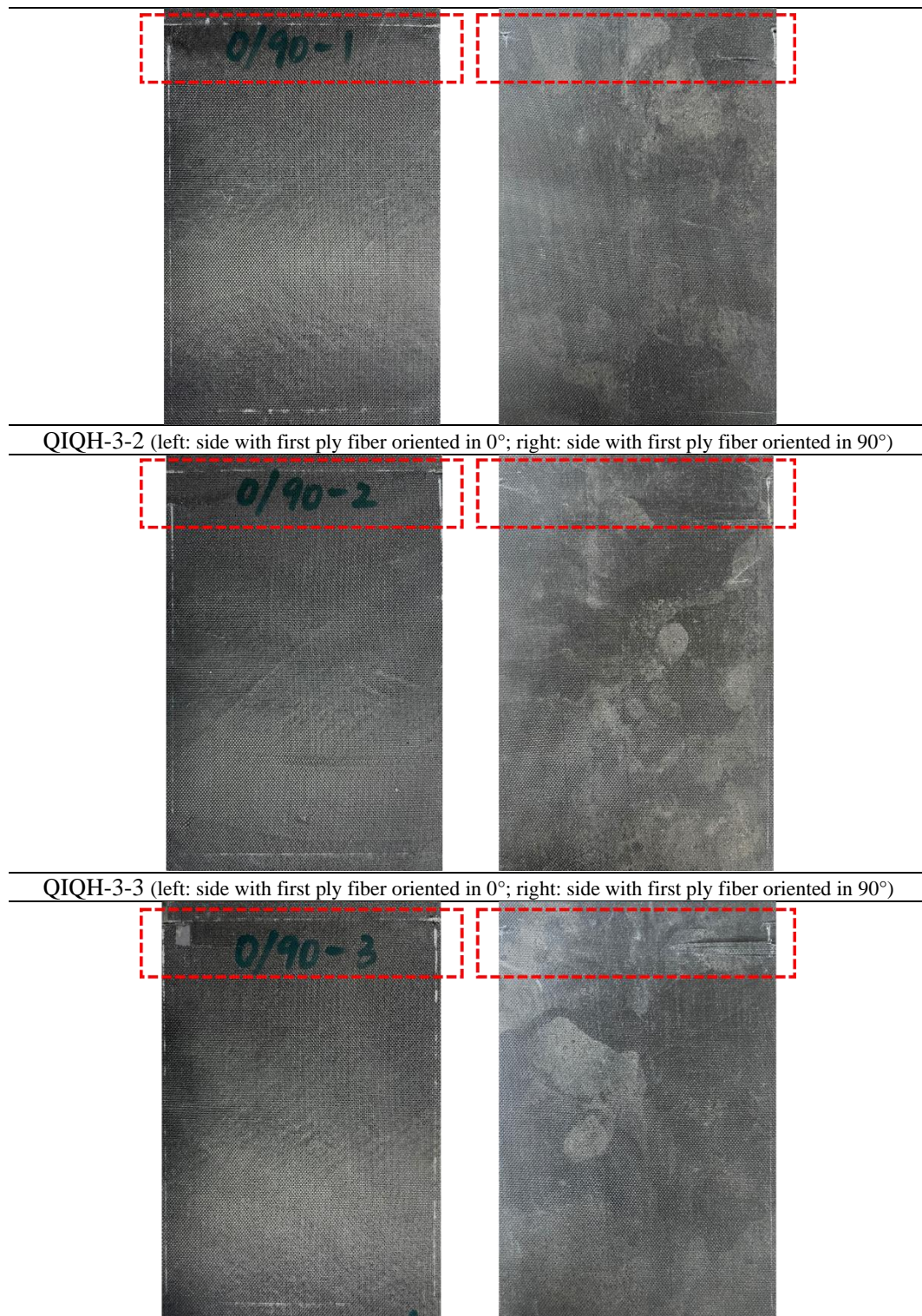
QIQH-2-1 (left: side with first ply fiber oriented in 0° ; right: side with first ply fiber oriented in 45°)



QIQH-2-2 (left: side with first ply fiber oriented in 0° ; right: side with first ply fiber oriented in 45°)



QIQH-3-1 (left: side with first ply fiber oriented in 0° ; right: side with first ply fiber oriented in 90°)



It is interesting to examine in detail the fracture region on the surface with more visible cracks (the compressive side) of QIQH-1 and QIQH-2 in **Figure 4-10**.

As can be seen in **Figure 4-10** (a) for QIQH-1, on the surface of first ply fiber at 0°, a large

number of cracks are orientated along the fiber of the first ply. Besides, the path of crack propagation through the cross section can be guided by 90° plies even by 45° and -45° plies. For QIQH-2, on the side having the first ply fiber at 45°, the path of crack propagation through the cross section follows globally 45° and 90°, but the trace of crack propagation along -45° and 0° can be also identified. As a results, it can be concluded that the cracks on the surface of QIQH is not only influenced by the orientation of the fiber of the surface ply, but also those of the nearby three plies.

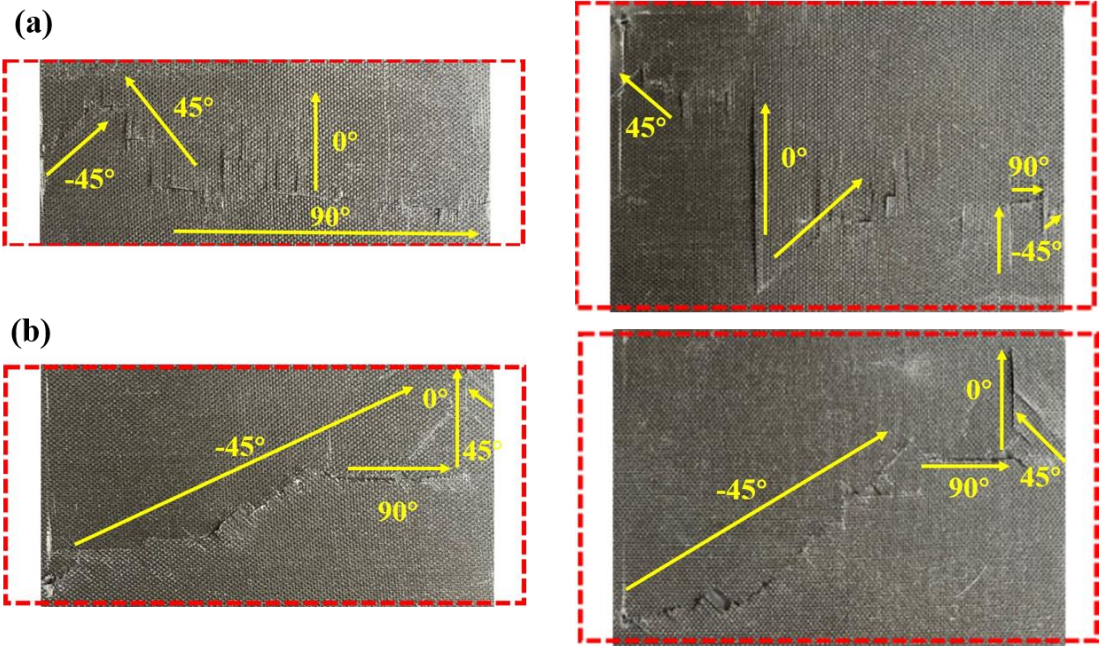


Figure 4-10. Details of fracture surfaces

- (a) QIQH-1 the surface with first ply fibers at 0° (left: QIQH-1-1;right QIQH-1-3);
- (b) QIQH-2 the surface with first ply fibers at 45° (left: QIQH-2-1; right QIQH-2-2)

4.4 Compression-compression fatigue test

4.4.1 Experiments

The compression fatigue tests were conducted at room temperature using Instron servo hydraulic machine (8800) capable of a maximum static or dynamic load of 250kN, as shown in **Figure 4-11**. The tested specimen was fastened by a modified fixture, which is placed between the top and bottom grip. The distance between the two pairs of knife edges on the left

and right sides of the fixture has been modified to be adapted to the width of the specimen, as illustrated in **Figure 4-12**. The compression-compression, load-controlled fatigue tests were performed with a frequency of 5 Hz and stress ratio of $R=10$ on the specimen. Throughout the testing, the specimens were monitored by a FLIR X6800sc Series IR camera. The basic parameters of the camera were already stated in section 2.3.1. Optical FOV conditions were achieved by installing the IR camera at a distance of approximately 1.20m in front of the specimen. The recording rate of temperature data is 520 Hz. 2 specimens were tested for each stacking sequence to ensure the repeatability. Successive steps of cyclic loading at given stress ratio were applied to the specimen. In the first step, fatigue load was set as 30% UCS for a duration of 6000 cycles, which was sufficient to achieve temperature stabilization. In the next steps, fatigue loads increased by 5% UCS up to ultimate failure. After each step, the load has been entirely relaxed for 10 minutes to yield again thermal equilibrium. The average temperature rise $\Delta T = T - T_0$ was measured all along the tests.

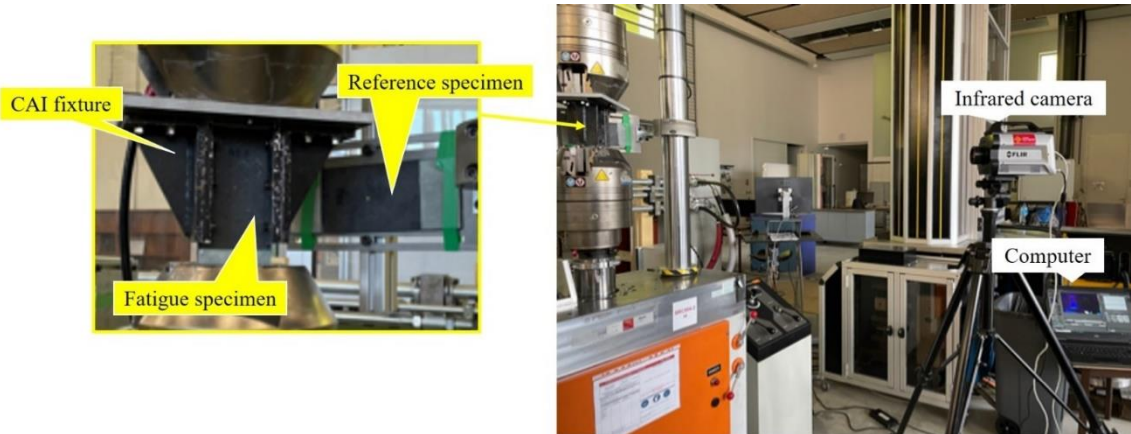


Figure 4-11. Experimental set-up of fatigue and post-impact fatigue tests

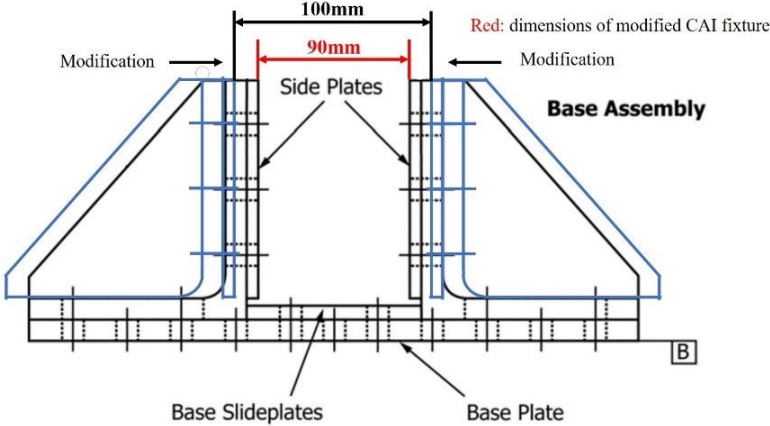


Figure 4-12. Modification of CAI fixture

4.4.2 Determination of the fatigue limit

An example of the plot of average temperature rise obtained using IR camera versus number of cycles of one specimen of QIQH-1 is illustrated in **Figure 4-13**. The maximum stress is illustrated at the end of each curve in the plot. As can be seen in the figure, the temperature profile reached a stabilized plateau at the end of each curve for the maximum stresses from 30 to 85% UCS. **Figure 4-14** (a) shows the stabilized temperature rise as a function of maximum stress, based on which fatigue limit can be determined by using the method proposed in section 2.3. According to the proposed fatigue limit determination method, the normalized angle change θ_i^c is calculated as a function of sequence number of point, as presented in **Figure 4-14** (b). The number of points corresponding to the peak value of normalized angle change θ_i^c is 9, which corresponds to a maximum stress of 70% UCS. Consequently, the fatigue limit and stabilized temperature rise corresponding to the fatigue limit are determined as 70% UCS and 0.893 °C. Using the same method, the determined fatigue limits and corresponding stabilized temperature rise of the other specimens are listed in **Table 4-7**.

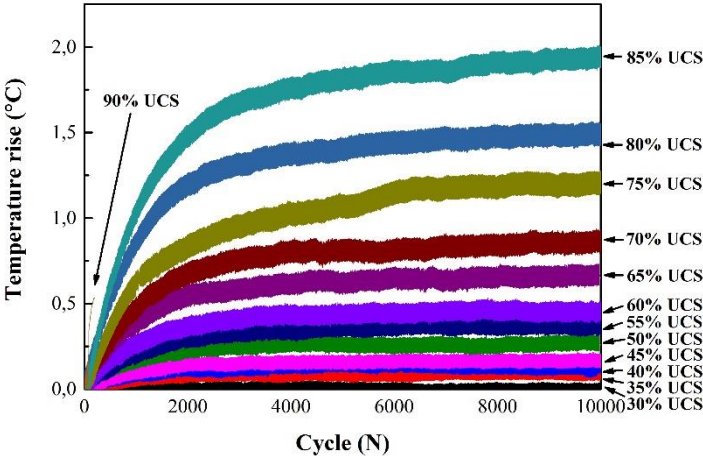


Figure 4-13. Variation of temperature rise vs number of loading cycles

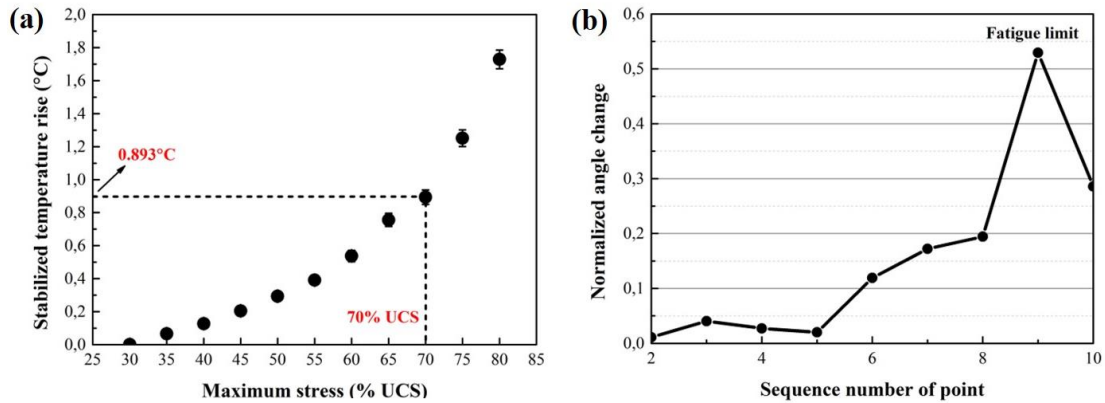


Figure 4-14. Fatigue limit determination of QIQH-1-1: (a) stabilized temperature rise vs maximum stress; (b) loci of normalized angle change vs. sequence number of point

Table 4-7. Fatigue limit of each specimen using proposed method

	Specimen 1		Specimen 2	
	Fatigue limits/ %UCS	$\Delta T_{stab}/^{\circ}\text{C}$	Fatigue limits/ %UCS	$\Delta T_{stab}/^{\circ}\text{C}$
QIQH-1	70	0.893	Problem during experiments	
QIQH-2	70	0.833	65	0.788
QIQH-3	70	0.865	70	0.932

4.4.3 S-N curves

In this section, the method proposed in Chapter 3 is employed to determine the S-N curves of three QIQH laminates. If the fatigue limits of two specimens are identical, the protocol proposed in Chapter 3 could be adopted to determine the more reliable S-N curves. This is the case of QIQH-3. The procedure and calibration details for QIQH-3 are presented step by step as follows:

Step 1: determine the fatigue limit and corresponding stabilized temperature rise based on thermographic data

For each stacking sequence, the determined fatigue limit and corresponding stabilized temperature rise of each specimen are already listed in **Table 4-7**. In particular, QIQH-3 have two specimens with same fatigue limit, so “average process” proposed in Chapter 3 can be

applied. The stabilized temperature rise of each specimen is first normalized with its own maximum value to obtain ΔT_{stab}^* corresponding to each stress level. Then, the average ΔT_{stab}^* of two specimens is calculated to obtain $\overline{\Delta T_{stab}^*}$ corresponding to each stress level. The method proposed in Chapter 2 is adopted to determine the fatigue limit and corresponding normalized stabilized temperature rise ΔT_{stab}^* , whose values are 70% UTS and 0.77, respectively.

Step 2: calibrate the value of p , q and r

The average normalized stiffness degradation is employed to first plot against the number of loading cycles and average normalized stabilized temperature rise. Eq. (3-11) is then adopted to fit the experimental data using MATLAB[®] 3D surface fitting Toolbox. The best fit values of p , q and r are shown in **Table 4-8**.

Step 3: calculate the failure threshold stiffness

Both $k_{fl}(N_{fl} = 10^6 \text{ cycles})$ and $k_{fl}(N_{fl} = 10^7 \text{ cycles})$ were chosen for the calculation of failure threshold stiffness according to Eq. (3-11). The determined values are also listed in **Table 4-8**.

Table 4-8. Determined parameters for different stacking sequences

	p	q	r	$k_f(N_{fl} = 10^6 \text{ cycles})$	$k_f(N_{fl} = 10^7 \text{ cycles})$
QIQH-1-1	0.11	27.17	0.590	0.890	0.881
QIQH-2-1	4.618×10^{-2}	24.73	0.602	0.946	0.940
QIQH-2-2	0.11	29.52	0.567	0.858	0.846
QIQH-3-1	3.18×10^{-2}	22.76	0.602	0.945	0.939
QIQH-3-2	6.06×10^{-2}	21.14	1.431	0.907	0.896
Average of QIQH-3	4.94×10^{-2}	21.70	1.025	0.929	0.921

Step 4: prediction of S-N curve

A plot of determined fatigue life calculated using modified model is shown in **Figure 4-15**.

The same process can be applied to each specimen without “average process” in step 1. That means the ΔT_{stab}^* should be used instead of $\overline{\Delta T_{stab}^*}$. The obtained parameters are also listed in **Table 4-8**. The S-N curves obtained for each specimen are also presented in **Figure 4-15**.

As can be seen from the **Figure 4-15 (a)**, for QIQH-2, the S-N curves of two specimens seems to be parallel. For QIQH-3 (**Figure 4-15 (c)**), the determined S-N curves of two specimens are close to each other. The more reliable S-N curves are a little more conservative compared to the individual S-N curves of each specimen.

Figure 4-16 compares the S-N curves of specimens with identical fatigue limits. It can be seen that there is little difference between the S-N curves of three different stacking sequences. The influence of stacking sequence on the S-N curve does not seem significant. Therefore, the results from all specimens can be considered as the same population to obtain only one “average” S-N curve by “average process” proposed in chapter 3.

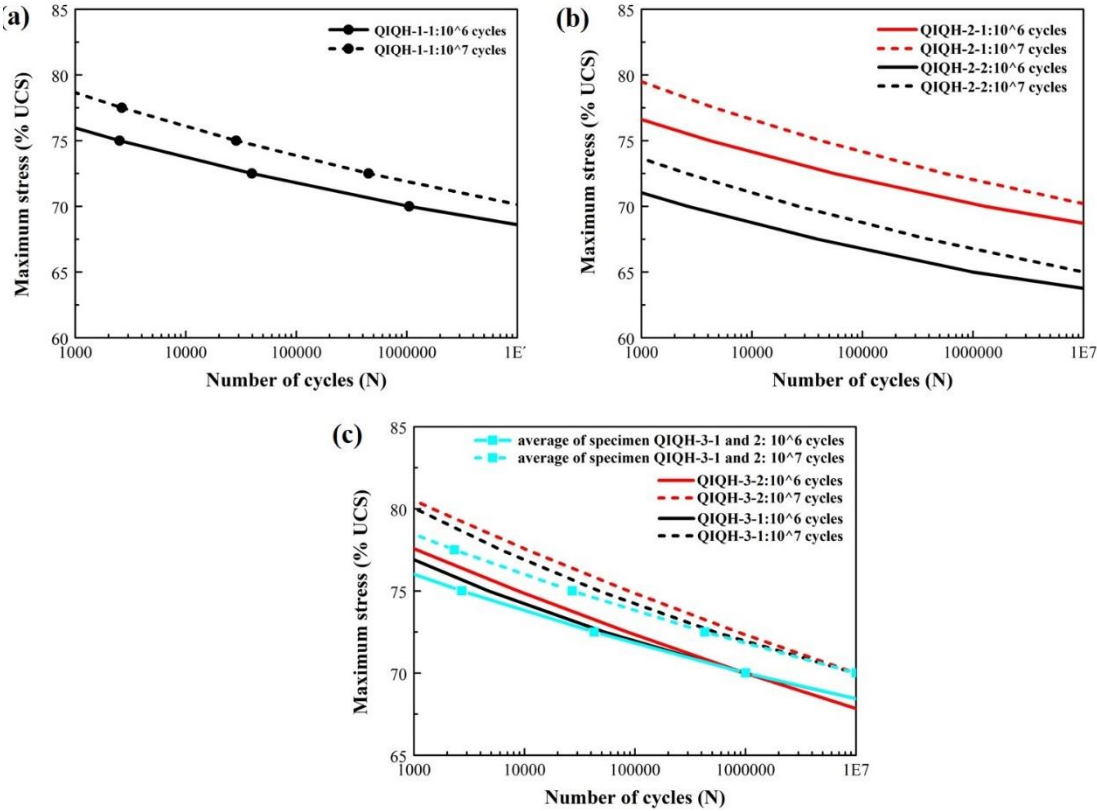


Figure 4-15. Determined fatigue lives for three QIQH stacking sequences:

(a) QIQH-1; (b) QIQH-2; (c) QIQH-3

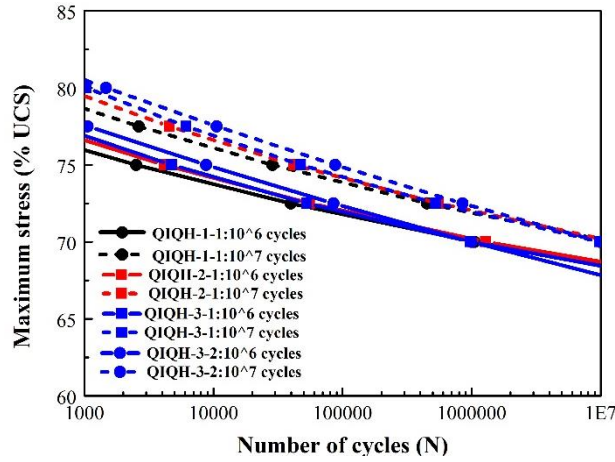


Figure 4-16. S-N curves of specimens with identical fatigue limits but different stacking sequences

4.4.4 Determination of a more overall average reliable S-N curve

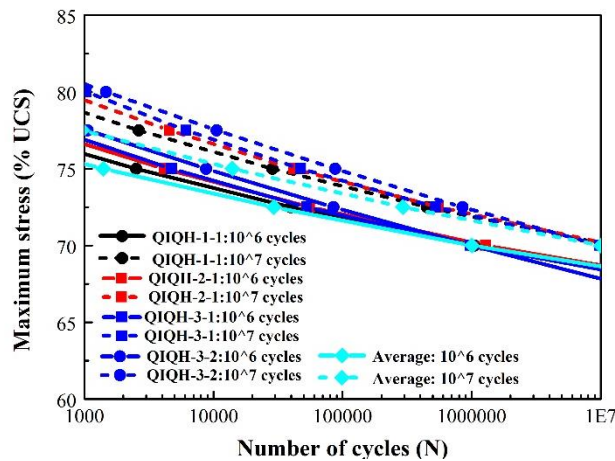
Among the six specimens, since the fatigue limits of 4 specimens in **Figure 4-16** are identical, which satisfies the condition of protocol proposed in section 3.3. It is possible to determine a single more reliable S-N curve for these three stacking sequences utilizing the data of four specimens by “average process”.

In the step 1, the average normalized stabilized temperature rise $\overline{\Delta T_{stab}^*}$ of four specimens is first calculated as a function of maximum stress. The fatigue limit determination method proposed in chapter 2 is adopted. The determined fatigue limit and corresponding normalized stabilized temperature rise are depicted in **Table 4-9**. In the step 2, 3D surface fitting in MATLAB[®] is employed to fit the average normalized stiffness degradation as a function of average stabilized temperature rise $\overline{\Delta T_{stab}^*}$ and number of cycles. The obtained values of p , q and r and coefficients of determination R^2 are also listed in **Table 4-9**. In the step 3, the failure threshold stiffness corresponding to $N_{fl} = 10^6$ and 10^7 cycles are calculated based on Eq. (3-11). The obtained values are listed in **Table 4-9**. Finally, in step 4, the obtained S-N curves based on the ‘average’ of four specimens and the individual S-N curves of each specimen are depicted in **Figure 4-17**.

Table 4-9. Fatigue limit and calibration parameters

Parameters	'average' values
Fatigue limit	70 % UTS
$\Delta T_{stab_fl}^*$	0.62
p	0.66
q	24.41
r	0.90
$k_f(N_{fl} = 10^6 \text{ cycles})$	0.924
$k_f(N_{fl} = 10^7 \text{ cycles})$	0.917
R^2	0.98

As can be seen from the figure, the 'average' S-N curves corresponding to both $N_{fl} = 10^6$ cycles and $N_{fl} = 10^7$ cycles are little lower than the individual S-N curves. Compared to the individual predicted S-N curves of these 4 specimens, the average S-N curves are more conservative.

**Figure 4-17.** Individual predicted S-N curves and more reliable S-N curves for QIQH laminates

4.4.5 Damage morphology

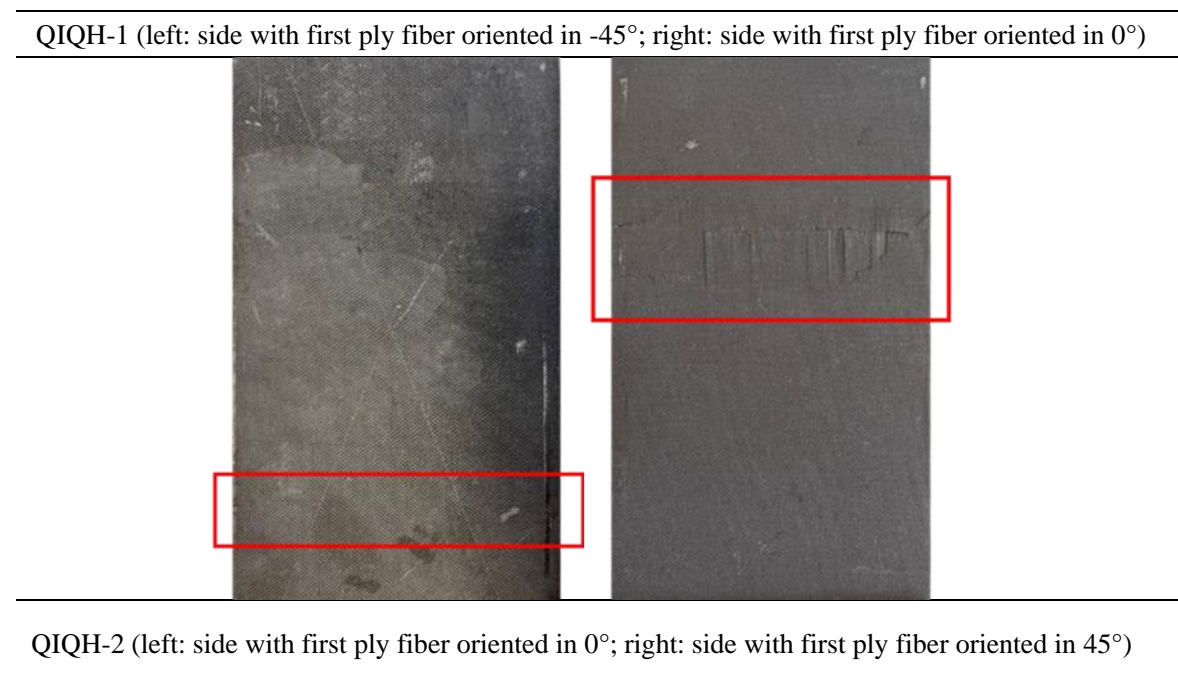
After the compression fatigue tests, the fracture surfaces of the specimens were examined visually and microscopically. Microscopic examination did not provide any extra information to that already observed by visual analysis. Therefore, only damage morphology of failed specimens observed by visual inspection (tabs excluded) is shown here, in **Table 4-9**. A good repeatability is observed for each stacking sequence, therefore, only one specimen is taken as an example here. The region at which final failure occurred was highlighted by the red

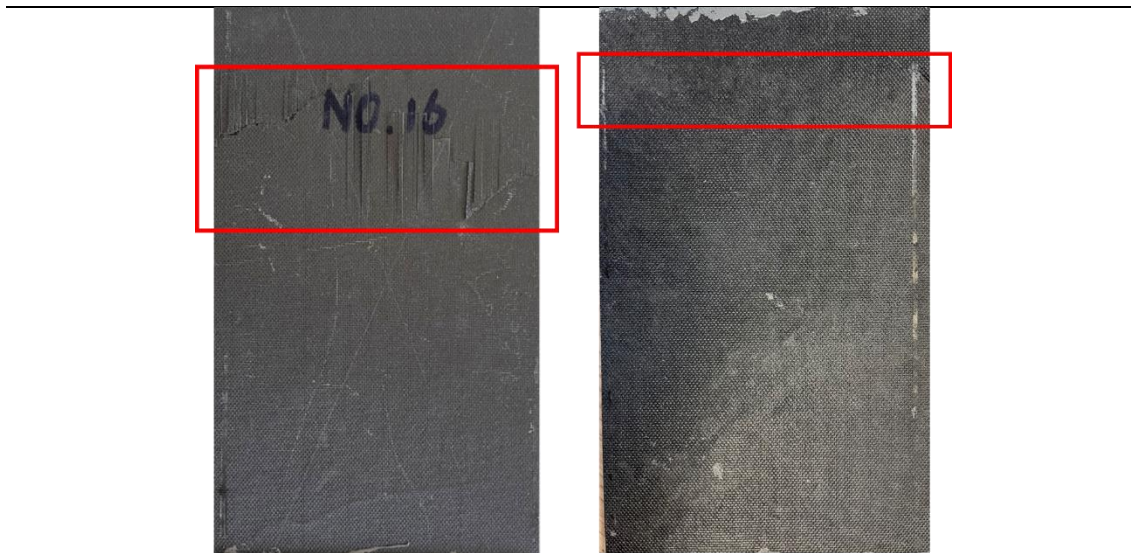
rectangle.

It is interesting to note that for all specimens, much more cracks are observed on the surface with first ply fiber oriented in 0° . In the other fracture surfaces, only short cracks oriented as the fiber direction of the first ply are observed near the edges of the specimens. It seems that the first ply fibers in 0° promote local buckling under fatigue compressive loading and this surface should be compressive side at final fracture caused by buckling-flexion.

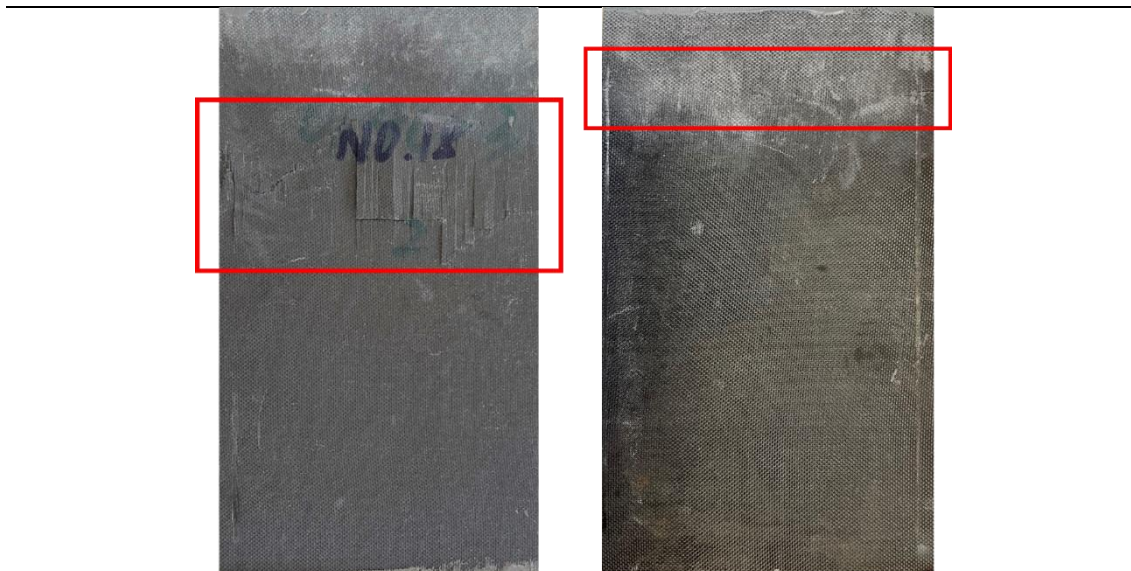
If we compare the fracture surfaces with the first ply fibers at 0° of three configurations, as can be seen in **Figure 4-18**, all the specimens have a large number of cracks orientated along the fiber 0° at the first ply, their length is less longer in QIQH-1. But these 0° cracks have been much more developed than those under static loading. Besides, the path of crack propagation through the cross section can be guided by 90° plies even by 45° and -45° plies. However, the cracking at $\pm 45^\circ$ are located principally at the edges of the specimens whatever the stacking sequence of the laminates tested.

Table 4-10. Damage morphology of compression fatigue specimens





QIQH-3 (left: side with first ply fiber oriented in 0° ; right: side with first ply fiber oriented in 90°)



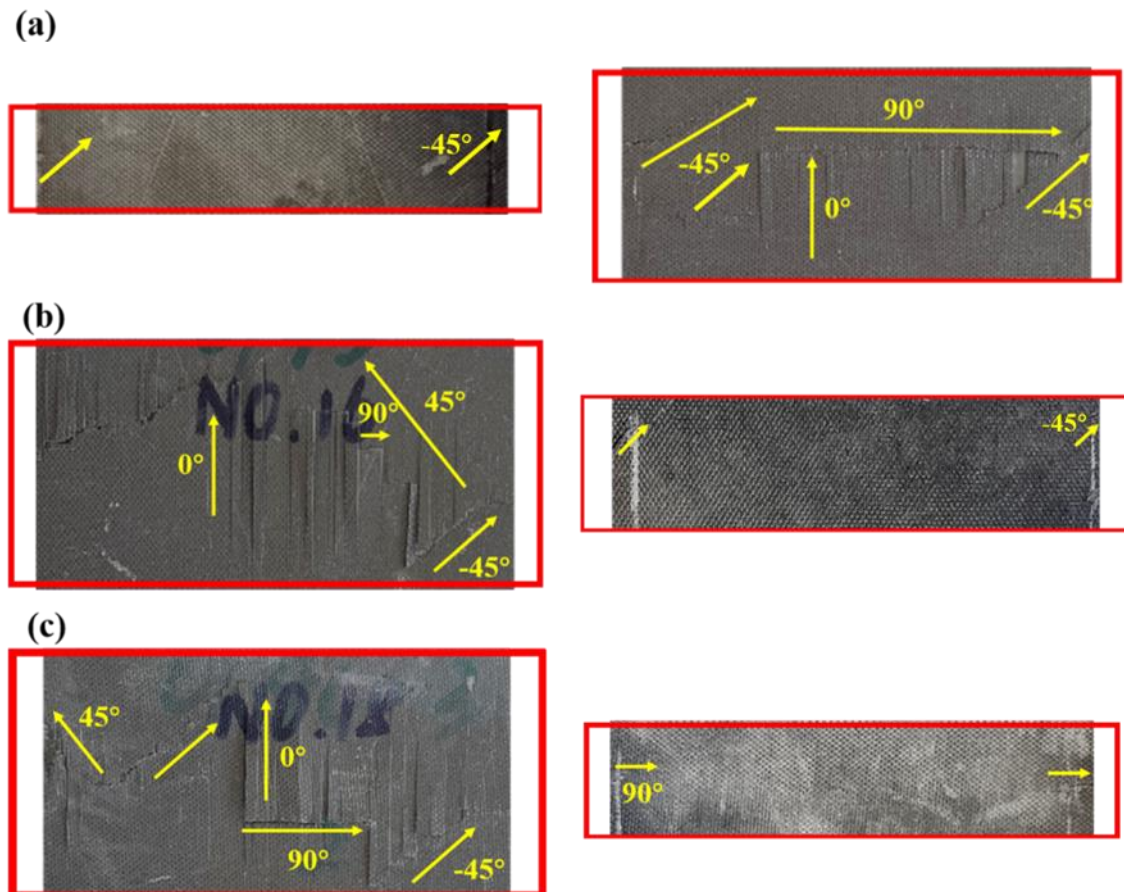


Figure 4-18. Fracture surfaces of compression fatigue specimens:

(a) QIQH-1 (left: first ply fibers at -45° ; right: 0°); (b) QIQH-2 (left: first ply fibers at 0° ; right: 45°); (c) QIQH-3 (left: first ply fibers at 0° ; right: 90°)

4.5 Chapter summary

In this chapter, static compression and compression-compression fatigue tests monitored by infrared camera have been conducted on three CFRP QIQH laminates, which are uncoupled and isotropic with identical bending and membrane elastic properties. The results of static compression tests indicate that the load-displacement curves of QIQH-1 and QIQH-2 are found to be similar with a good repeatability. The values of UCS, as well as the initial stiffness, are closed to each other. For QIQH-3 laminates, the load-displacement curves of QIQH-3 give the stiffness and strength much smaller compared to those of QIQH-1 and QIQH-2. In fact, due to their one surface ply fiber at 90° , it is difficult, by using our experimental fixture, to obtain valid values of UCS and their initial stiffness. The

observation of the fracture surfaces shows that the cracks observed on the tensile side under final buckling-flexion fracture is mainly influence by the fiber orientation of the first ply, while on the compressive side, the cracking path can be influenced by the fiber orientation of the first four plies.

Whereafter, the QIQH specimens were tested under compression-compression fatigue loading. The fatigue limit determination method and the modified fatigue life model proposed in Chapter 2 and 3 have been applied to the experimental data of these QIQH laminates. It is demonstrated that the difference between three configurations of laminates in global fatigues proprieties is not significant, even though the local damage process should be different. The fatigue limit determined for each specimen is 70% UCS except for one specimen. Concerning fatigue life determined for each specimen in terms of S-N curve, the difference does not seem significant. Therefore, an “average” S-N curve has been obtained by using protocol proposed in section 3.3 based on the data of 4 specimens with three different stacking sequences. This overall average S-N curve is found more conservative than the individual curves of these specimens. The observation of facture surfaces of compression fatigue specimens shows that for all specimens, much more cracks are observed on the surface with first ply fiber oriented in 0° . In the other fracture surfaces, only short cracks oriented as the fiber direction of the first ply are observed near the edges of the specimens. The first ply fibers à 0° seems to promote local bucking under compressive fatigue loading, this surface should be compressive side at final fracture caused by buckling-flexion. Moreover, all the specimens have a large number of cracks orientated along the fiber 0° at the first ply, whose lengths are less longer in QIQH-1. But these 0° cracks have been much more developed than those under static loading. Besides, the path of crack propagation through the cross section can be guided by 90° plies even by 45° and -45° plies. However, the cracking at $\pm 45^\circ$ are located principally at the edges of the specimens whatever the stacking sequence of the laminates tested.

Chapter 5 Post-impact compression fatigue behavior

The mechanical properties of composite materials can be significantly reduced by the impact. The Compression After Impact (CAI) properties, in particular, can be seriously degraded even if the impact damages are not detectable by the naked eyes. The objective of this section is to investigate the impact, CAI and post-impact compression fatigue behavior of QIQH laminates. The proposed method for fatigue limit determination and the modified fatigue life model, described in chapter 2 and chapter 3, will be applied to post-impact compression fatigue experimental data of QIQH laminates to validate the generality of both methods.

5.1 Impact tests

5.1.1 Materials and specimens

The material used for the preparation of specimens in this chapter is the same as that stated in Chapter 4. Still, the stacking sequences of the specimens are the same as that stated in section 4.2.1. The dimensions of specimens used for the CAI tests were L150×W100 mm, with thickness of 3.65 mm, according to the standard ASTM D7136 [231]. While for the post-impact compression fatigue specimens, no standards are available. As previously described, standard ASTM D7136 [231] suggests the use of L150×W100 mm specimens with thickness close to 4mm for the impact tests while in the fatigue test standard ASTM D3479 [187], the use of tensile specimens with dimensions of L250×W25 mm (useful area of L150×W25 mm) is recommended. In order to meet both standards, the width of the post-impact compression fatigue specimens is kept the same as that of impact test specimens, while the length is equal to that of tension fatigue specimens, as illustrated in **Figure 5-1**. As shown in **Figure 5-2**, the dimensions of CAI specimens were perfectly suited for the fixture of impact tower. Nevertheless, the width of the fatigue and post-impact fatigue specimens must be decreased to 90mm to be adapted to the fixture.

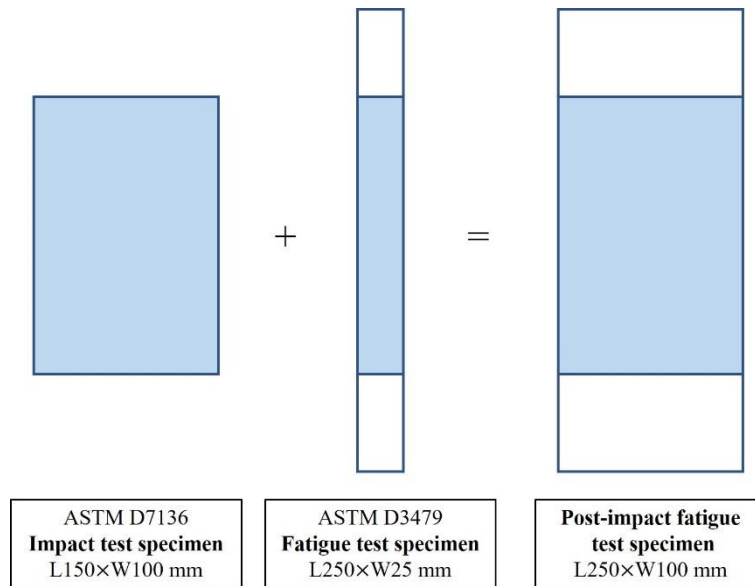


Figure 5-1. Theoretical dimensions of post-impact fatigue test specimens [243]

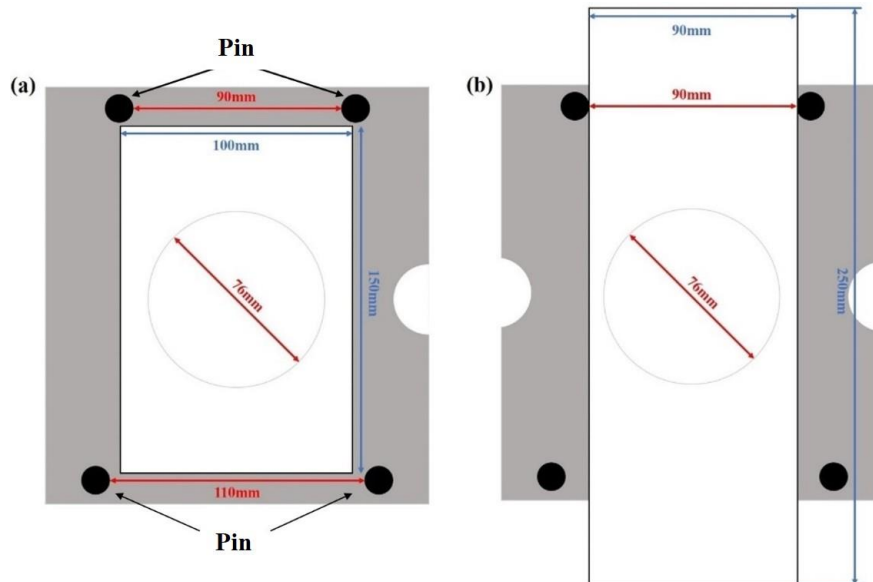


Figure 5-2. Schematic illustration of adaptation of specimens to fixture of impact tower: (a) specimens with dimensions of L150×W100 mm; (b) L250×W90 mm

5.1.2 Preliminary impact tests

Preliminary impact tests were conducted to determine the energy needed to generate Barely Visible Impact Damage (BVID, indentation depth $\leq 0.3 \text{ mm}$) with a delamination area suitable for the CAI/post-impact fatigue test (width of the damaged area should be lower than 42 % of the width of the sample). The stacking sequence of the specimens is those of QIQH-2 ([0/45/90/-45/90/-45/45/-45/0/90/0/45/0/45/-45/45/90/0/90/-45/90/-45/0/45]). Two specimens

with dimensions of L150×W100×Thickness 3.65 mm were tested to ensure the repeatability of test results. The energy chosen for the preliminary impact tests is 15 J. The details of the test procedure are described in section 4.1.2. The impacted surface is defined as impact front surface or side and another side as back surface or side. After impact tests, projected delamination area was observed on the back side around the impact point of the tested specimens by ultrasonic C-scan. Specimens were then cut off at the middle of indentation by manual circular saw. As reported by Ramulu [241], the QIQH stacking sequence eliminated membrane-bending coupling, which brings about less chance of delamination and debonding during the cutting process and therefore, observation of the cut section is not disturbed by artefacts due to cutting process. Both cut-sections were observed by optical microscope (VHX-7000, Keyence Corporation) to measure the indentation depth on each side.

Figure 5-3 shows the C-scan images of preliminary impact test specimens observed on the back sides. A good repeatability is observed in the test results. The projected delamination area is assumed as quasi-circular shape. The diameter of projected delamination area is around 75.25 (± 0.35) mm for both specimens, that is nearly the same dimension as that of impact window (76 mm). According to the standard ASTM D7137/7137M [240], it is recommended that the damage size should be limited to 42 mm to minimize interaction between damages and edge-related stress-strain field in the subsequent CAI tests. In consideration of the two criterions, the impact energy chosen for the preliminary tests appears to be too high.

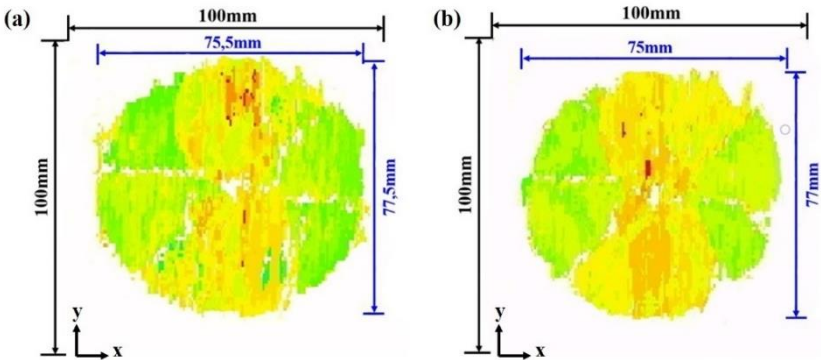


Figure 5-3. C-scan images of preliminary impact test specimens: (a) specimen 1; (b) specimen 2

Two cut sections (**Figure 5-4**) were defined along the loading direction, which is the vertical direction (y-direction) in the ultrasonic scanning images shown in **Figure 5-3**. **Figure 5-5** shows these cut-sectional photographs of preliminary impact test specimens. The indentation was first observed at relatively low magnification ($\times 20$) to determine the edge and center of indentation, which were then both marked with a pen. Afterwards, at higher magnification ($\times 100$ times), the thickness of the specimen is measured at two different places: the site without impact damage $d_{[1]}$ and impacted site $d_{[2]}$. The value of $d_{[1]}$ was measured at 3 different places without impact damage to define the reference plane used to measure the maximum indentation depth. The value indicated in **Figure 5-5** was the average of measured values. The indentation depth on each cut section (side 1 and site 2) can be then obtained by the difference between the two thicknesses $d_i = d_{i,[1]} - d_{i,[2]}$ ($i=1$ or 2). However, the indentation depth measured on two cut-sections is actually not the real indentation depth, because the thickness of circular saw ($e = 2mm$) has also to be taken into account. Therefore, in the following part, the procedure to calculate the real indentation depth is presented.

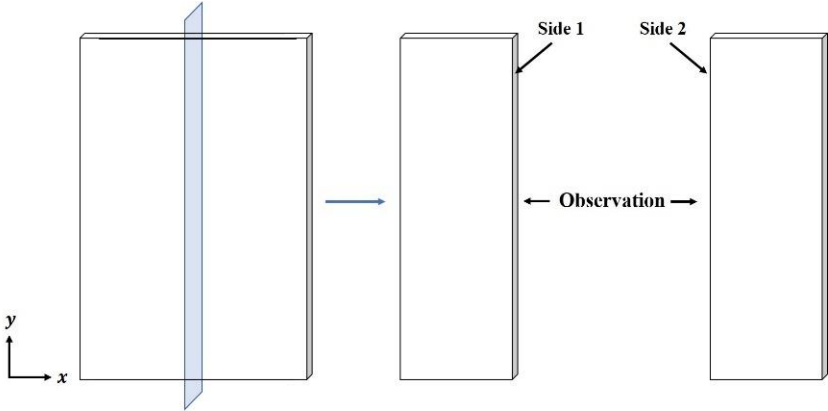


Figure 5-4. Observation of cut-sections of laminates defined as Side 1 and Side 2

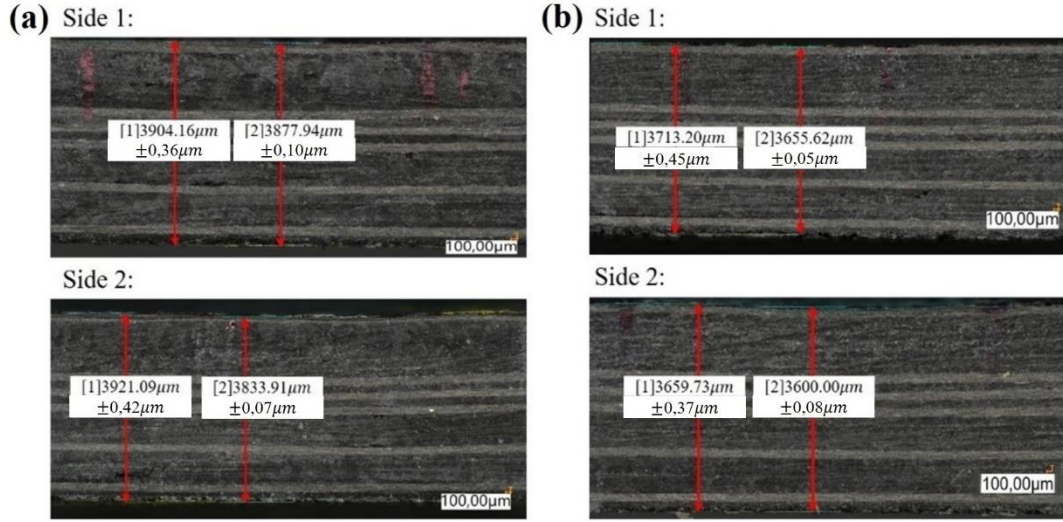


Figure 5-5. Cut-sectional photographs of preliminary impact test specimens:

(a) specimen 1; (b) specimen 2

Figure 5-6 illustrates the front view of indentator at the front surface of specimen. In this figure, FH (d_1) and EG (d_2) denote the indentation depth measured by two cut-sections. The indentation is assumed to be in a circular shape and its diameter is R_1 . The real indentation depth could be calculated according to:

$$d = ID = AD - AI = AD - \sqrt{AC^2 - CI^2} = 10 - \sqrt{10^2 - R_1^2} \quad (5-1)$$

Supposing the distance between the cross-section of side 1 and the center line of indentator (AD) is x . The expressions for the two indentation depths d_1 and d_2 are:

$$d_1 = FH = IJ = AJ - AI \rightarrow d1 = \sqrt{10^2 - x^2} - \sqrt{10^2 - R_1^2} \quad (5-2)$$

$$d_2 = EG = IK = AK - AI \rightarrow d2 = \sqrt{10^2 - (2 - x)^2} - \sqrt{10^2 - R_1^2} \quad (5-3)$$

Subtracting Eq. (5-2) from Eq. (5-3), the common term $\sqrt{10^2 - R_1^2}$ on the right side of the equations is eliminated:

$$d_1 - d_2 = \sqrt{10^2 - x^2} - \sqrt{10^2 - (2 - x)^2} \quad (5-4)$$

The right side of Eq. (5-4) is only a function of x . Since the values of d_1 and d_2 are already known, by solving the Eq. (5-4), the value of x could be determined.

By taking the value of x into Eq. (5-2) or Eq. (5-3), the value of R_1 could also be computed.

The value of real indentation depth d can then be obtained.

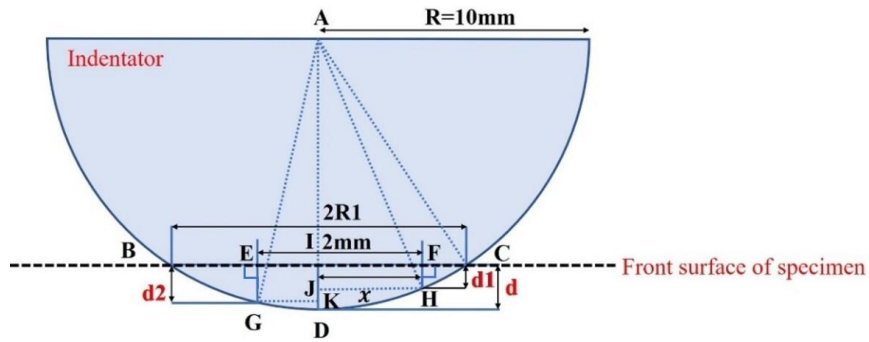


Figure 5-6. Schematic diagram of indentor at the front surface of specimen (front view)

The real indentation depth calculated based on the above procedure is 0.109 mm and 0.111 mm for the two preliminary impact test specimens. Both values are inferior to 0.3 mm, which implies the impact damage created is lower than a BVID. According to Ref. [242], the indentation depth increases with the increasing of impact energy. Therefore, for the impact energy below 15 J, the damages will also be definitely inferior to BVID.

In the subsequent tests, two impact energies below 15 J were chosen for the tests: 5 and 10 J. After the impact tests, the diameters of projected delamination area observed from the back sides are 28.5 mm and 50 mm for the impact energy of 5 J and 10 J, respectively. The delamination area under impact energy of 10 J still does not meet the condition imposed by standard ASTM D7137/7137M [240]: “the width of the damaged area should be lower than 42% of the width of the sample”. Consequently, impact energy of 5 J is chosen for the following impact tests.

5.1.3 Experiments

The low-velocity impact tests have been conducted with the drop weight impact tower Instron Dynatup 9250HV, as presented in **Figure 5-7**. The impactor has a stainless steel hemispherical impact head, with a diameter of 20.0 mm and a mass of 4.97 kg. The rectangular specimens were clamped on all four edges using a steel plate. A circular cutout of 76 mm in diameter is left for impact window (**Figure 5-7**). The impact energy used for the whole tests was 5 J (**Table 5-1**). The impactor was dropped on the geometric center of the specimen and was captured by an anti-rebound system to avoid secondary impact. Relative to the length of

the specimen (y direction in **Figure 5-8**) the fiber orientation of the first ply on impacted front surface is -45° and that of back side is 0° for QIQH-1, while for QIQH-2 and QIQH-3 specimens, the first ply fiber orientation of impacted front surface is both 0° , but that at back side is 45° and 90° , respectively. For each stacking sequence, impact tests were performed on at least three specimens to take into account of the dispersion and ensure the repeatability of the results. The force acting on the impactor's head and the displacement of the head were measured by the sensor of the impactor.

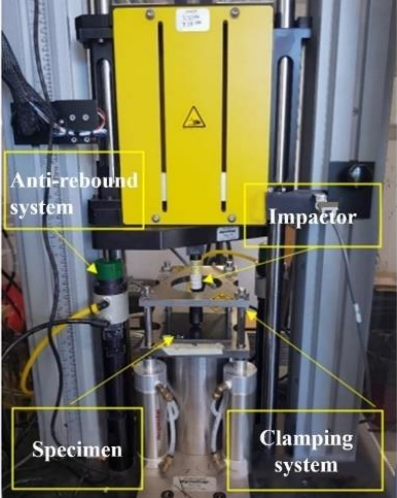


Figure 5-7. Impact testing instrument

Table 5-1. Impact testing conditions

Dimensions/mm	Number of specimens	Drop mass/kg	Impact energy/J	Drop height/cm	Impact velocity/ $m \cdot s^{-1}$
150*100	3	4.97	5	10.26	1.418
250*90	4				

All the specimens were examined using the Omniscan MX C-scan ultrasonic inspection system, manufactured by Olympus Inc.. The experimental set-up is displayed in **Figure 5-8**. The inspection was performed prior to impact to access the structural integrity of specimen, and after impact and after 48 h relaxation to monitor the induced delamination, which is one of the main impact damage modes. The specimens were immersed in the water to achieve ultrasonic coupling and scanned by an ultrasonic emitter-receiver transducer in the in-plane x-y direction. The scanning was carried out along both the front and back surfaces.

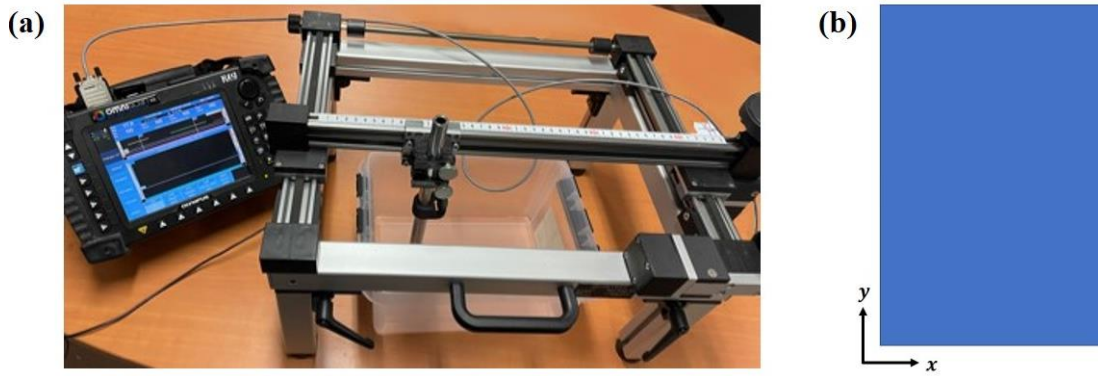


Figure 5-8 C-scan inspection: (a) experimental set-up; (b) scanning directions

5.1.4 Results and discussion

Force-time curve

The original force-time curve of QIQH-1-3 with dimensions of 150×100 mm is presented in **Figure 5-9** as an example. Initially between approximately 1 s and 2.5 s, the force-time curve revealed strong high-frequency oscillations as the load approached the maximum value. This is due to impact waves generated during contact and propagating until attenuation, which perturbs the indication of load history associated with the damage initiation and propagation. Therefore, a Fast Fourier Transform (FFT) filter with a window size of 50 data points is adopted to filter the load data. This window size is chosen as it can effectively filter the signal while preserving the mean value of the signal.

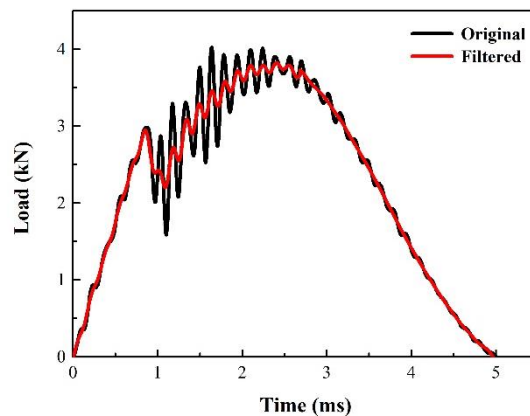


Figure 5-9. Raw and filtered force-time curve of QIQH-1-3 with dimensions of 150*100mm

The filtered force-time curves of three configurations are plotted in **Figure 5-10**, **Figure 5-11** and **Figure 5-12**. A good repeatability can be seen for each series of the tests. Moreover, the

effect of specimen dimensions on impact behavior does not seem to be significant. As illustrated in the figures, consistent force-time history is observed for all laminates. At the start of loading, there is a linear increase of force with time indicating the purely elastic response of the specimens. When the force reaches the characteristic impact force F_H , the first load drops occur due to Hertzian failure [244][245], as shown in **Figure 5-10**. In the Hertzian contact law, the contact force when a rigid sphere pressed into an elastic isotropic half space is given as [246]:

$$F = k\alpha^{3/2} \quad (5-5)$$

Where F is the contact force, α is the indentation depth and k is the rigidity associated with deformation, expressed by:

$$k = \frac{4}{3} \frac{R_s^{1/2}}{\left(\frac{1 - \nu_s^2}{E_s} + \frac{1 - \nu_b^2}{E_b}\right)} \quad (5-6)$$

Where R_s is the radius of the sphere; ν_s , E_s and ν_b , E_b are the Poisson's ratio and Young's modulus of the sphere and half space, respectively. The Hertzian law which was based on linear elasticity is also valid for rigid sphere. When the contact force surpassed F_H , the relationship between the contact force and deformation does not conform to the Hertzian contact law, the Hertzian failure occurs. A Hertzian failure is the main source of initial damage that generally develops in the form of delamination and matrix cracking [247]-[250].

When the impact force further increased, fluctuations were observed, which indicates the generation of impact waves during contact. After the peak point was reached, the force has a monotonical decrease with the increasing of time, which corresponds to the release of elastic energy. The mean value of characteristic impact force and peak force of each configuration with two different dimensions are listed in **Table 5-2**. It can be seen that the characteristic impact force and peak force of different configurations are similar to each other, which is expected since these stacking sequences give QIQH laminate with identical stiffness matrix **A**, **B**, **D** and the impact window is circular, which results in axisymmetric loading.

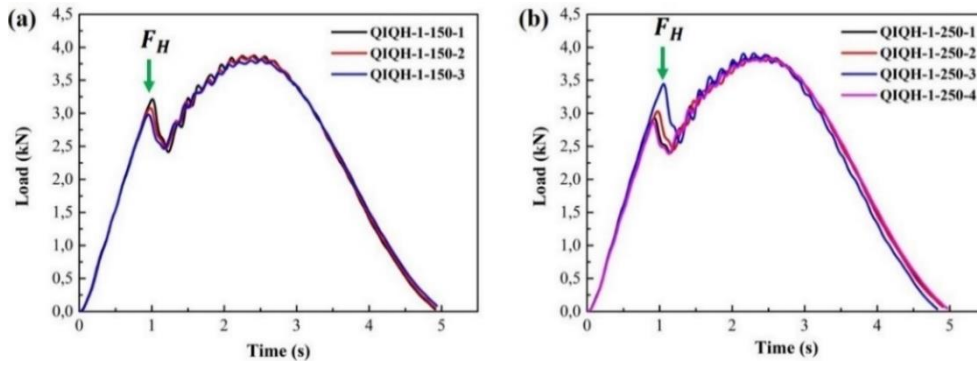


Figure 5-10. Load-time curves for QIQH-1: (a) 150×100mm; (b) 250×90mm

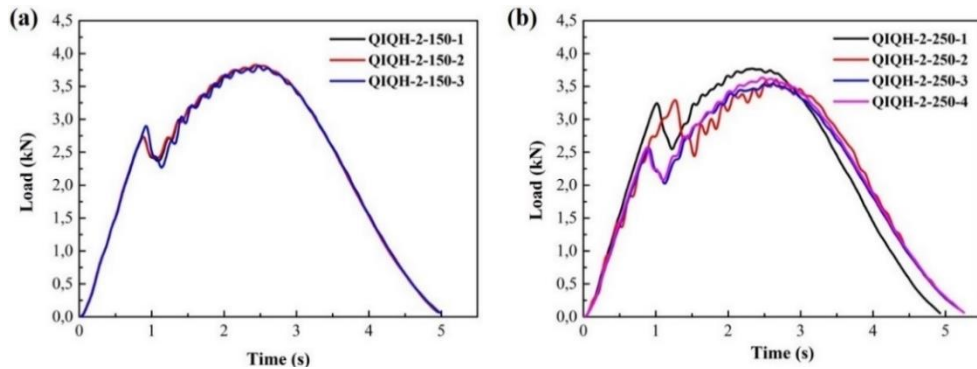


Figure 5-11. Load-time curves for QIQH-2: (a) 150×100mm; (b) 250×90mm

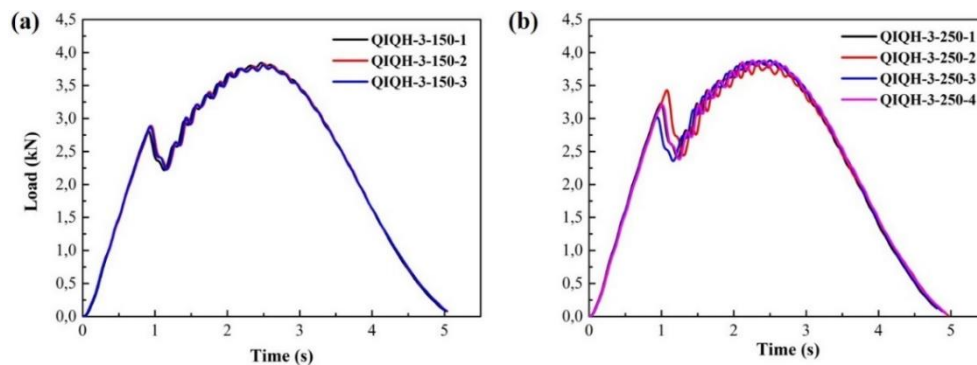


Figure 5-12. Load-time curves for QIQH-3: (a) 150×100mm; (b) 250×90mm

Load-displacement curve

Typical filtered load-displacement plots corresponding to each configuration are illustrated in **Figure 5-13**, **Figure 5-14** and **Figure 5-15**. The entire force-displacement plots of all the specimens were quite identical, which means that the stacking sequence does not influence their impact behavior if they are QIQH.

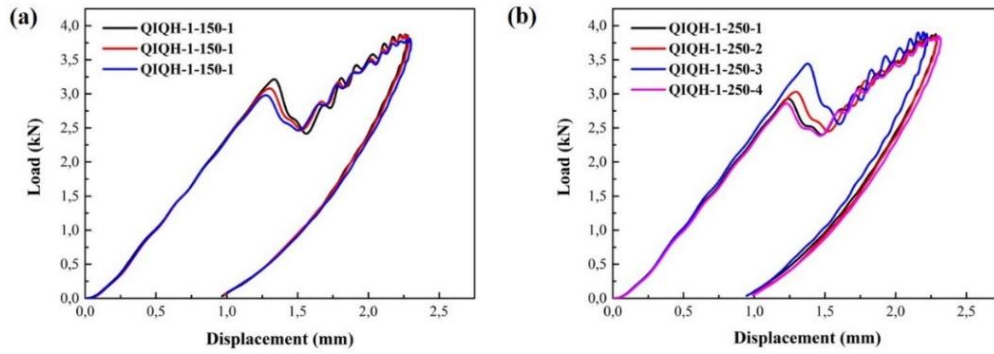


Figure 5-13. Load-displacement curve for QIQH-1: (a) 150×100mm; (b) 250×90mm

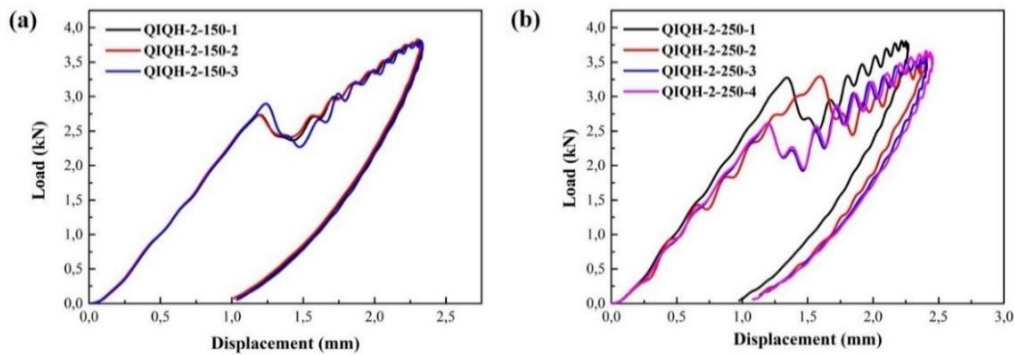


Figure 5-14. Load-displacement curve for QIQH-2: (a) 150×100mm; (b) 250×90mm

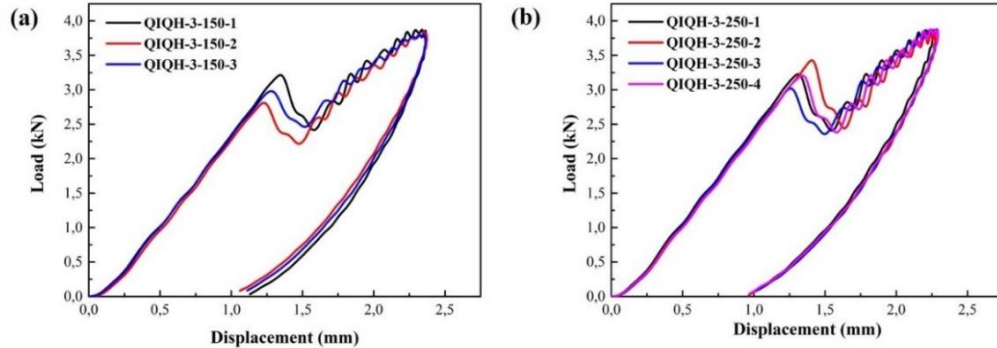


Figure 5-15. Load-displacement curve for QIQH-3: (a) 150×100mm; (b) 250×90mm

All curves exhibit closed shapes with two peaks, which indicates that the specimens did not experience any penetration. Analogous to the force-time curves, the abrupt drop in force right after the linear force-displacement curve reaching the initial peak suggests the occurrence of damages. The rise of the force to the greatest peak with oscillations should be associated with delamination, matrix cracking within plies, i.e., damage propagation [251][252]. The curve ends up in damping with force falling off to zero, which indicates the rebounding of specimens due to the gradual recovery of elastic energy and the return of impactor by the

stored elastic energy in the laminates. The displacement at the end of the curve indicates the residual plastic, permanent deformation of the laminates [253]. The exact values of residual deflections were summarized also in **Table 5-2**.

Energy-time curve

Energy is a primary parameter for characterizing the damage tolerability. **Figure 5-16**, **Figure 5-17** and **Figure 5-18** depict the energy-time curves determined by calculating the area under the filtered load-displacement curve. It is evident that the energy-time history curves are very similar for all the specimens. In the impact tests, as soon as the contact between the impactor and specimen was made, energy dissipation starts to appear accompanied with the deformation of specimen. The kinetic energy of the impactor began to be absorbed by the specimen via the processes of elastic deformation, damage dissipation and in the form of vibration and noises. When the velocity of impactor turned to zero and the displacement reached the maximum, the elastic energy of the specimen was transformed into the kinetic energy of the impactor and drove the impactor to rebound. Since the energy absorbed through the vibration of specimens and noises is small enough to be considered as negligible, the final absorbed energy is thought to be mainly attributed to the damage dissipation [254]. Here, the absorbed energy is defined as the difference between the initial values and flat portions of energy-time curves [255]. The ratio between the absorbed energy and peak energy can be used to determine the efficiency of the material to absorb the energy. This ratio is able to demonstrate the percentage of impact energy that is absorbed by the specimen to create the irreversible damages [256], as presented also in **Table 5-2**. The efficiency of energy absorption of all laminates is almost identical, with values close to 62.50%, independent of the stacking sequence.

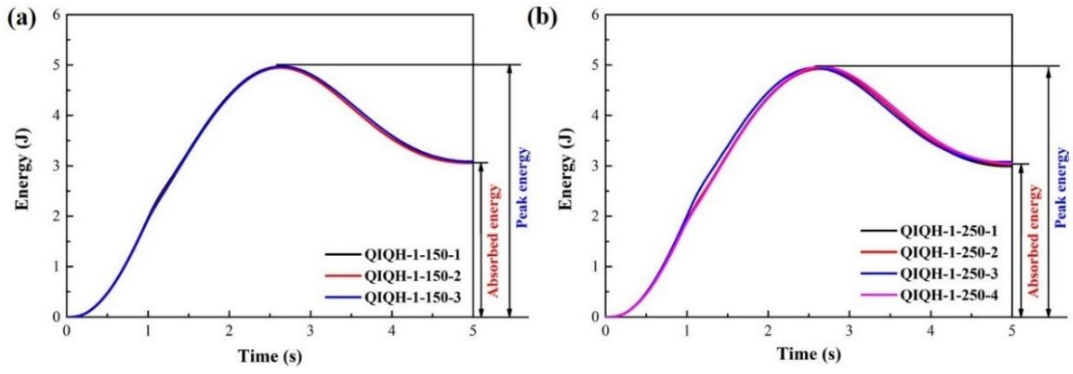


Figure 5-16. Energy-time curve for QIQH-1: (a) 150×100mm; (b) 250×90mm

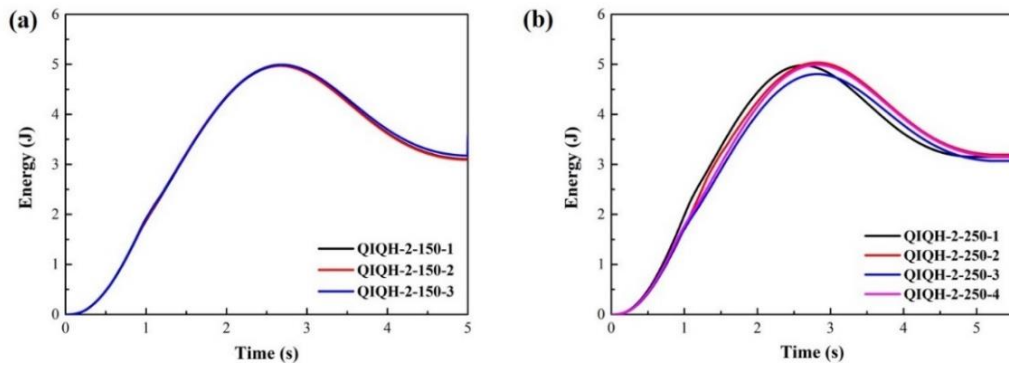


Figure 5-17. Energy-time curve for QIQH-2: (a) 150×100mm; (b) 250×90mm

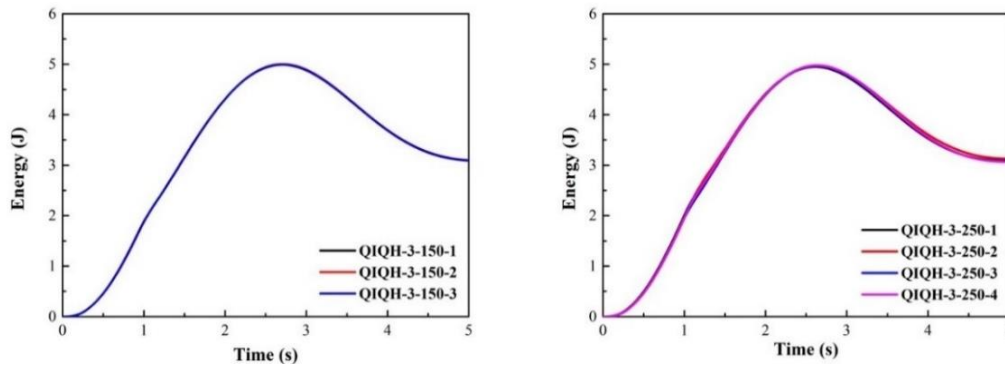


Figure 5-18. Energy-time curve for QIQH-3: (a) 150×100mm; (b) 250×90mm

Table 5-2. Impact testing results

Configurations	150×100mm			250×90mm		
	QIQH-1	QIQH-2	QIQH-3	QIQH-1	QIQH-2	QIQH-3
F_H /kN	3.09 ± 0.12	2.79 ± 0.09	2.86 ± 0.04	3.07 ± 0.26	2.93 ± 0.14	3.22 ± 0.17
Peak force/kN	3.85 ± 0.03	3.82 ± 0.01	3.83 ± 0.02	3.87 ± 0.03	3.64 ± 0.10	3.86 ± 0.02
Absorbed energy/J	3.07 ± 0.02	3.11 ± 0.02	3.09 ± 0.02	3.04 ± 0.04	3.08 ± 0.10	3.09 ± 0.03
Peak energy/J	4.96 ± 0.01	4.97 ± 0.003	4.99 ± 0.01	4.94 ± 0.02	4.94 ± 0.09	4.96 ± 0.01
Efficiency of energy absorption/%	61.98 ± 0.20	62.62 ± 0.45	61.87 ± 0.03	62.62 ± 0.68	63.48 ± 0.30	62.32 ± 0.63
Residual deflection/mm	0.98 ± 0.02	1.03 ± 0.01	1.04 ± 0.01	0.98 ± 0.02	1.09 ± 0.09	0.99 ± 0.04

Visual and microscope inspections

Since the damage morphology of the specimens in the same stacking sequence and dimension were similar, the morphology of the first specimen in each group was selected for comparison, as shown in **Table 5-3**. The white point on front surface marks the impact point. As can be seen from the figures, the damage morphologies of specimens with different dimensions and stacking sequences are similar macroscopically. A slight circular indent was observed on the front plies. On the back sides of specimens, visual damage was barely detectable by the naked eye. In order to obtain more detailed damage information of the back sides, the damaged area was observed via the optical microscope.

At lower magnification (×20 times), extensive matrix cracks are observed for each stacking sequence with two different dimensions. At higher magnification (×50 times), as presented in **Table 5-4**, it is observed that the orientation of cracks stays parallel to the orientation of fibers in the last ply. This phenomenon can be explained by the fact that under low-velocity impact loadings, the local contact led to visible bending deformation. The lower sections of the specimen are mainly subjected to tensile stress, which increases linearly away from the neutral axis (bending stress = 0). The maximum tensile and interlaminar shear stress occur at the bottom of the specimen (the back side), leading to the cracking of matrix.

Table 5-3. Visual inspections of BVID impact damage (dimensions of each image: 76×76mm)

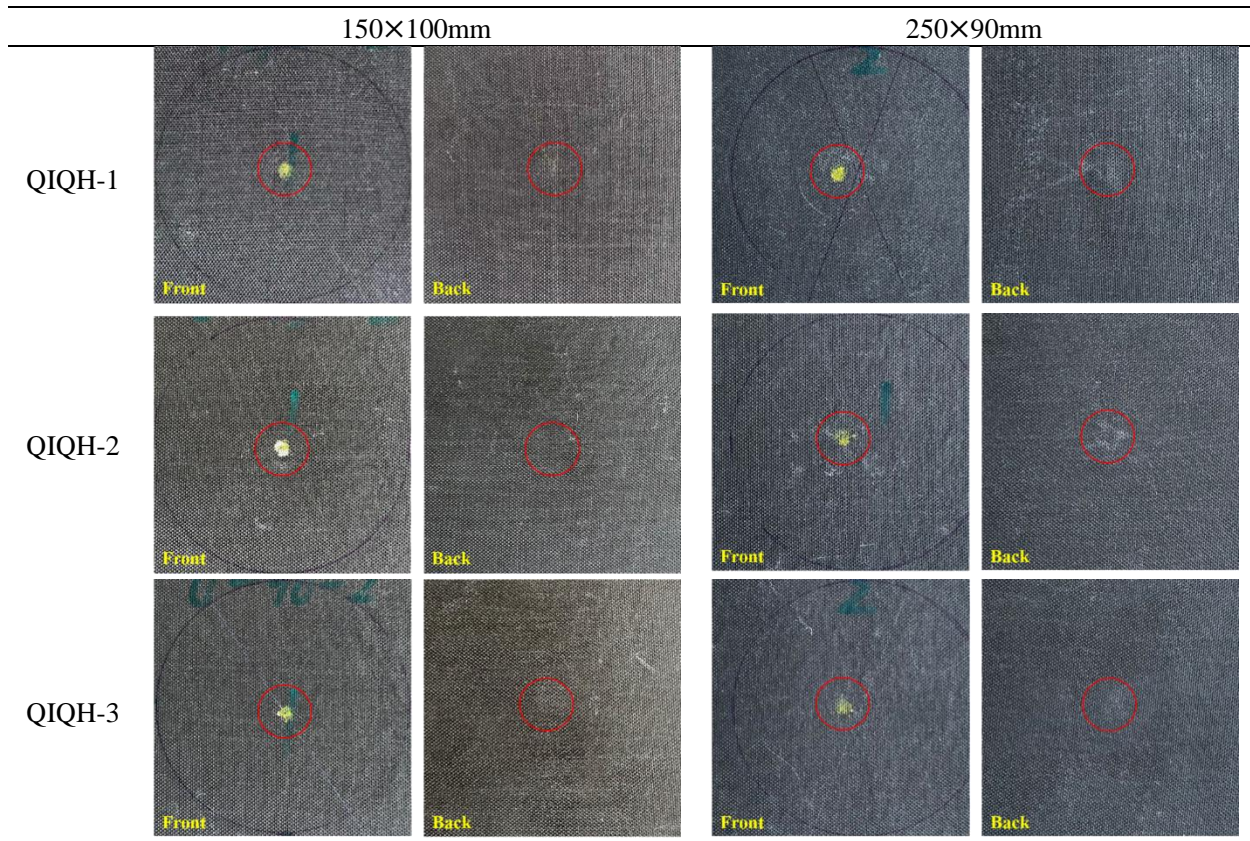
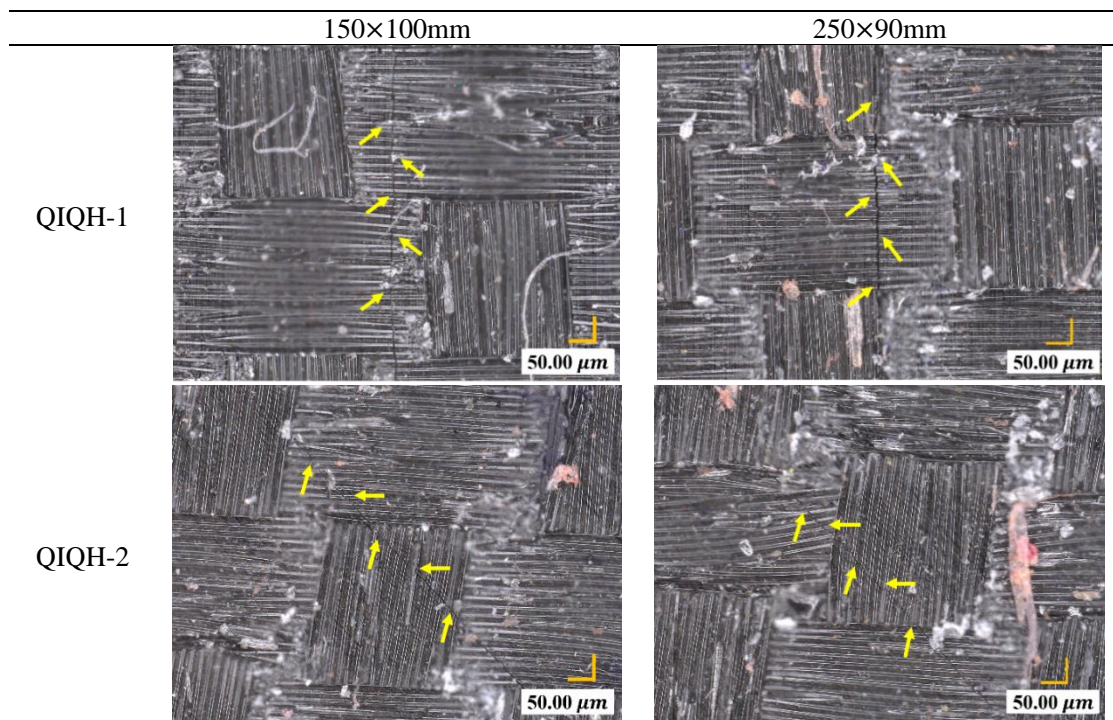
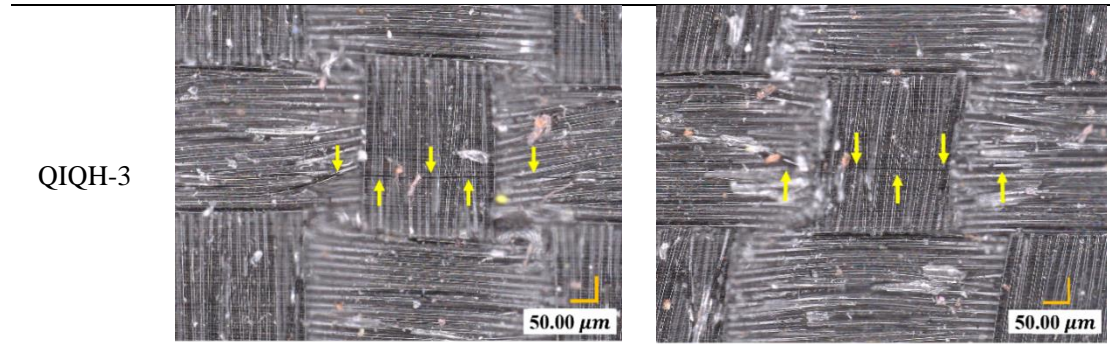


Table 5-4. Matrix cracks observed by optical microscope at back surface of the specimens

(The yellow arrows in the figure help readers to find the orientation of the crack.)





C-scan observations

In the previous section, visual inspection provides a certain indication of damage presence, but it cannot provide complete and quantitative information about internal damages because the material is opaque. Therefore, ultrasonic C-scan is employed to characterize the internal damages. The delamination was observed at locations around the impact indentations from the front and back sides. The projected delamination area A_{proj} was taken as the mean value of the projected delamination areas from two observations:

$$A_{proj} = \frac{A_{front} + A_{back}}{2} \quad (5-7)$$

To obtain A_{front} and A_{back} , the Image J program was used.

The ultrasonic C-scan inspections revealing the shapes and sizes of delaminated surfaces through the thickness of three kinds of laminates were shown in **Table 5-5** and **Table 5-6**. It can be seen from the figures, that the projected delamination area is in a circular shape for all of the three stacking sequences, which indicates that the influence of stacking sequence on the shape of delamination area is not significant. The ply-by-ply delamination appears to be bow-tie shaped, with their main axis being coincident with the fiber orientation of the layer above the interface (seen from back surface). As is well known, the distribution of delamination through the thickness has been found to be in a conical shape, with the largest damage extent closer to the back surface. Due to the axisymmetric loading, the values of projected delamination area A_{proj} listed in **Table 5-7** of three laminates are also close to each other. If projected damage area for all specimen is considered circular, the corresponding diameter, d_{proj} can be added to **Table 5-7**. Its value varies from 26 to 27 mm.

Table 5-5. C-scan results of impacted specimens with dimensions of 150×100mm

(left: front side; right: back side)

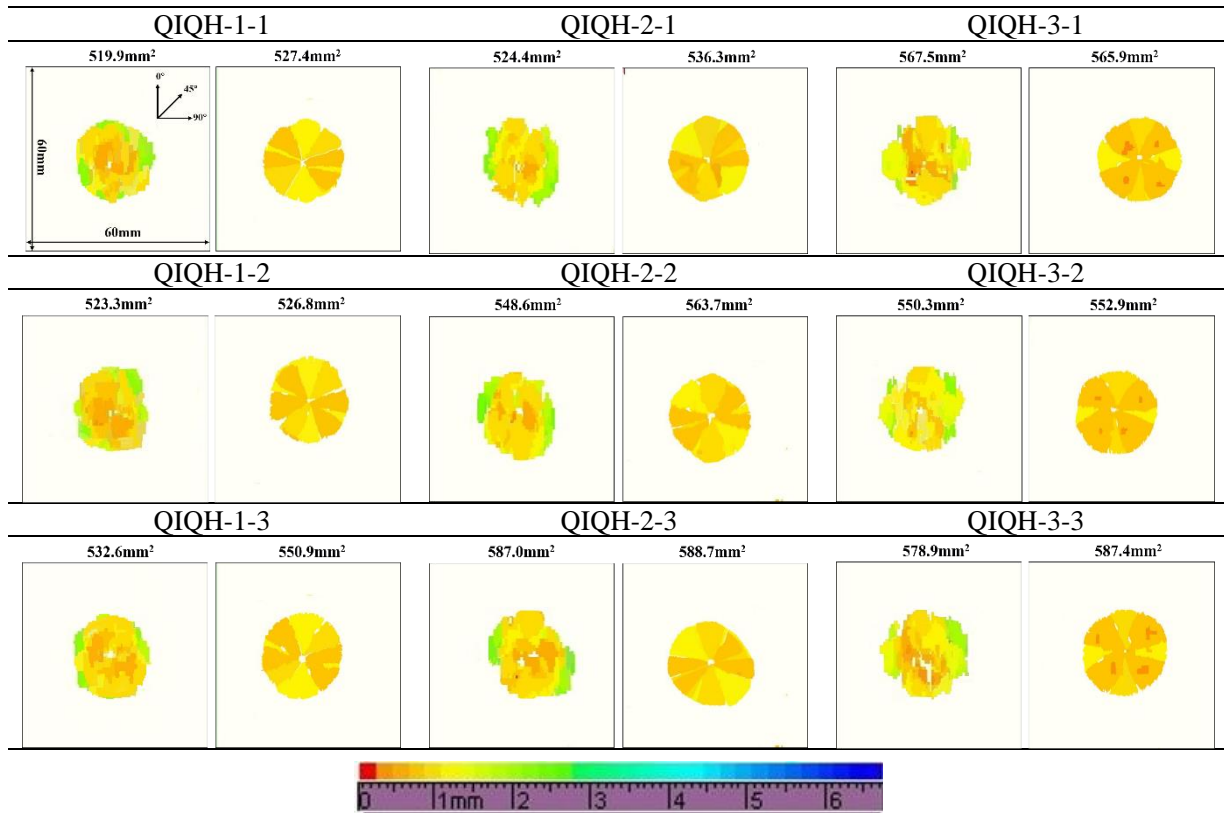
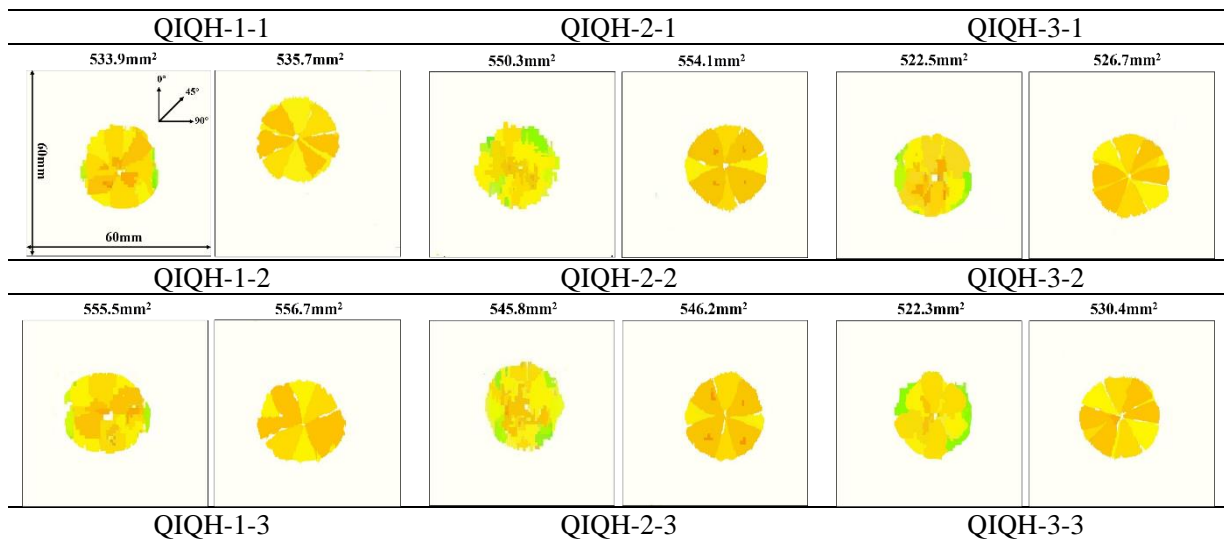


Table 5-6. C-scan results of impacted specimens with dimensions of 250×90mm

(left: front side; right: back side)



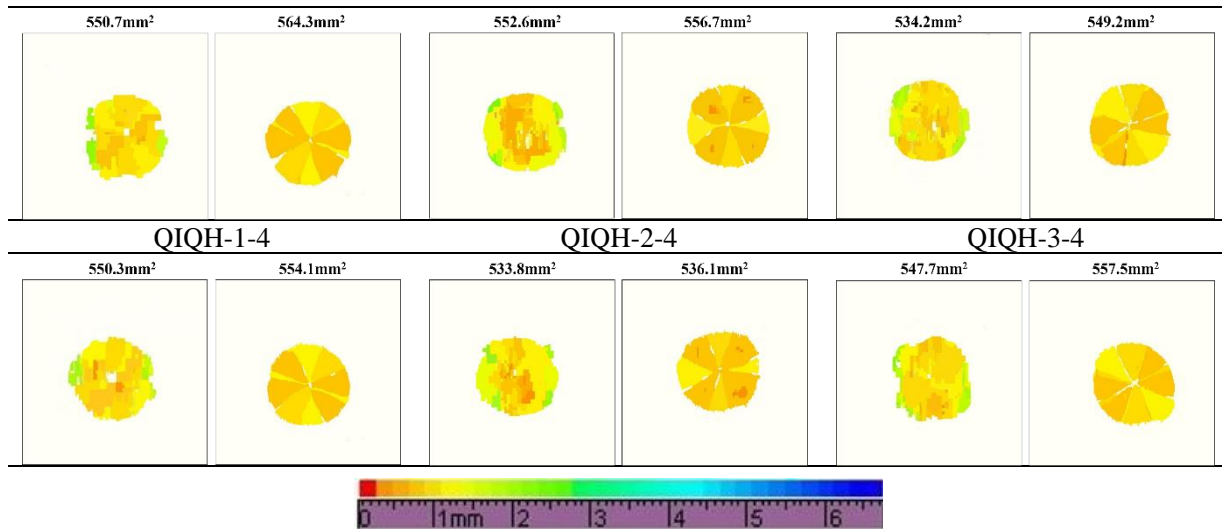


Table 5-7. Projected delamination area A_{proj} and diameter d_{proj}

	QIQH-1	QIQH-2	QIQH-3
150×100 A_{proj} (mm ²)	558.13 ± 28.80	530.15 ± 10.09	567.2 ± 15.8
150×100 d_{proj} (mm)	26.65 ± 0.69	25.98 ± 0.25	26.87 ± 0.37
250×90 A_{proj} (mm ²)	549.64 ± 11.50	545.59 ± 8.11	536.31 ± 13.32
250×90 d_{proj} (mm)	26.45 ± 0.28	26.36 ± 0.20	26.13 ± 0.32

5.2 Compression After Impact (CAI) tests

The CAI tests were first conducted to determine the UCS of impacted specimens, which will be subsequently used in the post-impact compression fatigue tests.

5.2.1 Experiments

The experimental set-up and procedure of CAI tests are the same as the static compression tests, as mentioned previously in section 4.3.1.

5.2.2 Static CAI test results

The load versus displacement curves of static CAI tests are presented in **Figure 5-19** for three stacking sequences. A good repeatability is observed for each stacking sequence. It can be seen that the load-displacement curves of different stacking sequences are quite similar to each other. The global load-displacement curves can still be divided into three stages, as that

already shown in **Figure 4-9** in previous chapter.

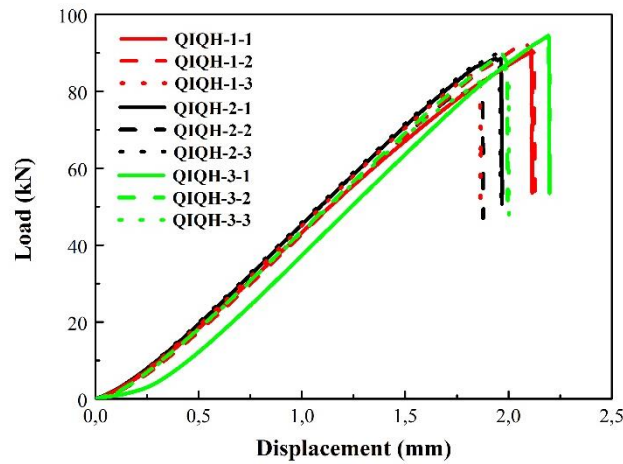


Figure 5-19. Load vs. displacement curves of CAI tests

Table 5-8 presents the values of UCS of impacted specimens calculated from the load-displacement curves using Eq. (4-23). The transverse cross-sectional area before the impact test is still used as the denominator. In the table, the initial stiffness of impacted specimens is determined by the slope of load-displacement curve where the displacement is between 0.75 and 1.5mm. The UCS and the stiffness of non-impacted specimens are also added in the same table for comparison. As can be seen from the table, the average UCS of impacted specimens of three different stacking sequences as well as the stiffness are similar to each other. Compared to non-impacted specimens, there is only a slight decrease of UCS and the stiffness in the impacted specimens, which is true for QIQH-1 and QIQH-2. Taking into account of the scatter of these experimental results, the variation of UCS and the stiffness in impacted specimens does not be significant. This implies that the impact energy chosen for the tests is below the impact threshold energy (the energy that caused a significant decrease of UCS in the impacted specimens compared to non-impacted specimens), as evidenced by the impact damage morphology (**Table 5-5** and **Table 5-6**) that at more damaged side, the diameter of damaged area (from 26 to 27mm) represents a little more than a quarter of the total width of the cross section (100mm). Even though the compression behavior should be influenced by the impact damages, it is not severe enough to affect significantly global residual stiffness and strength of the specimens. This phenomenon is also reported by Sun et al [258].

Table 5-8. Compression test results of non-impacted and impacted specimens

Stacking sequence	UCS/MPa	Initial Stiffness /kN·mm ⁻¹	Relative variation in strength/%	Relative variation in stiffness/%
QIQH-1	258.88 ± 8.40	51.89 ± 0.28		
QIQH-1-impacted	243.45 ± 9.63	50.80 ± 0.75	-5.96	-2.10
QIQH-2	243.61 ± 5.83	52.03 ± 1.57		
QIQH-2-impacted	240.90 ± 14.46	51.27 ± 0.89	-1.11	-1.46
QIQH-3	192.66 ± 8.61*	45.10 ± 0.37*		
QIQH-3-impacted	252.04 ± 11.21	50.56 ± 0.24	No value	No value
Non-impacted (average)	251.25 ± 10.80	51.96 ± 0.10		
Impacted (average)	245.46 ± 5.84	50.88 ± 0.37	-2.30	-2.08

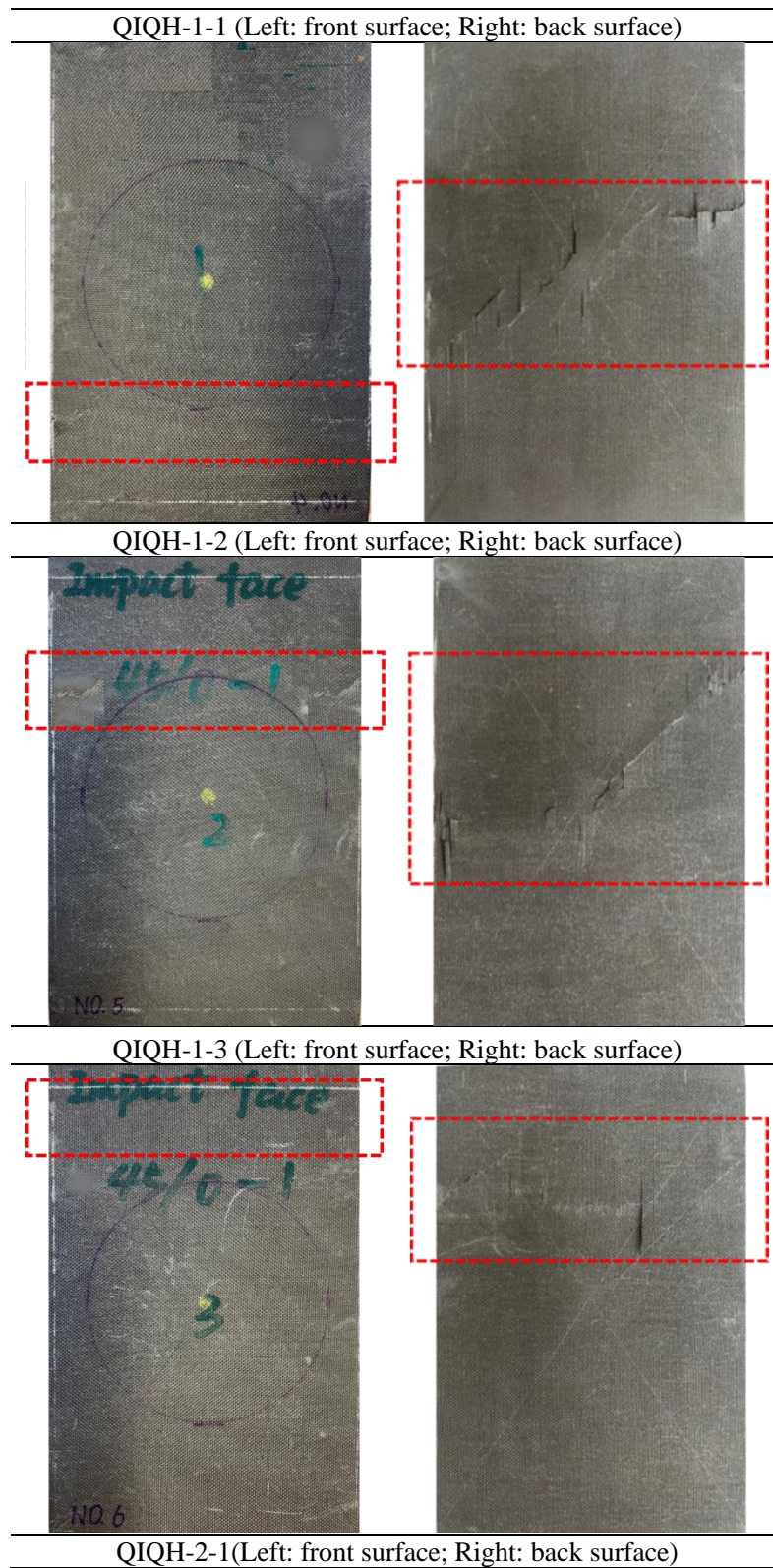
* the measure value is not used in following studies.

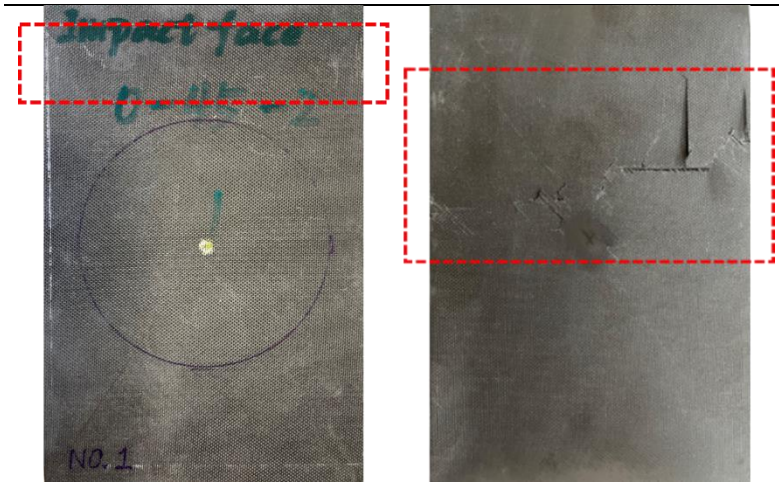
5.2.3 Fracture surfaces observations

Table 5-9 gives the fracture surfaces of all the CAI specimens. According to standard ASTM D7137/7137M [240], three-place failure code shall be used to describe the failure modes. This code uses the first place to describe failure type, the second to describe failure area, and the last to describe failure location. **Figure 5-20** illustrates commonly observed acceptable CAI failure modes. The explanation for each letter of the code can be seen in

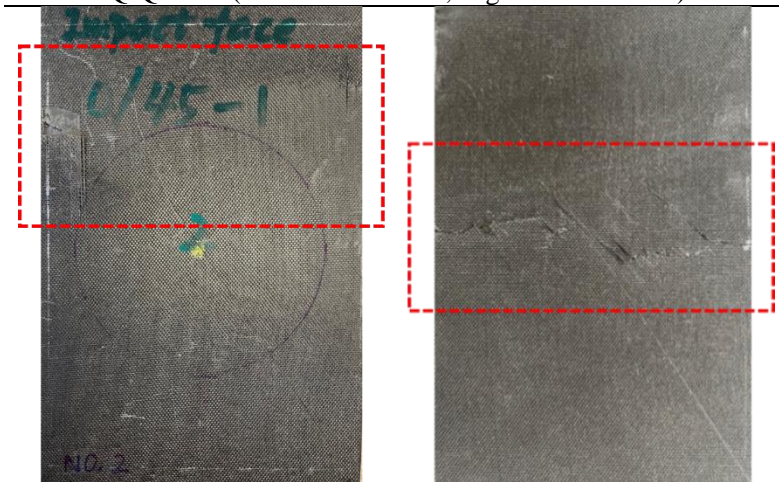
Table 5-10. For all the specimens, the cracks on the back side of the specimen are found to run through the width of the specimen. Therefore, the failure type is L (i.e., lateral). Then, since all the specimens were broken at the section including impact damage except for QIQH-1-3 and QIQH-3-2. The damage area can be characterized by D (i.e., at/through damage failure area). For QIQH-1-3 and QIQH-3-2, the damage area can be characterized by G (i.e., gauge, away from damage). Finally, since the cracks are found to be in the middle of the specimens, therefore, the third code is all M (i.e., middle). Putting it together, the three-place failure code for QIQH-1-3 and QIQH-3-2 are LGM, while those of other specimens are LDM.

Table 5-9. Fracture surfaces of impacted specimens under CAI loading

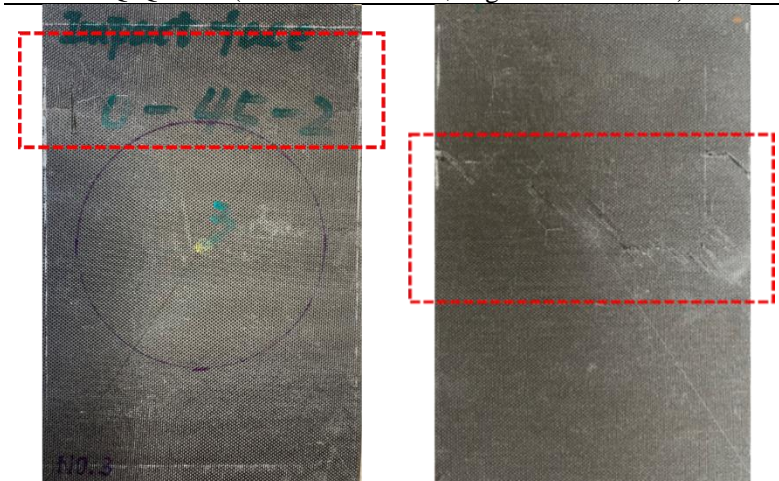




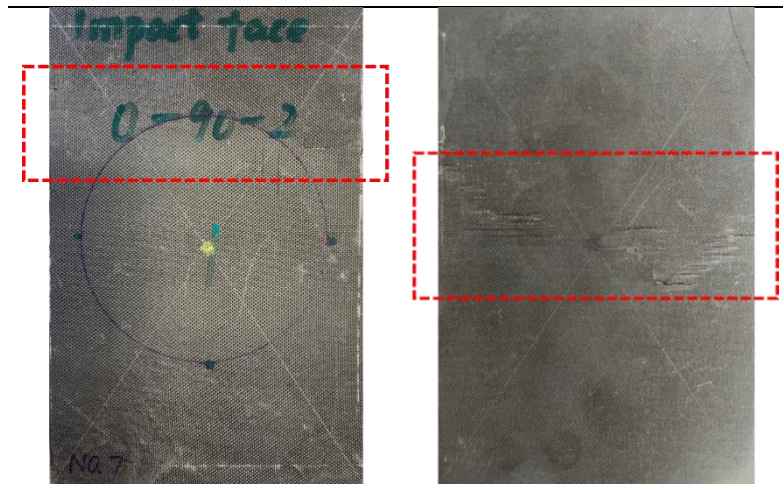
QIQH-2-2 (Left: front surface; Right: back surface)



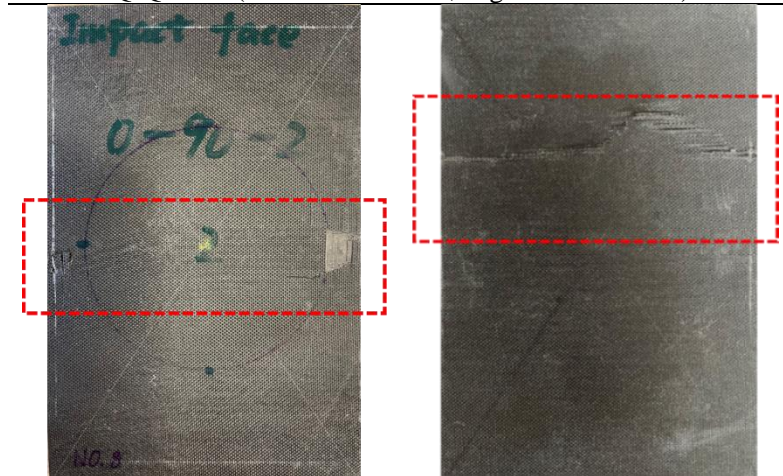
QIQH-2-3 (Left: front surface; Right: back surface)



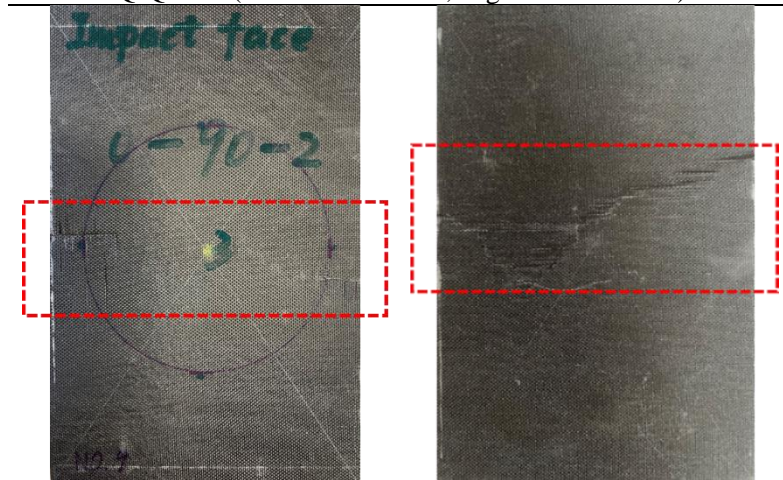
QIQH-3-1 (Left: front surface; Right: back surface)



QIQH-3-2 (Left: front surface; Right: back surface)



QIQH-3-3 (Left: front surface; Right: back surface)



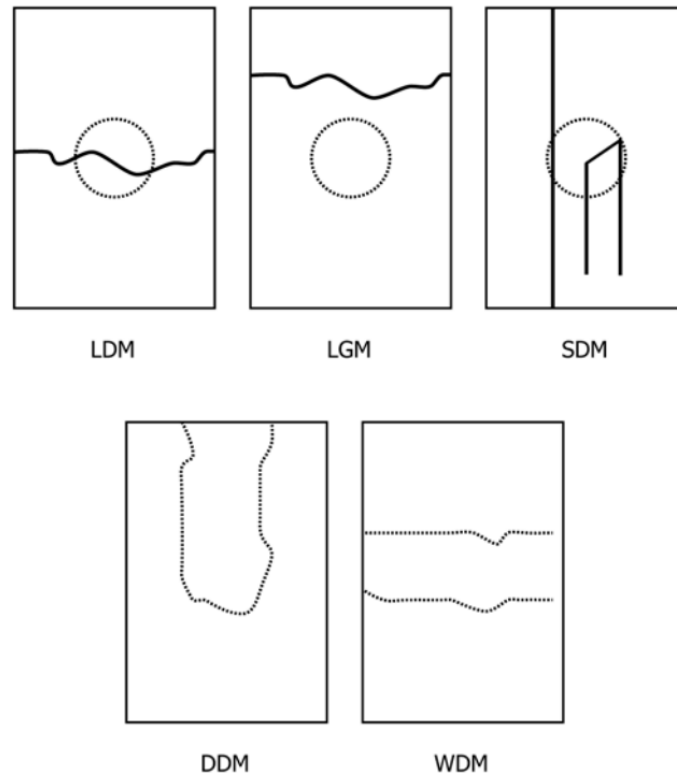


Figure 5-20. Commonly observed acceptable CAI failure modes [240]

Table 5-10. Three-place failure mode codes [240]

First character	
Failure type	Code
Delamination growth to one length edge at final failure	D
Lateral	L
long, Splitting	S
Delamination growth to width edges at final failure, Widthwise	W
Second character	
Failure area	Code
At/through Damage	D
Gage, away from damage	G
Third character	
Failure location	Code
Middle	M

Then, only the fracture region in the red window of one specimen that failed in LDM of each stacking sequence will be discussed. Taking QIQH-1-1, QIQH-2-1, QIQH-3-1 as examples, as can be seen in **Figure 5-21**, for all of the stacking sequences, on the front surfaces, some cracks along the first ply fiber direction can be seen near the two free edges of the specimens.

Only in QIQH-3, the second ply also has an influence on the orientation of cracks; while on the back surfaces, the path of the cracking seems to be different between these three stacking sequences. It is shown that the dominant cracks on back surface are along the first ply fibers for QIQH-1(0°) and QIQH-3 (90°), but the cracks along -45° and 90° for QIQH-1 and the cracks along ±45° for QIQH-3 can be also found. Concerning QIQH-2, the cracks of all orientations (0, ±45, 90°) can be identified on the back side. Herein, adjacent ply even sub-adjacent plies, as well as their interface should play an important role in damage process of the QIQH specimens under CAI loading whatever their stacking sequence is.

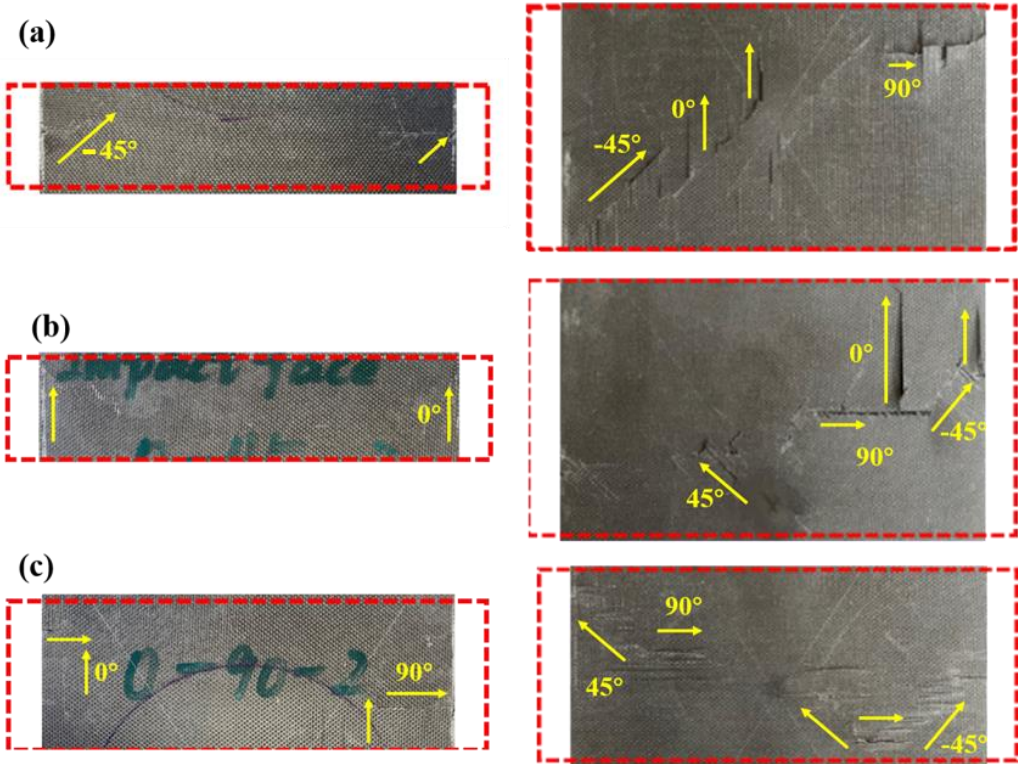


Figure 5-21. Details of fracture surfaces:

- (a) QIQH-1 (left: front side with first ply fibers at -45°; right: back side with first ply fibers at 0°);
- (b) QIQH-2 (left: front side with first ply fibers at 0°; right: back side with first ply fibers at -45°);
- (c) QIQH-3 (left: front side with first ply fibers at 0°; right: back side with first ply fibers at 90°)

5.3 Post-impact compression-compression fatigue test

5.3.1 Experiments

The experimental set-up and procedure for the post-impact fatigue test are the same as compression-compression fatigue test described in chapter 4. The only difference lies in the definition for temperature rise.

A typical thermographic image during the post-impact fatigue tests is shown in **Figure 5-22**, in which the temperature presents different distributions on the surface of the specimen. Three sections named as ‘fatigue’, ‘impact’ and ‘reference’ are adopted and the mean temperature of these sections is extracted separately. The temperature in the zone ‘impact’ shows the maximum temperature due to the stress concentration, impact damage and the friction, while the temperature in the zone ‘reference’ shows the minimum. According to Ref. [259], the real-time surface temperature rise, which is defined as $\Delta T = T_{impact} - T_{ref}$, i.e., the difference between the average temperature of zone ‘impact’ and ‘reference’ under the same fatigue cycle, can be used to analyze the temperature variation. This definition is adopted in the following study. It should be noted that even though the projected delamination area is in a circular shape, the exact delamination area between two layers are not perfectly the same, which may have an influence on the post-impact fatigue test results. Therefore, 3 specimens were repeated for QIQH-1 and 4 specimens were repeated for stacking sequence QIQH-2 and QIQH-3.

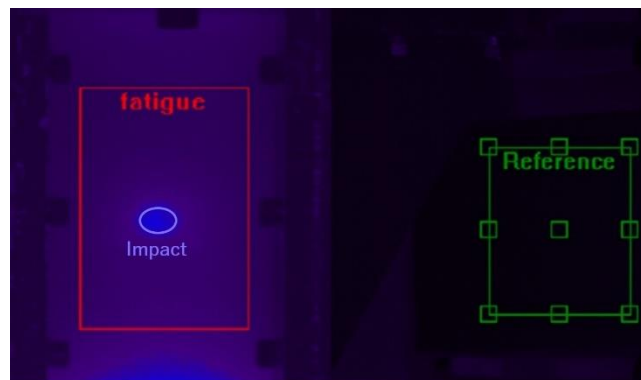


Figure 5-22. Temperature distribution on the specimen surface during post-impact fatigue tests

5.3.2 Temperature distribution

During the fatigue tests, the thermographic images are gathered as shown in **Figure 5-23**. For small loading maximum stresses, the temperature distribution is nearly homogenous in the whole observed area, as shown in **Figure 5-23** (a). When the stress level is close to the maximum stress at fracture, hot spot appears at the impact damage region (see **Figure 5-23** (b)) and gradually extends perpendicular to the loading direction along the cross section, demonstrating the increase of internal damages. At fracture, the hot spot area runs through the width of specimen (**Figure 5-23** (c)), which corresponds to the transverse cracks observed by the naked eyes (**Figure 5-23** (d)). In order to get more information of the damage modes, the region at one edge of the specimen, in the red window, was inspected under optical microscope. More severe fiber fracture and matrix cracking are observed near the two free edges of the specimens (**Figure 5-23** (e)), which releases abundant heat near the failure of specimen, leading to more prominent temperature increase in both sides.

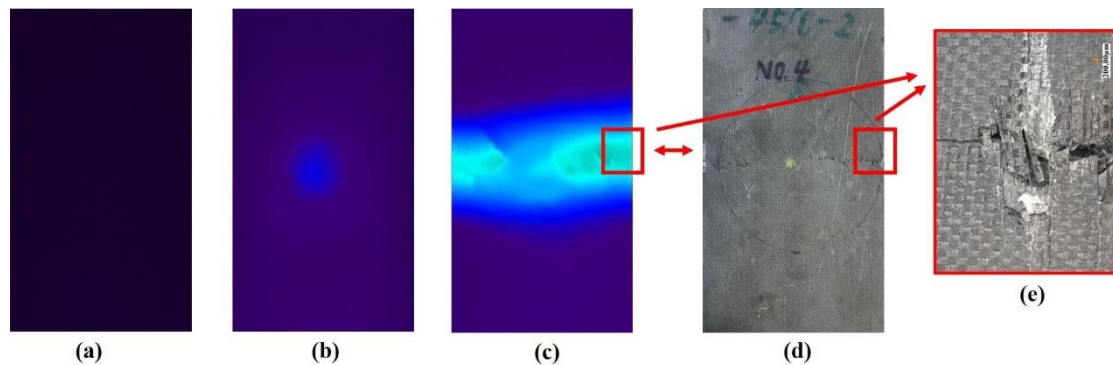


Figure 5-23. Thermographic images and damage characteristics: (a) - (c): thermographic images in different stages; (d) specimen profile after failure (front impacted surface); (e) fracture at one edge of the specimen observed by optical microscope

5.3.3 Rapid determination of the fatigue limit

Figure 5-24 depicts an example of the temperature rise of impact damage zone recorded using IR camera versus number of loading cycles of one post-impact fatigue test specimen of QIQH-1. The maximum stress of each loading step is illustrated at the end of each curve in the plot. As can be seen from the figure, the temperature profiles reached a stabilized plateau

at the end of each curve for the maximum stresses from 30 to 75% UCS.

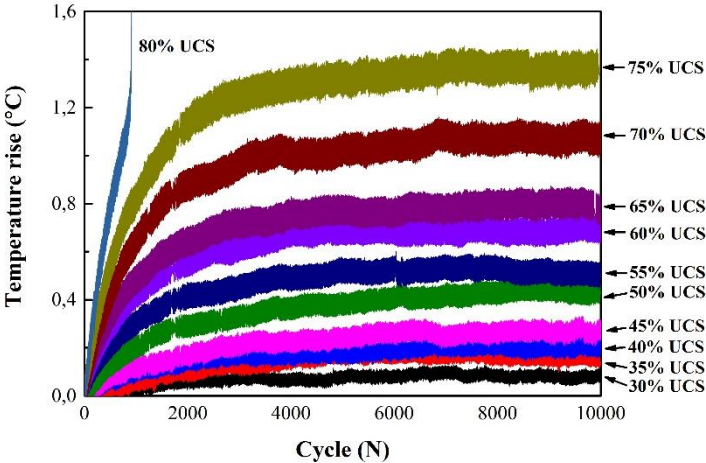


Figure 5-24. Variation of temperature rise of impact damage zone as a function of number of loading cycles.

The obtained values of stabilized temperature rise for each loading step within a given test were plotted against the applied maximum stress to determine the fatigue limit following the method proposed in section 2.3, as presented in **Figure 5-25**. Still, according to the proposed method, the normalized angle change θ_i^c is calculated with respect to the sequence number of point. The number of the point corresponding to the peak value of normalized angle change θ_i^c is 8, which corresponds to a maximum stress of 65% UCS. Consequently, the fatigue limit and stabilized temperature rise corresponding to the fatigue limit are determined as 65% UCS and 0.783°C, respectively. Using the same method, the fatigue limit determined and corresponding stabilized temperature rise for all specimens are listed in **Table 5-11**.

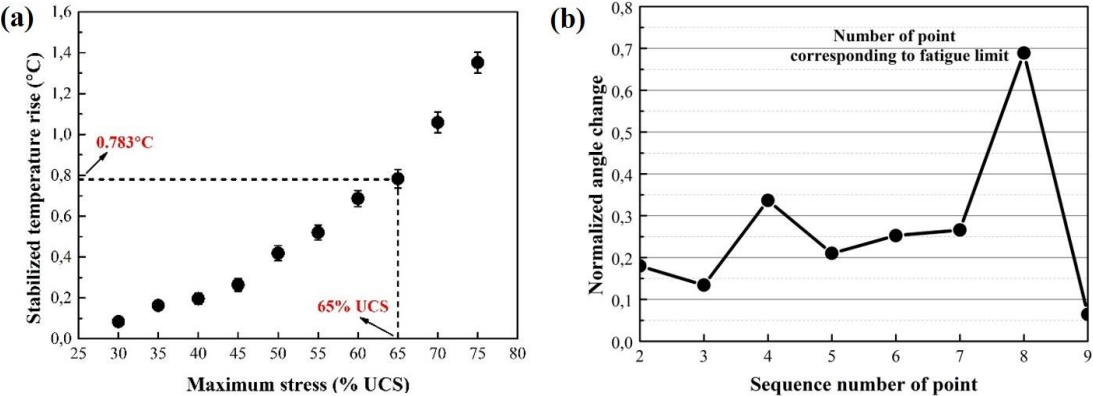


Figure 5-25. Fatigue limit determination of impacted QIQH-1 specimen.

Table 5-11. Determined fatigue limit and corresponding stabilized temperature rise of each QIQH specimen

	No.1		No.2		No.3		No.4	
	Fatigue limit /%UCS	ΔT_{stab} /°C	Fatigue limit /%UCS	ΔT_{stab} /°C	Fatigue limit /%UCS	ΔT_{stab} /°C	Fatigue limit /%UCS	ΔT_{stab} /°C
QIQH-1	65	0.78	70	1.05	65	0.80		
QIQH-2	65	0.83	70	1.05	65	0.81	45	0.30
QIQH-3	65	0.80	65	0.76	60	0.59	45	0.29

5.3.4 Determination of S-N curves for each configuration

For each stacking sequence, the fatigue limits of 2 among 3 or 4 specimens are identical, i.e., 65% UCS. Therefore, the protocol proposed in section 3.3 is applied to determine a “average” S-N curve for each configuration.

Step 1: determine the fatigue limit and corresponding stabilized temperature rise based on thermographic data

The average ΔT_{stab}^* value of two specimens with the same fatigue limits for each stacking sequence is calculated to obtain $\overline{\Delta T_{stab}^*}$ corresponding to each stress level. The proposed method in Chapter 2 is employed to determine the fatigue limit using the data sets $(\sigma, \overline{\Delta T_{stab}^*})$. The fatigue limit and corresponding average normalized stabilized temperature rise $\overline{\Delta T_{stab}^*}$ are determined as 65% UCS and 0.66, 65% UCS and 0.64 and 65% UCS and 0.76 for stacking sequences QIQH-1 to QIQH-3, respectively.

Step 2: calibrate the values of p , q and r

The average normalized stiffness degradation is plotted as a function of the number of loading cycles and average normalized stabilized temperature rise under stress level of 50% to 70% UCS. 3D surface fitting Toolbox in MATLAB[®] software is used to fit the data. The best fit values of p , q and r for each stacking sequence are shown in

Table 5-12. The corresponding coefficient of determination is 0.974, 0.924 and 0.964 for

QIQH-1 to QIQH-3, respectively.

Table 5-12. Determined parameters for different stacking sequences

	p	q	r	$k_f(N_{fl} = 10^6 \text{ cycles})$	$k_f(N_{fl} = 10^7 \text{ cycles})$
QIQH-1	6.436×10^{-2}	38.17	0.314	0.919	0.914
QIQH-2	3.649×10^{-2}	27.45	0.599	0.954	0.950
QIQH-3	0.102	43.05	0.300	0.881	0.875

Step 3: calculate the failure threshold stiffness

Still, both $k(N_{fl} = 10^6 \text{ cycles})$ and $k(N_{fl} = 10^7 \text{ cycles})$ were considered for the calculation of failure threshold stiffness. According to Eq. (3-11), the determined values are also listed in

Table 5-12.

Step 4: determination of S-N curves

A plot of determined fatigue life calculated using modified model in Chapter 3 is shown in **Figure 5-26**. It is observed from the figure that for each stacking sequence, the S-N curves with the same determined fatigue limits stay close to each other. For QIQH-1, the more reliable S-N curves are less conservative compared to the individual S-N curves of each specimen, while for QIQH-2, the more reliable S-N curves are more conservative. For QIQH-3, the more reliable S-N curves are nearly coincided with the two individual S-N curves.

For better comparison of the difference between the S-N curves of three different stacking sequences, the six individual S-N curves of all specimens having the same fatigue limit (65% UCS) are plotted together in the same figure (see **Figure 5-27**). It can be seen from the figure, there is nearly no difference between the determined S-N curves of three different stacking sequences, which implies that the influence of stacking sequence on the S-N curves is

insignificant. Therefore, the overall ‘average’ S-N curves can be determined based on these specimens.

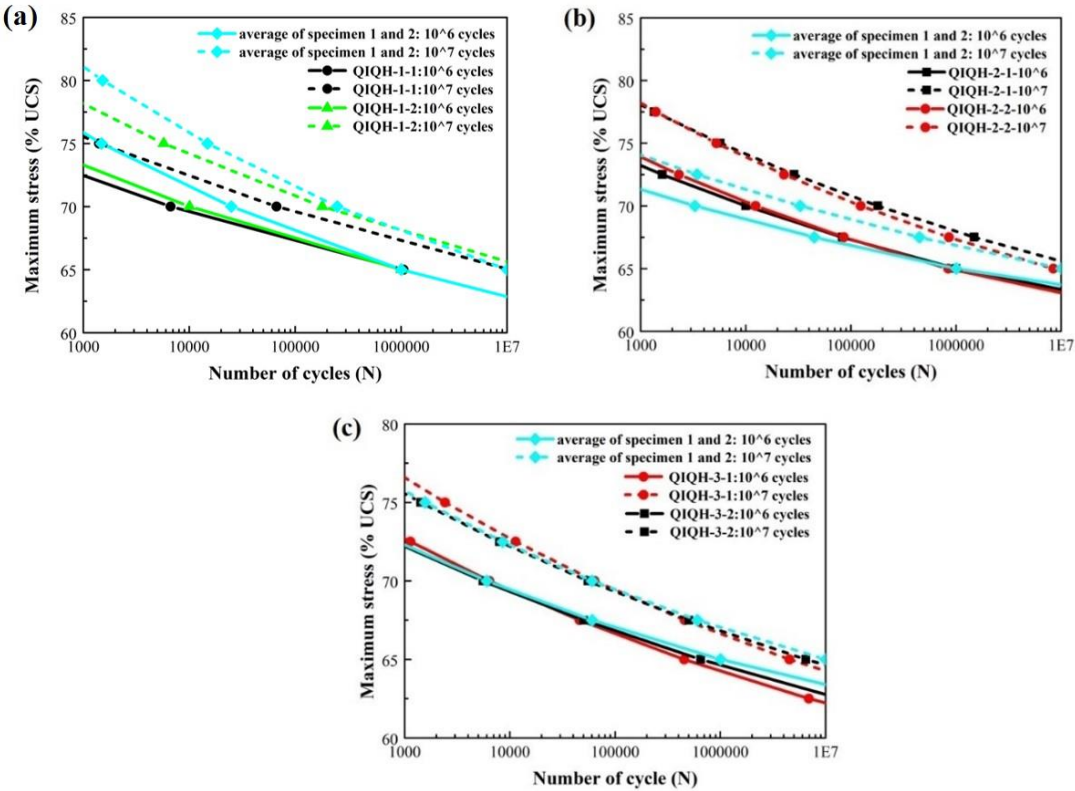


Figure 5-26. Determined post-impact fatigue lives for three QIQH stacking sequences: (a) QIQH-1; (b) QIQH-2; (c) QIQH-3

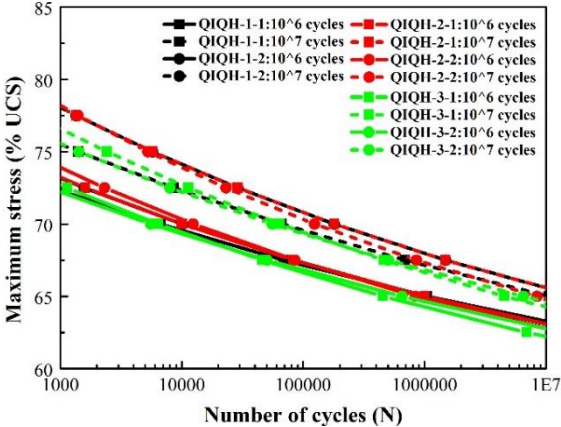


Figure 5-27. S-N curves of all post-impact fatigue specimens having identical fatigue limits

5.3.5 Determination of overall “average” S-N curves based on the data of all specimens

Among the 12 specimens tested, since the fatigue limits of 6 specimens in **Figure 5-27** are identical, which satisfies the condition of protocol proposed in section 3.3, it is possible to

determine the overall “average” S-N curves for these three stacking sequences utilizing the data of 6 specimens.

In the step 1, the average normalized stabilized temperature rise $\overline{\Delta T_{stab}^*}$ of 6 specimens is first calculated as a function of maximum stress. The fatigue limit determination method proposed in chapter 2 is employed to determine one fatigue limit and corresponding normalized stabilized temperature rise, as depicted in **Table 5-13**. In the step 2, 3D surface fitting in MATLAB[®] is employed to fit the average normalized stiffness degradation as a function of average stabilized temperature rise $\overline{\Delta T_{stab}^*}$ and number of loading cycles. The best-fit values of p , q and r and coefficients of determination R^2 are also listed in **Table 5-13**. In the step 3, the failure threshold stiffness corresponding to $N_{fl} = 10^6$ and 10^7 cycles are calculated based on Eq. (3-11). The obtained values are presented in **Table 5-13**. Finally, in the step 4 the obtained S-N curves based on the ‘average’ of 6 specimens and the individual S-N curves of each specimen are compared in **Figure 5-28**.

Table 5-13. Fatigue limit and calibration parameters

Parameters	‘Average’ values
Fatigue limit	65 % UTS
$\Delta T_{stab_fl}^*$	0.62
p	0.66
q	39.65
r	0.27
$k_f(N_{fl} = 10^6 \text{ cycles})$	0.918
$k_f(N_{fl} = 10^7 \text{ cycles})$	0.913
R^2	0.89

As can be seen from the figure, the overall ‘average’ S-N curves corresponding to both $N_{fl} = 10^6$ cycles and $N_{fl} = 10^7$ cycles are higher than the individual S-N curves. These overall “average” S-N curves seem less conservative, especially for the low and medium fatigue life.

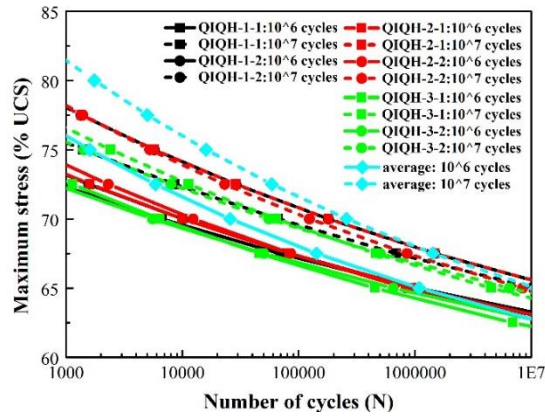


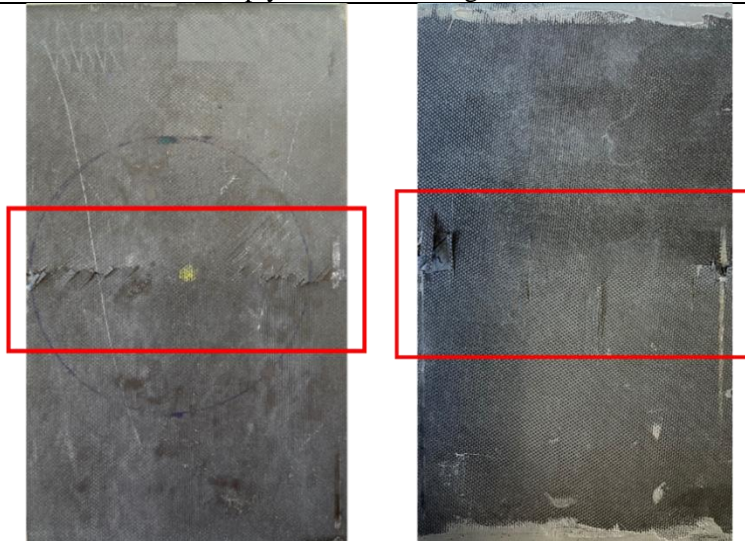
Figure 5-28. Individual predicted S-N curves and more reliable S-N curves for post-impact compression fatigue QIQH laminates

5.3.6 Fracture surfaces observations

The damage morphology of front surfaces of post-impact compression fatigue specimens observed by the naked eyes is presented in **Table 5-14**. One specimen of each stacking sequence is taken as an example here. Among the 12 specimens, except for one QIQH-3 specimen failed in LGM mode, all the other specimens failed in a similar mode as the CAI specimens. The three-letter failure code is LDM, where L stands for lateral, D corresponds to at/through damage failure area, and M is the middle location.

Table 5-14. Fracture surfaces of post-impact compression fatigue specimens

QIQH-1 (Left: front surface with first ply fiber at -45° ; Right: back surface with first ply fiber at 0° ;)



QIQH-2 (Left: front surface with first ply fiber at 0° ; Right: back surface with first ply fiber at 45° ;)



QIQH-3 (Left: front surface with first ply fiber at 0°; Right: back surface with first ply fiber at 90°;)

The details of fracture surfaces are shown in **Figure 5-29**. As can be seen from the figures, on the front surfaces, the overall direction of the crack is horizontal. Plenty of matrix cracks oriented the same as the fiber orientation of first ply can be observed. On the back surfaces, the cracks still oriented the same as the fiber orientation of first ply. More cracks are located near the two free edges of the specimens. For QIQH-1 and 2, several cracks can be found in the center of the specimen due to local buckling. If the front fracture surfaces of first ply fiber oriented at 0° of QIQH-2 and 3 are compared, their fracture morphology looks very similar, even though their adjacent and sub-adjacent plies have different fiber orientations. Moreover, for each stacking sequence, the fracture surfaces of CAI specimens and those of post-impact

compression fatigue specimens look quite different. More cracks can be observed on back side of CAI specimen, while for post impact compression fatigue specimen, more cracks can be observed on front side whatever the stacking sequence is.

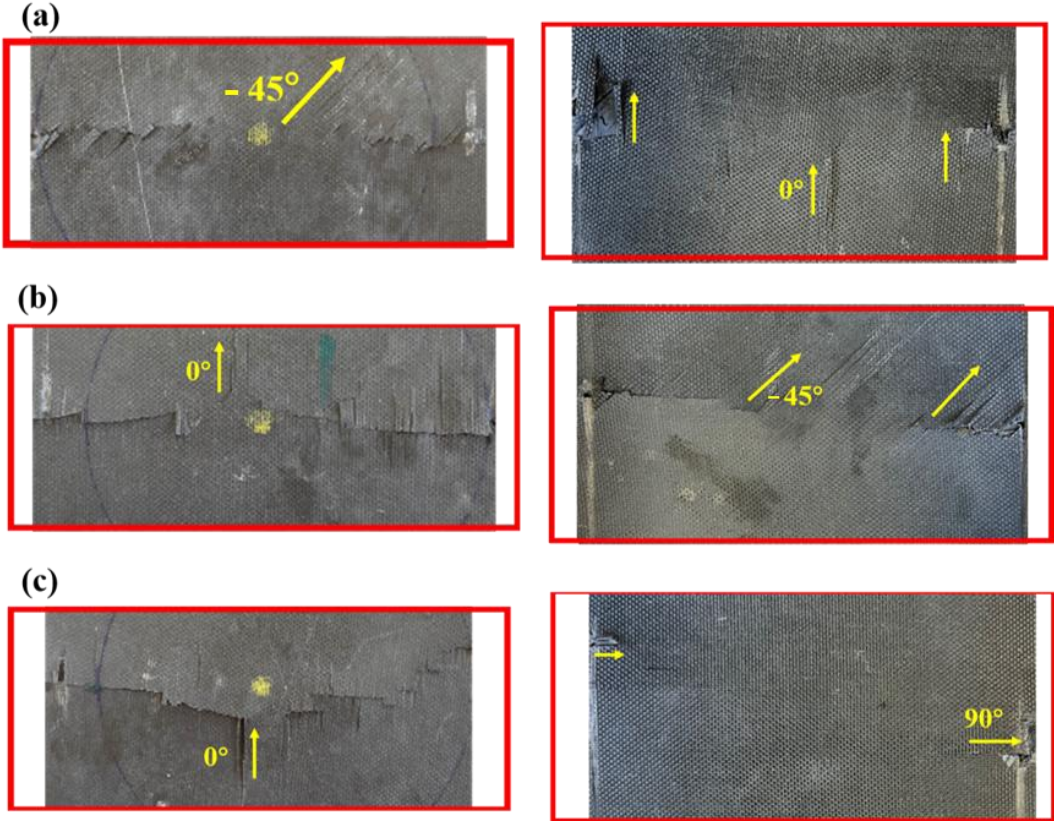


Figure 5-29. Details of fracture surfaces: (a) QIQH-1 (left: -45°; right:0°); (b) QIQH-2 (left: 0°; right: 45°); (c) QIQH-3 (left: 0°; right: 90°)

5.4 Comparison of non-impacted and impacted specimens

5.4.1 Static compression properties

For the impacted specimens and non-impacted specimens, it is demonstrated that their measured stiffness and the strength under static compression loading are very close (to see **Table 5-8**). Moreover, as already been stated in section 4.3.2 and 5.2.2, the static compressive load-displacement curve for all QIQH specimens, impacted or not, presents the similar trend, which can be divided into three stages (**Figure 4-9**). However, if we examine the stage II between the end of linear behavior (point B) and the final failure of the specimens (point C), it can be seen that the stage II lasts longer for the impacted specimens. If the load at point B and

at point C (UCS) is determined, their relative difference defined as $d_{B \text{ and } C} = (F_C - F_B)/F_C$ % can be determined for impacted or non-impacted specimens.

The comparison of difference between forces at point B and at the point C of non-impacted and impacted specimens are listed in **Table 5-15**. It is obvious that this relative difference of impacted specimens is more significant, which means that even though the impacted specimens have the same compression strength as that of non-impacted specimens, their damage process is not the same. In the impacted specimen, the existence of impact damage promotes the onset of local buckling. Therefore, the start of stage II of impacted specimens is earlier compared to the non-impacted specimens.

Table 5-15. Comparison of relative difference between the forces at point B and at the point C for the non-impacted and impacted specimens

	Non-impacted specimen/%	Impacted specimen/%
QIQH-1	3.62 ± 2.25	9.91 ± 6.65
QIQH-2	2.58 ± 0.14	7.53 ± 4.41
QIQH-3	1.42 ± 1.12	11.57 ± 6.50

5.4.2 Fatigue limit

The fatigue limits of non-impacted and impacted specimens are plotted in **Figure 5-30**. The presented results show that the repeatability of the performed tests is very high, which is confirmed by the error bars in the figure. Compared to the non-impact specimens, a reduction of 4.76%, 1.23% and 9.53% is observed in the impacted specimens for QIQH-1, 2 and 3, respectively. By taking into consideration of the scatter of the results from all tests, whether the observed variation has physical sense or not remains problematic. Verification of the determined values needs further comparison with the traditional fatigue test results.

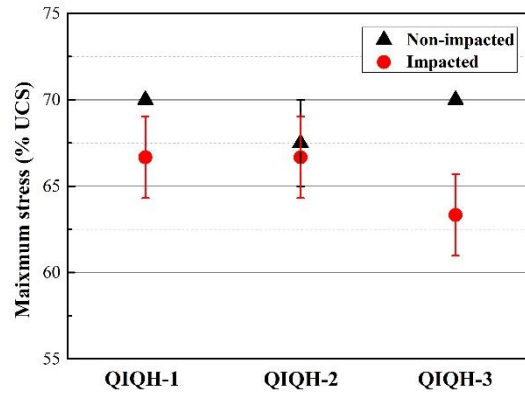


Figure 5-30. Comparison of fatigue limits between non-impacted and impacted specimens

5.4.3 S-N curves

A comparison of determined S-N curves between non-impacted and impacted specimens is depicted in **Figure 5-31**. To avoid confusion, only the curves corresponding to $N_{fl} = 10^6$ cycles are illustrated in the figure. As can be seen from the figure, the S-N curves of non-impacted specimens are located above those of impacted specimens. This implies that the fatigue life of impacted specimens is shorter than that of non-impacted specimens under the same maximum stresses. Moreover, it is observed that the fatigue strength of specimens with impact damage decreased more rapidly than that of the specimens without impact. It is different from the observations in the study of Uda et al [168] and N.H. Tai et al [260] where the S-N curves of impacted QI CFRP laminates are found to be parallel with those of non-impacted ones.

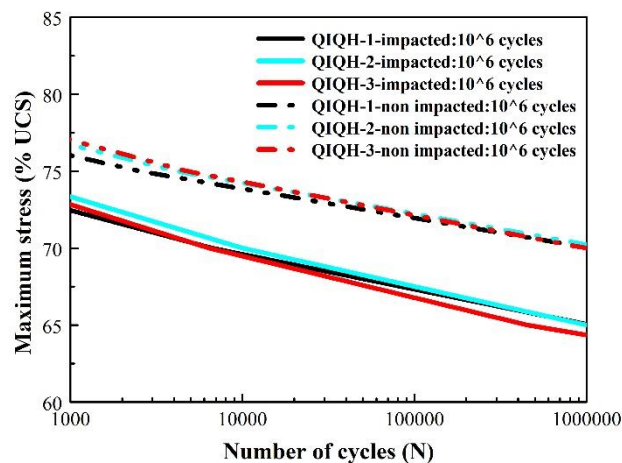


Figure 5-31. Comparison of predicted S-N curves ($N_{fl} = 10^6$ cycles) between non-impacted and impacted specimens

5.4.4 Fracture surface observations

The fracture surfaces of static compression (**Figure 4-10**) and CAI specimens (**Figure 5-21**) are first compared with each other. For both impacted and non-impacted specimens, on the one side, short cracks oriented the same as the fiber orientation of first ply are observed near the two free edges of the specimens. On another side, both cracks run through the width of specimens and the orientation of the cracks is generally influenced by the fiber orientation of first four plies. However, more cracks are observed always on back side for impacted specimens, while for non-impacted specimens the side where have more cracks can be arbitrary. Moreover, for impacted specimens, the cross-section cracking runs through the impact site, while that for non-impacted specimens can be located at any section.

The fracture surfaces of the specimens under compression fatigue loading can be quite different. For all of non-impacted specimens (**Figure 4-18**), much more cracks are observed on the surface with first ply fiber oriented in 0° . In the other fracture surfaces, only short cracks oriented as the fiber direction of the first ply are observed near the edges of the specimens. It seems that the first ply fibers at 0° promote local buckling under fatigue compressive loading. This surface should be compressive side at final fracture caused by buckling-flexion. However, for all the impacted specimens under compressive fatigue loading (**Figure 5-29**), more cracks can be observed on front side. The propagation of delamination zone should be much more rapid at front side than that at back side. The direction of the overall cracking is nearly along the cross-section in the damaged zone.

5.5 Chapter summary

In this chapter, the compression after impact (CAI) and post-impact compression fatigue behavior of QIQH laminates were investigated.

The preliminary impact tests were first conducted to determine the optimal impact energy for the subsequent impact tests. The QIQH laminates with three different stacking sequences

were subjected to the impact tests with the pre-determined impact energy. The impact test results of different stacking sequences were found to be similar with each other, which means that the stacking sequence does not influence their impact behavior if they are QIQH and their loading is asymmetrical. The visual combined with microscopic inspections shows there is only slight indentation on the front surface and a relatively small number of matrix cracks orientated as the fiber direction of last ply on the back surface. The C-scan results show that the projected delamination is in a circular shape, with delamination area around 547.7 ± 13.7 mm². The delamination area of different stacking sequences are similar to each other, which indicates that the influence of stacking sequence on the delamination area is not significant.

Thereafter, the impacted specimens were subjected to the compression tests to determine the CAI strength for the post-impact fatigue tests. The results of CAI tests revealed that the load-displacement curves, UCS and initial stiffness, measured on the load-displacement curves, of QIQH laminates with three different stacking sequences are similar with each other. Only an average reduction of 2.30% and 2.08% in the UCS and slope of load-displacement curve were observed for the impacted specimens, compared to those without impact. It conduces to suggest that the impact energy chosen is below impact threshold energy. Visual inspection of the CAI specimens after failure shows that the except for two specimens which failed in LGM mode, all the other seven specimens failed in LDM mode. Detailed observation of failure surfaces shows that on the front surfaces of QIQH-1 and 2, short cracks oriented in the same direction as the fiber orientation of first ply can be seen near the two free edges of specimens. For QIQH-3, the second ply also have an influence on the orientation of cracks. As for the back surfaces, all the cracks run through the width of specimens. The adjacent ply even sub-adjacent plies, as well as their interface play an important role in the crack propagation process of the QIQH specimens under CAI loading.

The fatigue limit determination method and fatigue life prediction model proposed in chapter 2 and in chapter 3 have been applied to post-impact compression fatigue QIQH specimens.

The fatigue limit was determined as 65% UCS and the S-N curves were well predicted by the model for each stacking sequence. In fact, if all the S-N curves for each specimen are compared together, the influence of stacking sequence on S-N curve is shown to be negligible. So, an “average” S-N curve representative of all the three QIQH stacking sequences is determined by applying the protocol proposed in section 3.3.

Finally, the mechanical behavior of impacted specimen and non-impacted specimen is compared at the end of this chapter. Under static loading, even though the impacted specimens have practically the same compression strength and stiffness as that of non-impacted specimens, their damage process is not the same. In impacted specimen, the existence of impact damage promotes the onset of local buckling. Therefore, the start of damage propagation of impacted specimens is earlier compared to the non-impacted specimens.

Under compressive fatigue loading, determined fatigue limit and fatigue lives of non-impacted and impacted specimens were compared. A slight reduction between 1.23 and 9.53% in the determined fatigue limits was observed for the impacted specimens, compared to non-impacted specimens. Concerning S-N curves, for a given stacking sequence, the maximum stress of impacted specimens decreases more rapidly as a function of number of loading cycles than non-impacted specimens.

When we compare the fracture surfaces between impacted and non-impacted specimens under static compression loading, it is shown that more cracks are observed always on back side for impacted specimens, while for non-impacted specimens the side where have more cracks can be arbitrary. Under compression fatigue loading the fracture surfaces of the specimens can be quite different. For all the non-impacted specimens, much more cracks are observed on the surface with first ply fiber oriented in 0° . It seems that the first ply fibers à 0° promote local buckling under fatigue compressive loading. This surface should be compressive side at final

fracture caused by buckling-flexion. However, in all the impacted specimens under compressive fatigue loading, more cracks can be observed on front side. The propagation of delamination zone should be much more rapid at front side than that at back side. The direction of the overall cracking is nearly along the cross section in the damaged zone.

Conclusions and perspectives

In this thesis, new methodologies are developed to determine fatigue properties of MD CFRP laminates in a short time, based on IRT data. Then, this developed method has been applied to study the compression and CAI behaviors of QIQH CFRP laminates with different stacking sequences under static and fatigue loading. The main contributions of this work can be cited as follows:

1. A new fatigue limit determination method is proposed to overcome the limit of graphic methods (Risitano and Luong's method) when the thermographic data does not satisfy the assumption of these methods. Normalized angle change calculated based on the thermographic data is used to describe the temperature increase rate. The stress amplitude corresponding to the peak value of normalized angle change is defined as the fatigue limit. The method was validated by the experimental data of cross-ply and QI CFRP laminates under tensile fatigue loading. The data of various composite materials with different stacking sequences in the literature has been analyzed to evaluate this new method. It is demonstrated that the proposed method allows to determine the fatigue limit for a large number of materials, very close to that measured by traditional fatigue test. The relative difference between traditional fatigue test results and that determined by the proposed method is less than 13.04% for all data from literature and from the tests in this study.
2. In order to determine the whole fatigue life as a function of applied stress level, in terms of S-N curve, a fatigue life model, which combines the stiffness degradation with thermographic data, has been proposed in previous study. This model has been successfully applied to UD and angle-ply ($\pm 45^\circ$) CFRP laminates but it failed for some MD laminates. This model is so modified in this study so as to take into account of more complex damage mechanisms in MD laminates. Firstly, for each tested specimen the

variable “stabilized temperature rise” at a loading level used in the original model is replaced by “stabilized temperature rise normalized by its maximum value”: $\overline{\Delta T_{stab}^*}$. This modification facilitates the comparison between the results from different specimens. Secondly, a new parameter r is introduced into the expression of residual stiffness to overcome the conservative predictions resulted from the original model. The modified model is firstly verified by the experimental results of cross-ply CFRP laminates, and then successfully applied to QI CFRP laminates. It is observed that for both stacking sequences, the S-N curves corresponding to $N_{fl} = 10^7$ cycles predicted by the modified model lie totally within the 95% confidence intervals of traditional fatigue test results.

3. In order to reduce the error of the results from the measurement of temperature change, the influence of loading step length on thermographic data has been discussed. For composite materials, not more than 5% UTS as loading step length has been recommended. Moreover, a protocol was proposed to determine an ‘average’ more reliable S-N curve from the individual predicted S-N curves of several specimens. First, each test must be carried out on a number of specimens until at least the fatigue limits of two specimens are identical; Then, the ‘new’ fatigue limit and corresponding stabilized temperature rise are determined based on the data of average normalized stabilized temperature rise $\overline{\Delta T_{stab}^*}$ as a function of maximum stress σ , using the method proposed in chapter 2. Thereafter, the parameters of p , q and r are determined based on the data of averaged normalized stiffness degradation and corresponding average normalized stabilized temperature rise $\overline{\Delta T_{stab}^*}$ and number of cycles, by 3D surface fitting with help of a program in MATLAB[®]. Then, in the next step, the failure threshold stiffness corresponding to $N_{fl} = 10^6$ cycles and 10^7 cycles could be computed by the modified normalized stiffness degradation model proposed in chapter 3. And finally, the more reliable ‘average’ S-N curves ($N_{fl} = 10^6$ cycles and 10^7 cycles) can be obtained. This protocol has been evaluated by experimental data of cross-ply laminates, the results seem convincing.

4. To extend the scope of application of proposed methodologies, the fatigue limit determination method and fatigue life model stated above were applied to the QIQH CFRP laminates with different stacking sequences under compression loading. The results of static compression tests show that the load-displacement curves, UCS and stiffness of three different stacking sequences are similar. The results of compression fatigue tests monitored by IRT imply that fatigue limits of different QIQH laminates determined by the proposed method are all 70% UCS. Besides, the predicted S-N curves of three different stacking sequences are close to each other. If all specimens in the same population is considered, an overall 'average' S-N curve can be determined based on the individual predicted S-N curves of 4 specimens having identical fatigue limits. So, this S-N curve is representative of all specimens of three QIQH stacking sequences. After static and fatigue tests, a fractographic study has been realized. The observation on the fracture surfaces of each specimen can be summarized as:

- for a given specimen, much more cracks across the section can be observed on one surface, and a few cracks at the edges of another surface. Because final fracture of the specimens under compression occurs due to buckling-flexion combination, the side with more cracks should be the compressive side due to flexion (C-side) and that with few cracks tensile side (T-side);
- under static loading, C-side is arbitrary, where the crack's orientation can be not only along the fiber direction of the surface ply, but also along the fiber orientation of the adjacent even sub-adjacent plies; while under fatigue compression loading, the C-side is always the surface having the first ply fibers at 0° whatever the stacking sequence;
- different morphology on the fracture surfaces of the specimens with different stacking sequence indicates that even though the global properties of QIQH laminates under compression do not be impacted by their stacking sequence, the damage propagation process is different in one stacking sequence from others.

5. In the study of impact, CAI and post-impact compression fatigue behavior of QIQH specimens, the influence of stacking sequence is also shown insignificant. All the tested laminates gave similar impact results (load-time, energy-time, load-displacement) under the same impact condition. Visual/microscope observation of indentation and C-scan inspection also gave similar results. The CAI strengths of three different laminates are also similar to each other, so does the damage modes. Under compression fatigue loading, the determined fatigue limits on the impacted specimens of different stacking sequences are nearly the same (65% UCS) and the predicted S-N curves are also close to each other. The overall 'average' more reliable S-N curves calculated based on the individual predicted S-N curves of 6 specimens with identical determined fatigue limits but three different stacking sequences were also obtained.

The observation on the fracture surfaces of CAI and post-impact compression fatigue specimens can be summarized as:

- the cross-section cracking is always located at the damaged zone introduced par impact;
- under static loading, C-side is always on back side, while under post impact compression fatigue loading, the C-side is always on the front side.
- different morphology on the fracture surfaces of the specimens with different stacking sequence indicates that even though the global properties of QIQH laminates under CAI and under post-impact compression fatigue do not be affected by their stacking sequence, but the damage propagation process is different in one stacking sequence from others.

6. Comparing the impacted specimens with non-impacted ones, under static compression loading, the global strength and the initial stiffness have essentially the same values. However, the existence of impact damages in impacted specimens promotes the onset of local buckling. Therefore, the start of stiffness degradation in the load-displacement curves of impacted specimens is earlier than that of non-impacted specimens and the damage propagation process is different. Under compression fatigue loading, the

reduction between 1.23% and 9.53% is observed in the determined fatigue limits of impacted specimens, while the predicted S-N curves of impacted specimens are also shown less strength than those of non-impacted laminates. The fractographic study has shown that under static compressive loading, the C-side is arbitrary for non-impacted laminate, while for impacted ones, the C-side is always at back side. However, under compressive fatigue loading, the C-side is always located on the side whose first ply has the fibers at 0° for non-impacted specimens, while for impacted specimens, the C-side is found on impact front side whatever the stacking sequence is. Moreover, the crack orientations on C-side of non-impacted compression fatigue specimens are mainly influenced by the fiber orientations of their first four plies, but in the post-impact fatigue specimens, only the influence of first ply is seen. Concerning the final cracking, the path of cracking throughout the cross section follows a zigzag pattern, accompanied by 0° fiber splitting in unimpacted specimens, while in impacted specimens under compression fatigue loading, the cracking runs throughout the width of the section damaged by impact with linear manner.

This work still leaves many questions unanswered and gives rise to ideas to be explored. Here are a number of perspectives from this work:

- Experimental aspect

1. Based on thermographic data, the proposed method for rapid determination of fatigue limit of composite laminates, the modified model for the establishment of a more reliable S-N curve, as well as the protocol proposed in this study need to be further validated by more experimental results, especially by the results from traditional fatigue tests;
2. To characterize fatigue behavior of impacted laminates, it is interesting to know what is the best choice of the calibrated area on which the temperature rise will be measured, and to understand its influence on measured fatigue properties;
3. More investigation is required to have a better understanding of the damage propagation and damage mechanisms during the fatigue tests of QIQH laminates with three different

stacking sequences, which may be achieved by performing stop-tests and by using different NDT methods, such as in-situ C-scan, Tomography, DIC, Acoustic emission, Scanning Electron Microscope (SEM)...

- Theoretical aspect

4. More theoretical framework is needed to explain the mechanisms of heat generation during fatigue tests and their transmission in composite laminates;
5. Analysis of 3D stresses state in MD laminates, especially to determine all interlaminar stresses at different interfaces of QIQH laminates is recommended;
6. Development of damage onset criterion to translate the physical phenomena observed during the experimentation is required.

- Numerical aspect

7. It is important to be able to perform numerical simulations of fatigue tests. On the one hand, the associated numerical thermomechanical model will enable us to understand the damage process and heat generation and transfer in MD laminates under different loading conditions; on the other hand, through the dialogue of experimental and numerical results, the more robust numerical models including more physical phenomena could be validated, which in turn could predict the residual fatigue life of in-service structures and aid in engineering design. For CAI and post-impact compression fatigue tests, the numerical simulation consists to:

- Modelling of impact tests to obtain the damage detail in the QIQH laminates
- Modelling CAI tests to understand the damage propagation
- Modelling Post-impact compression tests to predict fatigue life and fatigue limit
- Modelling the self-heating phenomena in MD laminates and the interaction between heat generation, heat transfer and damage propagation in the material...

References

- [1] Pascual F G, Meeker W Q. Estimating fatigue curves with the random fatigue-limit model. *Technometrics*, 1999, 41(4): 277-289.
- [2] Feng Y, Gao C, He Y, An T, Fan C, Zhang H. Investigation on tension–tension fatigue performances and reliability fatigue life of T700/MTM46 composite laminates. *Composite Structures*, 2016, 136: 64-74.
- [3] Harris B. *Fatigue in composites*. Cambridge: Woolhead Publishing Ltd, 2003.
- [4] Fargione G, Giudice F, Risitano A. The influence of the load frequency on the high cycle fatigue behaviour. *Theoretical and Applied Fracture Mechanics*, 2017, 88: 97-106.
- [5] Mohammadi B, Fazlali B. Off-axis fatigue behaviour of unidirectional laminates based on a microscale fatigue damage model under different stress ratios. *International Journal of Fatigue*, 2018, 106: 11-23.
- [6] Lopes H P, Elias C N, Vieira M V B, Vieira V T, de Souza L C, Dos Santos A L. Influence of surface roughness on the fatigue life of nickel-titanium rotary endodontic instruments. *Journal of Endodontics*, 2016, 42(6): 965-968.
- [7] Bagehorn S, Wehr J, Maier H J. Application of mechanical surface finishing processes for roughness reduction and fatigue improvement of additively manufactured Ti-6Al-4V parts. *International Journal of Fatigue*, 2017, 102: 135-142.
- [8] Brunbauer J, Pinter G. Effects of mean stress and fibre volume content on the fatigue-induced damage mechanisms in CFRP. *International Journal of Fatigue*, 2015, 75: 28-38.
- [9] Brunbauer J, Stadler H, Pinter G. Mechanical properties, fatigue damage and microstructure of carbon/epoxy laminates depending on fibre volume content. *International Journal of Fatigue*, 2015, 70: 85-92.
- [10] Gamstedt E K, Talreja R. Fatigue damage mechanisms in unidirectional carbon-fibre-reinforced plastics. *Journal of Materials Science*, 1999, 34(11): 2535-2546.
- [11] Dong H, Li Z, Wang J, Karihaloo B L. A new fatigue failure theory for multidirectional fiber-reinforced composite laminates with arbitrary stacking sequence. *International Journal of Fatigue*, 2016, 87: 294-300.
- [12] Vedrtnam A. Novel method for improving fatigue behavior of carbon fiber reinforced epoxy composite. *Composites Part B: Engineering*, 2019, 157: 305-321.
- [13] Large-Toumi B, Salvia M, Vincent L. Fiber-matrix interface effect on monotonic and fatigue behavior of unidirectional carbon/epoxy composites, fiber, matrix, and interface properties. *ASTM International*, 1996, 1290: 182-200.
- [14] Huang Y, Li S X, Lin S E, Shih C N. Using the method of infrared sensing for monitoring fatigue process of metals. *Materials Evaluation (United States)*, 1984, 42(8).
- [15] Jiang L, Wang H, Liaw P K, Brooks C R, Chen L, Klarstrom D L. Temperature evolution and life prediction in fatigue of superalloys. *Metallurgical and Materials Transactions A*, 2004, 35(3): 839-848.

- [16] Yang B, Liaw P K, Wang G, Morrison M, Liu C T, Buchanan R A, Yokoyama Y. In-situ thermographic observation of mechanical damage in bulk-metallic glasses during fatigue and tensile experiments. *Intermetallics*, 2004, 12(10-11): 1265-1274.
- [17] Huang J, Pastor M L, Garnier C, Gong X. Rapid evaluation of fatigue limit on thermographic data analysis. *International Journal of Fatigue*, 2017, 104: 293-301.
- [18] Huang J, Pastor M L, Garnier C, Gong X J. A new model for fatigue life prediction based on infrared thermography and degradation process for CFRP composite laminates. *International Journal of Fatigue*, 2019, 120: 87-95.
- [19] Huang J, Garnier C, Pastor M L, Gong X. Investigation of self-heating and life prediction in CFRP laminates under cyclic shear loading condition based on the infrared thermographic data. *Engineering Fracture Mechanics*, 2020, 229: 106971.
- [20] Auer J A, Von Rechenberg B, Bohner M, Hofmann-Antenbrink M. Bone grafts and bone replacements. *Equine Surgery*, 2012, 1081-1096.
- [21] Morales Ibarra R. Carbon fiber recovery using subcritical and supercritical fluids for chemical recycling of thermoset composite materials. 2014, 15.
- [22] Mouritz A P. Introduction to aerospace materials. Elsevier, 2012, 16: 394–410.
- [23] Khayal O. Advancements in polymer composite structures. 2019.
- [24] Fazeli M, Florez J P, Simão R A. Improvement in adhesion of cellulose fibers to the thermoplastic starch matrix by plasma treatment modification. *Composites Part B: Engineering*, 2019, 163: 207-216.
- [25] Y. Liu, B. Zwingmann, M. Schlaich, Carbon fiber reinforced polymer for cable structures—A review, *Polymers* 7(10) (2015) 1501.
- [26] Sekaran S C, Yap H J, Liew K E, Kamaruzzaman H, Tan C H, Rajab R S. Haptic-based virtual reality system to enhance actual aerospace composite panel drilling training. *Structural health monitoring of biocomposites, fibre-reinforced composites and hybrid composites*. Woodhead Publishing, 2019, 113-128.
- [27] Ozkan D, Gok M S, Karaoglanli A C. Carbon fiber reinforced polymer (CFRP) composite materials, their characteristic properties, industrial application areas and their machinability. *Engineering Design Applications III*. Springer, Cham, 2020, 235-253.
- [28] Syamsir A, Nor N M. Comparative study on Aluminium alloy and carbon fiber reinforced polymer (cfrp) for military bridges. *Conference on Engineering and Technology Education*, 2010.
- [29] Hamada H, Oya N, Yamashita K, Maekawa Z I. Tensile strength and its scatter of unidirectional carbon fibre reinforced composites. *Journal of Reinforced Plastics and Composites*, 1997, 16(2): 119-130.
- [30] Mallick P K. *Fiber-reinforced composites: materials, manufacturing, and design*. CRC press, 2007.
- [31] Chae H G, Kumar S. Making strong fibers. *Science*, 2008, 319(5865): 908-909.
- [32] Pozegic T R, Anguita J V, Hamerton I, Ayawardena K D I, Chen J S, Stolojan V, Walsh R, Silva, S R P. Multi-functional carbon fibre composites using carbon nanotubes as an alternative to polymer sizing. *Scientific reports*, 2016, 6(1): 1-11.

- [33] Crutchlow R. Changing from open to closed moulding. *Reinforced Plastics*, 2004, 48(8): 40-41.
- [34] Jaafar M, Shawkataly A K. Properties of bagasse fibre-reinforced unsaturated polyester (USP) composites. *Research on natural fibre: reinforced polymer composite*, 2009: 63-83.
- [35] Yi X S, Du S, Zhang L. *Composite Materials Engineering, Volume 2*. Berlin/Heidelberg, Germany: Springer, 2018:54.
- [36] Tatara R A. Compression molding. *Applied plastics engineering handbook*. William Andrew Publishing, 2017: 291-320.
- [37] Mazumdar S. *Composites manufacturing: materials, product, and process engineering*. CrC press, 2001.
- [38] Sapuan S M. *Composite materials: Concurrent engineering approach*. Butterworth-Heinemann, 2017: 80.
- [39] Open molding - processes. CompositesLab. (n.d.). Retrieved May 25, 2022, from <http://compositeslab.com/composites-manufacturing-processes/open-molding/>
- [40] Closed molding - processes. CompositesLab. (n.d.). Retrieved May 25, 2022, from <http://compositeslab.com/composites-manufacturing-processes/closed-molding/>
- [41] Soutis C. Fibre reinforced composites in aircraft construction. *Progress in aerospace sciences*, 2005, 41(2): 143-151.
- [42] Vosteen L F, Hadcock R N. *Composite chronicles: a study of the lessons learned in the development, production, and service of composite structures*. NASA, 1994: 27-43.
- [43] Wanhill R J H. *Carbon fibre polymer matrix structural composites*. Aerospace materials and material technologies. Springer, Singapore, 2017: 309-341.
- [44] Chalmers D W. The potential for the use of composite materials in marine structures. *Marine structures*, 1994, 7(2-5): 441-456.
- [45] Rubino F, Nisticò A, Tucci F, Carlone P. Marine application of fiber reinforced composites: A review. *Journal of Marine Science and Engineering*, 2020, 8(1): 26.
- [46] Beardmore P. Composite structures for automobiles. *Composite structures*, 1986, 5(3): 163-176.
- [47] McConnell V P. Application of composites in sporting goods. *Comprehensive Composite materials*, 2000, 6: 787-809.
- [48] Hollaway L C. The evolution of and the way forward for advanced polymer composites in the civil infrastructure. *Construction and Building Materials*, 2003, 17(6-7): 365-378.
- [49] Tai N H, Ma C C M, Wu S H. Fatigue behaviour of carbon fibre/PEEK laminate composites. *Composites*, 1995, 26(8): 551-559.
- [50] Konur O, Matthews F L. Effect of the properties of the constituents on the fatigue performance of composites: a review. *Composites*, 1989, 20(4): 317-328.
- [51] Hiremath C, Senthilnathan K, Guha A, Tewari A. Effect of volume fraction on damage accumulation for a lattice arrangement of fibers in CFRP. *Materials Today: Proceedings*, 2015, 2(4-5): 2671-2678.
- [52] Talreja R. Fatigue of composite materials: damage mechanisms and fatigue-life diagrams. *Proceedings of the Royal Society of London. A. Mathematical and Physical Sciences*, 1981, 378(1775): 461-475.

- [53] Xin Q. Durability and reliability in diesel engine system design. *Diesel Engine System Design*, 2013: 113-202.
- [54] Müller C. Zur statistischen Auswertung experimenteller Wöhlerlinien. Clausthal-Zellerfeld, Germany: Universitätsbibliothek Clausthal, 2015.
- [55] Collins J A. Failure of materials in mechanical design: analysis, prediction, prevention. John Wiley & Sons, 1993.
- [56] Talreja R. Fatigue of composite materials. *Modern trends in composite laminates mechanics*. Springer, Vienna, 2003: 281-294.
- [57] Kellas S. Environmental effects of fatigue damage in notched carbon fibre composites. University of London, 1988.
- [58] Dorey G. Fracture of composites and damage tolerance. *Practical Considerations of Design, Fabrication and Tests for Composite Materials*. 1982, 6.
- [59] Cantwell W, Morton J, Curtis P. A study of the impact resistance and subsequent o-compression fatigue performance of non-woven and mixed-woven composites. Elsevier Science Publishing Co., Inc., *Structural Impact and Crashworthiness.*, 1984, 2: 521-531.
- [60] Kirk J N, Munro M, Beaumont P W R. The fracture energy of hybrid carbon and glass fibre composites. *Journal of materials science*, 1978, 13(10): 2197-2204.
- [61] Ogin S L, Brøndsted P, Zangenberg J. Composite materials: constituents, architecture, and generic damage. *Modeling Damage, Fatigue and Failure of Composite Materials*. Woodhead Publishing, 2016: 3-23.
- [62] Mohammadi B, Pakdel H. Fatigue driven matrix crack propagation in laminated composites. *Materials & Design*, 2018, 146: 108-115.
- [63] Ogin S L, Smith P A, Beaumont P W R. Matrix cracking and stiffness reduction during the fatigue of a (0/90) s GFRP laminate. *Composites Science and Technology*, 1985, 22(1): 23-31.
- [64] Smith P A, Wood J R. Poisson's ratio as a damage parameter in the static tensile loading of simple crossply laminates. *Composites Science and Technology*, 1990, 38(1): 85-93.
- [65] Boniface L. Damage development in fibre-reinforced plastics' laminates. University of Surrey, 1989.
- [66] Clyne T W, Hull D. An introduction to composite material. Cambridge university press, 2019.
- [67] Matthews F L, Rawlings R D. Composite materials: engineering and science. CRC press, 1999.
- [68] Olsson R. Factors influencing the interlaminar fracture toughness and its evaluation in composites. *STIN*, 1992, 93: 29076.
- [69] Cantwell W J, Morton J. The significance of damage and defects and their detection in composite materials: a review. *The journal of strain analysis for engineering design*, 1992, 27(1): 29-42.
- [70] Gamstedt E K, Andersen S I. Fatigue degradation and failure of rotating composite structures—materials characterisation and underlying mechanisms. Riso National Laboratory, Denmark, 2001.
- [71] Mehrman J M. Effect of Hold Times on Fatigue Behavior of NEXTEL (trademark) 720/Alumina Ceramic Matrix Composite at 1200 deg C in Air and in Steam Environment. Air force institute of technology Wright-Patterson Airforce Base Ohio school of engineering and management, 2005.

- [72] Bunsell A R, Ramirez J M H, Le Clerc C. Tensile fatigue of thermoplastic fibers. Handbook of Properties of Textile and Technical Fibres. Woodhead Publishing, 2018: 595-618.
- [73] Müller A, Weidner A, Biermann H. Influence of reinforcement geometry on the very high-cycle fatigue behavior of aluminium-matrix-composites. Materials Science Forum. Trans Tech Publications Ltd, 2015, 825: 150-157.
- [74] Agarwal K, Kuchipudi S K, Girard B, Houser M. Mechanical properties of fiber reinforced polymer composites: A comparative study of conventional and additive manufacturing methods. Journal of Composite Materials, 2018, 52(23): 3173-3181.
- [75] Yang W, Guo X, Guo Q, Fan J. Rapid evaluation for high-cycle fatigue reliability of metallic materials through quantitative thermography methodology. International Journal of Fatigue, 2019, 124: 461-472.
- [76] Yang W P, Fan J L, Guo Q, Guo X L. Experimental procedure for energy dissipation estimation during high-cycle fatigue loading of metallic material. Experimental Mechanics, 2020, 60(5): 695-712.
- [77] Callen H B. Thermodynamics and an Introduction to Thermostatistics. 1998, 164-167.
- [78] Lemaitre J, Chaboche J L. Mechanics of solid materials. Cambridge university press, 1994.
- [79] Boulanger T, Chrysochoos A, Mabru C, Galtier A. Calorimetric analysis of dissipative and thermoelastic effects associated with the fatigue behavior of steels. International journal of Fatigue, 2004, 26(3): 221-229.
- [80] Ireman P, Nguyen Q S. Using the gradients of temperature and internal parameters in continuum thermodynamics. Comptes Rendus Mécanique, 2004, 332(4): 249-255.
- [81] Chrysochoos A, Louche H. An infrared image processing to analyze the calorific effects accompanying strain localisation. International journal of engineering science, 2000, 38(16): 1759-1788.
- [82] Maquin F, Pierron F. Heat dissipation measurements in low stress cyclic loading of metallic materials: From internal friction to micro-plasticity. Mechanics of Materials, 2009, 41(8): 928-942.
- [83] Thomson W, Kelvin L. On the thermo-elastic and thermo-magnetic properties of matter. 2007.
- [84] Roesner H, Sathish S, Meyendorf N. Nondestructive characterization of fatigue damage with thermography. Nondestructive Evaluation of Materials and Composites V. International Society for Optics and Photonics, 2001, 4336: 167-175.
- [85] Meneghetti G. Analysis of the fatigue strength of a stainless steel based on the energy dissipation. International journal of fatigue, 2007, 29(1): 81-94.
- [86] Du S, Guo Z S, Zhang B, Wu Z. Cure kinetics of epoxy resin used for advanced composites. Polymer international, 2004, 53(9): 1343-1347.
- [87] Adams R D, Cawley P. A review of defect types and nondestructive testing techniques for composites and bonded joints. NDT international, 1988, 21(4): 208-222.
- [88] Yang S, Gu L, Gibson R F. Nondestructive detection of weak joints in adhesively bonded composite structures. Composite structures, 2001, 51(1): 63-71.
- [89] Palumbo D, Tamborrino R, Galietti U, Aversa P, Tati A, Luprano V A M. Ultrasonic analysis and lock-in thermography for debonding evaluation of composite adhesive joints. Ndt & E International, 2016,

78: 1-9.

- [90] Tamborrino R, Palumbo D, Galietti U, Aversa P, Chiozzi S, Luprano V A M. Assessment of the effect of defects on mechanical properties of adhesive bonded joints by using non destructive methods. *Composites Part B: Engineering*, 2016, 91: 337-345.
- [91] Planck M. The theory of heat radiation. *Entropie*, 1900, 144(190): 164.
- [92] The International System of Units (SI) (PDF) (9th ed.), Bureau International des Poids et Mesures, 2019: 129.
- [93] Derby J J, Yeckel A. Heat transfer analysis and design for bulk crystal growth: Perspectives on the Bridgman method. *Handbook of Crystal Growth*. Elsevier, 2015: 793-843.
- [94] Maldague X. NDT Techniques: Thermographic. *Encyclopedia of Materials: Science and Technology*, 2011: 6036-6039.
- [95] Maldague X. Applications of infrared thermography in nondestructive evaluation. *Trends in optical nondestructive testing*, 2000: 591-609.
- [96] Herraiz Á H, Marugán A P, Márquez F P G. A review on condition monitoring system for solar plants based on thermography. *Non-Destructive Testing and Condition Monitoring Techniques for Renewable Energy Industrial Assets*. Butterworth-Heinemann, 2020: 103-118.
- [97] Li Y, Zhang R, Li L, Bao P P, Zhang W, Yang Z W, Tian G, Ming A B. Temperature variation and damage characteristic of impacted CFRP laminate using infrared thermography: Experimental investigation. *International Journal of Fatigue*, 2018, 112: 130-137.
- [98] Liaw P K, Wang H, Jiang L, Yang B, Huang J Y, Kuo R C, Huang J G. Thermographic detection of fatigue damage of pressure vessel steels at 1,000 Hz and 20 Hz. *Scripta Materialia*, 2000, 42(4): 389-395.
- [99] B Yang, Thermographic detection of fatigue damage of reactor pressure vessel (RPV) steels. *Journal of Materials Engineering and Performance*, 2003, 12(3): 345-353.
- [100] Yang B, Liaw P K, Wang H, Jiang L, Huang J Y, Kuo R C, Huang J G. Thermographic investigation of the fatigue behavior of reactor pressure vessel steels. *Materials Science and Engineering: A*, 2001, 314(1-2): 131-139.
- [101] Naderi M, Khonsari M M. A thermodynamic approach to fatigue damage accumulation under variable loading. *Materials Science and Engineering: A*, 2010, 527(23): 6133-6139.
- [102] Naderi M, Kahirdeh A, Khonsari M M. Dissipated thermal energy and damage evolution of Glass/Epoxy using infrared thermography and acoustic emission. *Composites Part B: Engineering*, 2012, 43(3): 1613-1620.
- [103] Montesano J, Fawaz Z, Bougherara H. Non-destructive assessment of the fatigue strength and damage progression of satin woven fiber reinforced polymer matrix composites. *Composites Part B: Engineering*, 2015, 71: 122-130.
- [104] Steinberger R, Leitão T I V, Ladstätter E, Pinter G, Billinger W, Lang R W. Infrared thermographic techniques for non-destructive damage characterization of carbon fibre reinforced polymers during tensile fatigue testing. *International Journal of Fatigue*, 2006, 28(10): 1340-1347.

- [105] Dattoma V, Giancane S. Evaluation of energy of fatigue damage into GFRC through digital image correlation and thermography. *Composites Part B: Engineering*, 2013, 47: 283-289.
- [106] Charles J A, Appl F J, Francis J E. Thermographic determination of fatigue damage. 1978, 100 (2): 200-203.
- [107] Barile C, Casavola C, Pappaletta G, Pappalettere C. Analysis of crack propagation in stainless steel by comparing acoustic emissions and infrared thermography data. *Engineering Failure Analysis*, 2016, 69: 35-42.
- [108] Plekhov O, PALIN-LUC T, Saintier N, Uvarov S, Naimark O. Fatigue crack initiation and growth in a 35CrMo4 steel investigated by infrared thermography. *Fatigue & fracture of engineering materials & structures*, 2005, 28(1-2): 169-178.
- [109] Wagner D, Ranc N, Bathias C, Paris P C. Fatigue crack initiation detection by an infrared thermography method. *Fatigue & Fracture of Engineering Materials & Structures*, 2010, 33(1): 12-21.
- [110] Dassios K G, Kordatos E Z, Aggelis D G, Matikas T E. Crack growth monitoring in ceramic matrix composites by combined infrared thermography and acoustic emission. *Journal of the American Ceramic Society*, 2014, 97(1): 251-257.
- [111] Geraci A L, La Rosa G, Risitano A, Grech M. Determination of the fatigue limit of an austempered ductile iron using thermal infrared imagery. *Digital Photogrammetry and Remote Sensing'95. International Society for Optics and Photonics*, 1995, 2646: 306-317.
- [112] Geraci A, La Rosa G, Risitano A. On the new methodology for the determination of the fatigue limit of materials using thermal infrared techniques. *Risk minimization by experimental mechanics*, 1992, 23(20): 183-190.
- [113] La Rosa G, Risitano A. Thermographic methodology for rapid determination of the fatigue limit of materials and mechanical components. *International journal of fatigue*, 2000, 22(1): 65-73.
- [114] Fargione G, Geraci A, La Rosa G, Risitano A. Rapid determination of the fatigue curve by the thermographic method. *International journal of fatigue*, 2002, 24(1): 11-19.
- [115] Risitano A, Risitano G. Cumulative damage evaluation of steel using infrared thermography. *Theoretical and Applied Fracture Mechanics*, 2010, 54(2): 82-90.
- [116] Luong M P. Infrared thermographic scanning of fatigue in metals. *Nuclear engineering and design*, 1995, 158(2-3): 363-376.
- [117] Luong M P. Fatigue limit evaluation of metals using an infrared thermographic technique. *Mechanics of materials*, 1998, 28(1-4): 155-163.
- [118] Luong M P. Infrared thermography of fatigue in metals. *Thermosense XIV: An International Conference on Thermal Sensing and Imaging Diagnostic Applications. International Society for Optics and Photonics*, 1992, 1682: 222-233.
- [119] Luong M P, Van K D. Metal fatigue limit evaluation using infrared thermography. *Proceedings of AITA*, 1994: 245-253.
- [120] Ricotta M, Meneghetti G, Atzori B, Risitano G, Risitano A. Comparison of experimental thermal methods for the fatigue limit evaluation of a stainless steel. *Metals*, 2019, 9(6): 677.

- [121] Foti P, Santonocito D, Ferro P, Risitano G, Berto F. Determination of fatigue limit by static thermographic method and classic thermographic method on notched specimens. *Procedia Structural Integrity*, 2020, 26: 166-174.
- [122] Risitano G, Guglielmino E, Santonocito D. Energetic approach for the fatigue assessment of PE100. *Procedia Structural Integrity*, 2020, 26: 306-312.
- [123] Risitano G, Guglielmino E, Santonocito D. Rapid Energetic Approaches for the Fatigue Limit assessment in a medium carbon steel. *Procedia Structural Integrity*, 2021, 33: 748-756
- [124] Corigliano P, Crupi V. Fatigue analysis of Ti6Al4V/INCONEL 625 dissimilar welded joints. *Ocean Engineering*, 2021, 221: 108582.
- [125] Guo S, Liu X, Zhang H, Yan, Z., & Fang, H. Fatigue Performance Evaluation of AZ31B Magnesium Alloy Based on Statistical Analysis of Self-Heating. *Materials*, 2021, 14(9): 2251.
- [126] Adam T J, Exner W, Wierach P. Taurine-Modified Boehmite Nanoparticles for GFRP Wind Turbine Rotor Blade Fatigue Life Enhancement. *Materials*, 2021, 14(22): 6997.
- [127] Fargione G, Giudice F, Barbagallo R, et al. Combined experimental methods to assess the fatigue limit. *IOP Conference Series: Materials Science and Engineering*. IOP Publishing, 2022, 1214(1): 012014.
- [128] Paiva V E L, Gonzáles G L G, Vieira R D, Maneschy J E, Vieira R B, Freire J L F. Fatigue monitoring of a dented piping specimen using infrared thermography. *Pressure Vessels and Piping Conference*. American Society of Mechanical Engineers, 2018, 51586: V01AT01A034.
- [129] Lipski A. Determination of the SN curve and the fatigue limit by means of the thermographic method for ductile cast iron[C]. *AIP Conference Proceedings*. AIP Publishing LLC, 2018, 2028(1): 020008.
- [130] Corigliano P, Cucinotta F, Guglielmino E, Risitano G, Santonocito D. Thermographic analysis during tensile tests and fatigue assessment of S355 steel. *Procedia Structural Integrity*, 2019, 18: 280-286.
- [131] Giudice F, La Rosa G, Savio F L, Clienti, C. Comparison between thermal energy and acoustic emission for the fatigue behavior of steels. *Procedia Structural Integrity*, 2019, 18: 886-890.
- [132] Martins G C P, Bandeira C F C, Lima G W, de Castro J T P. Fatigue limit evaluations of Al 6351-T6 by thermographic and ϵN methods. *Journal of the Brazilian Society of Mechanical Sciences and Engineering*, 2021, 43(1): 1-14.
- [133] Hajshirmohammadi B, Khonsari M M. An approach for fatigue life prediction based on external heating. *International Journal of Mechanical Sciences*, 2021, 204: 106510.
- [134] Santonocito D, Cucinotta F, Guglielmino E, Risitano, G. Fatigue damage assessment of welded HDPE details evaluating their energy release. *Procedia Structural Integrity*, 2021, 33: 724-733.
- [135] Santonocito D, Foti P, Risitano G, Berto F. Fatigue damage assessment in AM polymers evaluating their energy release. *Procedia Structural Integrity*, 2021, 34: 211-220.
- [136] Li A, Huang J, Zhang C. Enabling rapid fatigue life prediction of short carbon fiber reinforced polyether-ether-ketone using a novel energy dissipation-based model. *Composite Structures*, 2021, 272: 114227.
- [137] Risitano G. Fatigue strength evaluation of PPGF35 by energy approach during mechanical tests.

- Frattura ed Integrità Strutturale, 2022, 16(59): 537-548.
- [138] Curà F, Curti G, Sesana R. A new iteration method for the thermographic determination of fatigue limit in steels. *International Journal of Fatigue*, 2005, 27(4): 453-459.
- [139] Huang J. Rapid determination of fatigue behaviour for carbon fiber reinforced polymer laminates based on thermodynamic phenomena observed by IR thermography. Toulouse 3, 2019.
- [140] Krapez J C, Pacou D, Gardette G. Lock-in thermography and fatigue limit of metals. OFFICE NATIONAL D ETUDES ET DE RECHERCHES AEROSPATIALES ONERA-PUBLICATIONS-TP, 2000 (187).
- [141] Krapez J C, Pacou D. Thermography detection of damage initiation during fatigue tests. *Thermosense XXIV. International Society for Optics and Photonics*, 2002, 4710: 435-449.
- [142] Krapez J C, Taillade F, Balageas D. Ultrasound-lockin-thermography NDE of composite plates with low power actuators. Experimental investigation of the influence of the Lamb wave frequency. *Quantitative InfraRed Thermography Journal*, 2005, 2(2): 191-206.
- [143] Kurilenko G A. Advanced infrared examining of the metals fatigue. *Proceedings of International workshop on Advanced Infrared Technology and Applications*. 1995: 253-262.
- [144] Bérard J Y, Rathery S, Béranger A S. Détermination de la limite d'endurance des matériaux par thermographie infrarouge. Application sur un bras de suspension. *Matériaux & Techniques*, 1998, 86(1-2): 55-57.
- [145] Bremond P, Potet P. Lock-in thermography: a tool to analyze and locate thermomechanical mechanisms in materials and structures. *Thermosense XXIII. International Society for Optics and Photonics*, 2001, 4360: 560-566.
- [146] Fargione G, Geraci A, La Rosa G, Risitano A. Rapid determination of the fatigue curve by the thermographic method. *International journal of fatigue*, 2002, 24(1): 11-19.
- [147] Amiri M, Khonsari M M. Rapid determination of fatigue failure based on temperature evolution: Fully reversed bending load. *International Journal of Fatigue*, 2010, 32(2): 382-389.
- [148] Amiri M, Khonsari M M. Life prediction of metals undergoing fatigue load based on temperature evolution. *Materials Science and Engineering: A*, 2010, 527(6): 1555-1559.
- [149] Ranc N, Wagner D, Paris P C. Study of thermal effects associated with crack propagation during very high cycle fatigue tests. *Acta Materialia*, 2008, 56(15): 4012-4021.
- [150] Jiang L, Wang H, Liaw P K, Brooks C R, Klarstrom D L. Characterization of the temperature evolution during high-cycle fatigue of the ULTIMET superalloy: experiment and theoretical modeling. *Metallurgical and Materials Transactions A*, 2001, 32(9): 2279-2296.
- [151] Rilo N F, Ferreira L M S. Experimental study of low-velocity impacts on glass-epoxy laminated composite plates. *International Journal of Mechanics and Materials in Design*, 2008, 4(3): 291-300.
- [152] Cantwell W J, Morton J. Geometrical effects in the low velocity impact response of CFRP. *Composite Structures*, 1989, 12(1): 39-59.
- [153] Suemasu H, Sasaji W, Aoki Y, Ishikawa T. Compressive behaviour of impact damaged laminates. *Proceedings of the 16th International Conference on Composite Materials, Kyoto*, 2007.

- [154] Guedra-Degeorges D. Recent advances to assess mono-and multi-delaminations behaviour of aerospace composites. *Composites science and technology*, 2006, 66(6): 796-806.
- [155] Davies G A O, Olsson R. Impact on composite structures. *The Aeronautical Journal*, 2004, 108(1089): 541-563.
- [156] Clark G. Modelling of impact damage in composite laminates. *Composites*, 1989, 20(3): 209-214.
- [157] Zheng D. Low velocity impact analysis of composite laminated plates. University of Akron, 2007.
- [158] Craven R, Iannucci L, Olsson R. Delamination buckling: A finite element study with realistic delamination shapes, multiple delaminations and fibre fracture cracks. *Composites Part A: Applied Science and Manufacturing*, 2010, 41(5): 684-692.
- [159] Heslehurst R B. *Defects and damage in composite materials and structures*. Boca Raton, FL, USA:: CRC press, 2014: 39.
- [160] Olsson R, Iwarsson J, Melin L G, Sjögren A, Solti J. Experiments and analysis of laminates with artificial damage. *Composites science and technology*, 2003, 63(2): 199-209.
- [161] Sjögren A, Krasnikovs A, Varna J. Experimental determination of elastic properties of impact damage in carbon fibre/epoxy laminates. *Composites Part A: Applied Science and Manufacturing*, 2001, 32(9): 1237-1242.
- [162] Schoeppner G A, Abrate S. Delamination threshold loads for low velocity impact on composite laminates. *Composites Part A: applied science and manufacturing*, 2000, 31(9): 903-915.
- [163] Bahei-El-Din Y A, Rajendran A M, Zikry M A. A micromechanical model for damage progression in woven composite systems. *International journal of solids and structures*, 2004, 41(9-10): 2307-2330.
- [164] Krajcinovic D. *Damage mechanics: accomplishments, trends and needs*. *International Journal of Solids and Structures*, 2000, 37(1-2): 267-277.
- [165] Elber W. *Failure mechanics in low-velocity impacts on thin composite plates*. National aeronautics and space administration Hampton V Langley research center, 1983.
- [166] Mitrovic M, Hahn H T, Carman G P, Shyprykevich P. Effect of loading parameters on the fatigue behavior of impact damaged composite laminates. *Composites Science and Technology*, 1999, 59(14): 2059-2078.
- [167] Stellbrink K K U. Influence of low-velocity impact on the fatigue behaviour of CFRP-laminates. *Fatigue and creep of composite materials*, 1982: 319-327.
- [168] Uda N, Ono K, Kunoo K. Compression fatigue failure of CFRP laminates with impact damage. *Composites Science and Technology*, 2009, 69(14): 2308-2314.
- [169] Broutman L J, Sahu S. A new theory to predict cumulative fatigue damage in fiberglass reinforced plastics. *Composite materials: Testing and design (second conference)*. ASTM International, 1972, 170-188.
- [170] Kang K W, Kim J K. Fatigue life prediction of impacted carbon/epoxy laminates under constant amplitude loading. *Composites Part A: Applied Science and Manufacturing*, 2004, 35(5): 529-535.
- [171] Hwang W, Han KS. Fatigue of composite laminates-damage model and life prediction. *Composite materials: fatigue and fracture, second volume*. ASTM International, 1989, 1012: 87-102.

- [172] Caprino G. Residual strength prediction of impacted CFRP laminates. *Journal of Composite Materials*, 1984, 18(6): 508-518.
- [173] Koo J M, Choi J H & Seok C S. Evaluation for residual strength and fatigue characteristics after impact in CFRP composites. *Composite Structures*, 2013, 105: 58-65.
- [174] de Vasconcellos D S, Sarasini F, Touchard F, Chocinski-Arnault L, Pucci M, Santulli C, Tirillò J, Iannace S, Sorrentino L. Influence of low velocity impact on fatigue behaviour of woven hemp fibre reinforced epoxy composites. *Composites Part B: Engineering*, 2014, 66: 46-57.
- [175] Epaarachchi J A, Clausen P D. An empirical model for fatigue behavior prediction of glass fibre-reinforced plastic composites for various stress ratios and test frequencies. *Composites Part A: Applied science and manufacturing*, 2003, 34(4): 313-326.
- [176] Kosmann N, Riecken B T, Schmutzler H, Knoll J B, Schulte K, Fiedler B. Evaluation of a critical impact energy in GFRP under fatigue loading. *Composites science and technology*, 2014, 102: 28-34.
- [177] Garnier C, Pastor M L, Lorrain B, Pantalé O. Fatigue behavior of impacted composite structures. *Composite Structures*, 2013, 100: 443-450.
- [178] Schmutzler H, Alder M, Kosmann N, Wittich H, Schulte K. Degradation monitoring of impact damaged carbon fibre reinforced polymers under fatigue loading with pulse phase thermography. *Composites Part B: Engineering*, 2014, 59: 221-229.
- [179] Tuo H, Wu T, Lu Z, Ma X. Evaluation of damage evolution of impacted composite laminates under fatigue loadings by infrared thermography and ultrasonic methods. *Polymer Testing*, 2021, 93: 106869.
- [180] Li Y, Yang Z, Zhu J, Ming A B, Zhang W, Zhang J Y. Investigation on the damage evolution in the impacted composite material based on active infrared thermography. *Ndt & E International*, 2016, 83: 114-122.
- [181] Li Y, Zhang W, Ming A, Yang Z W, Tian G. A new way for revealing the damage evolution of impacted CFRP laminate under compression-compression fatigue load based on thermographic images. *Composite Structures*, 2017, 176: 1-8.
- [182] Katunin A, Pivdiablyk I, Gornet L, Rozycki P. A hybrid method for determination of fatigue limit and non-destructive evaluation of composite structures after low-velocity impact loading. *Composites Part B: Engineering*, 2022, 238: 109898.
- [183] Ferri O M, Ebel T, Bormann R. Influence of surface quality and porosity on fatigue behaviour of Ti-6Al-4V components processed by MIM. *Materials Science and Engineering: A*, 2010, 527(7-8): 1800-1805.
- [184] ISO 527-4: 2021, *Plastics - Determination of tensile properties - Part 4: Test conditions for isotropic and orthotropic fibre-reinforced plastic composites*, 2021.
- [185] Li X, Saedifar M, Benedictus R, Zarouchas D. Damage accumulation analysis of cfrp cross-ply laminates under different tensile loading rates. *Composites Part C: Open Access*, 2020, 1: 100005.
- [186] Mohd Tahir M, Wang W X, Matsubara T. Failure behavior of quasi-isotropic carbon fiber-reinforced polyamide composites under tension. *Advanced Composite Materials*, 2018, 27(5): 483-497.
- [187] ASTM, D 3479/D 3479M-96. Standard test method for tension-tension fatigue of polymer matrix

- composite materials. ASTM, International, 2007.
- [188] Habtour E, Cole D P, Riddick J C, Weiss V, Robeson M, Sridharan R, Dasgupta A. Detection of fatigue damage precursor using a nonlinear vibration approach. *Structural Control and Health Monitoring*, 2016, 23(12): 1442-1463.
- [189] M'Saoubi R, Axinte D, Soo S L, Nobel C, Attia H, Kappmeyer G, Engin S, Sim W M. High performance cutting of advanced aerospace alloys and composite materials. *CIRP Annals*, 2015, 64(2): 557-580.
- [190] De Los Rios E R, Rodopoulos C A, Yates J R. A model to predict the fatigue life of fibre-reinforced titanium matrix composites under constant amplitude loading. *Fatigue & Fracture of Engineering Materials & Structures*, 1996, 19(5): 539-550.
- [191] Colombo C, Vergani L, Burman M. Static and fatigue characterisation of new basalt fibre reinforced composites. *Composite structures*, 2012, 94(3): 1165-1174.
- [192] Colombo C, Libonati F, Pezzani F, Salerno A, Vergani L. Fatigue behaviour of a GFRP laminate by thermographic measurements. *Procedia Engineering*, 2011, 10: 3518-3527.
- [193] Karama M. Determination of the fatigue limit of a carbon/epoxy composite using thermographic analysis. *Structural control and health monitoring*, 2011, 18(7): 781-789.
- [194] Bagheri Z S, El Sawi I, Bougherara H, Zdero R. Biomechanical fatigue analysis of an advanced new carbon fiber/flax/epoxy plate for bone fracture repair using conventional fatigue tests and thermography. *Journal of the mechanical behavior of biomedical materials*, 2014, 35: 27-38.
- [195] Gornet L, Westphal O, Burtin C, Bailleul J L, Rozycki P, Stainier L. Rapid determination of the high cycle fatigue limit curve of carbon fiber epoxy matrix composite laminates by thermography methodology: Tests and finite element simulations. *Procedia Engineering*, 2013, 66: 697-704.
- [196] Gornet L, Westphal O, Rozycki P, Stainier L, Kemlin G. Rapid determination of the fatigue properties of carbon fiber epoxy matrix composite laminates by self-heating tests. *ECCM16-16th European Conference on Composite Materials*, 2014.
- [197] Fernández-Canteli A, Castillo E, Argüelles A A, Fernández P, Canales M. Checking the fatigue limit from thermographic techniques by means of a probabilistic model of the epsilon–N field. *International journal of fatigue*, 2012, 39: 109-115.
- [198] Munier R, Doudard C, Calloch S, Weber B. Determination of high cycle fatigue properties of a wide range of steel sheet grades from self-heating measurements. *International Journal of Fatigue*, 2014, 63: 46-61.
- [199] Guo Q, Guo X. Research on high-cycle fatigue behavior of FV520B stainless steel based on intrinsic dissipation. *Materials & Design*, 2016, 90: 248-255.
- [200] Liu X, Zhang H, Yan Z, Wang W, Zhou Y, Zhang Q. Fatigue life prediction of AZ31B magnesium alloy and its welding joint through infrared thermography. *Theoretical and Applied Fracture Mechanics*, 2013, 67: 46-52.
- [201] Guo S, Zhou Y, Zhang H, Wang W, Sun K, Li Y. Thermographic analysis of the fatigue heating process for AZ31B magnesium alloy. *Materials & Design*, 2015, 65: 1172-1180.

- [202] Morabito A E, Dattoma V, Galietti U. Energy analysis of fatigue damage by thermographic technique. *Thermosense XXIV*. SPIE, 2002, 4710: 456-463.
- [203] Harizi W, Azzouz R, Martins A T, Hamdi K, Aboura Z, Khellil K. Electrical resistance variation during tensile and self-heating tests conducted on thermoplastic polymer-matrix composites. *Composite Structures*, 2019, 224: 111001.
- [204] Zhang H X, Wu G H, Yan Z F, Guo S F, Chen P D, Wang W X. An experimental analysis of fatigue behavior of AZ31B magnesium alloy welded joint based on infrared thermography. *Materials & Design*, 2014, 55: 785-791.
- [205] Guo S, Liu X, Zhang H, Yan Z, Zhang Z, Fang H. Thermographic study of AZ31B magnesium alloy under cyclic loading: Temperature evolution analysis and fatigue limit estimation. *Materials*, 2020, 13(22): 5209.
- [206] Lipski A. Accelerated determination of fatigue limit and SN curve by means of thermographic method for X5CrNi18-10 steel. *Acta Mechanica et Automatica*, 2016, 10(1): 22-27.
- [207] Krapez J C, Pacou D, Gardette G. Lock-in thermography and fatigue limit of metals. Office National d'études et de Recherches Aérospatiales ONERA-Publications-TP, 2000 (187).
- [208] Faria J J R, Fonseca L G A, de Faria A R, Cantisano A, Cunha T N, Jahed H, Montesano J. Determination of the fatigue behavior of mechanical components through infrared thermography. *Engineering Failure Analysis*, 2022, 134: 106018.
- [209] Ogawa Y, Horita T, Iwatani N, et al. Evaluation of fatigue strength based on dissipated energy for laser welds. *Engineering Proceedings*, 2021, 8(1): 6.
- [210] Kordatos E Z, Dassios K G, Aggelis D G, Matikas T E. Rapid evaluation of the fatigue limit in composites using infrared lock-in thermography and acoustic emission. *Mechanics Research Communications*, 2013, 54: 14-20.
- [211] Peyrac C, Jollivet T, Leray N, Lefebvre F, Westphal O, Gornet L. Self-heating method for fatigue limit determination on thermoplastic composites. *Procedia Engineering*, 2015, 133: 129-135.
- [212] Montesano J, Fawaz Z, Bougherara H. Use of infrared thermography to investigate the fatigue behavior of a carbon fiber reinforced polymer composite. *Composite structures*, 2013, 97: 76-83.
- [213] Shiri S, Yazdani M, Pourgol-Mohammad M. A fatigue damage accumulation model based on stiffness degradation of composite materials. *Materials & Design*, 2015, 88: 1290-1295.
- [214] Van Paepegem W, Degrieck J. Coupled residual stiffness and strength model for fatigue of fibre-reinforced composite materials. *Composites Science and Technology*, 2002, 62(5): 687-696.
- [215] Talreja R. Multi-scale modeling in damage mechanics of composite materials. *Journal of materials science*, 2006, 41(20): 6800-6812.
- [216] Jamison R D, Reifsnider K L, Schulte K, Stinchcomb W W. Characterization and analysis of damage mechanisms in tension-tension fatigue of graphite/epoxy laminates. *ASTM International*, 1984, 21-55.
- [217] Shokrieh M M, Lessard L B. Multiaxial fatigue behaviour of unidirectional plies based on uniaxial fatigue experiments - II. Experimental evaluation. *International Journal of Fatigue*, 1997, 19(3): 209-217.

- [218] Senthilnathan K, Hiremath C P, Naik N K, Guha A, Tewari A. Microstructural damage dependent stiffness prediction of unidirectional CFRP composite under cyclic loading. *Composites Part A: Applied Science and Manufacturing*, 2017, 100: 118-127.
- [219] Peng T, Liu Y, Saxena A, Goebel K. In-situ fatigue life prognosis for composite laminates based on stiffness degradation. *Composite Structures*, 2015, 132: 155-165.
- [220] Whitworth H A. A stiffness degradation model for composite laminates under fatigue loading. *Composite Structures*, 1997, 40(2): 95-101.
- [221] Tang R, Guo Y J, Weitsman Y J. An appropriate stiffness degradation parameter to monitor fatigue damage evolution in composites. *International Journal of Fatigue*, 2004, 26(4): 421-427.
- [222] Mao H, Mahadevan S. Fatigue damage modelling of composite materials. *Composite Structures*, 2002, 58(4): 405-410.
- [223] Tao C, Ji H, Qiu J, Wang Z, Yao W. Characterization of fatigue damages in composite laminates using Lamb wave velocity and prediction of residual life. *Composite Structures*, 2017, 166: 219-228.
- [224] Lee L J, Fu K E, Yang J N. Prediction of fatigue damage and life for composite laminates under service loading spectra. *Composites science and technology*, 1996, 56(6): 635-648.
- [225] Peng T, Liu Y, Saxena A, Goebel K. In-situ fatigue life prognosis for composite laminates based on stiffness degradation. *Composite Structures*, 2015, 132: 155-165.
- [226] Gamstedt E K, Talreja R. Fatigue damage mechanisms in unidirectional carbon-fibre-reinforced plastics. *Journal of materials science*, 1999, 34(11): 2535-2546.
- [227] Razvan A, Reifsnider K L. Fiber fracture and strength degradation in unidirectional graphite/epoxy composite materials. *Theoretical and applied fracture mechanics*, 1991, 16(1): 81-89.
- [228] Broutman L J, Sahu S. Progressive damage of a glass reinforced plastic during fatigue. *Proceedings of the 24th Annual Technical Conference, Society of the Plastics Industry*, 1969, 1-12.
- [229] Tohgo K, Nakagawa S, Kageyama K. Fatigue behavior of CFRP cross-ply laminates under on-axis and off-axis cyclic loading. *International Journal of Fatigue*, 2006, 28(10): 1254-1262.
- [230] Reifsnider K L, Jamison R. Fracture of fatigue-loaded composite laminates. *International Journal of Fatigue*, 1982, 4(4): 187-197.
- [231] International A. ASTM D7136/D7136M – 15, Standard Test Method for Measuring the Damage Resistance of a Fiber-Reinforced Polymer Matrix Composite to a Drop-Weight Impact Event. 2020.
- [232] Jones R M. *Mechanics of composite materials*. CRC press, 2018.
- [233] Tsai S W, Hahn H T. *Composite design guide*. Dayton, USA, 1985.
- [234] Tsai S W, Hahn H T. *Introduction to composite materials*. Routledge, 2018.
- [235] Vannucci P, Verchery G. A new method for generating fully isotropic laminates. *Composite Structures*, 2002, 58(1): 75-82.
- [236] Vannucci P, Verchery G. Stiffness design of laminates using the polar method. *International Journal of Solids and Structures*, 2001, 38(50-51): 9281-9294.
- [237] Verchery G. Designing with anisotropy. Part 1: Methods and general results for laminates. *Proceedings of ICCM*. 1999, 12.

- [238] Verchery G. Design rules for the laminate stiffness. *Mechanics of Composite Materials*, 2011, 47(1): 47-58.
- [239] Airbus Group, “A350 XWB composite bonded repair”, Flight Airworthiness Support Technology. Airbus technical Magazine, 2018, 61: 14.
- [240] International A. ASTM D7137/D7137M – 17, Standard test method for compressive residual strength properties of damaged polymer matrix composite plates. 2017.
- [241] Ramulu M. Machining and surface integrity of fibre-reinforced plastic composites. *Sadhana*, 1997, 22(3): 449-472.
- [242] Tuo H, Lu Z, Ma X, Zhang C, Chen S. An experimental and numerical investigation on low-velocity impact damage and compression-after-impact behavior of composite laminates. *Composites Part B: Engineering*, 2019, 167: 329-341.
- [243] Garnier C. Etude du comportement dynamique des structures composites réalisées par LRI: application à l’impact et à la fatigue. 2011.
- [244] Evci C, Gülgeç M. An experimental investigation on the impact response of composite materials. *International Journal of Impact Engineering*, 2012, 43: 40-51.
- [245] Panettieri E, Fanteria D, Montemurro M, Froustey C. Low-velocity impact tests on carbon/epoxy composite laminates: a benchmark study. *Composites Part B: Engineering*, 2016, 107: 9-21.
- [246] Sun C T. An analytical method for evaluation of impact damage energy of laminated composites. ASTM International, 1977.
- [247] Shyr T W, Pan Y H. Impact resistance and damage characteristics of composite laminates. *Composite structures*, 2003, 62(2): 193-203.
- [248] Davies GAO, Zhang X. Impact damage prediction in carbon composite structures. *International Journal of Impact Engineering*, 1995, 16(1): 149-170.
- [249] Dehkordi M T, Nosraty H, Shokrieh M M, Minak G, Ghelli D. Low velocity impact properties of intra-ply hybrid composites based on basalt and nylon woven fabrics. *Materials & Design*, 2010, 31(8): 3835-3844.
- [250] Wyrick D A, Adams D F. Residual strength of a carbon/epoxy composite material subjected to repeated impact. *Journal of Composite Materials*, 1988, 22(8): 749-765.
- [251] Xu Z, Yang F, Guan Z W, Cantwell W J. An experimental and numerical study on scaling effects in the low velocity impact response of CFRP laminates. *Composite Structures*, 2016, 154: 69-78.
- [252] Sztefek P, Olsson R. Tensile stiffness distribution in impacted composite laminates determined by an inverse method. *Composites Part A: Applied Science and Manufacturing*, 2008, 39(8): 1282-1293.
- [253] Ravandi M, Teo W S, Tran L Q N, Yong M S, Tay T E. Low velocity impact performance of stitched flax/epoxy composite laminates. *Composites Part B: Engineering*, 2017, 117: 89-100.
- [254] Tuo H, Lu Z, Ma X, Xing J, Zhang C. Damage and failure mechanism of thin composite laminates under low-velocity impact and compression-after-impact loading conditions. *Composites Part B: Engineering*, 2019, 163: 642-654.
- [255] AlOmari A S, Al-Athel K S, Arif A F M, Al-Sulaiman F A. Experimental and computational analysis

- of low-velocity impact on carbon-, Glass-and mixed-fiber composite plates. *Journal of Composites Science*, 2020, 4(4): 148.
- [256] James R, Joseph R, Giurgiutiu V. Impact damage detection in composite plates using acoustic emission signal signature identification. *Active and Passive Smart Structures and Integrated Systems XIV*. SPIE, 2020, 11376: 116-133.
- [257] Sun X C, Wisnom M R, Hallett S R. Interaction of inter-and intralaminar damage in scaled quasi-static indentation tests: Part 2–Numerical simulation. *Composite Structures*, 2016, 136: 727-742.
- [258] Sun X C, Hallett S R. Failure mechanisms and damage evolution of laminated composites under compression after impact (CAI): Experimental and numerical study. *Composites Part A: Applied Science and Manufacturing*, 2018, 104: 41-59.
- [259] Katunin A, Pivdiablyk I, Gornet L, Rozycki, P. A hybrid method for determination of fatigue limit and non-destructive evaluation of composite structures after low-velocity impact loading. *Composites Part B: Engineering*, 2022, 238: 109898.
- [260] Tai N H, Ma C C M, Lin J M, Wu, G. Y. Effects of thickness on the fatigue-behavior of quasi-isotropic carbon/epoxy composites before and after low energy impacts. *Composites Science and Technology*, 1999, 59(11): 1753-1762.

Relevant publications

- [1] Zijiao Jia, Marie-Laetitia Pastor, Christian Garnier, Xiaojing Gong. A new method for determination of fatigue limit of composite laminates based on thermographic data. *International Journal of Fatigue*. *International Journal of Fatigue*, 2023, 168: 107445.
- [2] Zijiao Jia, Marie-Laetitia Pastor, Christian Garnier, Xiaojing Gong. Fatigue life prediction based on infrared thermographic data for CFRP composite laminates (revised).
- [3] Zijiao Jia, Marie-Laetitia Pastor, Christian Garnier, Xiaojing Gong. Rapid fatigue life prediction of CFRP laminates by combining the data of self-heating with stiffness degradation. *Proceedings of the 20th European Conference on Composite Materials: composites meet sustainability*, 2022, 1: 1413-1420.
- [4] Xiaojing Gong, Marie-Laetitia Pastor, Christian Garnier, Zijiao Jia, Jia Huang. Détermination rapide des propriétés de fatigue des structures en composites stratifiés multidirectionnels basée sur la thermographie infrarouge (CNRIUT).
- [5] Zijiao Jia, Christian Garnier, Marie-Laetitia Pastor, Experimental investigation of impacted MultiDirectional (MD) laminates under compressive static and cyclic loading (Submitted).